Spectroscopic and Microscopic Characterisation of Carbon Nanostructures

HOUCHIN, RACHAEL,MAY

Spectroscopic and Microscopic Characterisation of Carbon Nanostructures

Rachael May Houchin

2011

Abstract

Currently, carbon nanotubes (CNTs) are produced using a variety of techniques which yield CNT materials with wide ranging levels of chemical purity and structural perfection. Consequently, characterising CNT materials accurately is of utmost importance if potential applications of CNTs are to be realised on a large scale. In this work four commercially available CNT samples are characterised using a number of techniques, namely: scanning electron microscopy (SEM); high resolution transmission microscopy (HRTEM); energy dispersive x-ray analysis (EDX); Auger electron spectroscopy (AES); low-loss electron energy loss spectroscopy (low-loss EELS); ultra-violet photoemission spectroscopy (UPS); x-ray photoemission spectroscopy (XPS) and Raman spectroscopy. The information provided by these techniques is assessed in their ability to characterise different CNT materials. The definition of CNT 'quality' is also discussed and the ability of these techniques to determine such a property is considered.

A significant part of ascertaining the 'quality' of a CNT sample lies in understanding the nature and number of defects in the walls of these materials. In this work, defects are introduced into the lattice of different CNT species using 1.5 keV Ar^+ ions and the effects are monitored using XPS. In particular, the resultant reactivity of irradiated CNTs to ambient atmospheric oxygen is investigated, which is found to be markedly enhanced for CNTs with one wall when compared to those with multiple walls. It is also demonstrated that the type of incident ion and irradiation dose can be used to selectively control the level and nature of the surface composition of oxygen functionalised SWCNTs.

Many applications of fullerenes require detailed understanding of how these molecules interact with surfaces and the perturbations this induces. In this work the interaction of C_{60} with highly ordered pyrolytic graphite (HOPG) and Ni(110) is studied using scanning tunnelling microscopy (STM), low energy electron diffraction (LEED), XPS and UPS. Investigation focuses on a novel two-dimensional solid-vapour phase in the C_{60}-HOPG system and the C_{60}-induced reconstruction of the Ni(110) surface.

Spectroscopic and Microscopic Characterisation of Carbon Nanostructures

Rachael May Houchin

A thesis presented for the degree of
Doctor of Philosophy

Department of Physics
University of Durham
2011

Contents

Abbreviations

1D	One-dimensional
2D	Two-dimensional
3D	Three-dimensional
5-1DB	Relaxed monovacancy in a SWCNT, comprising one pentagonal defect and a nine-membered ring containing one dangling bond (Chapters 5 and 6)
ΔA	Change in area (Chapter 7)
Δ	Change in particle coordination (Chapter 7)
θ	Diffraction angle
θ_C	Chiral angle
θ_E	Emission angle
θ_T	Take-off angle
λ	Wavelength
$\lambda(E_k)$	Inelastic mean free path
μ_m	Mass absorption constant
ν	Frequency
ρ	Density
σ_{ij}	Photoemission cross section of peak *I* from element *j*
φ	Workfunction
ϕ	Irradiation dose (Chapters 5 and 6)
Ψ *or* ψ	Electronic wavefunction
ω	Frequency
A	Atomic weight
A_s	Area occupied by solid (Chapter 7)
A_v	Area occupied by vapour (Chapter 7)
a	Distance between two lattice points
a_1, a_2	Unit vectors of the graphene lattice
$a_{c\text{-}c}$	Carbon-carbon bond length
AD	Arc-discharge
AES	Auger electron spectroscopy
BF	Bright field (image in TEM)

C	Mass thickness contrast (TEM)
C_{60}	Buckminsterfullerene
CB	Conduction band
CCVD	Catalytic carbon vapour deposition
$\boldsymbol{C_h}$	Chiral vector
CNT	Carbon nanotube
CVD	Chemical vapour deposition
D	Nanotube diameter
d	Width of potential barrier (in STM)
$\boldsymbol{d}_{hkl}$	Reciprocal lattice vector
DB	Dangling bond
DF	Dark field (image in TEM)
DOS	Density of states
DWCNT	Double-walled carbon nanotube
e	Electronic charge
E_a	Activation energy
E_b	Binding energy
E_{back}	Energy of a backscattered electron
E_n	Energy of atomic shell n
E_C	Energy threshold for ionisation
E_g	Energy gap
E_k	Kinetic energy
E_o	Energy of primary electrons
E_P	Plasmon energy
E_{pass}	Pass energy (XPS)
E_π	π-plasmon energy
E_S	Energy of a scattered electron
E_{second}	Energy of a secondary electron
EDX	Energy dispersive x-ray analysis
EELS	Electron energy loss spectroscopy
EM	Electron microscopy
FEL	Fast entry load-lock
FWHM	Full-width half-maximum
$\mathcal{H}(ij)$	Energy interaction between holes in energy levels i and j

h	Apparent height of a feature (in SPM)
(hkl)	Miller indices
hcp	Hexagonally close-packed
HiPCO	High pressure carbon monoxide disproportionation
HOMO	Highest occupied molecular orbital
HOPG	Highly oriented pyrolytic graphite
HRTEM	High resolution transmission electron microscopy
I	Current
I^*	Intensity (* indicates specific nature of that intensity)
IMFP	Inelastic mean free path
JDOS	Joint density of states
$\boldsymbol{k}^*$	Wavevector (* indicates nature of that wavevector)
k_B	Boltzmann constant
$\mathcal{L}$	Latent heat
L	Apparent width of a feature (in SPM)
$L_{display}$	Sample scale on display (in SEM)
L_{ik}	Angular asymmetry factor of orbital k
L_{sample}	Sample scale (in SEM)
LA	Laser ablation
LDOS	Local density of states
LEED	Low energy electron diffraction
LUMO	Lowest unoccupied molecular orbital
M	Magnification
m_e	Mass of an electron
m_e^*	Effective mass of an electron
ML	Monolayer (of C_{60})
MWCNT	Multiple-walled carbon nanotube
n	Number density
N_A	Avogadro constant
$\%n_i$	Atomic percent of element i
(n,m)	Hamada indices
$n_i(z)$	Concentration of element i at a distance z from surface
P	Pressure
P_{Auger}	Probability of Auger electron emission

$P_{fluorescence}$	Probability of fluorescence
P_{move}	Probability for a particle to move (Chapter 7)
PES	Photoemission spectroscopy
QH1	Partly commensurate hexagonal phase of C_{60} on Ni(110)
QH2	A phase of C_{60} on Ni(110) which comprises domains rotated by 30° to one another
QM	Quantum mechanical
R	Ideal gas constant
R_o	Mean radius of hemispherical analyser (in XPS)
R_{eff}	Effective tip radius (in SPM)
Raman	Raman spectroscopy
RBM	Radial breathing mode
RT	Room temperature
RTML	Room temperature monolayer
S	Scattering efficiency
SEM	Scanning electron microscopy
SPM	Scanning probe microscopy
STEM	Scanning transmission electron microscopy
STM	Scanning tunnelling microscopy
SWCNT	Single-walled carbon nanotube
T	Temperature
$\boldsymbol{T}$	Translation vector
t	Sample thickness (cm)
$T(E_k)$	Transmission function
TEM	Transmission electron microscopy
tMWCNT	Thin multiple-walled carbon nanotube
UHV	Ultra-high vacuum
UPS	Ultra-violet photoemission spectroscopy
VB	Valence band
VHS	Van Hove singularities
w	Analyser slit width (in XPS)
WDX	Wavelength dispersive x-ray analysis
XPS	X-ray photoemission spectroscopy
XRF	X-ray fluorescence
x	Distance (x-direction)

y	Distance (y-direction)
z	Distance (z-direction)
Z	Atomic number
ZLP	Zero-loss peak

Declaration

No part of this thesis has been submitted elsewhere for any other degree or qualification. The content of this thesis is the author's own work, unless stated in the text. All measurements and analysis were carried out by the author, with the exception of the following measurements: Chapter 4 SEM measurements were taken by Alex Jacobs in the Department of Physics, University of Durham. These images are presented in Figure 4.1 (a) to (d); Chapter 4 HRTEM; EDX measurements were taken by Dr. Vladimir Zaikovskii and Dr. Arcady Ischenko at the Boreskov Institute of Catalysis, Russia. These measurements are presented in: Figure4.1 (e) to (h), Figure 4.2; Figure 4.4 and Figure 4.5; Chapter 4 Raman measurements were taken by Dr. Lucas Applegarth in the Department of Chemistry, University of Durham. These results are presented in Figure 4.11; Chapter 5 O-Irradiation measurements were taken by Dr. Michael Hunt, Department of Physics, University of Durham. This data is presented in Figure 5.12 and Figure 5.13.

The following measurements were obtained by the author in conjunction with other people: EELS, AES and UPS measurements presented in Chapter 4 were obtained with the help of Dr Yuriy Butenko, Paul Coxon, and Dr. Michael Hunt; XPS measurements in Chapters 5 and 6 were obtained with the help of Dr. Michael Hunt; the atomistic simulation used in Chapter 7 was created with the help of Dr. Alexander Pym.

Acknowledgements

This thesis is the culmination of work carried out since October 2006. During this time I have had the fortune of meeting, collaborating with and receiving the help and support of many people, for which I am grateful.

In particular I would like to thank:

My Ph.D supervisor, Dr. Michael Hunt, for creating the opportunities without which this thesis would not exist;

Dr. Vin Dhanak at the University of Liverpool whose time, effort and resources led to the work presented in Chapter 7;

Dr. Danny Law, Dr. Graham Beamson and Bob Bilsborrow at the National Centre for Electron Spectroscopy and Surface Analysis for their technical support during the acquisition of the data that constitutes Chapters 5 and 6;

Dr. Lucas Applegarth, Dr. Yuriy Butenko, Paul Coxon, Dr. Arcady Ischenko, Alex Jacobs, Dr.Vladimir Zaikovskii for their time taken to perform the measurements presented in Chapter 4;

The technical staff in the Department of Physics, University of Durham;

George Miller and Andrew Malins (formerly of Daresbury Laboratory) for their willingness to offer support and equipment when it was needed;

Dr. Del Atkinson and Prof. Peter Hatton in the Department of Physics, University of Durham for conversations, support and motivation throughout my time at Durham;

My friends, who were always more than willing to provide a welcome distraction when it was most needed;

My parents whom I love dearly. They have striven to provide me with the very best education from a young age. Without them my love for learning – and now my ambitions to teach – would never have been realised.

For Moomin, Doofus and Sprog.

My family.

1. Introduction

This chapter presents an introduction to fullerenes and carbon nanotubes. The production methods of both types of carbon nanostructure are considered, and the electronic structure of these nanomaterials discussed. The current and potential applications of both fullerenes and carbon nanotubes are presented, placing the fundamental work carried out in this thesis into context.

1.1 Introduction to Carbon Nanostructures

In its commonly known forms of graphite and diamond, carbon is essential in many areas of industry, technology and manufacture. In 1985 the discovery of a new allotrope of carbon in the form of closed-shell molecules known as 'fullerenes' [1] opened up a new, wide ranging, area of research, with the promise of novel applications - now at the nanometre scale. This discovery was followed in 1991 by the (re-)discovery of extended, concentric fullerenes or 'carbon nanotubes' (CNTs) [2, 3]. The production of these carbon nanostructures can now be achieved in quantities which allow the development of an ever broadening area of nanoscale carbon-based research.

1.1.1 Bonding in Carbon

Elemental carbon has several different allotropes, ranging from the physically hard to the soft but chemically stable. The formation of such diverse materials from the same element arises from differences in the spatial arrangement of the atoms and in the bonding between them. Each carbon atom contains six electrons that, following Hund's rules, doubly occupy (spin up and spin down) the 1*s* and 2*s* orbitals and singly occupy two of the three 2*p* atomic orbitals when isolated and in the ground state. When a carbon atom bonds to atoms of the same or other elements, the wavefunctions of the four valence electrons which occupy the 2*s* and 2*p* atomic orbitals can mix, or hybridise. Different bonds occur depending on whether the 2*s* electronic wavefunction mixes with one, two, or all three 2*p* wavefunctions, known as *sp*, sp^2 and sp^3 hybridisation respectively. The energy cost for formation of the hybrid orbitals is offset by increased valence in the case of sp^2 and sp^3 hybridisation, or decreased electron overlap for *sp* hybridisation. The symmetries of the hybrid orbitals dictate the arrangement of atoms within the material under consideration (Figure 1.1). For example, sp^3 hybridised carbon has a tetragonal structure and is found in diamond, whilst sp^2 hybridised carbon has a planar structure and is found in carbon nanotubes.

Graphene, a single layer of graphite, represents the prototypical sp^2 hybridised carbon material and can be considered the 'parent' material of a variety of nano-carbons (fullerenes, nanotubes, carbon onions etc.) as well as being the subject of intense scientific investigation in its own right [4]. In the sp^2 state the three hybrid orbitals are arranged in a plane with an angle of 120º between them and an unmodified 2*p* orbital (conventionally

labelled $2p_z$) is oriented perpendicular to this plane. Bonding between the carbon atoms within the graphene layer occurs through the in-phase overlap of the sp^2 hybrid orbitals to form strong localised σ bonds and the (less efficient) overlap of the $2p_z$ atomic orbitals which form spatially delocalised π bonds. Out of phase overlap produces higher energy σ^* and π^* anti-bonding states associated with nodes in the electronic wavefunctions between the positions of the carbon nuclei. In undoped graphene only the bonding orbitals are occupied.

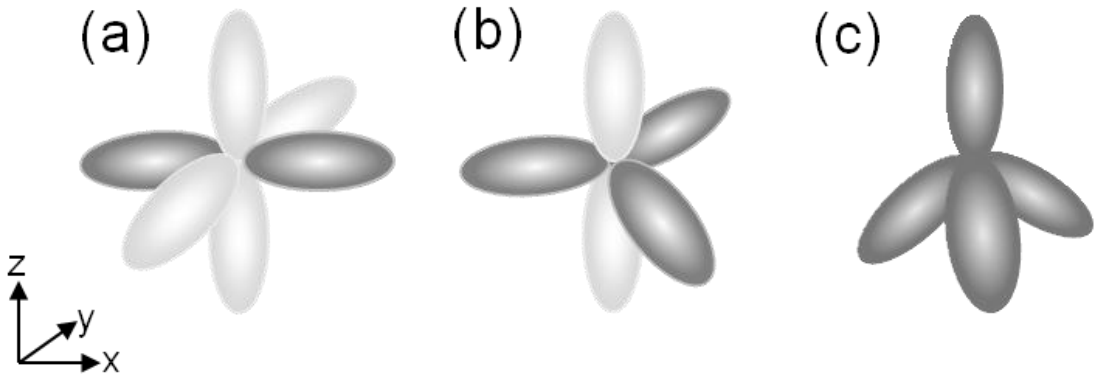

Figure 1.1

Schematic of the spatial arrangement of sp hybrid orbitals (shaded) (a) sp^2 orbitals (b) and sp^3 orbitals (c) [5].

The σ/σ^* and π/π^* band structure of graphene close to the Fermi level is shown in Figure 1.2 along a high symmetry direction in the Brillouin zone (Figure 1.3). Marked on this 'slice' through reciprocal space are the lowest (σ/σ^* (~6-10 eV) and π/π^* (~4.5-4.8 eV) [6]) optical interband transitions, which may be observed through electron energy loss spectroscopy (EELS) [7-9] in addition to optical techniques. It is apparent that only the π electrons are of importance when considering bands very near the Fermi level (red, Figure 1.2) [6, 10]: the π bands meet at the *K* point in reciprocal space at which the Fermi level of the undoped material is located. The density of states (DOS) vanishes at this point so producing a zero bandgap semiconductor. However, three-dimensional graphite behaves as a semimetal at room temperature due to inter-layer interactions inducing a small but finite electronic density of states at the Fermi level.

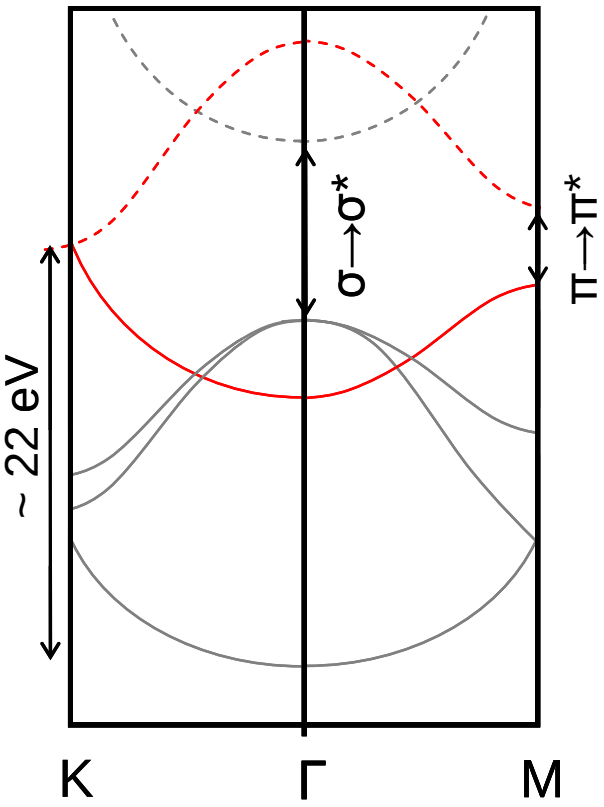

Figure 1.2

After [6]: A schematic diagram of the band structure of graphene along high symmetry Brillouin zone directions (shown as the triangle passing through the high symmetry points K, Γ and M in Figure 1.3). The σ bands are shown in grey and the π bands in red whilst the σ and π* bands are shown as respective grey and red dotted lines. σ→σ* and π→π* transitions are shown.*

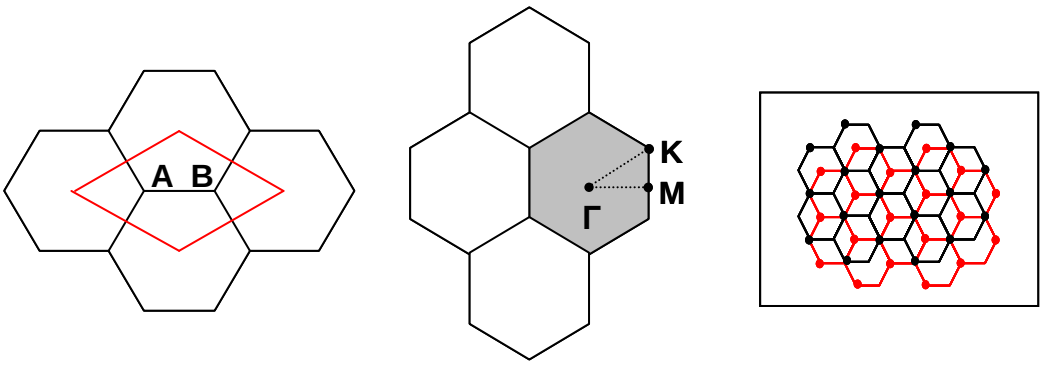

Figure 1.3

The unit cell (red rhombus, left) and Brillouin zone (shaded grey area, right) of the graphene lattice. The two inequivalent carbon atoms within the unit cell are labelled A and B, and the high symmetry points in the Brillouin zone are labelled.

(inset) The lowest energy stacking arrangement of adjacent graphene layers within three-dimensional (3D) graphite. The red and black graphene layers are respective lower and upper layers. The solid circles in each case represent the A atoms in the unit cell as shown on the left. In this way one can see that the uppermost A atom lies directly above a lower B carbon atom; this is referred to as 'AB stacking'.

1.2 Carbon Nanostructures

1.2.1 Fullerenes

In 1985 a third allotrope of carbon was discovered [1] - the fullerenes. A fullerene molecule is a completely closed 'cage' which may be produced through laser ablation of a graphite target [1, 11] or through arc discharge between carbon electrodes [12, 13]. The common principle underpinning these methods is the formation of a hot carbon plasma which then condenses into a soot containing stable fullerenes and other carbonaceous materials such as the multi-shell 'carbon onions' and carbon nanotubes. Extraction of the fullerenes from the soot is relatively easily achieved since fullerenes are soluble in certain organic solvents such as toluene [14].

The most stable of the fullerene molecules (and the first to be discovered) is buckminsterfullerene (C_{60}) which is shown in Figure 4; synthesis methods can be 'tuned' in order to favour the production of this particular fullerene [12]. As a result this molecule has been the subject of rigorous scientific investigation of electronic [15], chemical [16] and physical properties, and several applications have been demonstrated [17-19].

The C_{60} molecule can be viewed as being formed from a graphene fragment, with complete closure achieved through the introduction of a sufficient number of pentagonal rings (12) to satisfy Euler's theorem. The sixty carbon atoms within the C_{60} molecule are sp^2 hybridised and form three σ bonds and one π bond with their neighbours, though the high curvature of the molecule introduces some sp^3 character into the carbon-carbon bonds.

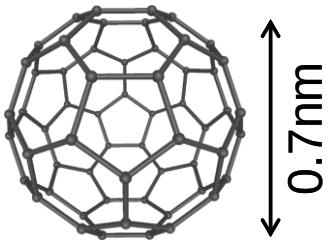

Figure 1.4

A ball-and-stick model of C_{60}, or 'buckminsterfullerene' [1]. The molecule is comprised of sixty carbon atoms which form a caged structure 7 Å in diameter. Geometrically, the structure consists of twenty hexagons and twelve pentagons.

As with graphene, only the π electron derived electronic states or, more correctly, the π derived molecular orbitals play a significant role in the electronic, optical and chemical properties of the fullerenes. If the electronic states are filled according to Hund's rules, all

states up to $\ell = 4$ are full whilst the $\ell = 5$ level is partially full and contains ten π electrons. Owing to the icosahedral symmetry of C_{60}, the $\ell = 5$ level is five fold degenerate and forms the highest occupied molecular orbital (HOMO), which is completely filled [20]. Consequently, C_{60} is non-conducting but has a high electron affinity due to the lowest unoccupied molecular orbital (LUMO), which can accept up to 6 electrons. Thus, interesting electrical properties may arise through doping of C_{60} (for example, K doped C_{60} is superconducting at 18 K [21]). Similarly it is found that, when adsorbed on a surface, the interaction between C_{60} and that surface can vary in strength and can occur via van der Waals forces [23] or be either covalent or ionic in character [22]. Such a variety of adsorbate-surface interactions result in the formation of different overlayer structures, a number of which involving a reconstruction of the surface. This is discussed in further detail in Chapter 7.

1.2.2 Carbon Nanotubes

CNTs can be divided into two distinct classes – those comprising a number of concentric carbon tubes, known as multi-walled carbon nanotubes (MWCNTs) and those which comprise a single layer, the single-walled carbon nanotubes (SWCNTs). MWCNTs were the first species of carbon nanotube to receive widespread attention after their (re-) discovery by Iijima [3]. MWCNTs are composed of between two to around fifty concentric layers and the inter-wall separation (~3.4.Å) is similar to the interlayer separation found in three-dimensional (3D) graphite. Each of the concentric nanotubes making up the MWCNT may have different chirality (see later), and do not exhibit the 'AB' atomic stacking usually found in 3D graphite (Figure 1.3). Consequently, understanding and therefore modelling the physical properties of MWCNTs accurately is difficult and is further complicated by the presence of inter-tubule interactions. It is for this reason that SWCNTs attract more fundamental interest while MWCNTs, which are cheaper and easier to produce on a commercial scale, have seen greater applications in science and technology.

SWCNTs are constructed from a single graphene sheet which, in a thought experiment, is rolled up to form a seamless tube with diameters ranging from 0.4 nm to ~10 nm. The physical properties of such structures inherently depend on the way in which they are wrapped. This can be described by the 'wrapping angle', θ, or a 'chiral' (or Hamada) vector, $\boldsymbol{C_h}$, which describes the circumference of the nanotube in terms of the two-dimensional

graphene mesh. When considering the graphene layer from which a CNT is to be constructed, it is convenient to define an arbitrary atomic site as the origin to which all other sites can be referenced. If another crystallographically equivalent site is chosen then a graphene tube can be formed by 'rolling up' the layer such that the two chosen atomic sites coincide. The resultant tube has a circumference described by $|\boldsymbol{C_h}|$ and a diameter, *D* ($= |\boldsymbol{C_h}/\pi|$), which can be written in terms of the coordinate system of the graphene lattice as,

$$C_h = |\boldsymbol{C_h}| = (\boldsymbol{C_h} \cdot \boldsymbol{C_h})^{\frac{1}{2}} = \sqrt{3}a_{C-C}(m^2 + mn + n^2)^{\frac{1}{2}}$$

Equation 1.1

where

$$\boldsymbol{C_h} = n\boldsymbol{a_1} + m\boldsymbol{a_2}$$

Equation 1.2

Here, $\mathbf{a_1}$ and $\mathbf{a_2}$ are the lattice vectors as shown in Figure 1.5 and $a_{c\text{-}c}$ is the carbon-carbon bond length (1.44 Å). In this way, the geometric nature of each nanotube can be described exclusively using Hamada indices [24] in the form (*n*, *m*) where *n* and *m* are given in Equation 1.2.

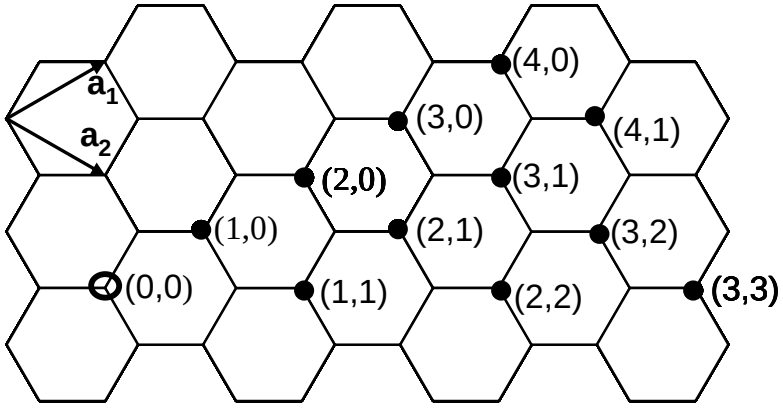

Figure 1.5

If an arbitrary atomic site is defined as the origin (open circle), then each crystallographically equivalent carbon atom (filled circles) can be labelled (n,m) where n and m are integer multiples of the 2D graphene lattice vectors a_1 and a_2 respectively.

Another parameter needed to fully describe the physical properties of a CNT is the chiral or 'wrapping' angle as displayed in Figure 1.6:

$$\cos\theta = \frac{\boldsymbol{C_h} \cdot \boldsymbol{a_1}}{|\boldsymbol{C_h}||\boldsymbol{a_1}|} = \frac{2n+m}{2(m^2+mn+n^2)^{\frac{1}{2}}}$$

Equation 1.3

Due to the symmetry of the graphene sheet the constraint $0 \leq \theta \leq 30^{\circ}$ is applied so that reproduction of equivalent CNTs is avoided. At the extremes of this limit lie the 'armchair' (n, n), $\theta = 30^{\circ}$ and 'zig-zag' (n,0), $\theta = 0^{\circ}$ nanotubes: the bounding cases of the chiral nanotubes (n, m) that lie in between.

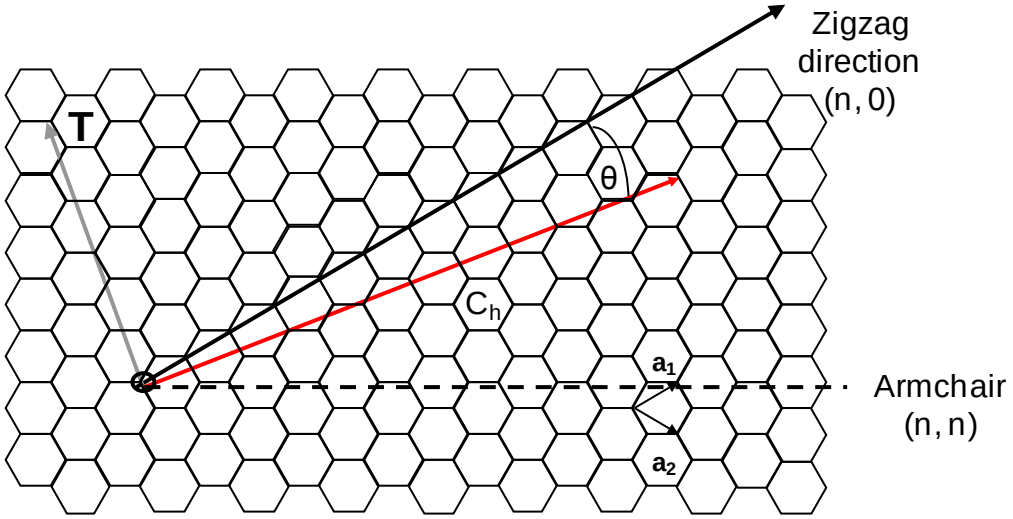

Figure 1.6

Relationship between chiral and translation vectors and the two-dimensional (2D) graphene lattice. The red arrow, C_h, shows the magnitude and direction of the circumference of the nanotube which lies at an angle, θ, to the 'zigzag' direction (so called because of the spatial arrangement of carbon-carbon bonds in this direction). Also defined are the unit vectors of the lattice, a_1 and a_2, and the translation vector, T, which lies parallel to the tube axis.

For CNTs created from a single graphene sheet, formation of the tubule results in the reduction of the Brillouin zone to a line segment along the direction of the translation vector (defined in Figure 1.6) with length $2\pi/T$. Whilst the allowed wavevectors along this direction are continuous (for a nanotube of infinite length), the boundary conditions imposed in the circumferential direction reduce the allowed wavevectors to a discrete set.

These allowed wavevectors effectively 'select' cross-sections of the 2D band structure of graphene (a 'slice' of which is shown in Figure 1.7) and therefore dictate the electronic behaviour of the nanotube: If the cross-section taken coincides with, or is close to, the K (Fermi) point (i.e. $\boldsymbol{C}_h \cdot \boldsymbol{k} = 2\pi q$, q is an integer [25]) then the resultant nanotube behaves metallically at room temperature, otherwise it is semiconducting with a band gap, E_g;

$$E_g = \frac{2\gamma_o a_{C-C}}{D}$$

Equation 1.4

where γ_o is the nearest-neighbour interaction overlap integral (~2.7 eV) and D is the nanotube diameter. This relationship breaks down at small diameters (less than 1 nm) due to the large curvature of the nanotube causing strong rehybridisation amongst the σ and π orbitals. Rehybridisation may also occur due to chemical functionalisation [26], suggesting that this also may result in energy gap changes in semiconducting nanotubes.

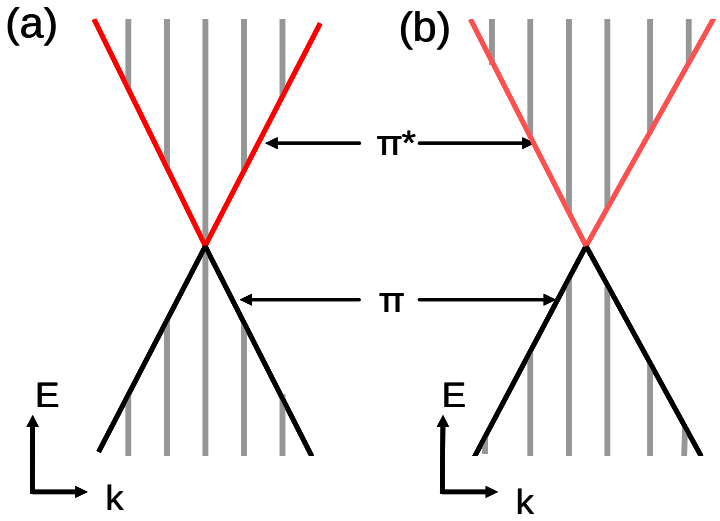

Figure 1.7

Adapted from [27]. Schematic diagram of the dispersion relation of (a) metallic and (b) semiconducting (with energy gap E_g) nanotubes. The red lines represent the π band whilst the black lines represent the π band of graphene. These two bands meet at the Fermi energy; the K point in reciprocal space. The gray lines represent the allowed wavevectors which result from the imposed boundary conditions upon the formation of a nanotube from a graphene sheet.*

The one-dimensional (1D) nature of carbon nanotubes also manifests itself in the electronic DOS through van Hove singularities (VHS) at the start of each new electronic sub-band [28-31]. Such features arise from consideration of a free electron model in which the electrons are confined to 1 dimension. This results in a quantisation of the electronic wavefunctions in the other two.

CNTs may be synthesised using a variety of techniques including carbon arc discharge (AD) [32], laser ablation (LA) [33] and chemical vapour deposition (CVD) [34] processes such as high pressure carbon monoxide disproportionation (HiPCO) [35]. These growth

methods often involve the use of a transition metal catalyst such as nickel [32, 33], iron [34, 35], or cobalt [33] and produce CNTs with varying diameters, number of walls, lengths, defect densities and contamination levels. The relative ease of production of CNTs is offset by the difficulty in obtaining chemically pure and structurally pristine samples; a necessity for many possible applications [36-39]. Even though a number of CNT purification methods have been developed [20, 32, 40-43] these methods usually involve oxidation of the sample which not only removes contaminants, but frequently degrades the nanotube structure [44].

1.3 Applications and Motivation

The potential applications [45] for CNTs are wide ranging and include material composites [46-48], field effect transistors [49], field emission displays [50], high sensitivity gas sensors [51, 52], water purification [53], gas separation [54, 55], transportation and storage [56]. The latter being of particular interest when considering fuel cell technologies [57]. Many of these applications of CNTs (for example, in composite materials) involve the use of MWCNTs, since the larger size of these structures makes them easier to manipulate and separate when compared to SWCNTs. However, if nanotubes are to be the technological 'building blocks' of future, it is clear that more usable CNT materials need to be synthesised (i.e., CNTs that are easily separated and have a well defined diameter, electrical conductivity and mechanical strength). Indeed, research into processes that achieve this is ongoing [32, 58, 59] but, until such processes are refined, CNT samples will continue to include a vast range of different structures. It is therefore apparent that CNT characterisation plays a significant role in the progression of future CNT applications. One might therefore ask a number of questions: Which techniques are best for characterising CNT materials? What information does that technique provide? Is that information comparable between different CNT species? Is that information comparable to data obtained using other techniques? These are significant questions, the answers to which would be of interest to the whole CNT community. However, since the focus of current CNT research is on pushing forward the potential applications, these (rather fundamental) questions remain unanswered.

It is also clear that some form of benchmark is needed to describe the 'quality' of CNT

materials. Such a definition would allow standardisation of CNT materials and make it more feasible for CNT applications be realised on a large scale. Decades into CNT research this has yet to be done. The reason for this is that, firstly, the definition of CNT quality varies depending on the intended use of the CNTs and, secondly, a method by which 'quality' can be measured and quantified accurately – for all CNT species – needs to be established. This issue is directly linked with those regarding CNT characterisation discussed above.

Whatever the definition of CNT 'quality', it is clear that the number of defects within the CNT lattice will play a significant role in defining it. The study of defects in CNTs is a research field in its own right, since their presence within the CNT lattice influences the chemical reactivity and both the mechanical and electronic properties of CNTs. Many questions may be asked regarding defects in CNTs, for example: How do such defects influence the environmental stability of the different CNT species? Can the level of defects within the CNT lattice be controlled? Can the number of defects in a CNT lattice be quantified? Might such defects be used to create more useable CNT materials? Are the defects in CNTs with one wall similar to those in CNTs with more than one wall? Does the subsequent behaviour of such defects differ in CNTs with a different number of walls?

The work on CNTs in this thesis aims to address some of the questions posed above. In Chapter 4, investigations into CNT characterisation and the definition of CNT 'quality' are carried out. This is done through the analysis of four different, commercially available, CNT materials using several analytical techniques (discussed in Chapter 2). The motivation for this work is four-fold: First, to not only thoroughly characterise the materials that are studied in this thesis, but to also provide valuable information for a community widely using these materials; second, to compare the information obtained between techniques for a given CNT species. By doing so we will be able to highlight any issues that may arise when comparing CNT studies in the literature. This is something that is already done by the community without directly addressing whether doing so is valid; third, to compare whether the data obtained from a single technique are comparable between different CNT species. Again, this is done within the literature without considering potential problems of doing so; fourth, to find a technique, or group of techniques, that are reliable and consistent for gauging the 'quality' of any given CNT sample.

In Chapters 5 and 6, the behaviour of ion-induced defects in different CNT species is investigated. In particular, the resultant reactivity of these materials to ambient atmosphere is examined. Such an investigation may help us understand how defects behave in different CNT materials and how they may be detected and quantified. It will also provide information on how the presence of such defects within the CNT lattice influences their environmental stability. This, in turn, may also provide information on possible routes for controlled functionalisation of CNTs, something that is significant when attempting to create more usable CNT materials.

The potential applications of C_{60} (and other fullerene derivatives) are as wide ranging as those of CNTs, from the formation of water repellent materials [60] to drug delivery systems [61]. Many applications include the use of a thin C_{60} film on a surface, for example, as an electron beam resist for nanolithography [19]. Thin films of C_{60} are also prevalent in the potential electronic applications of the molecule [17], for example in *n*-channel field effect transistors [18] or solar cells [62]. In order for such applications to achieve their maximum potential, it is clear that the nature of the C_{60}/surface interaction must be fully understood. Indeed, it is likely the overlayer-substrate interaction brings about the property that is of particular interest. In Chapter 7, the interaction of C_{60} with two different surfaces is studied - namely the (0001) surface of highly oriented pyrolytic graphite (HOPG) and the (110) surface of nickel. The investigation centres about the first layer growth of C_{60} on these surfaces at both room and elevated temperatures and the physical consequences of the different adsorbate-substrate interactions.

1.4 Summary

In this chapter carbon nanotube and fullerenes have been discussed. The electronic structure of these nanomaterials has been considered, along with current and potential applications of both these materials. Bearing such applications in mind, the motivations for the work in this thesis have been outlined.

1.5 References

1. Kroto, H.W., et al., *C_{60} - Buckminsterfullerene.* Nature, 1985. **318**(6042): p. 162-163.
2. Radushkevich, L.V. and V.M. Lukyanovich, *O strukture ugleroda, obrazujucegosja pri termiceskom razlozenii okisi ugleroda na zeleznom kontakte.* .Zurn Fisic Chim 1952. **26**.
3. Iijima, S., *Helical Microtubules of Graphitic Carbon.* Nature, 1991. **354**(6348): p. 56-58.
4. Geim, A.K., *Graphene: Status and Prospects.* Science, 2009. **324**(5934): p. 1530-1534.
5. Dresselhaus, M.S., G. Dresselhaus, and P. Avouris, *Carbon nanotubes : synthesis, structure, properties, and applications*. Topics in applied physics ; v. 80. 2001, Berlin: Springer. xv, 447 p.
6. Zunger, A., *Self-Consistent LCAO Calculation of Electronic Properties of Graphite .1. Regular Graphite Lattice.* Physical Review B, 1978. **17**(2): p. 626-641.
7. Ajayan, P.M., S. Iijima, and T. Ichihashi, *Electron-energy-loss spectroscopy of carbon nanometer-size tubes.* Physical Review B, 1993. **47**(11): p. 6859-6862.
8. Sato, Y., et al., *High energy-resolution electron energy-loss spectroscopy study of the electric structure of double-walled carbon nanotubes.* Journal of Electron Microscopy, 2006. **55**(3): p. 137-142.
9. Brzhezinskaya, M.M., E.M. Baitinger, and V.V. Shnitov, *π-plasmons in ion-irradiated multiwall carbon nanotubes.* Physica B-Condensed Matter, 2004. **348**(1-4): p. 95-100.
10. Saito, R., et al., *Electronic-Structure of Graphene Tubules Based on C_{60}.* Physical Review B, 1992. **46**(3): p. 1804-1811.
11. Laska, L., et al., *Fullerene production driven by long-pulses of near-infrared laser radiation.* Carbon, 1996. **34**(3): p. 363-368.
12. Kratschmer, W., et al., *Solid C_{60} - a New Form of Carbon.* Nature, 1990. **347**(6291): p. 354-358.
13. Suematsu, H., et al., *Preparation of fullerene by pulsed wire discharge.* Japanese Journal of Applied Physics Part 2-Letters, 2003. **42**(8B): p. L1028-L1031.
14. Diack, M., et al., *Contribution to the Isolation and Characterization of Buckminsterfullerenes.* Analytical Chemistry, 1992. **64**(18): p. 2143-2148.
15. Weaver, J.H., et al., *Electronic-Structure of Solid C_{60} - Experiment and Theory.* Physical Review Letters, 1991. **66**(13): p. 1741-1744.
16. Heath, J.R., et al., *Lanthanum Complexes of Spheroidal Carbon Shells.* Journal of the American Chemical Society, 1985. **107**(25): p. 7779-7780.
17. Al-Mohamad, A. and A.W. Allaf, *Fullerene-60 thin films for electronic applications.* Synthetic Metals, 1999. **104**(1): p. 39-44.
18. Kanbara, T., et al., *N-channel field effect transistors with fullerene thin films and their application to a logic gate circuit.* Chemical Physics Letters, 2003. **379**(3-4): p. 223-229.
19. Robinson, A.P.G., et al., *A Fullerene derivative as an electron beam resist for nanolithography.* Applied Physics Letters, 1998. **72**(11): p. 1302-1304.
20. Dresselhaus, M.S., G. Dresselhaus, and P.C. Eklund, *Science of fullerenes and carbon nanotubes*. 1996, San Diego: Academic Press. xviii, 965p.
21. Hebard, A.F., et al., *Superconductivity at 18°K in Potassium-Doped C_{60}.* Nature, 1991. **350**(6319): p. 600-601.
22. Maxwell, A.J., et al., *Electronic and geometric structure of C_{60} on Al(111) and Al(110).* Physical Review B, 1998. **57**(12): p. 7312-7326.
23. Liu, H. and P. Reinke, *C_{60} thin film growth on graphite: Coexistence of spherical and fractal-dendritic islands.* Journal of Chemical Physics, 2006. **124**(16): p. 5.
24. Hamada, N., S. Sawada, and A. Oshiyama, *New one-dimensional conductors - graphitic microtubules.* Physical Review Letters, 1992. **68**(10): p. 1579-1581.
25. Odom, T.W., et al., *Atomic structure and electronic properties of single-walled carbon nanotubes.* Nature, 1998. **391**(6662): p. 62-64.
26. Holzinger, M., et al., *Sidewall functionalization of carbon nanotubes.* Angewandte Chemie-

International Edition, 2001. **40**(21): p. 4002.
27. Collins, P.G. and P. Avouris, *Nanotubes for electronics*. Scientific American, 2000. **283**(6): p. 62.
28. Saito, R., G. Dresselhaus, and M.S. Dresselhaus, *Electronic-structure of double-layer graphene tubules*. Journal of Applied Physics, 1993. **73**(2): p. 494-500.
29. Rao, A.M., et al., *Diameter-selective Raman scattering from vibrational modes in carbon nanotubes*. Science, 1997. **275**(5297): p. 187-191.
30. Wildoer, J.W.G., et al., *Electronic structure of atomically resolved carbon nanotubes*. Nature, 1998. **391**(6662): p. 59-62.
31. Ishii, H., et al., *Direct observation of Tomonaga-Luttinger-liquid state in carbon nanotubes at low temperatures*. Nature, 2003. **426**(6966): p. 540-544.
32. Lv, X., et al., *Synthesis of high quality single-walled carbon nanotubes at large scale by electric arc using metal compounds*. Carbon, 2005. **43**(9): p. 2020-2022.
33. Kingston, C.T., et al., *Efficient laser synthesis of single-walled carbon nanotubes through laser heating of the condensing vaporization plume*. Carbon, 2004. **42**(8-9): p. 1657-1664.
34. Yan, H., et al., *Possible tactics to improve the growth of single-walled carbon nanotubes by chemical vapor deposition*. Carbon, 2002. **40**(14): p. 2693-2698.
35. Nikolaev, P., et al., *Gas-phase catalytic growth of single-walled carbon nanotubes from carbon monoxide*. Chemical Physics Letters, 1999. **313**(1-2): p. 91-97.
36. Liu, X.L., et al., *Carbon nanotube field-effect inverters*. Applied Physics Letters, 2001. **79**(20): p. 3329-3331.
37. Rueckes, T., et al., *Carbon nanotube-based nonvolatile random access memory for molecular computing*. Science, 2000. **289**(5476): p. 94-97.
38. Tans, S.J., A.R.M. Verschueren, and C. Dekker, *Room-temperature transistor based on a single carbon nanotube*. Nature, 1998. **393**(6680): p. 49-52.
39. Collins, P.G., et al., *Nanotube nanodevice*. Science, 1997. **278**(5335): p. 100-103.
40. Park, T.J., et al., *Purification strategies and purity visualization techniques for single-walled carbon nanotubes*. Journal of Materials Chemistry, 2006. **16**(2): p. 141-154.
41. Chen, X.H., et al., *Non-destructive purification of multi-walled carbon nanotubes produced by catalyzed CVD*. Materials Letters, 2002. **57**(3): p. 734-738.
42. Chattopadhyay, D., I. Galeska, and F. Papadimitrakopoulos, *Complete elimination of metal catalysts from single wall carbon nanotubes*. Carbon, 2002. **40**(7): p. 985-988.
43. Kim, Y. and D.E. Luzzi, *Purification of pulsed laser synthesized single wall carbon nanotubes by magnetic filtration*. Journal of Physical Chemistry B, 2005. **109**(35): p. 16636-16643.
44. Monthioux, M., et al., *Sensitivity of single-wall carbon nanotubes to chemical processing: an electron microscopy investigation*. Carbon, 2001. **39**(8): p. 1251-1272.
45. Baughman, R.H., A.A. Zakhidov, and W.A. de Heer, *Carbon nanotubes - the route toward applications*. Science, 2002. **297**(5582): p. 787-792.
46. Gogotsi, Y., *High-Temperature Rubber Made from Carbon Nanotubes*. 2010. p. 1332-1333.
47. Hualin, Z., *Electrospun poly (lactic-co-glycolic acid)/ multiwalled carbon nanotubes composite scaffolds for guided bone tissue regeneration*, in *Journal of Composite Materials*. 2011. p. 347-362.
48. Kim, H.S. and H.T. Hahn, *Graphite fiber composites interlayered with single-walled carbon nanotubes*, in *Journal of Composite Materials*. 2011. p. 1109-1120.
49. Bachtold, A., et al., *Logic circuits with carbon nanotube transistors*. Science, 2001. **294**(5545): p. 1317-1320.
50. Choi, W.B., et al., *Fully sealed, high-brightness carbon-nanotube field-emission display*. Applied Physics Letters, 1999. **75**(20): p. 3129-3131.
51. Collins, P.G., et al., *Extreme oxygen sensitivity of electronic properties of narbon Nanotubes*. 2000. p. 1801-1804.

52. Battie, Y., et al., *Gas sensors based on thick films of semi-conducting single walled carbon nanotubes*. Carbon. **49**(11): p. 3544-3552.
53. Corry, B., *Water and ion transport through functionalised carbon nanotubes: implications for desalination technology*. Energy & Environmental Science, 2011. **4**(3): p. 751-759.
54. Foroutan, M. and A.T. Nasrabadi, *Adsorption and separation of binary mixtures of noble gases on single-walled carbon nanotube bundles*. Physica E-Low-Dimensional Systems & Nanostructures. **43**(4): p. 851-856.
55. Lee, J. and N.R. Aluru, *Separation of gases from gas-water mixtures using carbon nanotubes*. Applied Physics Letters. **96**(13): p. 3.
56. Mantzalis, D., N. Asproulis, and D. Drikakis, *Filtering carbon dioxide through carbon nanotubes*. Chemical Physics Letters. **506**(1-3): p. 81-85.
57. Cheng, H.M., Q.H. Yang, and C. Liu, *Hydrogen storage in carbon nanotubes*. Carbon, 2001. **39**(10): p. 1447-1454.
58. Harutyunyan, A.R., et al., *Preferential Growth of Single-Walled Carbon Nanotubes with Metallic Conductivity*. 2009. p. 116-120.
59. Nie, J.Q., et al., *Synthesis of high quality single-walled carbon nanotubes on natural sepiolite and their use for phenol absorption*. Carbon. **49**(5): p. 1568-1580.
60. Wang, J.B., et al., *Self-Assembly Made Durable: Water-Repellent Materials Formed by Cross-Linking Fullerene Derivatives*. Angewandte Chemie-International Edition, 2009. **48**(12): p. 2166-2170.
61. Bakry, R., et al., *Medicinal applications of fullerenes*. International Journal of Nanomedicine, 2007. **2**(4): p. 639-649.
62. Brabec, C.J., N.S. Sariciftci, and J.C. Hummelen, *Plastic solar cells*. Advanced Functional Materials, 2001. **11**(1): p. 15-26.

2. Experimental Techniques

This chapter provides a brief overview of the techniques employed to acquire the data presented this thesis. The aim is to provide sufficient theoretical background for each technique and to briefly discuss how these techniques may be applied in the study of carbon nanostructures.

2.1 Introduction

As the dimensions of materials approach the nanometre scale the ratio of atoms at the surface to those in the bulk increases significantly. Consequently, when investigating such systems, it is the physics of surfaces and interfaces that dictate their properties. This is most apparent when considering structures such as carbon nanotubes, which can effectively be thought of as a structure which is comprised solely of a 'surface'. For this reason, the majority of the analytical techniques used in this thesis are surface sensitive. The surface sensitivity and limiting resolution of these techniques is dependent on (1) the probability of generating the signal (cross section) and (2) the ability of the signal to escape the sample. For techniques involving the use of electrons, information carried by their energy is lost upon an inelastic scattering event. As a result it is the inelastic mean free path (IMFP), $\lambda(E_k)$, of the electrons which dictates the information depth ($3\lambda(E_k)$). The IMFP is primarily dependent on the kinetic energy of the electron and, to a much lesser extent, the nature of the solid through which the electrons pass. Empirical analysis of pooled experimental data has found the IMFP of electrons in materials follows a 'universal curve' (Figure 2.1).

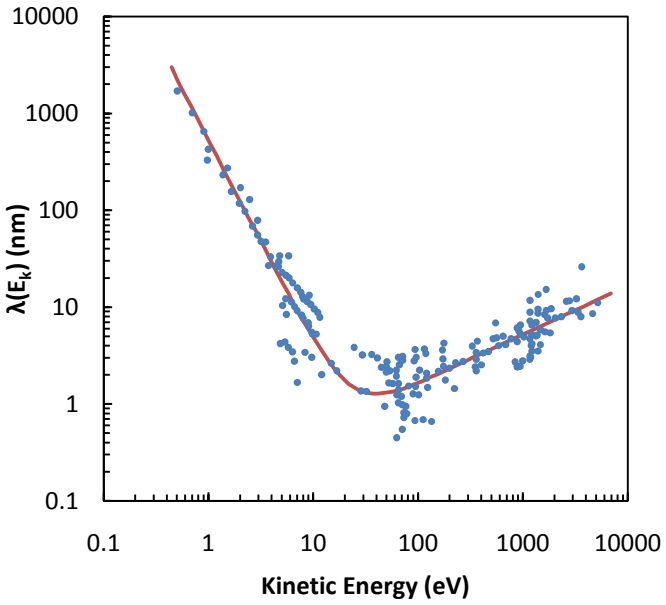

Figure 2.1

Adapted from reference [1]: the 'universal curve' for the inelastic mean free path (IMFP) of electrons within a sample.

Detail of the theoretical background to the experimental techniques employed to obtain the data presented this thesis is given below, whilst descriptions of the experimental apparatus and method are given in Chapter 3. Specific details regarding data analysis are provided within the appropriate chapters.

2.2 Photoemission Spectroscopy

Photoemission (photoelectron) spectroscopy (PES) was developed in the 1960s and has since become a common surface analysis technique. PES uses the photoelectric effect to probe the occupied electronic states of a sample. Due to the photon energy ranges of laboratory based sources, we often divide PES into ultra-violet PES (UPS) and x-ray PES (XPS), however the use of tuneable light from synchrotron sources blurs this boundary. Although one may probe both core and valence electronic states through x-ray photoelectron spectroscopy, ultra-violet light is often used as the excitation source for studies of the valence band of solid surfaces due to a higher cross-section for photoemission and the higher resolution typically achieved in laboratory based UV sources [2].

The simplest way to visualise the photoemission process is to consider a photon with energy, $h\nu$, incident on an atom. Any electrons with binding energy $E_b < h\nu$ may be emitted from the atom, with any surplus energy appearing as the kinetic energy, E_k of the photoemitted electron such that:

$$E_k = h\nu - E_b - \varphi$$

Equation 2.1

where φ is the workfunction of the electron energy analyser. Hence, by measuring the kinetic energy of the photoelectrons one can determine the binding energies of the electrons within the atom and hence information regarding identity and chemical state.

XPS is primarily concerned with core levels, which tend to be relatively unperturbed by the bonding within a solid sample and are therefore characteristic of the elements within that sample. This means that XPS can, at its most basic level, be used as a 'fingerprinting' tool to determine elemental composition. An example of an XP spectrum of a MWCNT sample is shown in Figure 2.2. This spectrum was acquired with a photon energy of 1496.6 eV.

The peaks within an XP spectrum are usually referred to by the atomic orbital from which they originate. For example, the main photoemission peak related to the presence of carbon is labelled C1*s*, since these photoelectrons originate from the carbon orbital with principal quantum number, n=1, and angular momentum quantum number , ℓ=0 (denoted

by the *s*). Also taken into account within the nomenclature is any energy level splitting due to spin-orbit coupling: for example, the Ni2*p* peak is split into the Ni2$p_{1/2}$ and the Ni2$p_{3/2}$ peaks where the subscripts '1/2' and '3/2' describe the total angular momentum of each atomic orbital. Also present within an XPS spectrum are Auger electron peaks, the physical origin of which will be discussed later. Auger electron peaks occur at fixed kinetic energy and may therefore be differentiated from photoemission peaks by varying the energy of incident photons: the kinetic energy, E_k, of photoelectrons increases with the energy of the primary beam but that of an Auger electron remains constant.

In addition to 'fingerprinting' the chemical composition of a sample, further information regarding composition can be gleaned through detailed analysis of a photoelectron peak: To relate the intensity of that peak to the precise elemental composition the photoionisation cross section of a given shell has to be accounted for. Additionally one must also account for the angle of the incident x-rays and the angle at which the photoelectrons are collected, the angle of acceptance of the electron analyser and the performance of the analyser itself. In summary, the intensity of a photoelectron peak, *i*, from element, *j*, is described by [3]:

$$I_{ij} = C.T(E_k).L_{ik}(\gamma).\sigma_{ij}.\int n_i(z)\,.exp\left(\frac{-z}{\lambda(E_k)cos\theta_T}\right)dz$$

Equation 2.2

where *C* is an instrumental constant; $T(E_k)$ is the transmission function of the analyser (which determines the efficiency of detection of a photoelectron of energy E_k); $L_{ik}(\gamma)$ is the angular asymmetry factor for the orbital, *k*, which is under consideration; σ_{ij} is the photoionisation cross section of peak *i* from element *j*; $n_i(z)$ is the concentration of element *i* at a distance z below the surface of the sample; $\lambda(E_k)$ is the IMFP at energy E_k, and θ_E is the emission angle of the photoelectrons measured with respect to the surface normal [3].

If it can be assumed that the elemental concentrations are homogeneous over the sampling depth the integral from Equation 2.2 can be removed, thus:

$$I_{ij} = C.T(E_k).L_{ik}(\gamma).\sigma_{ij}.n_i.\lambda(E_k)cos\theta_E$$

Equation 2.3

and the atomic percent concentration of element *i*, $\%n_i$, defined as:

$$\%n_i = \frac{n_i}{\sum n_i} \times 100$$

Equation 2.4

By using photons of lower energy, as in the case of UPS ($h\nu$ = 20-50 eV), the more weakly bound states of an atom can be probed with a larger cross section and resolution than is possible with XPS. High intensity, monochromated, synchrotron radiation may be used but, due to availability and cost issues, gas discharge lamps are often employed. Such low energy photon sources produce high intensity light with a small natural linewidth, meaning that measurements are, in general, limited by the analyser energy resolution. High intensity gas discharge lamps typically use inert gases such as helium, which generate photons of two different energies – 21.1 eV and 40.8 eV – both of which are used in this thesis, and neon (16.8 eV) [2].

Since the photoelectrons generated in UPS have low kinetic energies and therefore a small IMFP (5-10 Å, Figure 2.1), this technique is highly surface sensitive. However, the surface sensitivity of UPS also means that care is needed when acquiring spectra and attributing spectral features to specific surface/adsorbate properties, since understanding the relative surface and bulk contributions is difficult without extensive theoretical calculations. Furthermore, the relative intensity of spectral features is highly dependent on incident photon energy due to variations in photoionisation cross-section. Consequently, a number of methods have arisen (such as difference spectra) in which adsorbate/surface features may be assigned. Additionally, whereas the initial and final states of an atom after photoelectron ejection in XPS are well defined due to the high kinetic energy of the generated photoelectrons, the low kinetic energies of photoelectrons in UPS may result in a final state which is very close in energy to that of the most weakly bound state of the atom. Consequently, the photoemission spectrum may represent the joint density of states (JDOS) of both initial and final states, rather than just the initial state [2].

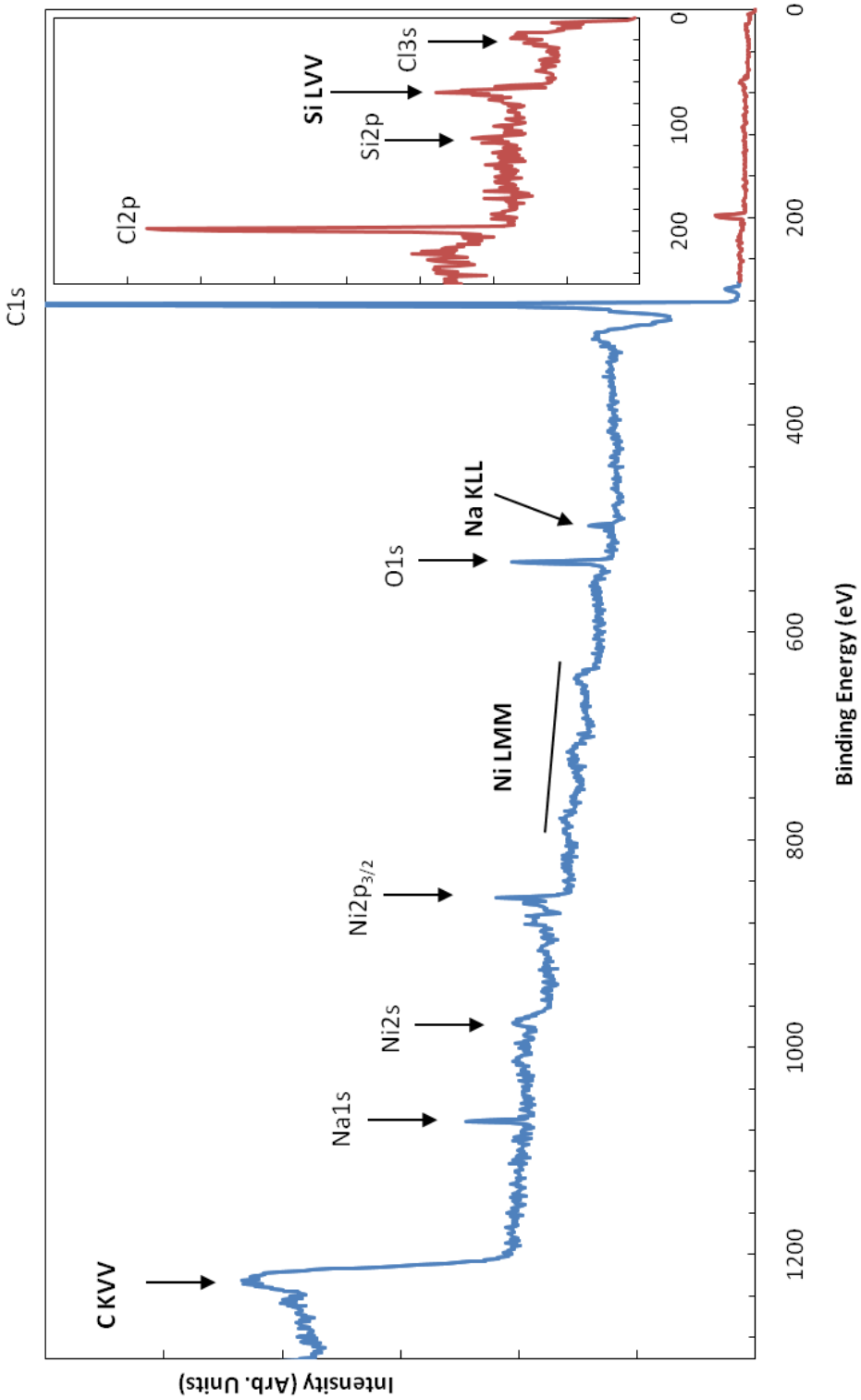

Figure 2.2

XPS 'survey' spectrum of a MWCNT sample. Each photoemission peak is labelled in normal typeface, whilst Auger electron peaks are labelled in bold typeface. The inset displays structure at low binding energies.

The valence band of CNTs is derived from the 2*s* and 2*p* atomic orbitals of carbon and has pronounced features at binding energies of ~3 eV and ~8 eV which are associated with π and σ bonding respectively (Figure 2.3). By monitoring the relative intensities of these two spectral features (and any broadening) when modifying CNTs one may infer changes in bonding within the CNT wall. For example, a reduction in the intensity and definition of the 'π peak' may be associated with a disruption of the sp^2 hybridised carbon network (i.e. the 'π peak' is indicative of 'graphite-like' bonding), which may occur due to the inclusion of functional groups or defects within the CNT wall [4].

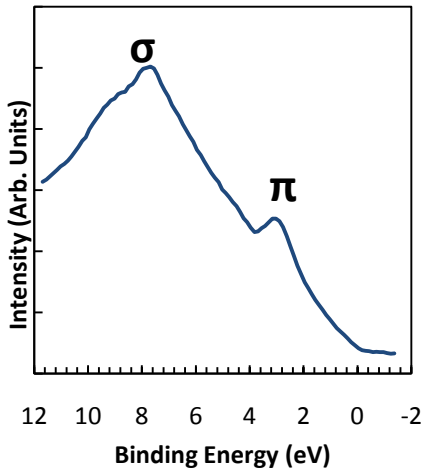

Figure 2.3

Intensity normalised, low temperature (~40 K) He II (40.8 eV) ultra-violet photoemission spectrum of a MWCNT sample. The π and σ features are labelled accordingly.

A detailed examination of the binding energy of a core hole can provide significant additional information regarding the chemical state of the elements within a sample and provide some insight into physical processes such as screening, which are dependent on the electronic state of the material. In Equation 2.1 the expression for photoelectron kinetic energy included E_b, the electron binding energy, with little discussion as to the factors contributing to it. The simplest assumption, known as Koopmans' theorem, is to assume that the binding energy is simply the negative of the energy of the atomic orbital from which the electron originates. However, this assumption breaks down even in the case of an isolated atom. Formation of a solid leads to a further deviation of binding energy from Koopmans' theorem values and this variation contains significant information regarding the local environment of the atom under consideration. The breakdown of Koopmans' theorem can be attributed to changes in the both the initial and final states associated with the photoemitted electron.

Initial state effects include variations of the atomic ground state of an atom through, for

example, the formation of chemical bonds with other atoms or molecules. These changes are referred to as the 'chemical shift'. Usually oxidation (formal loss of valence electrons) of an atom results in an increase in the binding energy of core electrons since the finite probability density of the valence electrons between the average core level position and the nucleus is reduced. This leads to less effective nuclear screening (for example, the binding energy of the C1*s* peak is observed to increase monotonically as carbon is bound to increasingly electronegative atoms). Reduction (formal gain of valence electrons) produces the opposite effect. Such shifts give insight into the bonding of surface atoms [3]. For example, oxygen containing components in the core photoemission peak of carbon (situated on the high binding energies side of the main C1*s* peak) can be used to determine the concentration and type of oxygen containing species on the surface of the sample (see Chapters 5 and 6).

Final state effects involve the relaxation of the system – both intra-atomically and extra-atomically. Intra-atomic relaxation arises from a re-arrangement of the remaining electrons in the presence of a core hole. This reduces the energy of the final state and, by conservation of energy, leads to a photoelectron of higher kinetic energy (or alternatively associated with a state of lower binding energy). The mechanism of extra-atomic relaxation depends on the material being studied and may include polarisation of neighbouring atoms, or metallic screening [3]. Further final state mechanisms include, but are not limited to: multiplet splitting, in which unpaired electrons created during photoelectron emission couple with those in an already incompletely filled shell; spin-orbit splitting, in which the spin and orbital angular momentum of the final state electron couples with orbital angular momentum; electron 'shake up', in which an electron is promoted to a higher bound state and electron 'shake off', in which an electron is excited to the continuum [5]. Such final state effects may be used to obtain detailed information on the system. For example, in the 'shake up' process an excited electron can only occupy a limited set of well defined energy levels. Thus, 'shake-up' peaks (also known as loss peaks because their energy is lower than that of the main peak) may be used to understand the electronic structure of the material. The 'shake off' process, which generates electrons with a continuous range of kinetic energies), does not produce a well defined spectral feature. Photoelectron spectra may also exhibit characteristic periodic loss peaks - or 'plasmon' peaks - due to an outgoing photoelectron coupling with the characteristic collective oscillations of the valence electrons [3].

2.3 Auger Electron Spectroscopy

In 1923 Pierre Auger discovered that when photons with sufficient energy to cause the ejection of a core electron were incident on a material, electrons were ejected that had characteristic kinetic energies which were independent of the energy of the incident radiation. These have since been termed *Auger electrons*, and today Auger electron spectroscopy (AES) is a commonly used tool in surface analysis. Conceptually, Auger electrons can be considered to be created by a sequence of events (although in reality Auger emission is a single step quantum mechanically coherent process): (1) a primary beam of photons or electrons ionises an atom, forming a core hole; (2) subsequent relaxation of the atom occurs and the core hole is filled by an electron from a higher energy level, either a shallower core level or a valence level; (3) the energy liberated by this transition is transferred, via a radiationless process, to another electron which is ejected (Figure 2.4). This ejected electron is the Auger electron, and it has an energy determined by the difference between its binding energy and the energy liberated by core hole relaxation which is independent of excitation energy [1, 3]:

$$E_{123} = E_1(Z) - E_2(Z+\Delta) - E_3(Z+\Delta) - \mathcal{H}(23) - \varphi$$

Equation 2.5

The measured kinetic energy of an Auger electron, E_{123}, generated from an element of atomic number Z involving energy levels 1, 2 and 3, is dictated by the individual energies of each of these levels (E_n), the degree to which they relax (Δ) due to the presence of the core-hole, the workfunction of the electron energy analyser, φ, and $\mathcal{H}(23)$ – the interaction energy of the holes created in levels 2 and 3 of the final state. The latter is especially important for systems in which core holes remain localised for significant lengths of time and has a notable influence on Auger lineshape [6-8].

Rather than the radiationless transfer of energy to a second electron, core hole decay can also lead to emission of a photon, a process known as x-ray fluorescence (see Section 2.5). X-ray fluorescence (XRF) occurs in direct competition with Auger electron emission, although the probability of each process varies differently with Z [9]:

$$P_{fluorescence} = \omega = (1 + \alpha Z^{-4})^{-1} \quad ; \quad P_{Auger} = 1 - \omega$$

Equation 2.6

where α is a constant dependent on the atomic shell ionised. Hence, Auger electron emission is more likely for light elements and XRF more probable in the heavier elements.

The nature of the Auger process means that each element emits Auger electrons with unique energies. Each Auger transition can be labelled according to the shell that (1) the core electron is ejected from, (2) the shell from which an electron relaxes into the core hole and (3) the shell from which the Auger electron is emitted. For the example given in Figure 2.4 the process is labelled KL_IL_{II} or simply *KLL*. These labels arise from x-ray spectroscopy where each atomic shell is labelled *K*, *L*, *M*… for principal quantum numbers 1, 2, 3… and the subscript I, II, III… denotes the total electronic angular momentum, increasing in magnitude (e.g., $l = 0, j = ½$ is denoted by the subscript 'I', and $l = 1, j = ½$ is denoted by the subscript 'II' etc.).

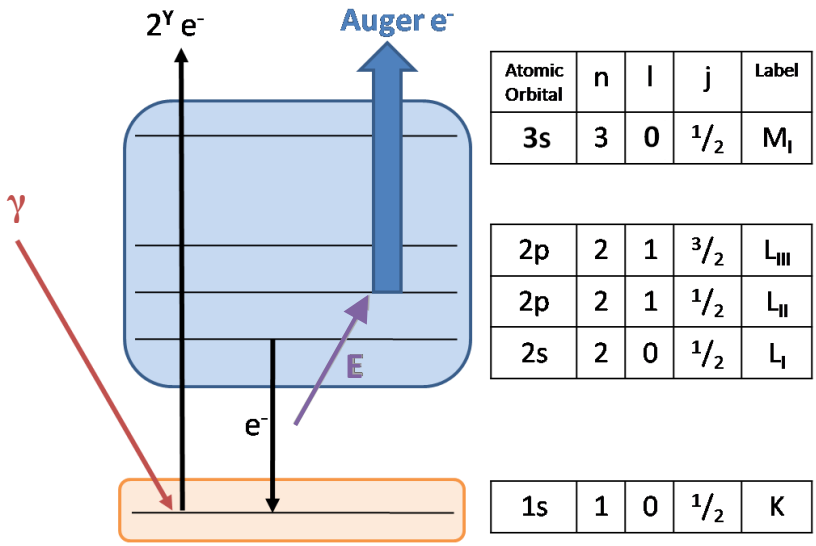

Figure 2.4

A schematic diagram representing the generation of a KLL Auger electron. An incident x-ray or high energy electron (shown in red) ejects a core electron from the atom. The energy, E, liberated from the relaxation of an upper core orbital is enough energy to eject a second, Auger electron. 2^Ye^- refers to a secondary electron.

Due to their relatively short IMFP only Auger electrons that are generated in the first few atomic layers of the sample (to a depth of approximately 5 Å to 25 Å) escape without being inelastically scattered and are detected.

For carbon, only *KLL* transitions are possible (since only *K* and *L* shells are occupied), this is often termed a '*KVV*' transition (*V* = 'valence band') since the *L* shell is the valence

shell of the carbon atom. A *KLL* transition in carbon results in the emission of Auger electrons with an energy centred at approximately 268 eV. A typical electron-excited Auger spectrum is shown in Figure 2.5 both in raw and differentiated form (since Auger peaks lead to a change in count rate which is much more rapid than the slowly varying secondary electron background, differentiation of the Auger peaks makes them easier to see).

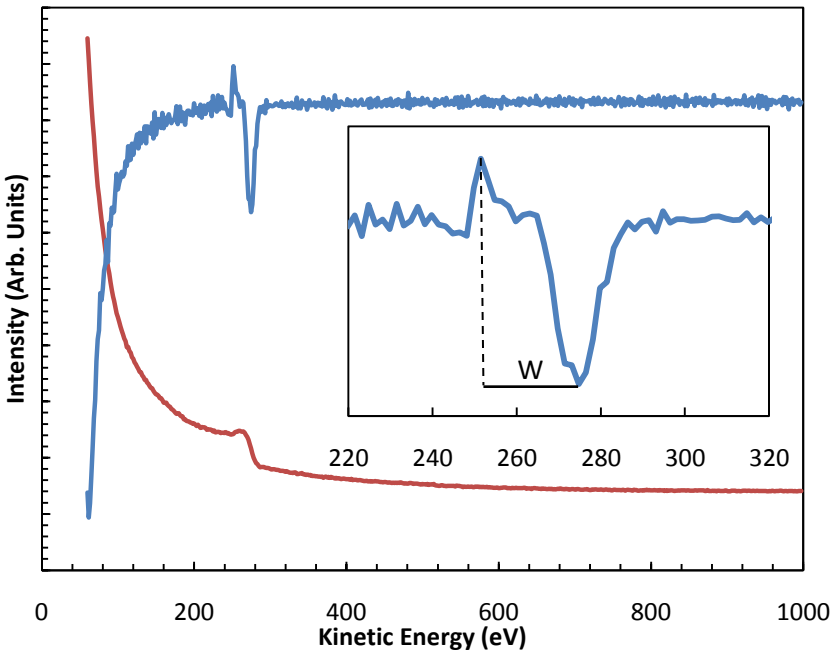

Figure 2.5

An Auger spectrum from a SWCNT sample: Raw data is shown in red, and the differentiated spectrum is shown in blue. Since only the C KVV peak (at 268 eV) is present this sample can be seen to contain only carbon. The inset displays detail of the C KVV peak on which the quantity W is shown (see main text).

AES is not commonly used to investigate carbon nanostructures but has been applied to 'fingerprint' the surface chemical composition and state of CNT samples [10, 11]. Such analysis allows elements to be detected and identified at levels of around 1 at.%. The dependence of the C *KVV* lineshape on the valence band structure of the material means that some additional information may be inferred from a detailed examination of the Auger peak. In particular, by comparison of the lineshape (the measurement of *W*, shown in Figure 2.5) with that of carbon-containing reference samples (graphite, diamond, carbides etc.), departure of the bonding within a sample from planar sp^2 bonding [10] can be inferred. Such changes may be induced, for example, by nanotube curvature and/or the presence of chemically bound species at the nanotube surface.

2.4 Electron Microscopy

In a scanning electron microscope (SEM) measurement a focussed electron beam (typically of energy between 5 and 20 keV) is incident upon the surface of a sample. The energy of this beam is deposited into a 'generation', or 'interaction', volume, the size and shape of which is dependent on a multitude of factors including incident beam energy, beam footprint on the sample surface, angle of incidence etc. From within this volume a number of signals originate (Figure 2.6), including secondary electrons (produced in a variety of ionisation events) and backscattered electrons which are the signals that contribute to the formation of a SEM image [12]. If the sample is sufficiently thin, a signal can be detected below the sample and comprises primary electrons and both eleatically and inelastically scattered electrons.

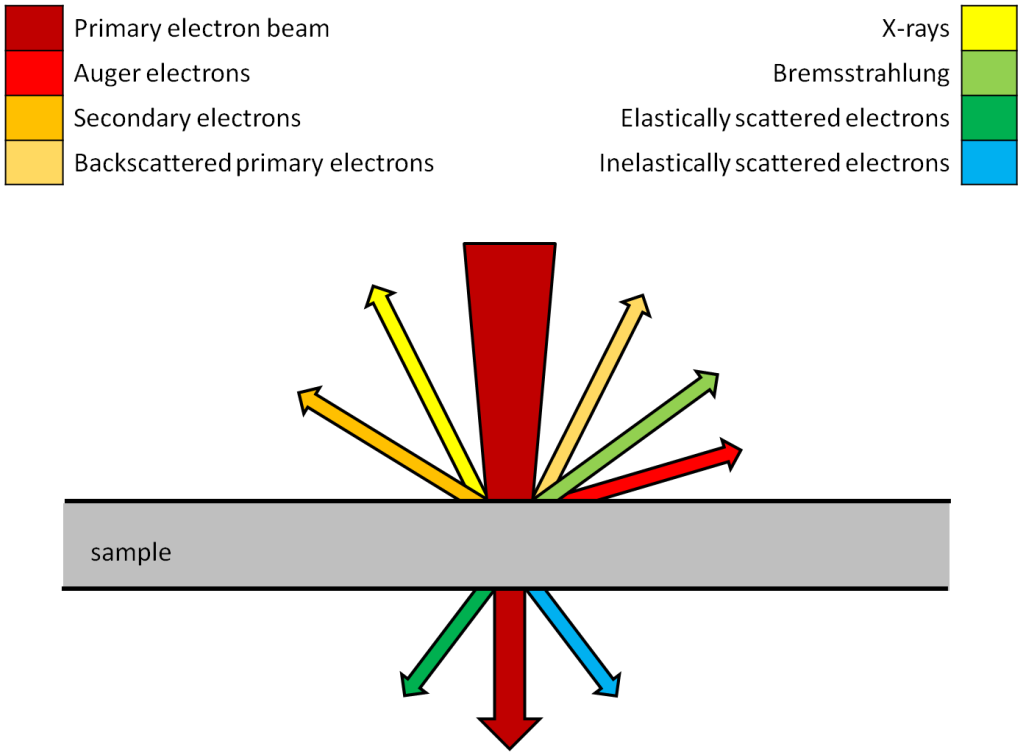

Figure 2.6

A schematic diagram of the signals generated when a primary electron beam is incident on a sample. Only if the sample is sufficiently thin will a signal be detected below the sample.

Each point of the sample onto which the beam is focussed, and from which information is collected, forms one pixel of an SEM image and may range from 1 nm to 10 μm in diameter. In order to create an image the primary beam is scanned across the surface of the sample in a raster pattern, and the information from each point displayed on the

corresponding area of a screen. Thus the magnification, M, in a SEM is accomplished through the mapping of the sample scale, L_{sample}, onto the larger scale of the display, $L_{display}$:

$$M = \frac{L_{sample}}{L_{display}}$$

Equation 2.7

The creation of topographical contrast in an SEM image comprises two components since it includes the detection of both backscattered and secondary electrons. The first, backscattered, component involves electrons with energy E_{back} in the range $0 \leq E_{back} \leq E_o$, where E_o is the primary beam energy. These electrons reach the detector by a 'line of sight' mechanism, so forming an image with a high level of contrast (i.e. largely containing black areas and white areas, with very few 'grey' areas). The second component, that contributed by secondary electrons of energies $E_{second} \approx 3 - 5$ eV, may be selectively included or excluded from the image through the application of a small positive or negative bias (~±50 V) to a Faraday cage surrounding the detector (a description of which is provided in Chapter 3). By including this component a signal is detected from all parts of the sample and the fine (greyscale) detail of the surface topography is revealed. These mechanisms are shown schematically in Figure 2.7 [12].

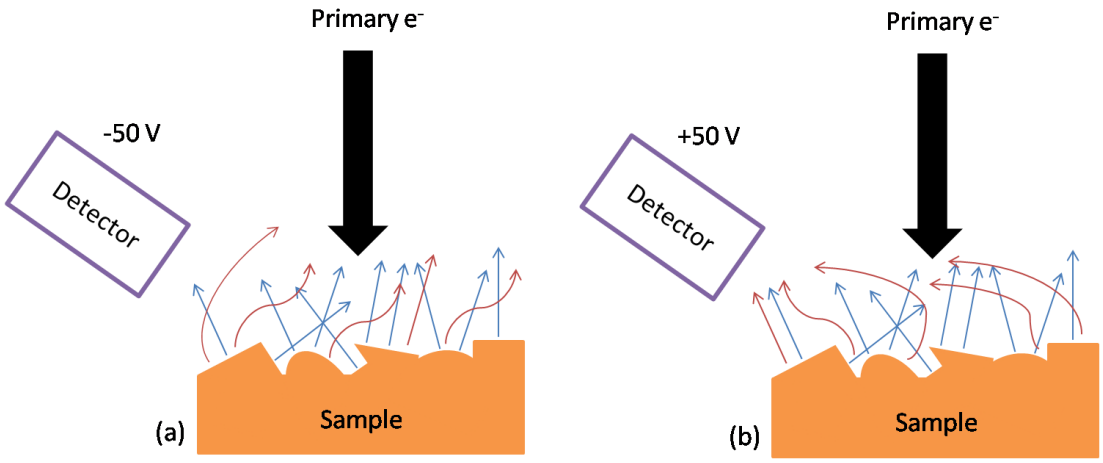

Figure 2.7

Schematic showing SEM contrast formation in (a) backscattered electron detection and (b) backscattered and secondary electron detection. In (a), secondary electrons (red arrows) are rejected from the detector through the application of a small negative bias. The relatively high energy backscattered electrons (blue arrows) are unaffected by this bias and still enter the detector if the line of sight is clear. In (b), the secondary electrons are accepted by the detector from all parts of the sample.

In general, SEM images contain both backscattered and secondary electron information which effectively creates a gnomonic projection of the surface of the sample. As with any such projection, there are inherent distortions in the plane perpendicular to the optical axis – distance is related to scan angle and an angular scan movement produces a smaller change in distance nearer the centre of field of view than at the edges. The result is a varying magnification across the field – an effect which is negligible at the high magnifications used in the images presented in this thesis [12].

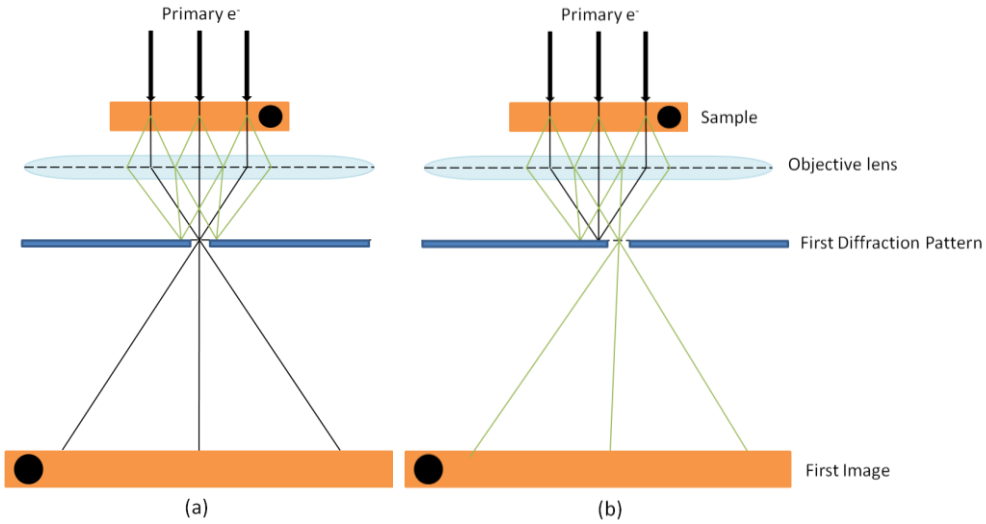

Figure 2.8

A schematic ray diagram showing the mechanism of formation of, (a), a bright field (BF) image and, (b), a dark field (DF) image. Direct beams are shown in black and diffracted beams are shown in green.

Transmission electron microscopy (TEM) is inherently different from SEM in that this technique involves the detection of primary electrons which have *passed through* a sufficiently thin sample. Transmission electron microscopes may use a scanned beam (STEM) as in the SEM or a less spatially focussed fixed beam more analogous to an optical microscope. Since the latter, 'traditional' TEM is used to obtain the data presented in this thesis we limit our discussion to this type. In a TEM measurement an electron beam is focussed onto a thin sample (typically up to a few tens of nm thick). The beam is of sufficiently high energy (typically >100 keV) that the majority of the electrons can pass through the sample. As the electrons pass through the sample, the uniform intensity of the primary beam is made non-uniform by scattering. In order to convert the scattered electron intensity into some meaningful form of contrast and allow easy image interpretation, TEM images are usually formed from either the direct beam (bright field, BF, image) or diffracted beam (dark field, DF, image).

An idealised TEM is shown in Figure 2.8 indicating the means by which BF and DF images are formed. The high energy primary electron beam passes through the sample, is focussed by an objective lens onto a phosphor screen which, in this case, displays a reversed 'first' image of the sample. A 'first' diffraction pattern occurs in the back focal plane of the objective lens and within this plane is the objective aperture which may be used to selectively allow either the direct beam through the microscope to form a BF image or a diffracted beam to form a DF image [13].

The contrast between two adjacent areas of a TEM image, I_1 and I_2, is usually one of two main types: mass-thickness contrast, which is of particular importance when imaging non-crystalline samples, and diffraction contrast. Mass-thickness contrast, C, arises from incoherent elastic scattering of the primary electrons and occurs in both BF and DF images using electrons scattered through low angles [13]:

$$C = \frac{I_2 - I_1}{I_1} = \frac{\Delta I}{I} = \frac{\rho \sigma N_A}{A} \Delta t$$

Equation 2.8

Mass-thickness contrast, as the name suggests, is dependent on variations of sample thickness, Δt, and the single atom scattering cross-section, σ, which is a function of atomic number, Z. ρ is the density of the sample, A the atomic mass and N_A is the Avogadro constant. In simple terms the consequences of this are as follows: higher Z elements have a larger scattering cross-section than lighter elements and so scatter electrons away from the trajectory of the primary beam more effectively. Increased sample thickness has the same effect. Thus, areas of a sample with a relatively high Z and t will appear as dark areas on a BF image and bright areas on a DF image. For samples which are composed primarily of a single element, as is the case for the CNT samples in this thesis, the contrast can be thought of as being a function of thickness. This approximation begins to fail at higher scattering angles as inelastic scattering and diffraction begin to dominate [13].

Where incoherent elastic scattering causes mass-thickness contrast, diffraction contrast arises due to coherent elastic (Bragg) scattering of electrons within the sample. The advantage of this is that the separation of the primary and diffracted beams by the objective aperture is relatively straight forward. The difficulty in such a measurement, however, arises in the precise orientation of the sample required to obtain the desired 'two-beam' condition

i.e., that the primary beam and one *hkl* diffracted beam dominate the diffraction pattern. Such a condition allows a specific set of *hkl* planes to contribute to the DF image, in which they will appear as bright areas. By reorienting the sample to a variety of two-beam conditions, specific orientation-specific information can be obtained. The theory behind diffraction contrast is a complex (due to the strong interaction of the primary electrons with the sample) and involves consideration of the dynamical theory of scattering - a subject which is beyond the scope of this thesis.

Both SEM and TEM are commonly used for investigation of CNT samples [14-17], an example of EM characterisation of MWCNTs is presented in Figure 2.9. Such analysis can be used to obtain a qualitative overview of the level of dispersion, bundling and aggregation of a CNT sample. The main drawback of SEM is that it is unable to probe beyond the external structure of a CNT sample. In contrast to this, the transmission of the primary beam in TEM readily yields additional information regarding the number and quality of the walls of a CNT and the condition of the inner channel, in addition to verifying the presence of material encapsulated within carbon layers. Furthermore, the stringent sample preparation requirements for TEM are greatly relaxed for CNTs, making this a quick and facile technique for CNT analysis.

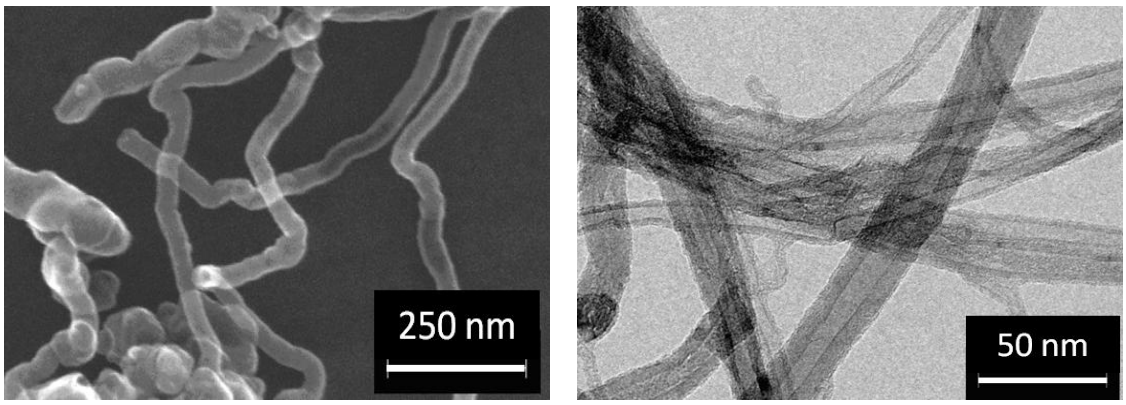

Figure 2.9

SEM (left) and HRTEM (right) images of MWCNTs. As can be seen, whilst SEM probes only the outer surface of the CNTs, HRTEM allows visualisation of the inner channel of the CNTs and the number of walls.

The main disadvantage of both SEM and TEM is that they are unable to yield information regarding the chemical composition of the structures seen in the images and so there is a need for supplementary techniques such as electron energy loss spectroscopy (EELS) or

energy dispersive x-ray analysis (EDX), if a more complete picture of the sample is to be obtained (both EELS and EDX may be carried out in an electron microscopy). Moreover, electron beam exposure has been shown to lead to sample degradation and damage [14], which may lead to difficulties in identifying weakly bound or sensitive species within the sample during subsequent analysis.

2.5 Energy Dispersive X-ray Analysis

As discussed above, x-ray fluorescence is, like AES, initiated by the generation of a core hole. Auger electron emission occurs in competition with x-ray fluorescence, though the latter is more likely for elements with larger atomic numbers.

The emitted x-rays have energies which are characteristic of the material from which they originate and therefore may be used to ascertain the chemical composition of a sample. Either the energies of the emitted photons (energy dispersive x-ray analysis, EDX), or their wavelength (wavelength dispersive x-ray analysis, WDX) may be measured. WDX achieves the higher spectral resolution but, since this method relies on the diffraction of the emitted x-rays, the likely composition of the sample needs to be known before analysis can take place. This fact, in addition to the stringent orientation requirements for WDX, means that EDX is the more widely used technique for chemical analysis.

Since the means for exciting fluorescence are already present, EDX is frequently carried out within an electron microscope. The benefits of using a high energy electron beam as the excitation source is that highly localised volumes of the sample can be analysed due to the ability to precisely focus the electron beam; specific points of interest in a SEM or TEM image can be chemically characterised. This is a particularly useful tool when analysing CNTs since any contaminants present can be identified and eliminated.

An example of EDX data from a MWCNT sample is presented in Figure 2.11. The spectrum produced is straightforward to understand, and provides the elemental composition of the material in question. However, unlike AES (see Section 2.3), EDX provides data from a highly localised region of the sample but does not allow elucidation of the chemical state of the elements present.

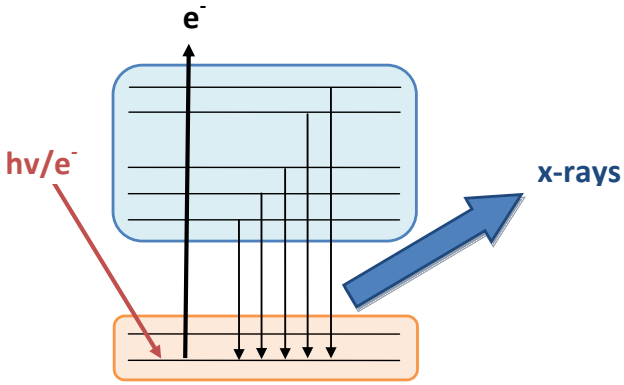

Figure 2.10

A schematic of the x-ray fluorescence process. A core hole generated by x-rays or high energy electrons is filled through relaxation of an electron in a higher shell, leading to emission of an x-ray of characteristic energy.

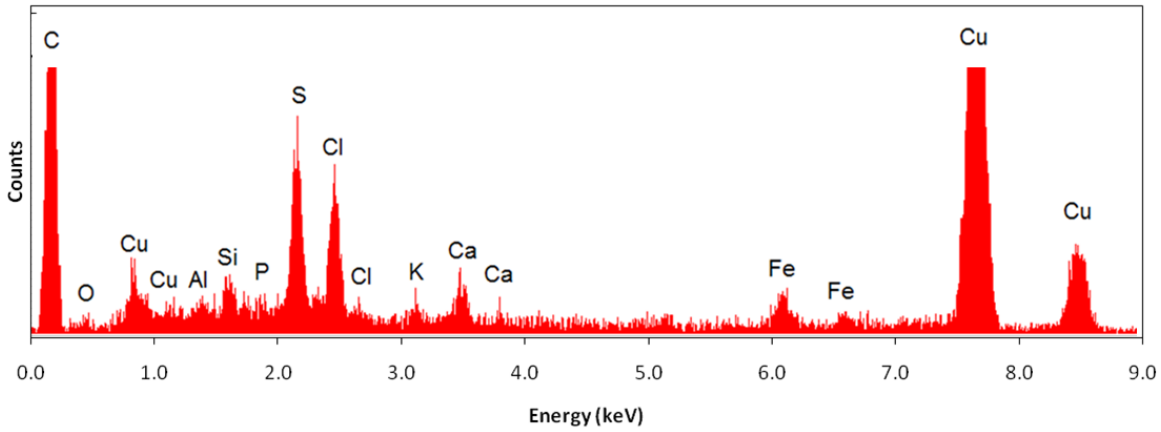

Figure 2.11

EDAX data from the MWCNT sample shown in Figure 2.9. The copper signal arises from the microscope grid, whilst chlorine is a residue of acid etching. Signals due to silicon, sulphur, calcium, potassium and phosphorous suggest contamination from the synthesis process (discussed in more detail in Chapter 4).

2.6 Scanning Tunnelling Microscopy

Scanning tunnelling microscopy (STM) was first used to image the surface structure of Au(110) in 1982 [18] and then Si(111) [19] and has since developed into one of the most important tools in surface science. In a STM measurement an 'atomically' sharp probe is moved above the surface of a conductive sample. The interaction giving rise to 'topographic' contrast is quantum mechanical tunnelling, which occurs between tip and surface (and vice versa). Images can be produced in either (1) 'constant current' mode,

where a constant tunnel current is maintained or (2) 'constant height' mode, where a constant height is maintained between tip and sample. By monitoring the movement of the probe in case (1), or the tunnelling current, in case (2), a 'topographic' image of the surface of the sample is produced. If it is assumed that there is no thermal excitation and that the electronic wavefunctions, Ψ, of the probe and surface are identical, the resulting tunnel current, I, is found to depend exponentially on the width, d, of the potential (vacuum) barrier between tip and sample:

$$I \propto |\Psi(z)|^2 = |\Psi(0)|^2 exp(-2\kappa d)$$

Equation 2.9

where $\Psi(0)$ is the electronic wavefunction at the potential barrier edge. This exponential dependence results in a large reduction of the measured tunnel current for small increments in the barrier width; early work by Binning *et al.* in 1982 confirmed this [20]. Tunnelling occurs simultaneously between tip and surface, producing stochastic noise (which may be used directly in Scanning Noise Microscopy [21]). To produce a net tunnel current a small applied bias is used between tip and sample. When the bias is significantly smaller than the workfunction of the tip and sample electrons tunnel from occupied electronic states very close to the Fermi energy of the negatively biased 'electrode' (which can be either tip or sample depending on the sense of the bias) to unoccupied states in the positive electrode.

STM images therefore contain a mixture of information derived from the topography and local density of states (LDOS) of both the tip and sample [22]. Hence, when obtaining molecular/atomic scale images caution should be taken in interpretation for several reasons: (1) variation in the LDOS of a surface may not coincide with atomic/molecular structure [23]; (2) deviations from tunnelling can occur due to chemical, electrostatic and magnetic interactions; (3) uncontrolled variations in chemical composition and electronic structure of the tip and sample can occur [24]; (4) the dimensions of the tip are typically not known. Issue (4) may be overcome through calibration of the tip by features of known dimension, e.g. the step edge of a standard sample such as the (0001) surface of highly oriented pyrolytic graphite (HOPG). If it is assumed that the step is a discontinuity on the surface, then the effective tip radius, R_{eff}, may be approximated through measurement of the apparent width, L, and height, h, of the step [25]:

$$R_{eff} = \frac{(L^2 + h^2)}{2h}$$

Equation 2.10

The tunnelling conditions used may lead to measurements of apparent height which are not consistent with the known geometry of the surface [23, 26], since the applied bias may coincide with filled/empty states which lie in a minimum (or maximum) in the LDOS (Figure 2.12, left). An example of an STM image of C_{60} deposited on HOPG is given in Figure 2.12 (right).

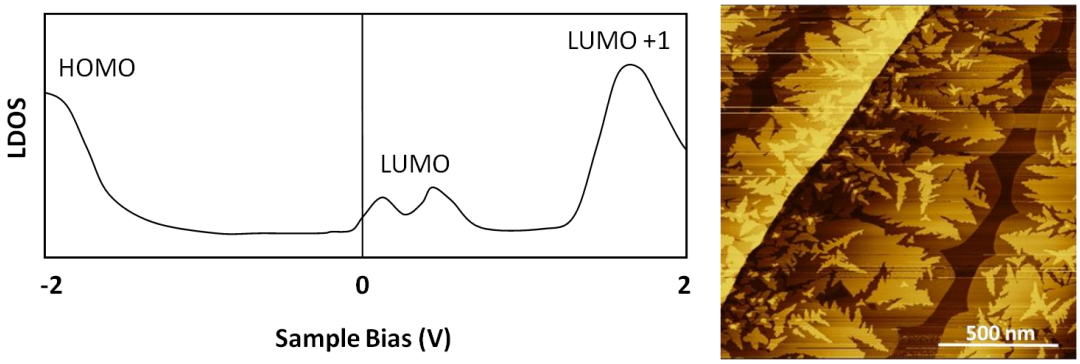

Figure 2.12

(left) Adapted from reference [26]: A schematic of the LDOS structure near the Fermi level of monolayer C_{60} on Ag(001). The highest occupied molecular orbital (HOMO) and lowest unoccupied molecular orbital (LUMO) and LUMO +1 are shown.
(right) An STM image of C_{60} deposited on HOPG; the growth of dendritic structures on second and subsequent layers is clearly visible.

2.7 Low Energy Electron Diffraction

The first low-energy electron diffraction (LEED) experiment was performed by Clinton Davisson and Lester Germer at the Bell Laboratories, U.S.A., in 1927 [27] and confirmed de Broglie's hypothesis of wave-particle duality. The pair directed electrons with a low kinetic energy at a nickel target at normal incidence and mapped the angular dependence of the scattered electron intensity, which was found to follow the pattern expected from the Bragg diffraction of x-rays. Thus the first LEED pattern was measured. However, at this time LEED was not feasible as a *routine* experimental probe of surface structure since the production of focussed electron beams with well defined energy was very difficult, as was creating the ultra high vacuum necessary for producing and maintaining surfaces clean

enough for successful diffraction experiments. It was not until the early 1960s, when vacuum technologies and methods of cleaning surfaces and maintaining them for prolonged periods had improved significantly, that interest in LEED as an analytical technique developed and the modern day LEED apparatus (Figure 2.13) was born.

The basic requirements of a LEED system include a method of producing and focussing a monoenergetic beam of electrons, usually by using an electron gun and focussing elements. The gun includes an electron source which may be a heated tungsten filament or LaB_6 source. The temperature of the source defines the energy spread of the electron beam ($3k_BT/2$) [28], which is one of the reasons that the expensive and delicate LaB_6 source is often employed, since it thermionically emits at much lower temperatures than a conventional W filament. Once generated, the electrons are focussed by a series of lenses and accelerated to the chosen incident energy before striking the sample. Backscattered electrons then pass through a series of retarding grids shown in Figure 2.13 which act to remove inelastically backscattered electrons leaving elastically scattered (diffracted) electrons to be accelerated towards a fluorescent viewing screen. The diffraction pattern may then be recorded by a camera and displayed on a computer screen.

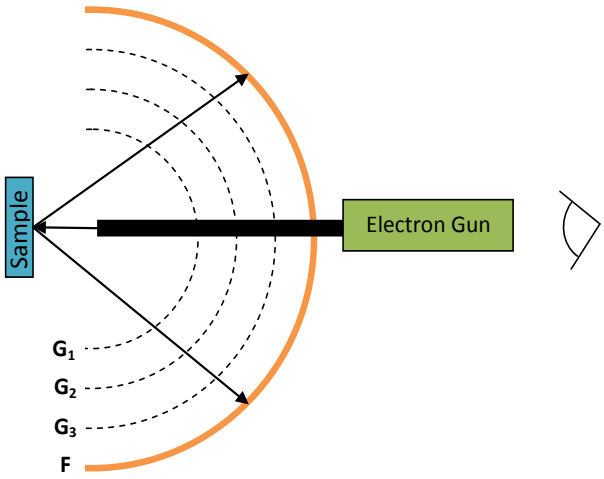

Figure 2.13

Schematic diagram of a typical LEED apparatus. Grid 1 (G_1) is grounded and defines a field-free region between sample and LEED system. Retarding grids (G_2 and G_3) are negatively biased such that inelastically scattered electrons are rejected. A positive bias between G3 and the fluorescent screen (F) causes acceleration of the elastically scattered electrons towards F. The fluorescence of F can be measured by an external detector.

The relatively low energies (~20 eV to 500 eV) of the electrons used in LEED mean that they are readily scattered by the sample, both elastically and inelastically. Consequently, such low energy electrons only probe the first two or three atomic layers of a sample and are ideally suited to revealing information about surface structure. Compared with techniques such as x-ray diffraction, LEED has a relatively short coherence length, typically of from 5 nm to 10 nm, depending on the incident beam energy [3]. Periodicities larger

than this length scale will not be apparent in LEED patterns.

One of the benefits of using a surface sensitive probe is that diffraction conditions from a two dimensional surface mesh are relaxed compared with those required for diffraction from a three dimensional bulk material. This is a consequence of the truncation of the real space lattice, which is now represented in reciprocal space by extended reciprocal lattice rods, which lie in a direction normal to the surface (Figure 2.14). A diffraction spot is observed for any reciprocal lattice rod that intersects the Ewald sphere and the number of rods doing so can be varied by altering the energy of the incident electrons (hence changing the radius of the Ewald sphere). Such changes are manifested as a changing diffraction spot density in the LEED pattern.

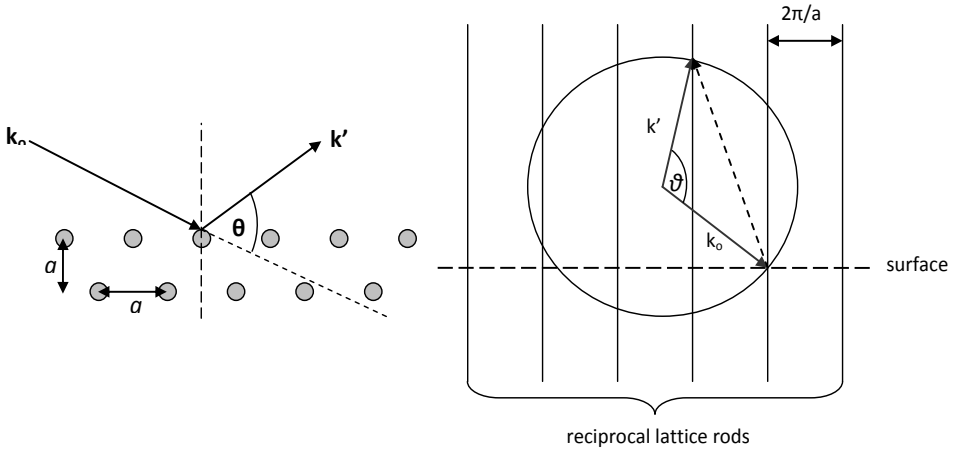

Figure 2.14

A schematic showing diffraction from a surface (left) in real space, and (right) in a 'slice' of reciprocal space. k_0 is the wavevector of the incident electron beam, k' is the wavevector of the scattered beam. This process represents elastic scattering since $|k_0| = |k'|$. a is the real space distance between points on the surface net and θ is the diffraction angle. Adapted from [3].

The LEED pattern is a representation of the symmetry of the surface of the sample (see Figure 2.15). The position of the diffraction spots yields information regarding the long range order of the surface, though the pattern offers no direct information on atomic positions. However, the intensity of the diffracted spots can, if studied as a function of incident energy, yield information regarding the basis when compared with theoretical data derived from appropriate structural models. Complete determination of the surface structure using LEED is therefore possible through the careful and rigorous application of a combination of theory and experiment.

The position of the diffraction spots can be treated in much the same way as they are in an x-ray diffraction experiment, in that the position of the spots in a LEED pattern is directly related to the surface net:

$$\lambda = d_{hk} sin\theta$$

Equation 2.11

where λ is the wavelength of the incident electrons, θ is the diffraction angle and, for a simple square net of lattice parameter, a (see Figure 2.14, left):

$$d_{hk} = \frac{a}{\sqrt{h^2 + k^2}}$$

Equation 2.12

where h and k are the Miller indices of the 'plane' (line of lattice points) giving rise to the measured diffraction spot.

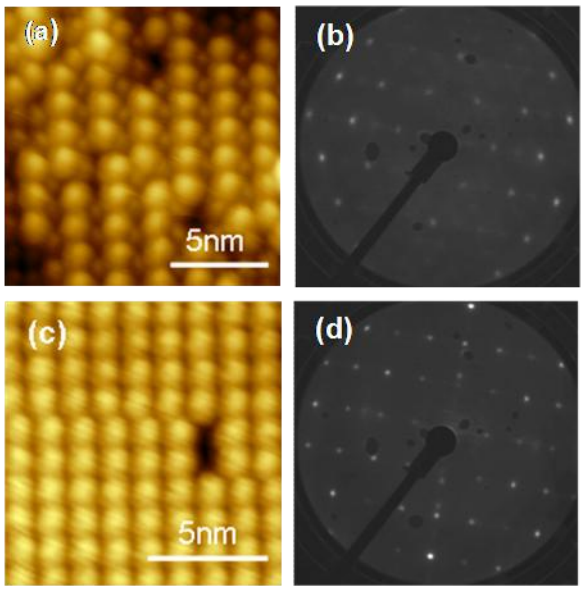

Figure 2.15

STM (a and c) and corresponding LEED images (b and d) of C_{60} deposited on Ni(110).

The strong probe-sample interaction (which leads to a high probability of multiple scattering events contributing to each diffracted beam) means that in order to model diffracted intensities dynamical scattering theory is used, which is beyond the scope of this thesis.

2.8 Electron Energy Loss Spectroscopy

A primary electron of energy, E_0, incident on a surface, may excite quantised excitations within the sample. The result is the emergence of a scattered electron with energy, E_S, defined by:

$$E_s = E_o - \hbar\omega_o$$

Equation 2.13

where $\hbar\omega_o$ is the energy of a quantised excitation (typically a plasmon or interband transition for the primary energy range used in this thesis). Thus, analysis of the energy spectrum of the scattered electrons provides information on the fundamental excitations of the surface. This technique is known as electron energy loss spectroscopy (EELS) and, if the energy of the primary electron beam is < 1 keV, the scattered electrons originate from the first few atomic layers of the sample meaning that, firstly, the information obtained is related to the surface and, secondly, that a *reflection*, rather than a transmission, geometry must be employed [29] .

The mechanisms by which electrons are inelastically scattered are complex due to the strong interactions between electrons and sample. However, such interactions can be split into three limiting cases between which there are no sharp or precisely defined boundaries:

(1) dipole scattering
(2) intermediate negative ion resonance, or 'resonance', scattering
(3) impact scattering

Unlike dipole scattering, both resonance scattering (formation of a complex between an electron and the surface, the lifetime of which is usually very short) and impact scattering (from atomic potentials) are short range interactions with large scattering angles and thus become much more pronounced as one approaches off-specular scattering geometries. The work in this thesis (Chapter 4) concerns only on-specular geometries and primary beam energies of ~150 eV, so further discussion of these rather complex topics will be avoided.

Dipole scattering occurs when the incident electron interacts with the long-range dipole field of the elementary excitations of a surface (which may include phonons, plasmons, excitons etc.). The immediate consequences of this are that only dipole-active excitations (i.e. those that undergo a change in dipole moment during the excitation process) will be

detected by this process. Furthermore, owing to the long range of the Coulomb potential, the dipolar interaction begins far away from the surface and occurs over an extended period of time. Consequently, a microscopic consideration of the interaction is unnecessary [43] and dielectric theory may be applied.

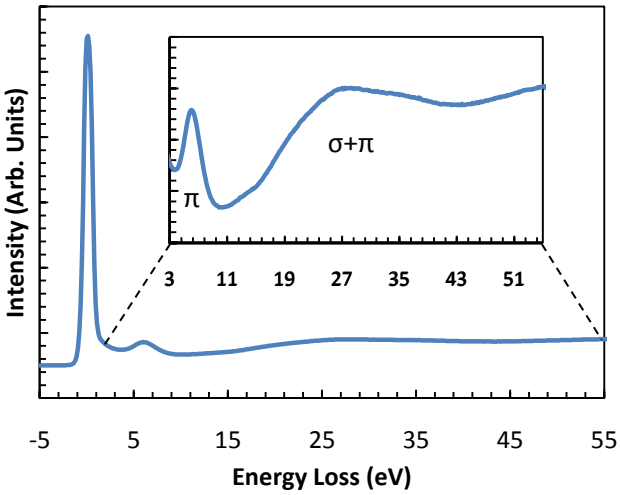

Figure 2.16

EEL spectrum from a MWCNT sample. The zero loss peak (ZLP) is shown at 0 eV energy loss. The inset displays the details of the loss region from 3 eV to 55 eV, on which the π and σ+π features are marked.

At the simplest level, dipole scattering theory assumes the electron to be a classical particle moving along the specular trajectory where the angle of incidence is not too large (<45°). It is also assumed that $E_o \gg \hbar\omega_o$ and that retardation (time variance of the electric field seen by the electron) does not occur - i.e., the timescale of the excitation is much longer than the timescale of interaction with the sample and so the electron 'sees' the instantaneous position of charges within the medium [30]. The energy lost by scattered electrons is defined by the loss function, $Im[-1/\varepsilon(E)]$. Such functions contain complete information regarding the dielectric behaviour of the medium, $\varepsilon(E)$, (where E represents the energy loss of the primary electron) and describes the structure of the loss spectra in the dipole scattering regime [2].

For the energies and system resolution used in this thesis the excitations that are most prominent in the EEL spectra are due to the excitation of plasmons. In this instance, the loss function is of the form [31]:

$$Im\left[\frac{-1}{\varepsilon(E)}\right] = \frac{E(\Delta E_P)E_P^2}{(E^2 - E_P^2)^2 + (E\Delta E_P)^2}$$

Equation 2.14

where E_P is the plasmon energy and $\Delta E_P = \hbar/\tau$ where τ is the plasmon relaxation time. The result of such a loss function is the presence of peaks within the loss spectrum centred about E_P with a full-width half-maximum (FWHM) ΔE_P.

In CNTs the structure of the low-loss region (in medium resolution spectra) consists of two main peaks at energy losses of ~ 5 eV and ~ 27 eV (Figure 2.16), corresponding to excitation of a π plasmon and a 'bulk' ($\pi+\sigma$) plasmon respectively (the shoulder to the left of this is the associated surface plasmon) [32, 33]. Previous studies [4, 11, 33] have shown that by monitoring the position and full-width half-maximum FWHM) of the π plasmon the surface defect density may be inferred. This is discussed further in Chapter 4.

2.9 Raman Spectroscopy

When light is incident on a sample, absorption, transmission and scattering may occur. Scattering may occur such that there is no change in the wavelength of the incident radiation (Rayleigh scattering) or there may be a small positive or negative change in the frequency of the scattered radiation. This small change in frequency occurs due to the Raman effect and was first observed experimentally in 1928 [34]. The origin of the Raman effect may be conceived as a scattering of incident photons through a 'virtual state' (Figure 2.17). The change in the frequency of the scattered radiation is associated with the exchange of quanta of vibrational energy between the incident photons and the lattice. Energy may be either lost by the photons to the lattice (Stokes line) or gained (Anti-Stokes line). The magnitude of the 'Stokes-shift' is therefore a measure of the (quadrupole-active) vibrational excitations of the sample and a Raman spectrum can be used to infer structural information about the sample.

Raman scattering only occurs for vibrational modes possessing dynamic electric quadrupole moments, so Raman spectroscopy is a selective analytical technique and species with modes not satisfying this selection rule cannot be detected. A typical Raman spectrum usually displays the 'Raman shift', which is the difference between the wavenumber of the incident photon and the scattered Stokes radiation. Stokes radiation is usually used since it is higher in intensity than the Anti-Stokes radiation due to the higher population of lower vibrational states at typical sample temperatures.

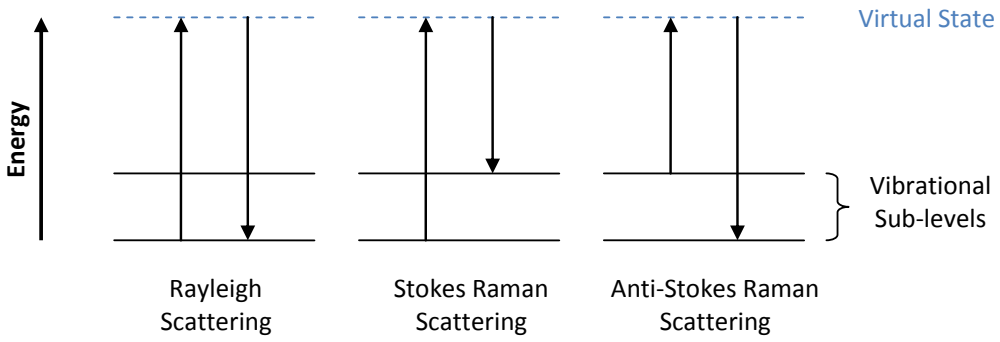

Figure 2.17

Schematic diagram showing the different scattering processes in which an incident photon may take part. Adapted from reference [35].

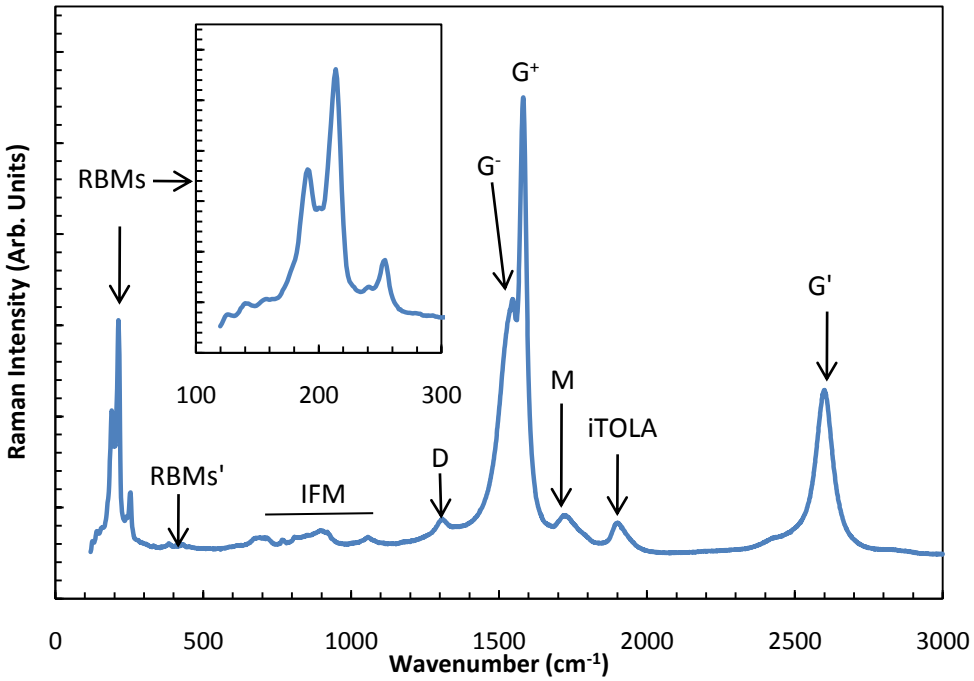

Figure 2.18

Raman spectrum from a SWCNT sample. The main features of interest are labelled and described in the text. The detail of the radial breathing modes is shown in the inset.

The Raman condition is satisfied by several modes within CNTs and so Raman spectroscopy can be utilised as an effective characterisation tool. A spectrum from a CNT sample will, in general, be dominated by CNTs that are in resonance with the incident laser. This resonance condition occurs when CNTs have optically allowed transitions between van-Hove singularities (VHS) in their density of states [36] that can be excited by the incident laser (i.e., the 'virtual transition' becomes, or is close to, a 'real transition' and the Raman intensity is increased).

The main features of interest in the Raman spectrum of a CNT sample (Figure 2.18) include the '*G*-band' at approximately ~1500 cm^{-1} to 1600 cm^{-1}, due to vibrations of a perfect graphitic lattice, and the '*D*-band' at ~1300 cm^{-1} which originates from topological defects within the nanotubes [37]. Also present are the *G'*-band at ~2600 cm^{-1}, the second harmonic of the *D*-band, and a series of smaller peaks, in the region ~ 400 cm^{-1} to ~1200 cm^{-1} which correspond to intermediate frequency phonon modes (IFM) and a combination of optical and acoustic modes (iTOLA). In addition to these modes, which have close analogues in planar graphite, the Raman spectra of CNTs include radial breathing modes (RBMs), which are particularly pronounced in SWCNT and DWCNT samples, and the *M*-band at ~1750 cm^{-1}, which is a combination of the RBMs and *G*-band.

The RBMs of SWCNTs and DWCNTs occur at frequencies of ~200 cm^{-1} (and their second harmonics, RBM', at ~400 cm^{-1}) and are associated with the radial motion of the nanotube [37]. The frequencies of the RBMs have a strong diameter dependence and can hence be particularly powerful for ascertaining the diameters of SWCNTs [4, 38, 39] and DWCNTs [40]. A Raman spectrum of a SWCNT sample is given in Figure 2.18, along with detail of the RBMs.

The *D*-band is associated with the presence of a 'disordered' or 'defective' graphitic structure in which the long range periodicity and symmetry of the graphite lattice is broken (for example, by defects, non-hexagonal ring structures etc.) and so is often used as a measure of the structural quality of the CNTs [4, 38, 39]. However, the approach of determining the quality of CNTs through the ratio of the *D* to the *G* bands, which is very commonly used in the literature, is only of value when comparing similar nanotube structures (number of walls, diameter distribution) under identical conditions. This is due to the dependence of this ratio on the resonant scattering process and, hence, excitation energy [41]. The *D* band also exhibits a downshift in energy from that of 2D graphite (1356 cm^{-1}) which is more pronounced for smaller diameter CNTs and is also dependent on the excitation energy used [37]. For SWCNTs, the *G*-band is split into two separate peaks; the G^- and G^+ peaks, which are associated with atomic displacements in the circumferential direction and along the nanotube axis respectively [37]. As a result, the G^- band is inherently dependent on nanotube diameter (a down-shift in the G^- band frequency from that of 2D graphite (1591 cm^{-1}) corresponds to reduced nanotube diameter [37]) whereas the G^+ band is not. However, shifts in the G^+ peak may be induced by charge

transfer through the presence of dopants such as alkali metals and protonic acids [37, 42-44] through bond softening in a rather similar way to that previously observed in the fullerenes [45].

2.10 Summary

In this chapter the theory behind the experimental techniques used in this thesis has been introduced and discussed. More detailed discussion of data processing and analysis, such as fitting of XPS spectra, is provided in the appropriate chapters.

2.11 References

1. *Practical surface analysis*. 2nd ed, ed. D. Briggs and M.P. Seah. 1990, Chichester: Wiley. 1430.
2. Ibach, H., et al., *Electron spectroscopy for surface analysis*, ed. H. Ibach. 1977, Berlin: Springer-Verlag. 255.
3. *Surface Analysis- The Principle Techniques*, ed. J.C. Vickerman. 1998, Guildford: John Wiley and Sons. 474.
4. Goldoni, A., et al., *Spectroscopic characterization of contaminants and interaction with gases in single-walled carbon nanotubes.* Carbon, 2004. **42**(10): p. 2099-2112.
5. Carlson, T.A., *Photoelectron and Auger spectroscopy*. 1975, New York: Plenum.
6. Cini, M., A. Pernaselci, and E. Paparazzo, *On Auger CVV line-shapes from covalently bonded solids.* Journal of Electron Spectroscopy and Related Phenomena, 1995. **72**: p. 77-81.
7. Cini, M., *Density of states of 2 interacting holes in a solid.* Solid State Communications, 1976. **20**(6): p. 605-607.
8. Sawatzky, G.A., *Quasi-atomic Auger-spectra in narrow-band metals.* Physical Review Letters, 1977. **39**(8): p. 504-507.
9. Bishop, H.E. and J.C. Riviere, *Estimates of Efficiencies of Production and Detection of Electron-Excited Auger Emission.* Journal of Applied Physics, 1969. **40**(4): p. 1740-1744.
10. Lascovich, J.C., R. Giorgi, and S. Scaglione, *Evaluation of the sp^2/sp^3 ratio in amorphous-carbon structure by XPS and XAES*. Applied Surface Science, 1991. **47**(1): p. 17-21.
11. Brzhezinskaya, M.M., E.M. Baitinger, and V.V. Shnitov, *π-plasmons in ion-irradiated multiwall carbon nanotubes.* Physica B-Condensed Matter, 2004. **348**(1-4): p. 95-100.
12. Goldstein, J.I., et al., *Scanning electron microscopy and x-ray microanalysis : a text for biologists, materials scientists, and geologists*. 2nd ed. ed. 1981, New York: Plenum. 686.
13. Williams, D.B. and C.B. Carter, *Transmission electron microscopy : a textbook for materials science*. Vol. 3. 1996, New York: Plenum Press. 549.
14. Monthioux, M., et al., *Sensitivity of single-wall carbon nanotubes to chemical processing: an electron microscopy investigation.* Carbon, 2001. **39**(8): p. 1251-1272.
15. Iijima, S., et al., *Structural flexibility of carbon nanotubes.* Journal of Chemical Physics, 1996. **104**(5): p. 2089-2092.
16. Iijima, S., *Helical Microtubules of Graphitic Carbon.* Nature, 1991. **354**(6348): p. 56-58.
17. Chen, X.H., et al., *TEM investigation on the growth mechanism of carbon nanotubes synthesized by hot-filament chemical vapor deposition.* Micron, 2003. **35**(6): p. 455-460.
18. Binning G., R.H., Gerber Ch., Weibel E., *Surface studies by scanning tunnelling microscopy.* Physical Review Letters, 1982. **49**(1): p. 5.
19. Binning G., R.H., Gerber Ch., Weibel E., *7x7 reconstruction on Si(111) resolved in real space.* Physical Review Letters, 1983. **50**(2): p. 4.
20. Binning G., R.H., Gerber Ch., Weibel E., *Tunnelling through a controllable vacuum gap.* Applied Physics Letters, 1982. **40**(2): p. 3.
21. Moller, R., A. Esslinger, and B. Koslowski, *Thermal noise in vacuum scanning tunneling microscopy at zero bias voltage.* Journal of Vacuum Science & Technology a-Vacuum Surfaces and Films, 1990. **8**(1): p. 590-593.
22. *Scanning Tunnelling Microscopy and Spectroscopy*, ed. D. Bonnell. 1993, New York: VCH. 436.
23. Tomanek, D., et al., *Theory and observation of highly asymmetric atomic-structure in scanning-tunneling-microscopy images of graphite.* Physical Review B, 1987. **35**(14): p. 7790-7793.
24. Hofer, W.A., A.S. Foster, and A.L. Shluger, *Theories of scanning probe microscopes at the atomic scale.* Reviews of Modern Physics, 2003. **75**(4): p. 1287-1331.
25. Biro, L.P., et al., *Scanning tunnelling microscopy (STM) imaging of carbon nanotubes.*

Carbon, 1997. **36**(5-6): p. 689-696.
26. Grobis, M., X. Lu, and M.F. Crommie, *Local electronic properties of a molecular monolayer: C_{60} on Ag(001).* Physical Review B, 2002. **66**(16): p. 4.
27. Davisson, T. and L. Germer, *The scattering of electrons by a single crystal of nickel.* Nature, 1927. **112**: p. 3.
28. Pendry, J.B., *Low energy electron diffraction : the theory and its application to determination of surface structure*. 1997, Chichester: Wiley. 457.
29. Ibach, H. and D.L. Mills, *Electron energy loss spectroscopy and surface vibrations*. 1982, New York: Academic Press. 366.
30. Thiry, P.A., et al., *Electron interaction mechanisms in high-resolution electron-energy loss spectroscopy.* Physica Scripta, 1987. **35**(3): p. 368-379.
31. Egerton, R.F., *Electron Energy-Loss in the Electron Microscope*. Second ed. 1996, New York: Plenum Press. 485.
32. Reed, B.W. and M. Sarikaya, *Electronic properties of carbon nanotubes by transmission electron energy-loss spectroscopy.* Physical Review B, 2001. **64**(19): 195404.
33. Ajayan, P.M., S. Iijima, and T. Ichihashi, *Electron-energy-loss spectroscopy of carbon nanometer-size tubes.* Physical Review B, 1993. **47**(11): p. 6859-6862.
34. Raman, C.V., *A new type of secondary radiation.* Nature, 1928. **121**(3048): p. 2.
35. Hollas, J.M., *Modern Spectroscopy*. 4th ed. 2004, Chichester: John Wiley and Sons. 452.
36. Jorio, A., et al., *Characterizing carbon nanotube samples with resonance Raman scattering.* New Journal of Physics, 2003. **5**: p. 17.
37. Dresselhaus, M.S., et al., *Raman spectroscopy of carbon nanotubes.* Physics Reports-Review Section of Physics Letters, 2005. **409**(2): p. 47-99.
38. Dillon, A.C., et al., *Systematic inclusion of defects in pure carbon single-wall nanotubes and their effect on the Raman D-band.* Chemical Physics Letters, 2005. **401**(4-6): p. 522-528.
39. Choi, H.C., et al., *X-ray photoelectron spectroscopy studies of double-walled carbon nanotube bundles synthesized using thermal chemical vapor deposition.* Chemical Physics Letters, 2004. **399**(1-3): p. 255-259.
40. Pfeiffer, R., et al., *Fine structure of the radial breathing mode of double-wall carbon nanotubes.* Physical Review B, 2005. **72**(16): p. 4.
41. Abrefah, J., et al., *Vapor-Pressure of Buckminsterfullerene.* Applied Physics Letters, 1992. **60**(11): p. 1313-1314.
42. Lemos, V., et al., *Li-inserted carbon nanotube Raman scattering.* Microelectronics Journal, 2005. **36**(11): p. 1020-1022.
43. Rauf, H., et al., *Detailed analysis of the Raman response of n-doped double-wall carbon nanotubes.* Physical Review B, 2006. **74**(23): p. 10.
44. Zhou, W., et al., *Charge transfer and Fermi level shift in p-doped single-walled carbon nanotubes.* Physical Review B, 2005. **71**(20): p. 7.
45. Pichler, T., et al., *Electronic transitions in KxC_{60} ($0 \leq x \leq 6$) from in situ absorption spectroscopy.* Solid State Communications, 1992. **81**(10): p. 859-862.

3. Instrumentation and Methods

In this chapter details of the equipment and sample preparation methods used to acquire data presented in this thesis are outlined. Emphasis is placed upon the construction of these systems.

3.1 Sample Preparation

3.1.1 Carbon Nanotubes

The carbon nanotube samples used in the experiments described in Chapters 4 and 5 were prepared from commercially produced materials. Four types of nanotube material were studied: SWCNTs sourced from Carbon Nanotechnologies Incorporated, U.S.A., produced by the HiPCO method [1] (in which high pressure carbon monoxide is heated with a catalyst, such as iron); DWCNTs and 'thin' MWCNTs (from Nanocyl, Belgium) grown by a commercially confidential catalytic carbon vapour deposition (CCVD) method [2]; and 'thick' MWCNTs from Aldrich produced by an undisclosed chemical vapour deposition (CVD) method. A summary of the manufacturer information provided for these samples is given in Table 3.1.

A uniform preparation approach was adopted to ensure that any differences between the materials studied were associated with intrinsic nanotube properties or defects and impurities associated with the growth process, rather than extrinsic factors introduced during sample preparation. Nanotubes were 'cleaned' by agitating as-received material in concentrated hydrochloric acid (HCl), at room temperature, for eight hours using a hotplate/stirrer. HCl etching is a relatively gentle process compared with many sample purification approaches reported in the literature [3-6] and removes the capped ends of the nanotubes, dissolves any external catalyst and eliminates the majority of graphitic particles present [7]. Although such a gentle oxidation process does not eliminate all residual contaminants (see Chapter 4) it has the advantage of not introducing a large number of defects or surface functional groups, as is often observed in nitric/sulphuric acid or peroxide etches, for example [8, 9]. After acid treatment, the nanotubes were filtered on a 450 nm pore diameter PTFE membrane filter under a rough vacuum, to remove small particles, and washed with copious amounts of deionised water. Ultrasonic suspension of the remaining solid in semiconductor grade residue-free isopropyl alcohol (IPA) ensured sample homogeneity and allowed drop deposition of the nanotubes onto an appropriate support (Table 3.2).

	Manufacturer	Batch Number	Synthesis method	Carbon Purity (%)	Diameter	Length
SWCNTs	Carbon Nanotechnologies Incorporated	HPR93S16	HiPCO[1]			
DWCNTs	Nanocyl	LDW-P/050411	CCVD (undisclosed)	90+	3.5 nm (average)	1-10 µm
tMWCNTs	Nanocyl	LMWA-P/050117	CCVD (undisclosed)	95+	9.5 nm (average)	1.5 µm (average)
MWCNTs	Aldrich	57680-8 05225JA	CCVD (undisclosed)	95+	20-50 nm	2-20 µm

Table 3.1

Summary of information provided by the manufacturer for each of the CNT samples used in this thesis.

3.1.2 C_{60} Film Growth

Highly ordered pyrolytic graphite (HOPG) substrates of (0001) orientation used in Chapter 6 were prepared by cleaving samples in air at room temperature using the 'scotch tape method'. The samples were then immediately introduced into the fast entry load-lock (FEL) of the UHV system (see below) and, after transfer to the main vacuum chamber, annealed under UHV (maximum pressure ~$7x10^{-9}$ mbar) at a nominal temperature of 500°C for at least 3 hours. It was found that shorter or lower temperature annealing cycles did not completely remove surface contamination and had a significant impact on the mode of fullerene growth. Ni(110) substrates used in the same chapter were cleaned using a standard approach [10] involving several sputter and anneal cycles until XPS and LEED indicated that the surface was clean and well ordered. High purity (99.95%, Strem Chemicals Incorporated) C_{60} powder was then thermally evaporated onto the clean HOPG or Ni(110) surfaces from a home-made tantalum cell held at a nominal temperature of 405°C, monitored by a K-type thermocouple fixed to the evaporation envelope.

Fullerene films grown on the Ni(110) substrate at Liverpool University were produced by evaporating C_{60} onto substrates held at the required temperature and a pressure of ~$4x10^{-9}$mbar or lower. Coverage was calibrated by the well-established approach of comparing the ratio of core-level signals from overlayer (C1*s*) and substrate (Ni2*p*) for a given film to that associated with a saturated physical monolayer. A saturated physical monolayer was produced by annealing a thick film to a temperature above the multilayer desorption temperature (~450ºC) [11] but below that for desorption of the monolayer (which is strongly substrate-dependent) [10], until no further changes could be detected.

For work presented on the C_{60}/HOPG system, carried out using the Omicron VT-SPM system based in Durham, film growth was carried out at ambient temperature at a pressure of ~2 x 10^{-9} mbar or lower. The similarity of adsorbate-adsorbate to substrate-adsorbate bonding strength in this system results in a multilayer desorption temperature which is identical to that of the monolayer, to within experimental error [12], therefore coverage cannot be calibrated by the same approach as that used for deposition on metal surfaces. Hence, the rate of deposition of C_{60} molecules was calibrated by direct observation of submonolayer films by STM. The similarity in sticking coefficient for deposition of C_{60} onto the bare substrate and previously deposited molecules ensures that the calibration is valid for all fullerene coverages.

Sample	Analytical Technique	Location	Support/Substrate
CNTs	SEM	Department of Physics, University of Durham, U.K.	HOPG (0001)
	TEM EDX	Boreskov Institute of Catalysis, Russia	Perforated carbon film mounted on a copper grid
	PES EELS AES	Beamline 3.2, Synchrotron Radiation Source, Daresbury, U.K.	Tantalum sample spade
	PES	NCESS, Daresbury, U.K.	
	Raman Spectroscopy	Department of Chemistry, University of Durham, U.K.	Glass microscope slide
C_{60}	LEED PES	Department of Physics, University of Liverpool, U.K.	HOPG (0001) Ni(110)
	STM	Department of Physics, University of Durham, U.K. Department of Physics University of Liverpool U.K.	HOPG (0001) Ni(110)

Table 3.2

A summary of the measurements carried out and presented in this thesis. A summary of the CNT supports and C_{60} substrates is also given.

3.2 Experimental Instrumentation

3.2.1.1 ESCA 300, National Centre for Electron Spectroscopy & Surface Analysis, Daresbury, U.K.

The X-ray photoemission spectroscopy (XPS) measurements presented in Chapters 4, 5 and 6 were carried out at the National Centre for Electron Spectroscopy and Surface Analysis (NCESS), Daresbury, U.K., using the Scienta ESCA300 photoelectron spectrometer (Figure 3.1). A monochromated Al Kα source (1486.6 eV) was used to acquire the spectra, which were obtained at 0° (normal) emission angle, with the system operating at a total instrumental resolution of 0.45 eV (calibrated by an Ag sample) and a pressure of 5 x 10^{-10} mbar. For these measurements, the CNT dispersions were deposited onto a home-built tantalum sample holder until an optically opaque sample was produced, thus ensuring that the measured signal originated from the nanotube material rather than the sample holder (wide-energy range XP spectra – 'survey spectra' – were also examined in order to ensure that no pinholes existed in the film through which the substrate could be detected). The samples were then heated to approximately 700°C for at least 3 hours under ultra-high vacuum conditions using an electron beam heater and cleanliness examined by ensuring that no residual contamination, particularly oxygen, remained in the XP spectra.

For the work presented in Chapter 4, CNT samples were irradiated using a defocused beam of positive Ar^+ ions with a beam energy of 1.5 keV in normal incidence geometry, ensuring uniform irradiation of the CNT sample. The irradiation dose of each sample was calculated by measuring the sample current, *I*, every 10 s using a pico-ammeter, where the sample current ranged from 0.5 μA to 8.9 μA. The total dose calculated in micro-Coulombs is:

$$Dose(\mu C) = I(\mu A).t(s) = \sum 10I$$

Equation 3.1

The NCESS ESCA300 system consists of two main chambers: the preparation chamber and the analysis chamber (indicated in Figure 3.1). Samples enter the preparation chamber via a turbo-molecular pumped FEL and are transferred into the preparation chamber using a transfer bar and 'wobble sticks'. The preparation chamber includes facilities for heating (through use of an electron-beam heater), and ion bombardment (using a saddle-field ion source). Samples are transferred from the preparation chamber to the analysis chamber via

a rack-and-pinion 'railway' mechanism.

The analysis chamber includes an XYZΘ high-precision manipulator, the geometry of which is such that the monochromated x-ray beam, manipulator axis and lens axis lie in a single plane [13]. In this system, Al Kα x-rays (1486.6 eV) are produced using a rotating anode source which works by directing a 20 keV electron beam onto the aluminium rim of a cooled 300 mm titanium alloy disk which rotates at speeds of up to 10,000 rpm. The x-rays generated pass through a differentially pumped port to a monochromator (see Figure 3.1) which consists of seven individually adjustable toroidally bent crystals of α-quartz (held under UHV and maintained at a fixed temperature of 55°C) arranged on a Rowland circle [13]. The monochromator removes the Bremsstrahlung and satellite lines and focuses the radiation onto the sample with a reduced spectral linewidth.

The photoelectrons are collected by the main electron lens system (five lens elements) which, for the experiments reported in this thesis, was always operated in 'high transmission' mode. In this mode the sample spot undergoes magnification of ×5 and the lens accepts electrons from the entire x-ray footprint on the sample. The electron lens focuses the photoelectrons onto a slit-aperture pair at the entrance of a hemispherical analyser. The hemispherical analyser at NCESS has a mean radius of 300 mm with 100 mm between the hemispheres and is operated in constant pass energy mode during spectral acquisition (resulting in a constant resolving power across the spectrum), with an energy resolution approximated by [14]:

$$\Delta E = \frac{E_{pass} w}{2R_o}$$

Equation 3.2

where E_{pass} is the pass energy of the system; w is the slit width and R_0 is the mean radius of the hemispheres. The best analyser resolution (E_{pass} = 20 eV, w = 0.2 mm, R_0 = 300 mm) is calculated as approximately 7 meV using Equation 3.2. In such instances the total resolution of the system is limited by the x-ray linewidth [13], as is the case for the measurements taken in Chapters 4 and 5, for which larger slit widths are used, allowing a higher electron throughput and therefore increased signal. For these measurements the system resolution is approximately 0.45 eV as determined by fitting the Fermi edge of a Ag test sample.

At the exit of the hemispherical analyser is a chevron multichannel plate detector which consists of two 40 mm diameter microchannel plates. The amplified electron signal is then detected through a P10 phosphor screen (KCl) and CCD camera [13].

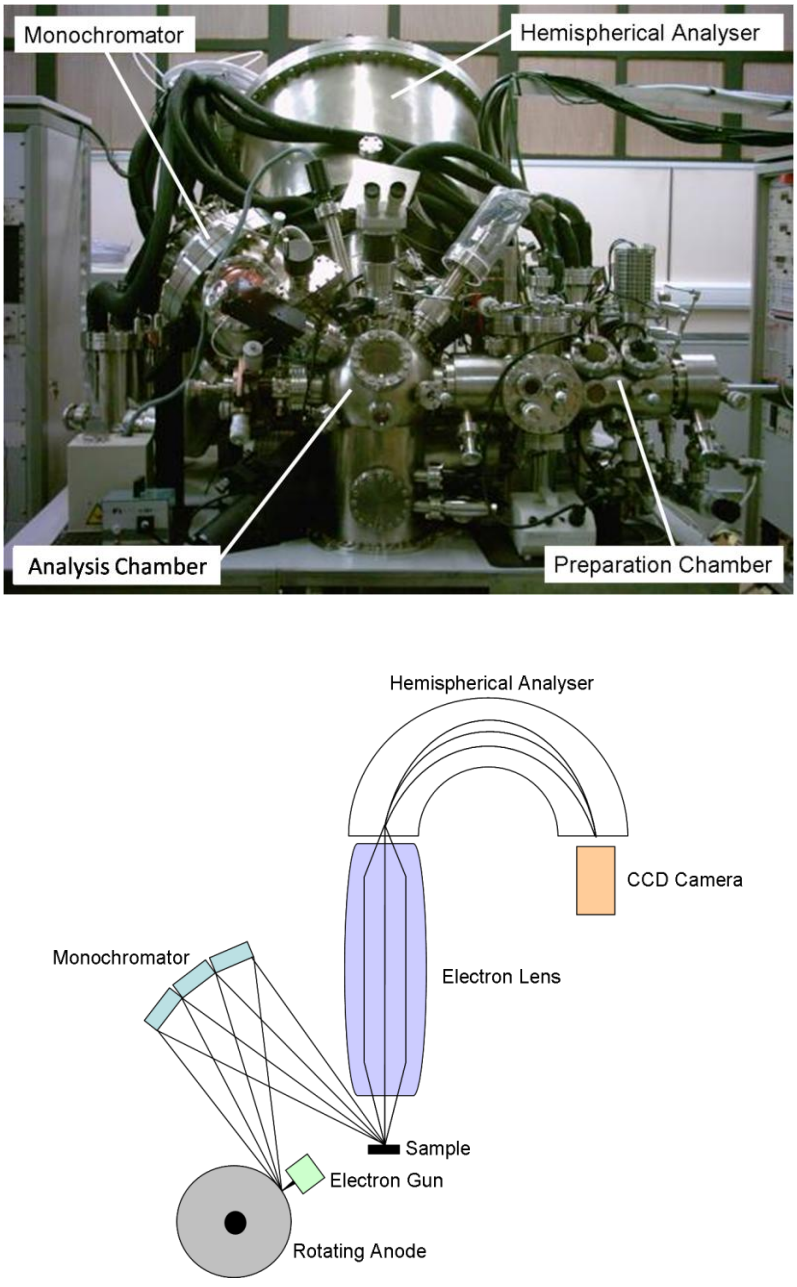

Figure 3.1

(top) The ESCA300 photoelectron spectrometer based at the National Centre for Electron Spectroscopy and Surface Analysis, Daresbury, U.K. (bottom) Schematic of the spectrometer adapted from [13].

3.2.2 UHV- SPM System, Department of Physics, University of Durham, U.K.

STM measurements of the C_{60}/HOPG system reported in Chapter 7 were obtained at the University of Durham using an Omicron Nanotechnology ultra-high vacuum variable temperature scanning probe microscope (VT-SPM), which has a chamber base pressure of ~6 x 10^{-11} mbar. The system comprises an analysis chamber, in which the STM is situated, a preparation chamber and a FEL. Such a layout allows samples to be prepared and analysed without breaking the vacuum maintained by an ion pump and a titanium sublimation pump. The preparation chamber houses the C_{60} source and a manipulator which allows XYZΘ motion of the sample.

The HOPG substrate was mounted in a bespoke Omicron sample holder comprising a molybdenum base plate, boron carbide heater and ceramic top plate. The sample is clamped to the top plate by means of two flexible tantalum strips. The STM images presented in Chapter 6 were obtained in constant tunnel current mode using manually cut Pt-Ir tips, which typically had effective tip radii of ~2 nm and were able to achieve atomic resolution on the graphite surface. The scanning probe microscope (SPM) may be used in a number of modes, including as an atomic force microscope, or a STM. The STM function of the SPM can be operated at temperatures ranging from 25 K up to 1500 K. Sample heating may be achieved resistively (up to temperatures of 1500 K) or radiatively (up to temperatures of 750 K), whilst sample cooling is achieved using a liquid He continuous flow cryostat.

When imaging at the atomic scale, vibration isolation to less than 1 Å is essential. The VT-SPM is mounted on an internal vibration isolation stage, which is suspended by four springs of low spring constant. The oscillations of these springs, in all directions, are damped by an eddy current mechanism. The SPM itself comprises of a scanner tube on which the tip holder is mounted. The scanner tube itself consists of a tube of lead zirconate titantate ceramic (PZT) which is metalised on both the inside and outside surfaces and has a permanent radial electric dipole. The outer metalised surface is split into four quadrants and the motion of the tube scanner is created by applying bipolar, symmetric, voltages to opposite quadrant pairs [15]. The SPM in this system has a maximum scan range of 10 μm × 10 μm with a maximum z – travel of approximately 1.5 μm. The z-resolution of the SPM is stated as 'better than 0.01 nm' [16]. The coarse motion of the scanner tube is controlled in 3 axes using a set of orthogonal piezoelectric 'slip-stick' motors.

When imaging, the tunnel current is preamplified close to the source in order to reduce the amount of electrical noise. At this stage the signal current is converted into a voltage. This amplified signal is then passed to the SPM control unit which, using a feedback loop, maintains a constant tunnel current (user specified value) between the tip and sample (through adjustments in the tip-sample separation) as the tip follows a raster pattern across the surface.

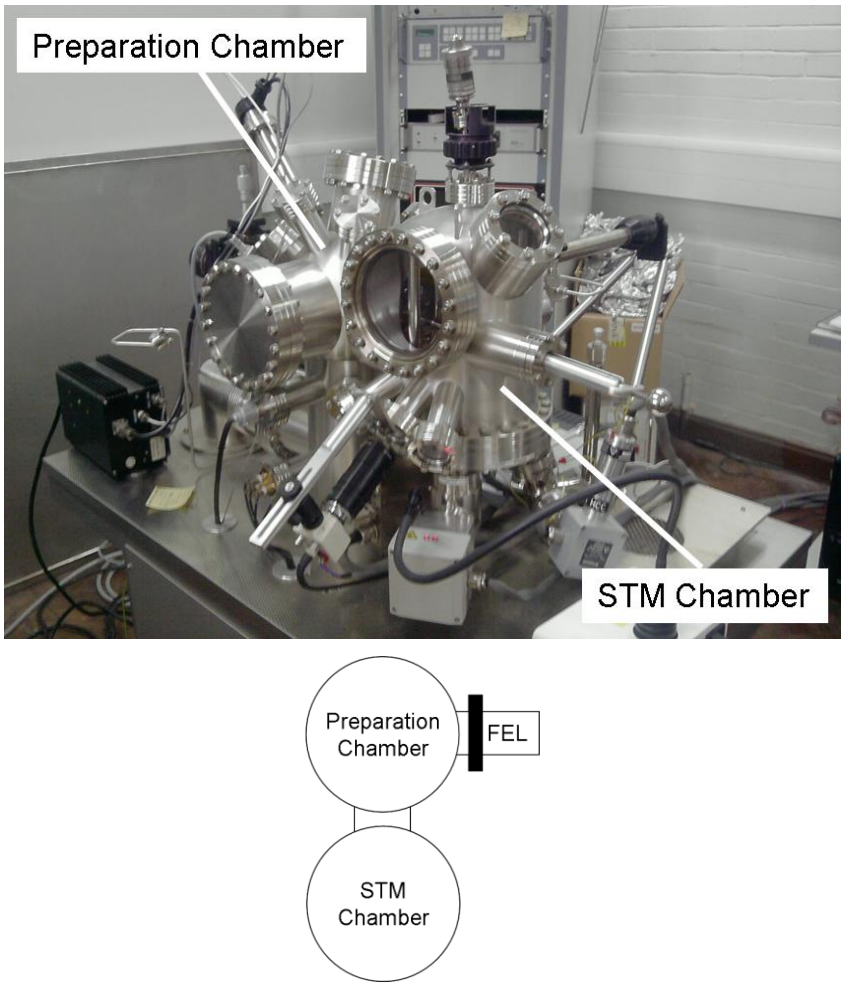

Figure 3.2

(top) Image of the UHV-SPM system based in the Department of Physics at the University of Durham. (bottom) Schematic layout of the system

3.2.3 Surface Analysis System, Department of Physics, University of Liverpool, U.K.

The measurements on the C_{60}/Ni(110) system presented in Chapter 7 were carried out in the Surface Analysis System (Figure 3.3), located initially at Daresbury Laboratory, U.K. and then at the University of Liverpool, U.K.. Throughout all measurements the pressure

of the system remained in the 10^{-10} mbar range, maintained through the use of ion pumps, turbo pumps and a titanium sublimation pump. The system comprises an analysis chamber, a preparation chamber and an STM chamber. Within the preparation chamber is situated an ion gun, used in the sample cleaning procedure, a C_{60} source (as described in Section 3.1.2) and facilities for sample heating, which are situated on a manipulator which is capable of XYZΘ motion. The Ni(110) crystal was mounted using tantalum foil, spot welded onto a tantalum sample plate and then slotted into grooves on the side of the crystal. Sample temperature was directly measured using an infra-red optical pyrometer matched to the sample emissivity.

3.2.3.1 Photoemission Measurements

UPS and XPS measurements presented in Chapter 7 were performed using standard laboratory sources: vacuum ultra-violet radiation for UPS was generated using a standard helium lamp in which helium gas flows through a quartz capillary tube and is excited as it passes between two electrodes. This produces photons of energy 21.2 eV due to the $2p \rightarrow 1s$ (He I) transition with a small satellite contribution (typically 1%, but dependent on the operating conditions of the source) at an energy of 40.8 eV (He II) corresponding to excited states of helium ions [17]. By reducing the He flow (pressure) through the lamp the He II emission line is favoured enabling spectra to be obtained at the higher photon energy. The photons produced in such a manner have well defined energies and a small natural linewidth, so that unless very high resolution studies are required there is no necessity for a monochromator. Al Kα x-rays (1486.6 eV) were generated using a standard water-cooled laboratory UHV x-ray source in which electrons are thermionically emitted from a tungsten filament and accelerated towards a water-cooled Al target. The resultant characteristic x-rays, generated due to the filling of a core vacancy by a radiative transition, are then allowed to exit the x-ray tube through a thin Be window and impinge on the sample. Core level photoemission spectra were referenced to the bulk Ni $2p$ peak of the clean Ni(110) surface, and the UPS spectra were referenced to the sample Fermi level.

Photoelectrons were analysed and detected using a 120 mm radius PSP Vacuum Technology hemispherical electron analyser (the functions of which have been described in Section 3.2.1.1) in conjunction with a five-channeltron electron multiplier array [18]. The measurements were obtained with the analyser placed at an emission angle of 45° from the sample normal for XPS and 40° for UPS. A constant pass energy of 10 eV was used in

conjunction with the 5 mm exit slits. This results in an analyser resolution of approximately 0.2 eV.

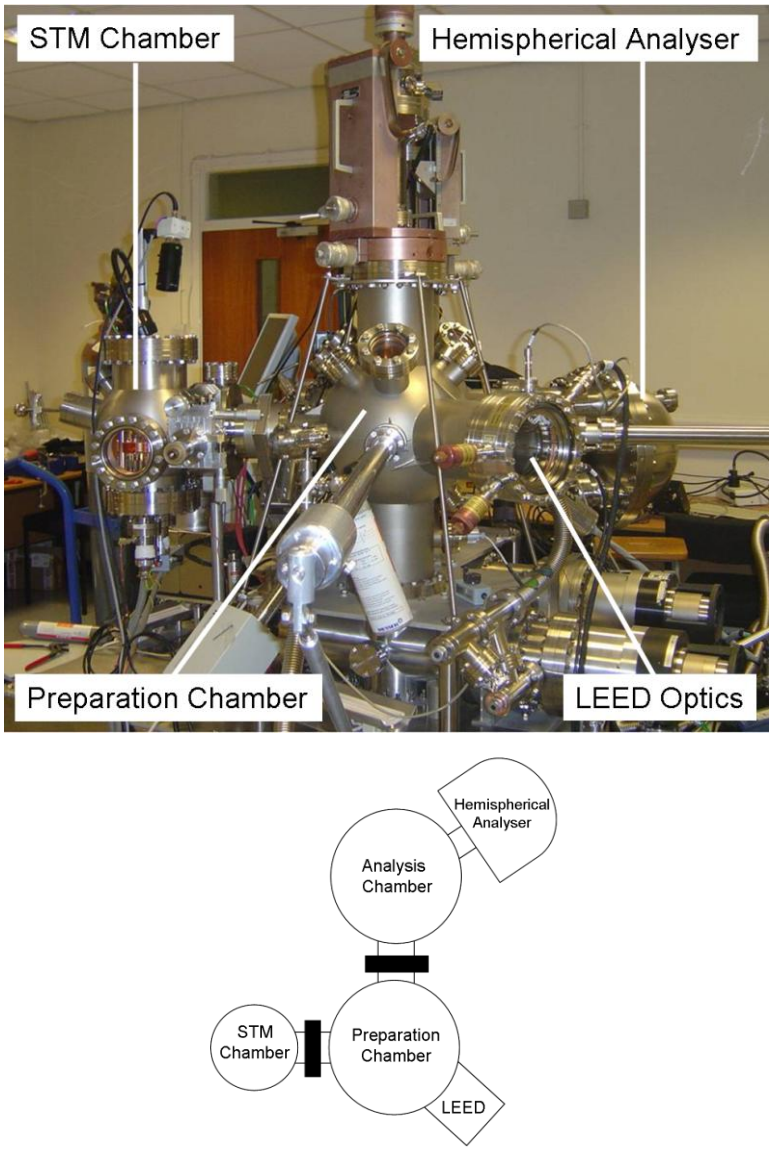

Figure 3.3

(top) The Liverpool Surface Analysis System, used to carry out STM, LEED and XPS measurements presented in Chapter 6. (bottom) A schematic of the layout of the system.

3.2.3.2 Scanning Tunnelling Microscope

STM measurements on the C_{60}/Ni(110) system were carried out using an Omicron Nanotechnology STM situated in an ultra-high vacuum chamber with a base pressure of $2x10^{-10}$ mbar (Figure 3.3). The measurements were performed using constant current mode at ambient temperature with tungsten tips which produced using a standard etching method [19]. The basic components of the STM situated in this system and the system

used in the UHV-VT STM (described in Section 3.2.2) are the same, although this STM has coarse motion only in two axes (z and x) and only possesses the capability of imaging at room temperature.

3.2.3.3 Low Energy Electron Diffraction

LEED measurements were carried out using an OCI Vacuum MicroEngineering BDL600IR optics system in normal incidence geometry. In this particular model, the primary beam energy can range from 5 eV up to 3 keV with a beam current of 100 – 250 μA [20]. The LEED optics are surrounded by mu-metal shielding and include three highly transparent tungsten hemispherical retarding grids and a P31 phosphor grid on which the LEED pattern is displayed and is recorded by a camera. The $I(V)$ LEED measurements were taken in constant beam current mode with primary beam energies ranging from 15 eV up to 300 eV.

3.2.4 HiRMES, Beamline 3.2, Synchrotron Radiation Source, Daresbury, U.K.

In Chapter 4, Auger Electron Spectroscopy (AES), low-loss Electron Energy Loss Spectroscopy (EELS) and Ultra-violet Photoemission Spectroscopy (UPS) measurements were undertaken offline on beamline 3.2 of the Synchrotron Radiation Source (SRS), Daresbury, U.K using the now decommissioned High Resolution Multichannel Spectroscopy (HiRMES) system. The carbon nanotube samples used in this instance were created by depositing the appropriate CNT suspension dropwise onto tantalum sample spades until an optically thick film was produced. This sample was then heated to approximately 550ºC under ultra-high vacuum (UHV) to remove adsorbed surface contaminants [21] and residual solvent, then thoroughly examined to ensure that no signal from the sample holder could be observed with the spectroscopic tools used.

A focussed, monoenergetic, primary electron beam was produced using a VSW electron gun capable of producing electron beams with energies ranging from 0-5 keV. AES measurements were taken using an electron energy of ~3 keV and a system resolution of ~800 meV whilst EELS measurements utilised an electron energy of ~200 eV and a system resolution of ~400 meV. For UPS measurements, the photon energy was 40.8 eV (helium II) and the system the resolution ~400 meV.

The HiRMES system comprised a single cylindrical UHV chamber with base pressure of ~5 x 10^{-10} mbar maintained through scroll-pump backed turbomolecular pumps and to a titanium sublimation pump surrounded by a liquid nitrogen cooled cold trap. A XYZΘ sample manipulator was situated along the axis of the cylinder and was capable of cooling the sample to cryogenic temperatures using liquid helium (base temperature 11 K). Sample heating was carried out resistively through the manipulator and sample temperatures were measured by a K-type thermocouple. For photoemission studies carried out in this system, the photons were generated by a helium discharge lamp (as outlined in Section 3.2.3.1). The electrons were analysed using a Vacuum Generators CLAM4 hemispherical analyser (operating on the principles outlined in 3.2.1.1) and detected using a twenty channel microchannel plate detector (2 mm pitch, 300 μm slits) developed by ESG [22] rather than the manufacturer-supplied channeltron.

3.2.5 Scanning Electron Microscope, Department of Physics, University of Durham, U.K.

The Scanning Electron Microscopy (SEM) images presented in Chapter 4 were obtained using a Philips FEI XL30 FEG SEM (Figure 3.4) at the University of Durham with a primary electron energy of 30 keV. Carbon nanotube samples were prepared by casting drops of purified material from a residue free IPA suspension onto the freshly cleaved (0001) surface of a highly oriented pyrolytic graphite (HOPG) sample. No further sample preparation was carried out.

The SEM has a limiting resolution of approximately 5 nm and is capable of achieving magnifications of over 300,000×. Four main components are used to produce the images: a Schottky field emission electron gun, a demagnification unit, a scan unit and a detection unit. The electron gun produces a beam with a small spatial volume and tuneable energy. This beam enters the demagnification unit consisting of several electromagnetic lenses which focus it to a much smaller diameter at the sample surface. The secondary electrons generated are detected by an Everhart Thornely detector. The primary electron beam is moved across the surface of the sample in a raster pattern and the changes in secondary and backscattered electron intensity produces on onscreen image [23].

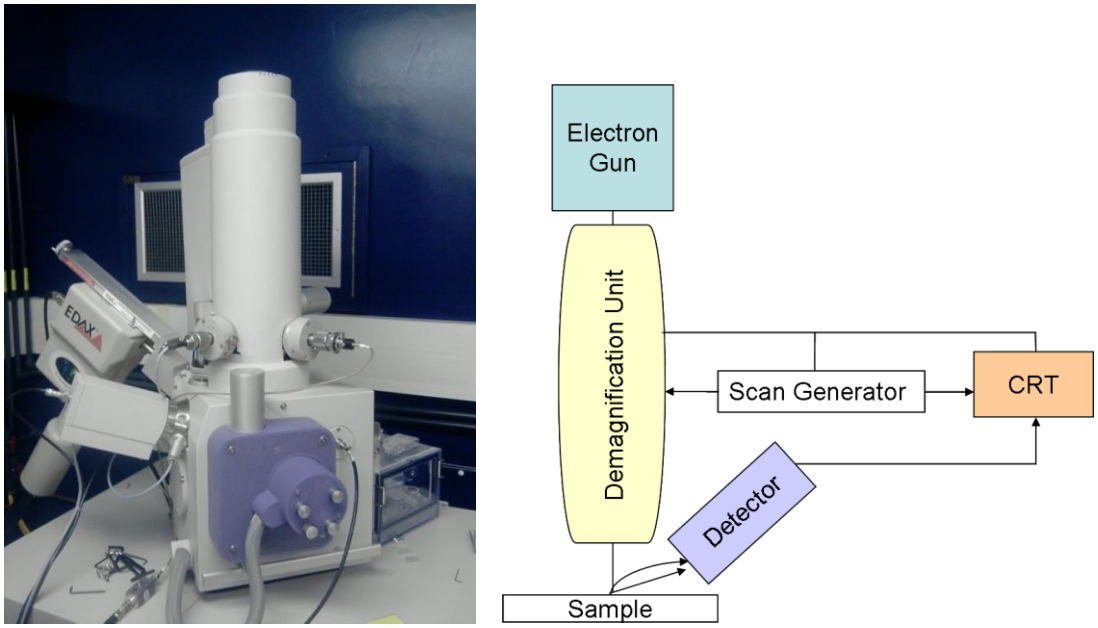

Figure 3.4

(top) The FEI XL30 FEG SEM at the University of Durham. A standard secondary electron detector and a primary electron energy of 30 keV was employed. The system has a limiting system resolution of ~ 5 nm. (bottom) Schematic layout of the SEM adapted from [23]

3.2.6 Raman Spectroscopy, Department of Chemistry, University of Durham, U.K.

The Raman spectroscopy measurements presented in Chapter 4 were carried out at the Department of Chemistry, University of Durham using a Horiba Jobin Yvon Ltd. LabRam Raman Spectrometer. The excitation source used was a helium-neon laser with an excitation wavelength of 632.831 nm with a total system resolution of 0.1 cm^{-1}. The samples were prepared by drop deposition of each of the suspensions onto a separate glass microscope slide. These samples were examined without further preparation.

The main components of the Raman spectrometer include the laser excitation source, focussing and collecting optics, monochromator, detector and recorder. A laser is used as the excitation source because it provides a coherent, monochromated beam of high intensity light such that the intrinsically weak Raman signals are of sufficient intensity to be detected. In order to further improve the Raman signal, the laser is usually focussed onto the sample since the Raman intensity is proportional to the irradiance of the exciting beam. The scattered light is then collected and focussed onto a notch or edge (high pass) filter to prevent any stray elastically scattered laser light from entering the monochromator [24]. After monochromation the scattered light is passed onto a CCD detector.

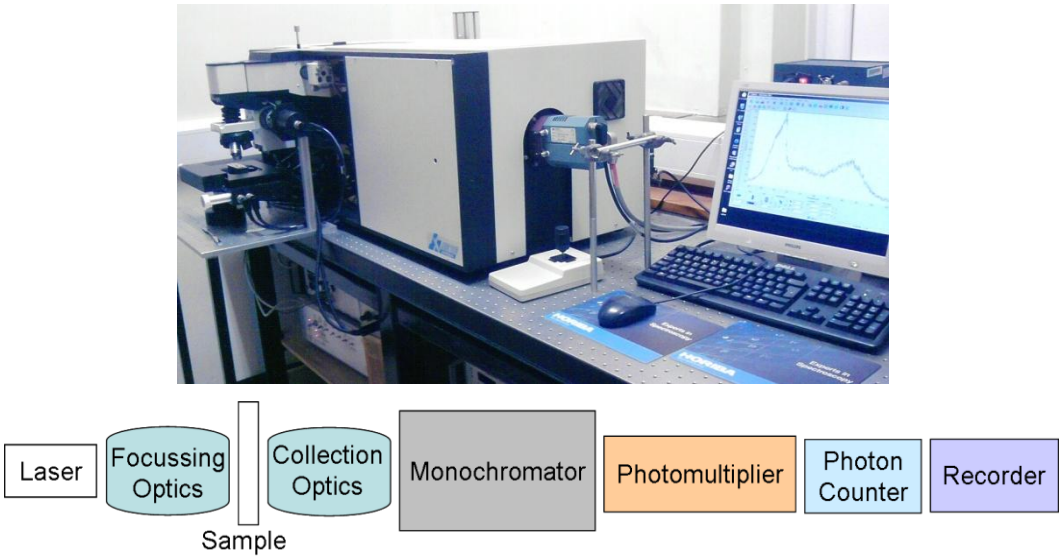

Figure 3.5

The Horiba Jobin Yvon Ltd. LabRam Raman Spectrometer used for the Raman measurements presented in Chapter 4.

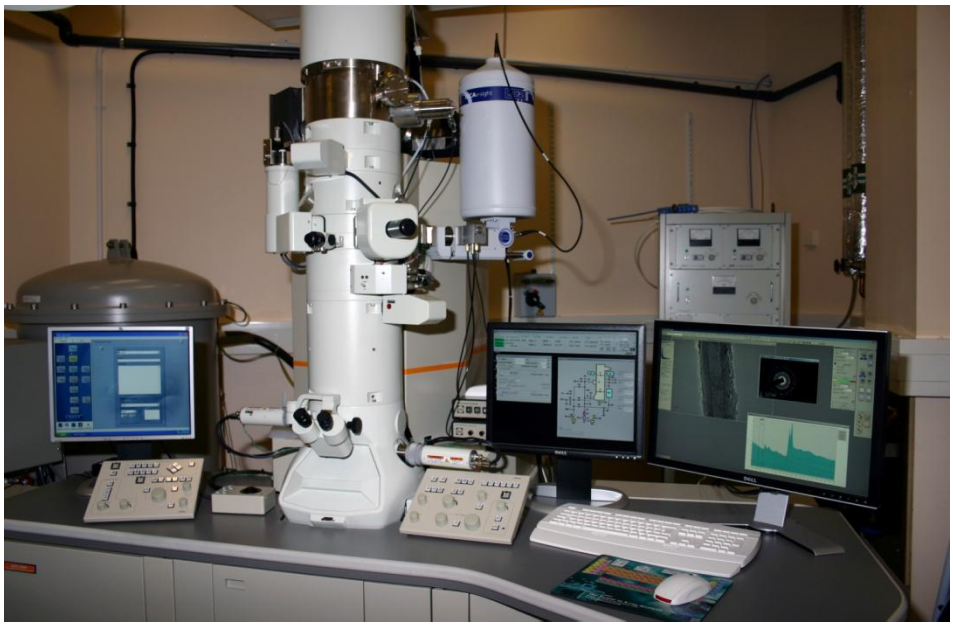

Figure 3.6

A JEOL JEM-2010 electron microscope as used to acquire the TEM images presented in Chapter 4.

3.2.7 High Resolution TEM, Boreskov Institute of Catalysis, Boreskov, Russia

The High Resolution Transmission Electron Microscopy (HRTEM) and Energy Dispersive X-ray Analysis measurements presented in Chapter 4 were carried out at the Boreskov Institute of Catalysis, Russia. For such measurements the suspension was deposited onto a

perforated carbon film mounted on a copper grid. HRTEM measurements were carried out using a JEOL JEM-2010 electron microscope with a limiting resolution of 0.14 nm and a primary electron energy of 200 keV. Local EDX analysis was carried out using an EDAX spectrometer (EDAX Co.) fitted with a Si(Li) detector (energy resolution of 130 eV) and a primary electron energy of 200 keV.

3.3 Summary

In this chapter technical information about the equipment used in obtaining the data presented in this thesis has been presented, in addition to details of the experimental procedures used in the preparation and analysis of the CNT and fullerene samples.

3.4 References

1. Nikolaev, P., et al., *Gas-phase catalytic growth of single-walled carbon nanotubes from carbon monoxide.* Chemical Physics Letters, 1999. **313**(1-2): p. 91-97.
2. Nanocyl. [cited 05-01-2010]; Available from: http://www.nanocyl.com/en/Products-Solutions/Products/Research-Grades.
3. Chattopadhyay, D., I. Galeska, and F. Papadimitrakopoulos, *Complete elimination of metal catalysts from single wall carbon nanotubes.* Carbon, 2002. **40**(7): p. 985-988.
4. Park, T.J., et al., *Purification strategies and purity visualization techniques for single-walled carbon nanotubes.* Journal of Materials Chemistry, 2006. **16**(2): p. 141-154.
5. Chen, X.H., et al., *Non-destructive purification of multi-walled carbon nanotubes produced by catalyzed CVD.* Materials Letters, 2002. **57**(3): p. 734-738.
6. Kim, Y. and D.E. Luzzi, *Purification of pulsed laser synthesized single wall carbon nanotubes by magnetic filtration.* Journal of Physical Chemistry B, 2005. **109**(35): p. 16636-16643.
7. Ebbesen, T.W., et al., *Purification of Nanotubes.* Nature, 1994. **367**(6463): p. 519-519.
8. Bower, C., et al., *Intercalation and partial exfoliation of single-walled carbon nanotubes by nitric acid.* Chemical Physics Letters, 1998. **288**(2-4): p. 481-486.
9. Zhang, J., et al., *Effect of chemical oxidation on the structure of single-walled carbon nanotubes.* Journal of Physical Chemistry B, 2003. **107**(16): p. 3712-3718.
10. Hunt, M.R.C., et al., *Charge-Transfer and Structure in C_{60} Adsorption on Metal-Surfaces.* Physical Review B, 1995. **51**(15): p. 10039-10047.
11. Maxwell, A.J., et al., *Photoemission, Autoionization, and X-Ray-Absorption Spectroscopy of Ultrathin-Film C60 on Au(110).* Physical Review B, 1994. **49**(15): p. 10717-10725.
12. Maxwell, A.J., et al., *Electronic and geometric structure of C_{60} on Al(111) and Al(110).* Physical Review B, 1998. **57**(12): p. 7312-7326.
13. Beamson, G., *High resolution XPS of organic polymers : the Scientia ESCA300 database / G. Beamson and D. Briggs.* 1992, Chichester :: Wiley.
14. Wannberg, B., U. Gelius, and K. Siegbahn, *Design Principles in Electron Spectroscopy.* Journal of Physics E-Scientific Instruments, 1974. **7**(3): p. 149-159.
15. Chen, C.J., *Part II - Instrumentation*, in *Introduction to Scanning Tunnelling Microscopy* 1993, OUP: New York. p. 412.
16. OmicronNanotechnology, *The VT AFM User's Guide & Service Manual.* 2004.
17. Carlson, T.A., *Photoelectron and Auger spectroscopy.* 1975, New York :: Plenum.
18. PSP Vacuum Technology. *Hemispherical Analyser Technical Information.* [cited 04-01-2010]; Available from: http://www.pspvacuum.com/ha.html.
19. Tahmasebipour, G., et al., *Effect of Fabrication Process Parameters on the Apex-Radius of STM Tungsten Nanotip.* Scanning, 2009. **31**(2): p. 65-74.
20. OCI Vaccum Microengineering. *BDL800IR-MCP and BDL600IR-MCP LEED Specifications.* [cited 19-10-2009]; Available from: http://www.ocivm.com/.
21. Musket, R.G., et al., *Preparation of Atomically Clean Surfaces of Selected Elements - a Review.* Applied Surface Science, 1982. **10**(2): p. 143-207.
22. Teehan, D. and A. Malins. *High Resolution Ultraviolet Photoelectron Spectroscopy of Solid Surfaces with HiRMES on Station 3.2.* [cited 07-10-2009]; Available from: http://www.srs.ac.uk/srs/news_archive05.html.
23. *The XL FEG/SFEG Scanning Electron Microscope Operating Manual.* 10/01/2001 ed. 2001: FEI Company.
24. Gilson, T.R. and P.J. Hendra, *Laser Raman spectroscopy : a survey of interest primarily to chemists, and containing a comprehensive discussion of experiments on crystals.* 1970, Chichester :: Wiley-Interscience. 266.

4. Multi-Technique Characterisation of Commercially Produced CNTs

In this chapter four commercially available carbon nanotube materials are analysed using a range of analytical techniques, including scanning electron microscopy (SEM), high resolution transmission electron microscopy (HRTEM), energy dispersive x-ray analysis (EDX), Auger electron spectroscopy (AES), low-loss electron energy loss spectroscopy (EELS), ultra-violet photoemission spectroscopy (UPS), x-ray photoemission spectroscopy (XPS) and Raman spectroscopy. The aim of this work was to properly characterise the materials used in subsequent chapters of this thesis and to compare the capability of these techniques in nanotube characterisation.

4.1 Introduction

The wide variety of methods for producing carbon nanotubes (CNTs) [1-3] and the various approaches to purification of the subsequent materials [4-7], leads to CNT samples which cover a vast spectrum of 'quality' (by which is meant purity, structural perfection, dispersion in nanotube diameter and number of walls etc.). Consequently, extensive analysis is needed so that the nature of the CNT material being produced, purchased, applied or analysed is known. Of course, the definition of the terms 'quality' and 'purity' when applied to a CNT sample often differ from researcher to researcher depending on the precise measurement or application and so an agreed definition of 'quality' – and the scale over which it is to be measured – is required.

This is a widely recognised obstacle [8, 9], with the main impasse being the definition of CNT 'quality' itself: are we referring to topographic defect density, elemental purity or degree of graphitisation? If referring to the degree of graphitisation, how do we differentiate graphite from a pristine CNT? This is a core problem to all fundamental and applied CNT research to which there is not a simple solution. Without such a framework in place comparing work on nanotubes within the literature will remain questionable and may impact on possible applications [10-13] of CNTs.

The availability of appropriate techniques and the limited time and resources available for sample preparation, analysis and data processing, usually dictates what characterisation is carried out. Therefore it is of utmost importance that the comparability and reliability of these techniques is understood, in particular, their ability to successfully characterise different CNT species. In this chapter, four commercially sourced samples (details of which are provided in Chapter 3) are processed in the same manner and several commonly used techniques (scanning electron microscopy (SEM), high resolution transmission electron microscopy (HRTEM), energy dispersive x-ray analysis (EDX), Auger electron spectroscopy (AES), low-loss electron energy loss spectroscopy (EELS), ultra-violet photoemission spectroscopy (UPS), x-ray photoemission spectroscopy (XPS) and Raman spectroscopy) are employed in their characterisation. The aim is to assess the reliability and compatibility of these techniques whilst providing a useful and thorough analysis of the CNT material used in our later studies.

4.2 Experimental

Nanotube dispersions were created from commercially produced single-walled CNTs (SWCNTs) double-walled CNTs (DWCNTs), 'thin' multiple-walled CNTs (tMWCNTs) and 'thick' multiple-walled CNTs (MWCNTs) and subsequently drop-deposited onto the appropriate support for analysis. Details of the CNT samples, their origins, in-house processing and supports used have previously been discussed in Chapter 3. Details of the equipment and experimental apparatus used are also provided in the appropriate section of Chapter 3. However, for convenience, a brief summary of the techniques employed to obtain the data presented in this chapter is provided in Table 4.1.

Analytical Technique	Primary Beam/Photon Energy	System Resolution
SEM	30 keV	5 nm
HRTEM	200 keV	0.14 nm
EDX	200 keV	130 eV
AES	3 keV	800 meV
Low-Loss EELS	200 eV	400 meV
UPS	40.8 eV (He II)	400 meV
Raman	1.96 eV	0.1 cm^{-1}
XPS	1486.6 eV (Al Kα)	0.45 eV

Table 4.1

A summary of the incident beam/photon energies and system resolution for each of the techniques employed in this chapter. Further detail of equipment is given in the appropriate section in Chapter 3.

4.3 Results and Discussion

Figure 4.1 displays SEM ((a) to (d)) and HRTEM ((e) to (h)) images of each of the four CNT samples studied. From large area SEM and HRTEM images (Figure 4.1, (a) to (d)), all samples are found to contain very little non-filamentary material. The SWCNT and DWCNT samples are seen to be highly bundled into ropes and the DWCNT sample contains material with a porous structure which appears to be coating the outer walls of the DWCNTs, giving them a speckled appearance in places. The DWCNT sample also contains some CNTs with more than two walls. The tMWCNTs are observed within large (loosely packed) ropes, the edges of which appear as free (or partially free) tMWCNTs (Figure 4.1(c)). The surrounding area of such ropes tends to be littered with individual tMWCNTs. The 'thick' MWCNT sample, contrary to the other nanotube samples, is found to be well-dispersed. Such contrasts in the mesoscopic structure of MWCNT samples compared with SWCNTs [14, 15] and DWCNTs [16] has previously been documented [17, 18] and it has been suggested that the smaller diameter distributions of SWCNTs and DWCNTs allow formation of a close packed triangular lattice. In contrast, MWCNTs have a larger diameter distribution so that close packing may only occur through a shared amorphous carbon layer that would coat the bundle [17]. Subsequent removal of this layer through purification processes results in the relatively easy separation of individual MWCNTs from a bundle, as observed here in the tMWCNT and MWCNT samples.

Information regarding the diameter distribution of the SWCNTs and DWCNTs is not accessible using SEM due to limited resolution (~5 nm). This information may be obtained through HRTEM, although the level of bundling makes this difficult, highlighting the need for the measurement of the radial breathing modes (RBMs) using Raman spectroscopy (details of which are given in Chapter 2, Section 2.9) [19]. The RBMs of SWCNTs and DWCNTs are associated with the radial motion of the nanotube [19] and occur at frequencies below ~350 cm^{-1}. The frequencies of the RBMs, ω_{RBM}, have a dependence on diameter, D, of [19] :

$$\omega_{RBM} = \frac{A}{D} + B$$

Equation 4.1

A and *B* are constants and are taken to be 234 cm^{-1} and 10 cm^{-1} respectively, which are the values determined for SWCNT bundles on a Si/SiO_2 substrate [20, 21]. Such spectral features are affected by factors including chemical processing [22], pressure [20, 23] and the formation of bundles (described in Equation 1 through the constant *B*) [20]. Therefore care should be taken when using Raman spectroscopy to ascertain the diameters of SWCNTs and DWCNTs; such measurements should be verified using additional techniques.

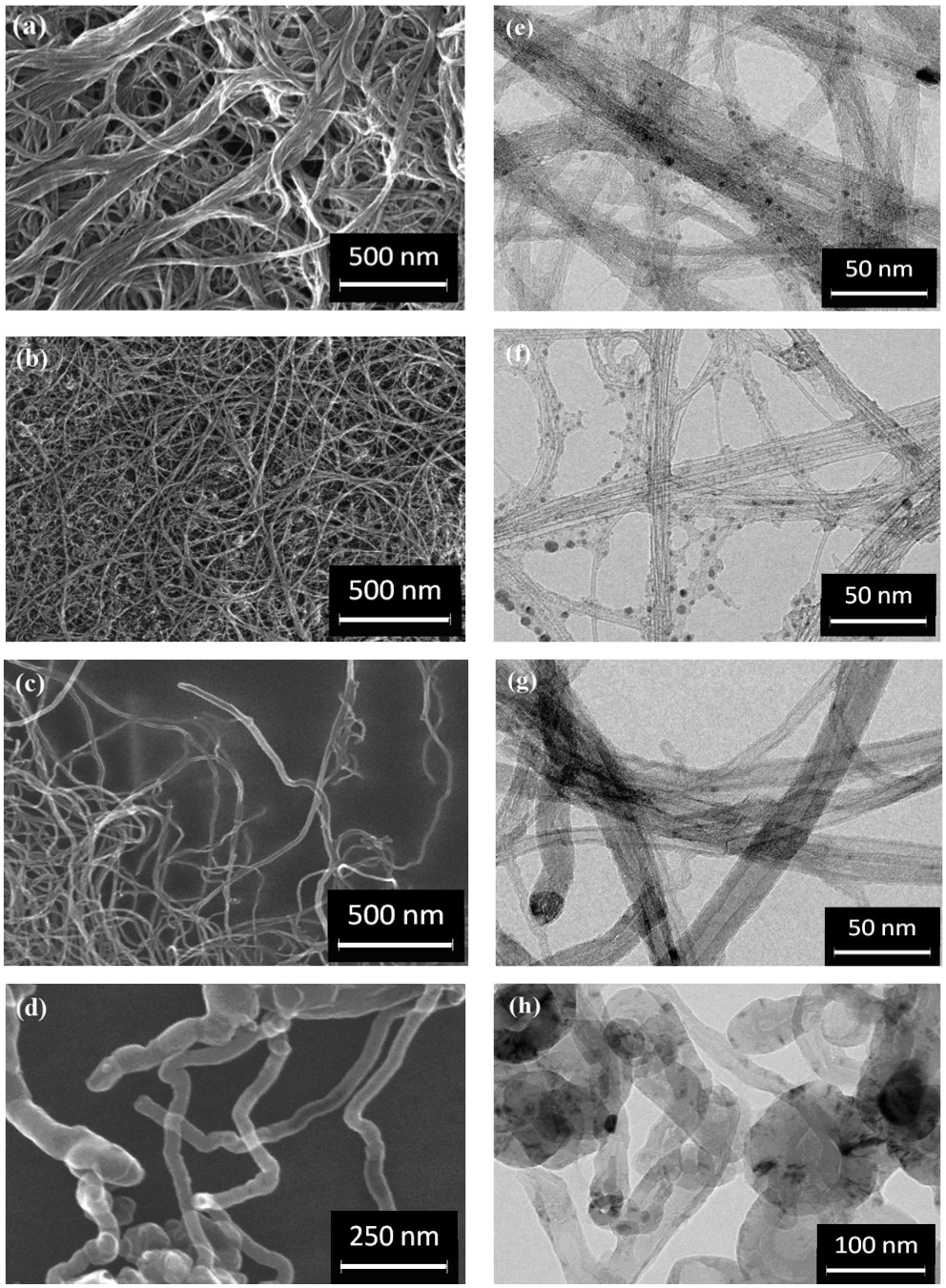

Figure 4.1

(a) to (d): Large area SEM, and (e) to (h) HRTEM images of SWCNT, DWCNT, tMWCNT and MWCNT samples respectively.

The strength of Raman spectroscopy is its ability to measure the diameter distribution of SWCNTs and DWCNTs within a sample (or at least those resonant with the laser energy) in a single measurement through fitting of the RBMs using Lorentzian components of the same FWHM (Figure 4.2) and weighting by Raman intensity. In this way, the average diameter of the CNTs *in resonance with the laser* and their relative abundance in the sample can be found. There is, however, the caveat that this is not a comprehensive diameter distribution of the sample as a whole – this would require the use of many different excitation energies so that the resonance condition is met for all of the SWCNTs present in the sample. The presence of a minority of MWCNTs within the DWCNT sample, as highlighted through HRTEM, is not of concern since RBM intensity of MWCNTs is greatly reduced (as can be seen in the Raman spectra from the tMWCNT and MWCNT samples, discussed below). The results of such analysis and the diameter measurements obtained from SEM and HRTEM are displayed in Table 4.2.

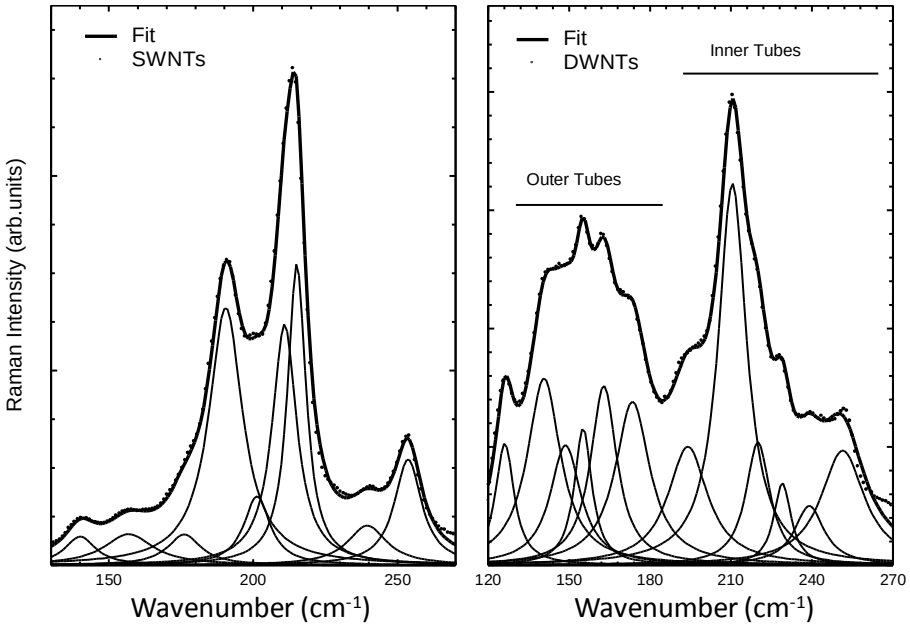

Figure 4.2

SWCNT and DWCNT RBMs. The DWCNT RBMs are split into two groups, attributed to the resonance of inner and outer nanotube components.

Clearly SEM, HRTEM and Raman spectroscopy are highly useful tools when ascertaining the diameters of CNT samples; the potential weakness of each technique (SEM/HRTEM measuring small diameter CNTs or Raman at measuring large diameter CNTs) can be compensated by the other. SEM and HRTEM tend to be the first choice of analytical

technique when characterising CNTs since these techniques not only give diameter/length measurements, but they are able provide visual verification of the wider structural nature of the sample. In particular, the small area cross-sectional view offered by HRTEM provides valuable information about the internal structure of CNTs such as the number and quality of the walls. This will be discussed later in this chapter.

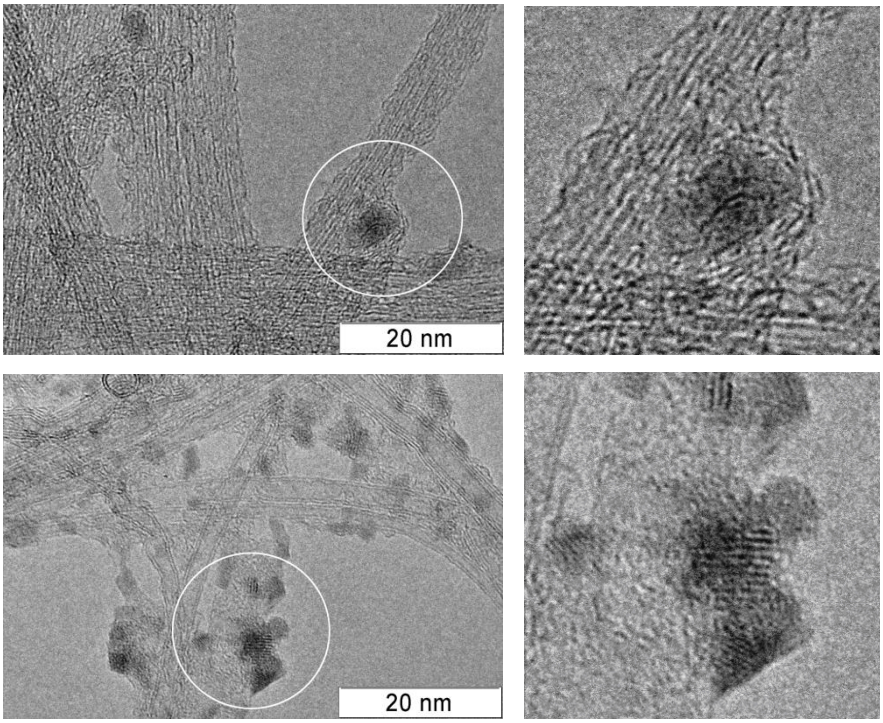

Figure 4.3

Small area HRTEM images of the (top panels) SWCNT and (bottom panels) DWCNT samples. The circled structures shown in the left images are expanded in the images on the right.

Small-area HRTEM images are also able to highlight the structure and nature of any contamination that is contained within the CNT samples. The visible contamination within the SWCNT sample is found to be in the form of dense nanoparticles, which appear to be closely associated with the SWCNT bundles (Figure 4.3, top panels), whilst within the DWCNT sample contamination includes tMWCNTs and pale amorphous 'clouds' containing small dense nanoparticles which surround bundles of DWCNTs (Figure 4.3, bottom panels), suggesting the acidic oxidation purification process was not fully effective. This contamination takes on a periodic structure in some places with lattice spacings of ~ 0.9 Å, 1.3 Å and 3.9 Å obtained through Fourier transformation of areas of the digital image in which they are contained. However, it is not possible to identify these species without further analysis. The most distinct contamination is contained within the MWCNT sample where carbon encapsulated nanoparticles (Figure 4.4) are observed. These

nanoparticles can be identified as nickel catalyst nanoparticles through EDX and XPS measurements (see below).

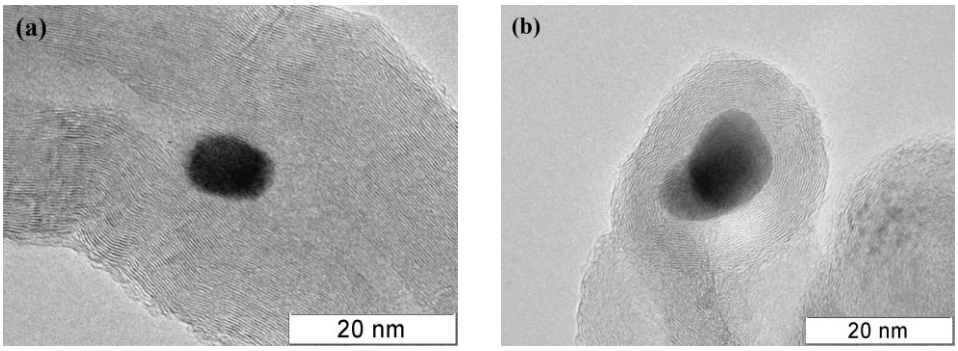

Figure 4.4

HRTEM images of the MWCNT sample showing the nature of the catalytic particles included within the (a) CNTs and (b) within carbon shells. The nanoparticles are identified as nickel through EDX.

Within the literature, chemical verification of the contamination observed by SEM/HRTEM is usually confirmed via EDX, since this can generally be carried out within the SEM/HRTEM. XPS and AES may also be used for such chemical analysis.

EDX and XPS measurements of the SWCNT and DWCNT samples (not shown) indicate the presence of small amounts of chemical contamination in the form of iron, chlorine and oxygen. Whilst the first two can be associated with the synthesis and in-house purification processes respectively, the third can be attributed to adsorbed oxygen species. EDX and XPS measurements of the tMWCNT sample (Figure 4.5 and Figure 4.6, respectively) show a wide range of contamination including silicon and small quantities of sulphur, calcium, potassium and phosphorous. Such contaminants are commonly present in commercially produced glassware which may be mixed into CNT samples during purification or preparation processes [24]. However, the presence of such contamination may also be explained through the use of zeolite supports that are commonly used during synthesis [25] or the use of common surfactants, such as sodium dodecylsulphate (SDS, $C_{12}H_{25}NaO_4S$) and sodium dodecylbenzene sulphonate (SDBS, $C_{18}H_{29}NaO_3S$), by the manufacturer during post-production purification (such information was not provided by the supplier). Additional AES analysis of the MWCNT sample (Figure 4.8) identifies oxygen and silicon contamination (peaks at kinetic energies of ~507 eV and ~75 eV) which may be associated with silica. Hence we suggest that this contamination originated either from zeolite or glassware particles. This conclusion is supported through the absence of charge transfer

to/from the CNTs in UPS (Figure 4.10) and Raman spectra (Figure 4.11) [19, 26-28]. The lack of such contamination in SWCNT and DWCNT samples leads us to believe that this contamination is sourced from the production process (i.e. the zeolite support) rather than purification (i.e. from glassware).

The absence of any detectable peaks apart from the C *KLL* line within the Auger spectra of the SWCNT, DWCNT and tMWCNT samples highlights the problem of the finite information depth of this technique (~5 nm); any contamination embedded within carbonaceous material will not be detected. Similarly, if small quantities of contamination are present, Auger spectroscopy may not have sufficient sensitivity to enable detection. It is also prudent to note that, when using AES, there may be problems identifying weakly bound groups which may be desorbed upon irradiation with the electron beam.

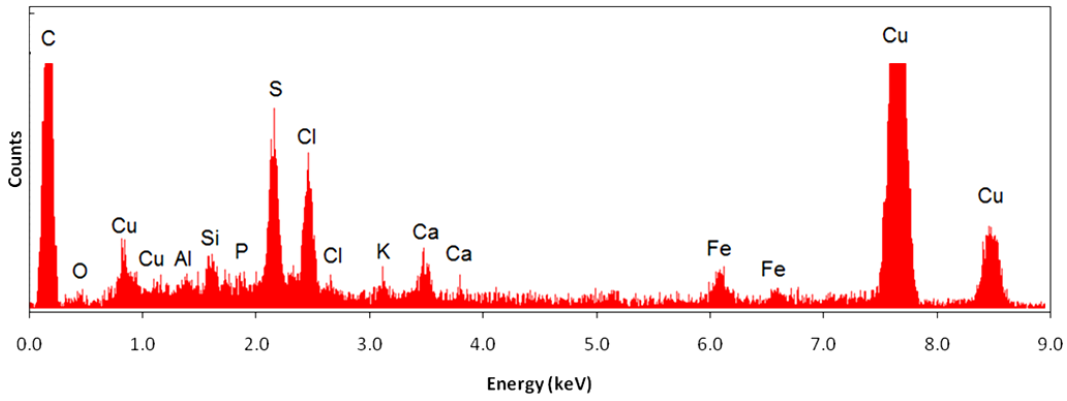

Figure 4.5

EDX spectrum of the tMWCNT sample. Signals from copper (the support used for the sample), chlorine (due to HCl etching process) and oxygen are observed. Signals due to silicon, sulphur, calcium, potassium, phosphorous may suggest the presence of silica [24] or the use of a zeolite support or surfactants by the manufacturer (see text for details).

As we have seen above, a range of techniques are needed to fully characterise the level of contamination within any given CNT sample, in addition to the structure and chemical nature of both the CNTs and contaminants. From the above discussion, it might be suggested that a minimum of three techniques are needed to achieve this: Raman spectroscopy and HRTEM for diameter measurement; HRTEM for visual verification of the structure and level of contamination of the sample; XPS for chemical characterisation of the samples. In the latter part of this chapter, analysis will focus on the structural 'quality' of each of the CNT samples, using methods that are commonly used in the literature [19, 29-34].

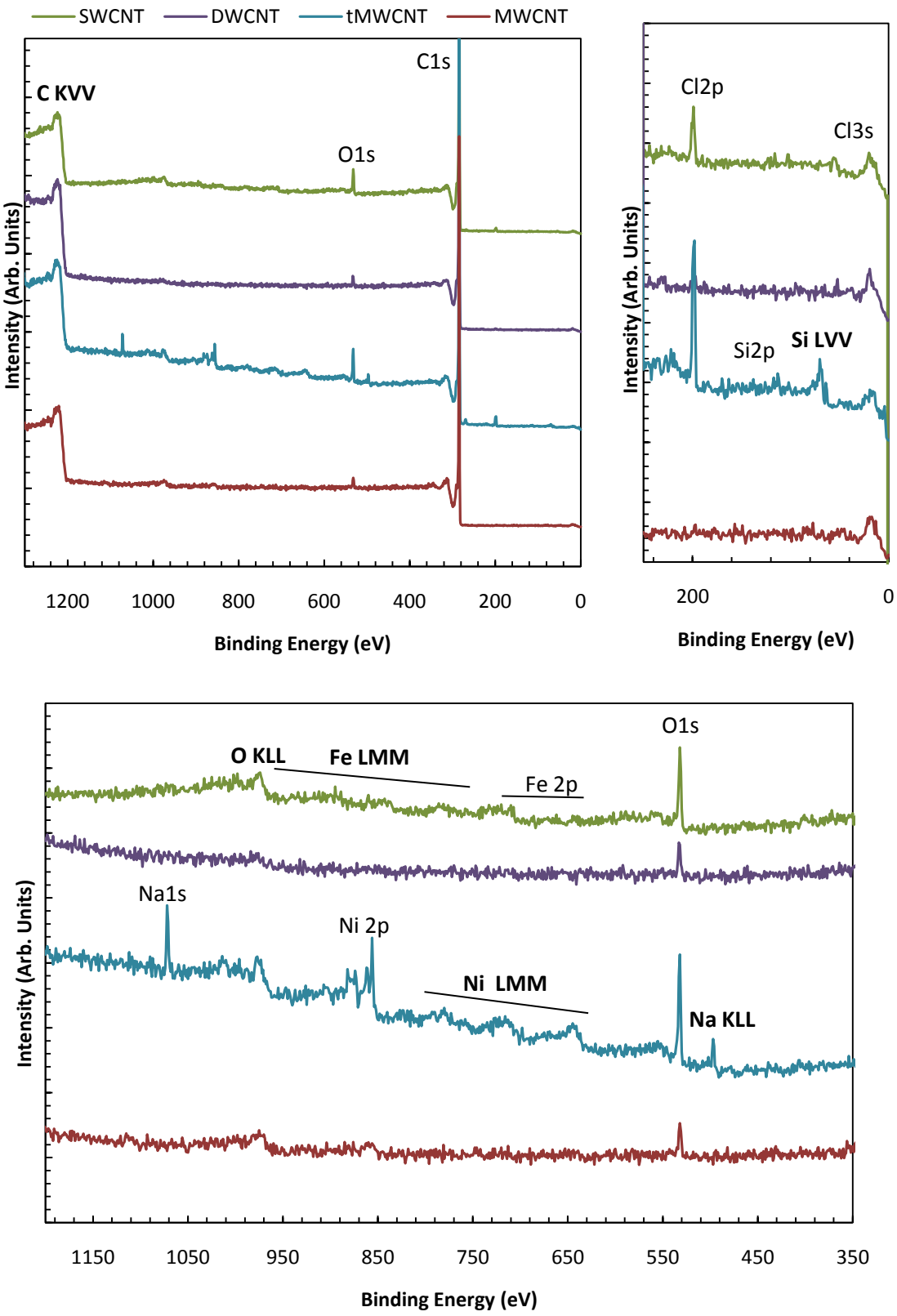

Figure 4.6

(top left) XPS wide scan of each of the CNT samples and (top right and bottom) the fine structure. In each case the main peaks are labelled. The data was obtained using a monochromated Aluminium K_α source (hν = 1486.6 eV) in normal emission geometry with a system resolution of ~ 0.45 eV.

Sample	Manufacturer	Synthesis Method	Diameter Distribution	Sample Structure	Chemical Contamination
SWCNT	Carbon Nanotechnologies Incorporated	HiPCO	1.2±0.1 nm Narrow distribution	Highly bundled into ropes of diameters varying fro m a few 10s nm to ~200nm, even after processing. Evidence of oxidation damage.	Associated with bundles. Fe O (3 at.%) Cl
DWCNT	Nanocyl	CVD	Inner: 1.2±0.1 nm (51± 2)% Outer ~ 1.6±0.2 nm ~(49± 2)%	Highly bundled into ropes of diameters varying fro m a few 10s nm to ~200nm even after processing.	Very little contamination. Fe O (2 at.%) Cl MWCNTs
tMWCNT	Nanocyl	CVD	~ 15 nm Large distribution (7 nm ≤ *d* ≤ 30 nm)	Partially separated through processing, implied poor structural quality.	O (5 at.%) Cl Fe Al, P, Si (6 at.%), S, K, Na (1 at.%), Ca ↓ Silica\Zeolite?
MWNT	Aldrich	CVD	~ 45 nm Very large distribution (25 nm ≤ *d* ≤ 90 nm)	Easily separated through processing. The structural quality appears poor and sometimes takes on a 'herringbone' structure. Debris within inner channel. Carbon encapsulated nanoparticles.	Carbon encapsulated nickel nanoparticles. Evidence of some Si from AES O (2 at.%)

Table 4.2

A summary of the characterisation for each of the commercially produced CNT samples. Approximate elemental surface composition is given in the column on the far right. Elements which do not have a bracketed value are present in amounts <1 at.%.

Figure 4.7 displays HRTEM images of each of the CNT samples. As can be seen the SWCNTs are barely resolvable within the bundles (Figure 4.7(a)), a noted result of acid oxidation techniques [35]. The walls of the DWCNTs sample are found to be continuous in most cases, indicating a low defect density, and some tubes are observed end on (top left corner, Figure 4.7(b)). The tMWCNTs (Figure 4.7(c)) are found to have largely continuous walls, though these are often kinked, suggesting a range of defect types [36] (Chapter 5, Section 5.3.3). The external walls display evidence of the damage inflicted by oxidation. The inner channels of the tMWCNTs (and the DWCNTs) appear clear, though where bending of a tMWCNT occurs the walls become folded into the inner channel, effectively cutting the tube in two (circled) [37]. Such information is valuable in applications involving the filling of CNTs. The MWCNT sample contains MWCNTs with continuous walls where, in some cases, the walls of the MWCNT take on a chevron, or herringbone-like arrangement (Figure 4.7(d)). In this instance, the wall terminates both internally and externally by curling back onto the main body of the tube (circled) where it is held in place by van der Waals forces. As a result, the outer edge of the nanotube appears irregular and the internal channel of the nanotube appears partially filled with debris. Such a chevron-like arrangement allows bending of the nanotube without the major structural changes observed in the tMWCNT sample and the structure is reminiscent of that of carbon fibres [38]. Through the introduction of voids within the nanotube walls (circled), the outer walls of the nanotube slide over the inner walls of the nanotube and as a result, the nanotube structure is corrected. From the bending and non-uniform diameters of the CNTs without kinking [36] or the introduction of voids within the CNT wall (Figure 4.7(d)), one may infer the defective nature of the sample. It is therefore implied that both the MWCNT and tMWCNT samples contain CNTs with a significant concentration of structural imperfections.

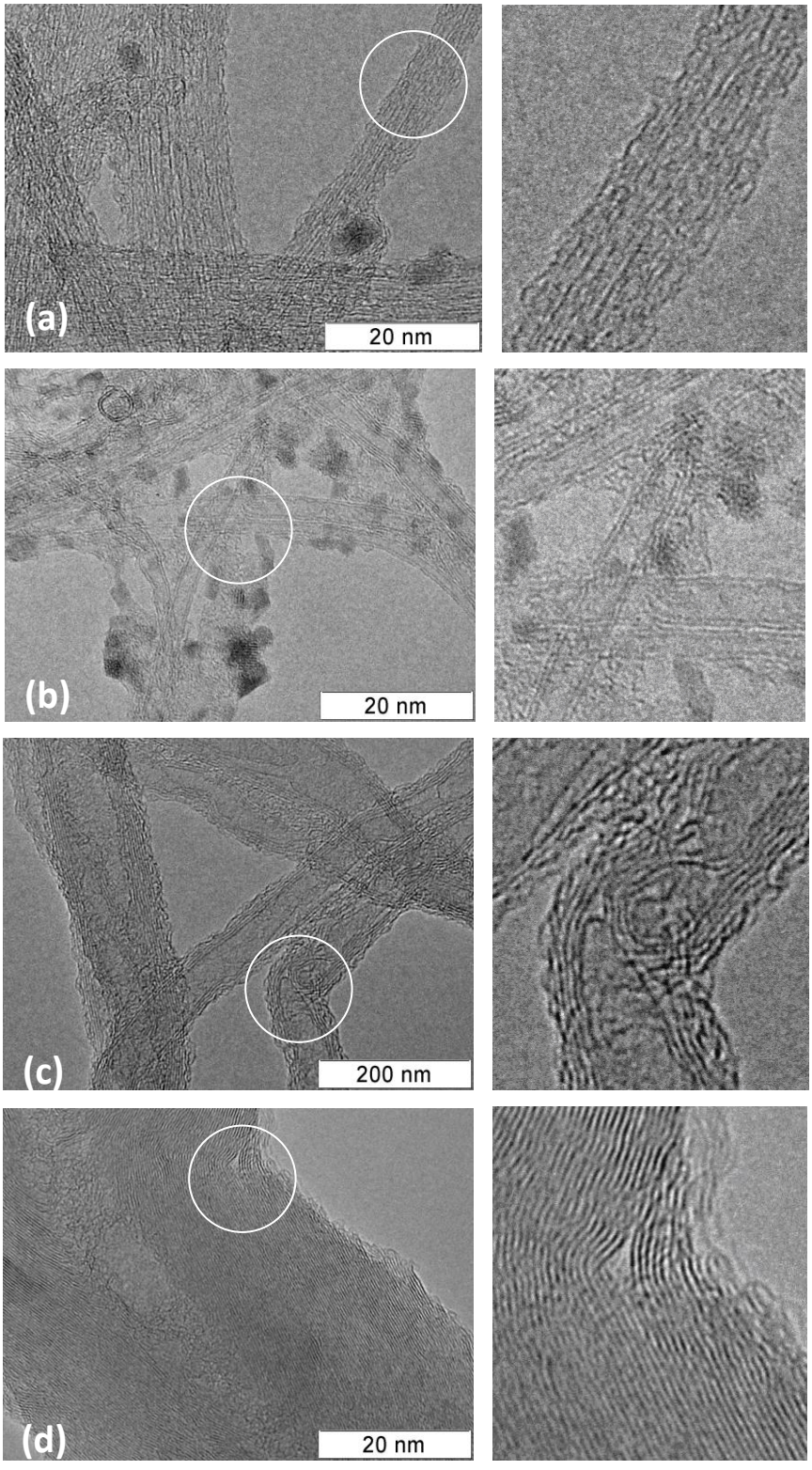

Figure 4.7

Small area HRTEM images of the (a) SWCNT, (b) DWCNT, (c) tMWCNT and (d) MWCNT samples. The circled structures shown in the left images are expanded in the images on the right.

Figure 4.8 (a) and (b), display differentiated and (c) raw Auger spectra and detail of the carbon *KVV* peak (kinetic energy ~264 ± 1 eV) for each of the nanotube samples. Auger electron energies include contributions due to chemical shifts and bonding within the sample [30] as discussed in Chapter 2. Therefore the observed differences in the positions of the measured peaks from that of pure graphitic carbon (~268 eV) may be attributed to deviation from planar sp^2 bonding. This may arise from changes in hybridisation (and therefore disruption of the π electron network) due to nanotube curvature and/or the presence of surface groups. A simple empirical measure of the degree of sp^2 bonding in a carbon sample can be obtained through measurement of the half-width of the major carbon *KVV* peak, *W* (defined in Figure 4.8(b)). *W* is effectively a measure of the width of the valence band and is expected to be approximately 22 eV for graphitic carbon and 14 eV for diamond-like carbon [31], corresponding to a shift in carbon-carbon bonding from sp^2 to sp^3. Thus, the value of *W* for a sample can indicate the degree of graphitisation which, in a CNT, can be translated into an indication of structural quality [29-31].

Column A of Table 4.3 presents the measured *W* values for each of the CNT samples. The SWCNT, DWCNT and tMWCNT samples have equivalent *W* values which are consistent with that of graphite, with differentiation between the samples being limited by the resolution of the system and spectral noise. However, the measured *W* value of the MWCNT sample is closer to that of diamond, and suggests that there is significant surface sp^3 hybridisation. Since it is clear that the *W* value provides only a crude means of determining nanotube structural perfection, further information may be derived through observation of the features marked '*a*' and '*b*' in Figure 4.8(b). In the literature [31] these have been related to the excitation of the π plasmon and the presence of defects in graphitic materials respectively.

From Figure 4.8(b) it can be seen that feature '*a*', that associated with the excitation of the π plasmon, appears to be more clearly defined in the in the SWCNT and tMWCNT samples when compared to the DWCNT and MWCNT samples. For the MWCNT sample this observation is in agreement with the measured *W* value, and suggests that there is significant disruption of the surface sp^2 hybridisation of the MWCNTs through the presence of defects or surface functionalisation. The feature marked '*b*', associated with the presence of defects in graphitic materials, appears more prominent in the SWCNT spectrum when compared to in the SWCNT sample, which would suggest that this is the

most defective sample. However, from XPS and Raman spectroscopy measurements presented later in this chapter, we will see that this is not the case. Issues in this form of CNT analysis may therefore arise due to insufficient signal-to-noise ratio (further studies should address this issue) which means that the robust use of *a* is not valid, or in the possibility that the feature '*b*' might be influenced by curvature-induced rehybridisation in SWCNTs.

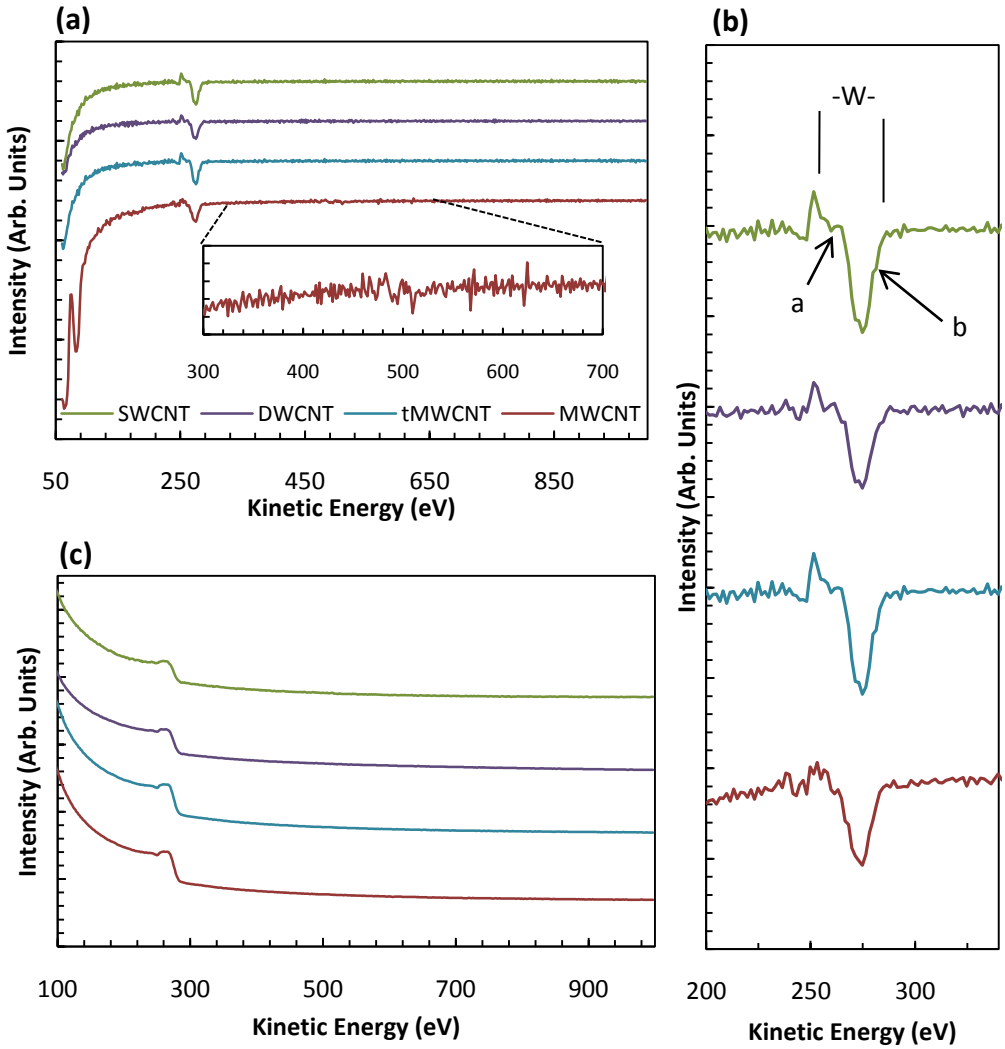

Figure 4.8

(a) Differentiated Auger spectra electron spectra of the CNT samples obtained using a primary electron energy of 3 keV and a resolution of 0.8 eV. The inset shows detail of the MWCNT AES spectrum. (b) Detail of the carbon KVV peak for each of the CNT samples. W indicates the energy difference between the peak and trough of the major positive and negative going incursions. The features labelled 'a' and 'b' correspond to the expected position of the π plasmon loss and a peak associated with the presence of defective graphite respectively. (c) The raw Auger spectra.

Sample	(A) AES	(B) low-loss EELS		(C) UPS				
		π Plasmon		After intensity normalisation of the valence band spectrum			After background removal & intensity normalisation	
				π peak				
	W ± 0.8 (eV)	Peak Position (eV)	FWHM (eV)	peak position (eV)	Relative intensity (a.u.)	peak-valley values	π peak height (a.u.)	FWHM (eV) System resolution is 0.4eV
SWCNT	22.5	5.98 ± 0.01	2.41 ± 0.03	2.871 ± 0.007	0.55	0.48	1.04	0.92 ± 0.05
DWCNT	22.5	6.27 ± 0.04	2.42 ± 0.04	2.91 ± 0.01	0.73	0.83	0.95	0.98 ± 0.01
tMWCNT	22.5	6.48 ± 0.04	2.51 ± 0.07	2.81 ± 0.01	0.83	0.55	0.84	1.19 ± 0.02
MWCNT	18.4	6.43 ± 0.05	2.51 ± 0.02	2.89 ± 0.01	1.00	1.00	0.86	1.08 ± 0.03

Table 4.3

Summary of the analysis of the AES, low-loss EELS and UPS data from the nanotube samples. See text for details.

Figure 4.9(a) displays the intensity normalised low-loss reflection EELS spectra from all four CNT samples. The structure of the low loss region consists of two main peaks; at energy losses of ~5 eV and ~27 eV corresponding to excitation of a π plasmon and a surface and bulk ($\pi + \sigma$) plasmon respectively [39, 40]. Figure 4.9(b) displays the π plasmon losses in detail, normalised in intensity after the removal of a linear background as shown by the black dashed lines in Figure 4.9(a).

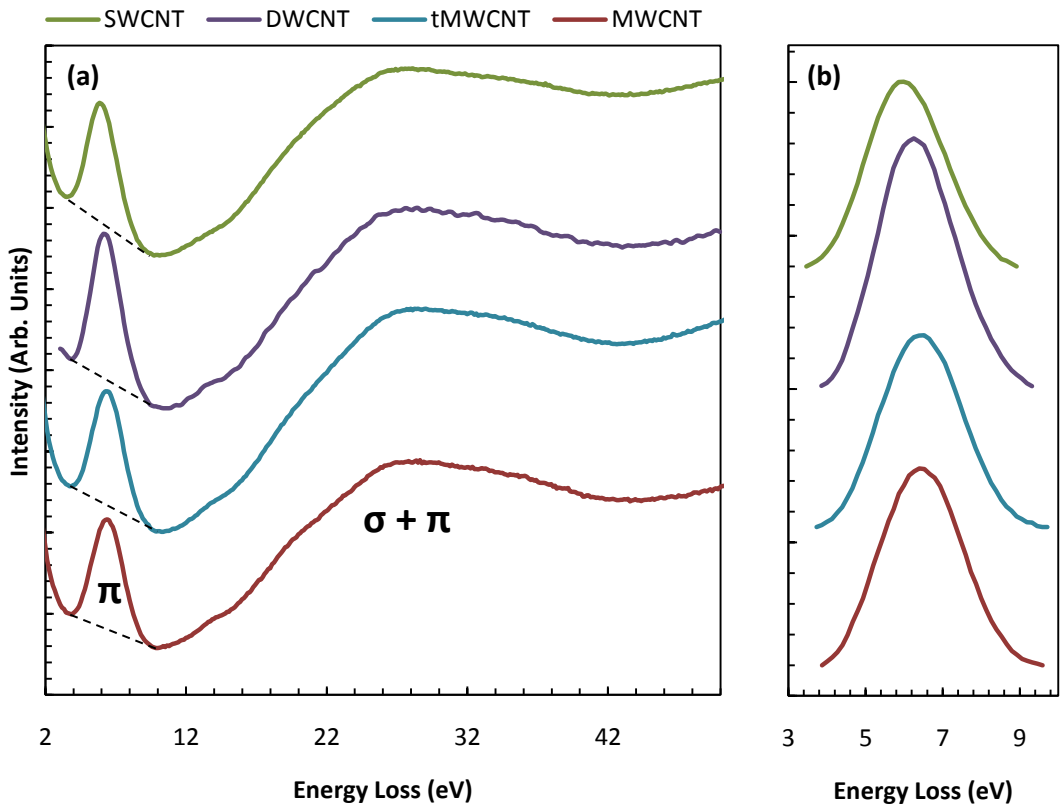

Figure 4.9

(a) Intensity normalised low-loss electron energy loss spectra of the four CNT samples. (b) Intensity normalised π Plasmon losses after removal of a linear background (shown as the dash black lines in (a)).

Column B of Table 4.3 displays the position and full width at half maximum (FWHM) of the π plasmon loss peak for each of the CNT samples. There is an observed increase in energy of the π plasmon peak to higher loss energies and an increase in FWHM on proceeding from the SWCNT to the MWCNT samples. Such an upward shift in energy (up to ~9 eV [39]) has been observed for MWCNTs with both an increased diameter and/or number of tubular components [39]. In controlled studies of the introduction of defects within MWCNTs by argon ion irradiation [29] a decrease in loss energy (maximum of ~0.8 eV [29]) and an increase in the FWHM of the π plasmon was observed. These

changes were associated with an increased disruption of the sp^2 hybridised carbon network within the CNTs and a possible decrease of the number of 'intact' tube walls and tube diameter. The degree of bundling within SWCNTs has also been found to influence the π plasmon energy [41], with bundled SWCNTs exhibiting lower π plasmon energies than isolated SWCNTs [42] and plasmon energies decreasing with increasing bundle diameter [43]. Due to the factors described above, it is not possible to use the π plasmon energy to compare the structural perfection *between* CNT species.

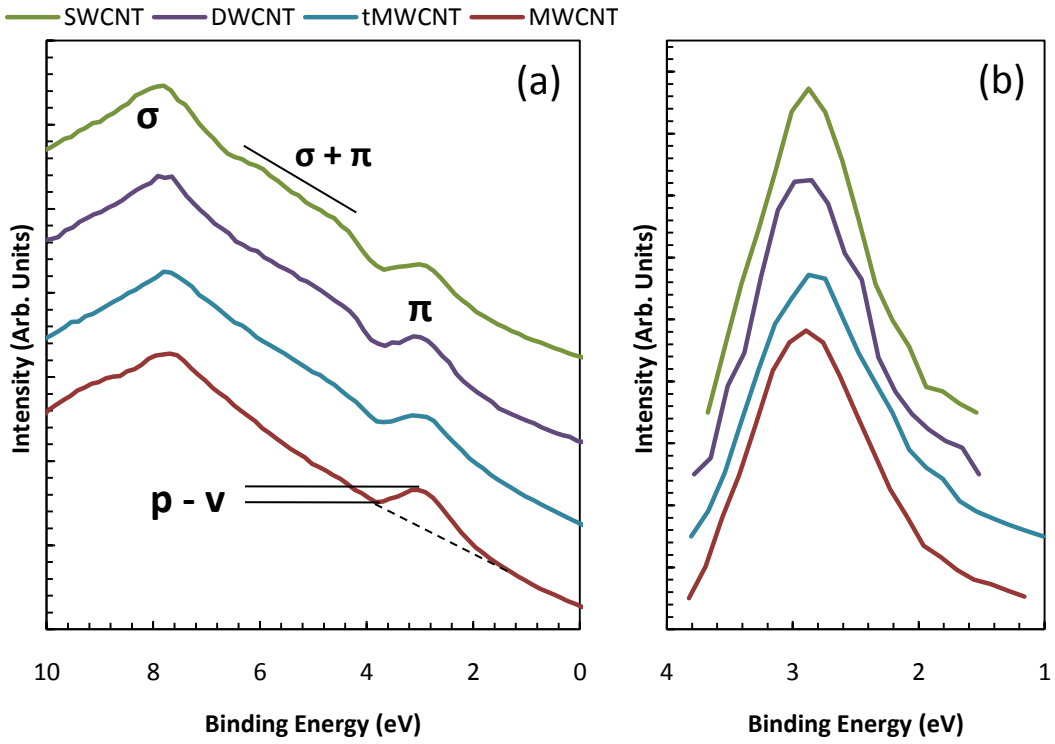

Figure 4.10

(a) Intensity normalised, low temperature (~40 K) He II ultra violet photoemission spectra of the CNT samples with a resolution on 400 meV. The incident photon energy (40.8 eV) allows the valence band of the samples to be characterised. (b) Intensity normalised π peaks after the removal of an arbitrary linear background.

Figure 4.10(a) presents the intensity normalised, low temperature (~40 K) He II (hν = 40.8 eV) valence band (VB) UPS spectra for each of the CNT samples obtained with a total resolution of ~400 meV. Both π and σ electronic states are probed by this technique and are observed at binding energies of ~3 eV and ~8 eV respectively [42, 44]. Figure 4.10(b) displays the intensity normalised π peaks after the removal of a linear background, an example of which is indicated in the bottom curve of Figure 4.10(a). This allows direct comparison of the spectral shape of the π peaks from the different samples. Summaries of

the π peak positions, relative intensities and peak to valley (p-v) measurements (as shown in Figure 6(a)) of the intensity normalised VB spectra and the height and FWHM of the intensity normalised π peaks are given in Column C of Table 4.3.

Peak-to-valley measurements (p-v), from which a qualitative measure of surface defect density has been determined in graphite [33, 34] have been used successfully to follow the evolution of defects in SWCNTs [24, 45]. Evaluation of the p-v ratio in normalised spectra (column C of Table 4.3) indicates that there is a reduction in defect density with increasing number of walls in our samples, contrary to HRTEM measurements and the results of Raman and XPS analysis (discussed below). To resolve this issue we instead remove a linear background and normalise the π peak intensity (area). We find an increase in FWHM suggesting a change in defect density consistent with HRTEM. We suggest that the reduction in the π peak p-v ratio with decreasing wall number is associated with rehybridisation due to increased curvature in the smaller nanotubes. These results indicate that care must be taken to select the correct metric when using UPS to undertake a (qualitative) comparison of structural perfection between nanotube species.

Information on the structural 'quality' of CNTs may also be sought through the application of Raman spectroscopy [19] and XPS [32]. Figure 4.11 displays Raman spectra obtained from each of the CNT samples after the removal of a linear background. The main features of the spectrum include the disorder induced *D*-band (~1300 cm^{-1}) and the graphite-related *G*-band (~1500 cm^{-1} to 1600 cm^{-1}) [19]. The *D*-band is associated with the presence of disorder and is often used as a measure of the structural quality of the CNTs [46] whilst the *G*-band is associated with graphitic-type atomic displacements. For SWCNTs, the *G*-band is split into two separate peaks; the $G^{-}$and G^{+} peaks, which are associated with atomic displacements in the circumferential and axial directions of the SWCNT [19].

Raman spectra are expected to be dominated by CNTs that are in resonance with the incident laser (i.e., CNTs with optically allowed transitions between van-Hove singularities (VHS) in their density of states [47] that can be excited by the incident laser (~2 eV)). In the case of SWCNTs and DWCNTs resonance conditions can be fulfilled for individual CNTs and the RBMs may be used to verify the presence of CNTs and directly measure the diameters of resonant tubes [47]. The CNT components in MWCNTs studied here are larger in diameter than individual SWCNTs and DWCNTs. This, in addition to the

presence of defects and carbonaceous contamination, may result in a loss of characteristic CNT Raman features such as the RBM [19, 48] (as observed in Figure 4.11) and a shift or broadening of others, such as the *G* band [48, 49]. RBMs may be observed for resonant small diameter MWCNT components (1 – 2 nm) in MWCNT samples of high structural quality and low levels of carbonaceous contamination [48], thus observations of RBMs within a MWCNT sample may be used to qualitatively gauge such factors.

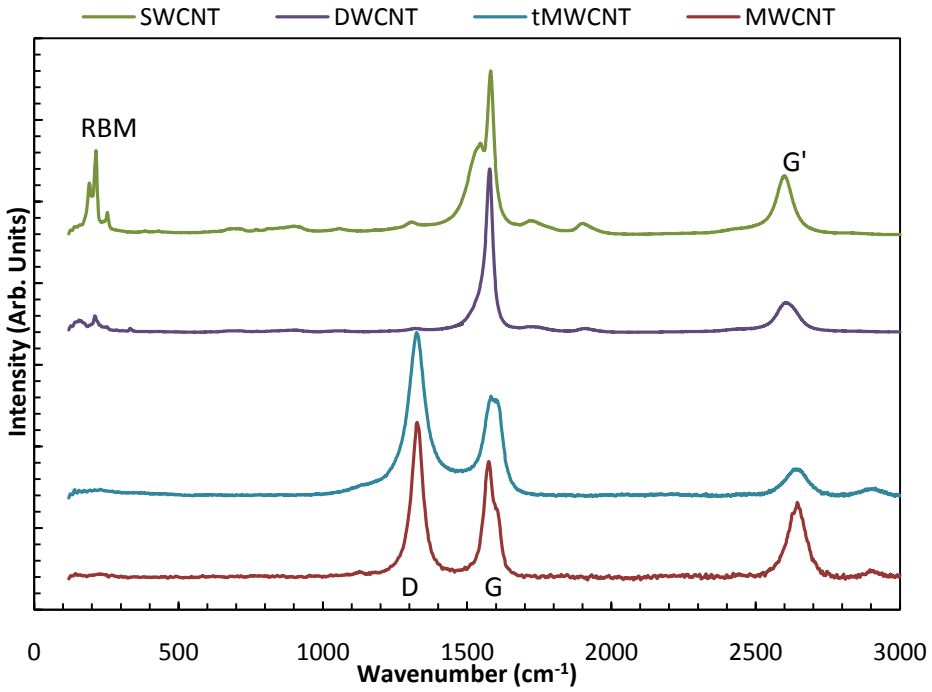

Figure 4.11

Intensity normalised Raman spectra of the SWCNT, DWCNT and tMWCNT and MWCNT samples.

Sample	Peak Position (cm-1)			Relative Raman Intensity (a.u.)		
	D Band	G Band		D Band (1 s.f.)	G Band (1 s.f.)	D/G Value (1.s.f)
		(G-)	(G+)			
SWCNTs	1318 ± 2	1530 ± 5	1582 ± 2	0.4	5	0.008
DWCNTs	1321 ± 1	1578 ± 2		0.04	3	0.01
tMWCNTs	1325 ± 1	1583 ±7		10	5	2
MWCNTs	1326 ± 1	1576 ± 3		7	2	4

Table 4.4

Summary of the D band and G band intensities for each of the samples in addition to the position of the composite G- and G+ peaks within the G band.

Figure 4.11 and the values given in Table 4.4 exhibit an increased *D*-band intensity (i.e. presence of disordered graphite for this excitation energy) for the tMWCNT and MWCNT samples compared to the DWCNT and SWCNT samples. This reflects the poor graphitisation of these samples and is in agreement with the SEM/HRTEM observations and suggests that the *D*-band is a good indication of the structural quality of any given CNT sample. The observed shift of the *D*-bands from that of graphite (1356 cm^{-1}), which is more prominent for the SWCNTs, is as expected [19].

The ratio of the intensities of the *D*/*G* lines are frequently used within the literature [46, 50] as a measure of the structural quality of a CNT sample (a well graphitised sample has a lower *D*/*G* value than a poorly graphitised sample). *D*/*G* values are shown in Table 4.4 and again suggest that the SWCNT and DWCNT samples are of a higher structural quality than the tMWCNT and MWCNT samples. However, discrepancies arise between *D*-band intensities and the *D*/*G* ratio since the *D*/*G* values show the SWCNTs, rather than the DWCNTs, have the highest degree of graphitisation and MWCNT, rather than the tMWCNT, have the least. Such problems with Raman analysis and the variations of *G*-band intensities and *G*/*D* ratios for identically prepared samples, especially those in solid form, have been noted [50] and may be a source of such contradictions. Despite these difficulties, the lack of specialised sample preparation required by Raman spectroscopy and the relative ease of the data analysis has meant that this technique has become a *de facto* standard for quick and qualitative comparison between CNT samples.

XPS may also be used to determine the structural quality of a CNT sample through fitting the C1*s* core line. Typically, several fit components are used (convolved with a Gaussian profile, representing instrumental broadening/sample inhomogeneity): a Doniach-Šunjić lineshape [51] attributed to sp^2 carbon bonding and four Lorentzian components corresponding to sp^3 hybridised carbon-carbon bonds, the $\pi \rightarrow \pi^*$ transition (π plasmon) and two peaks due to C-O and C=O groups bound to the nanotube surface [32]. The latter two components are included because broad XP spectra of the CNT samples show only two significant features: those due to carbon and oxygen. Thus chemisorption of oxygen on the CNTs, for example at the site of defect, cannot be ruled out.

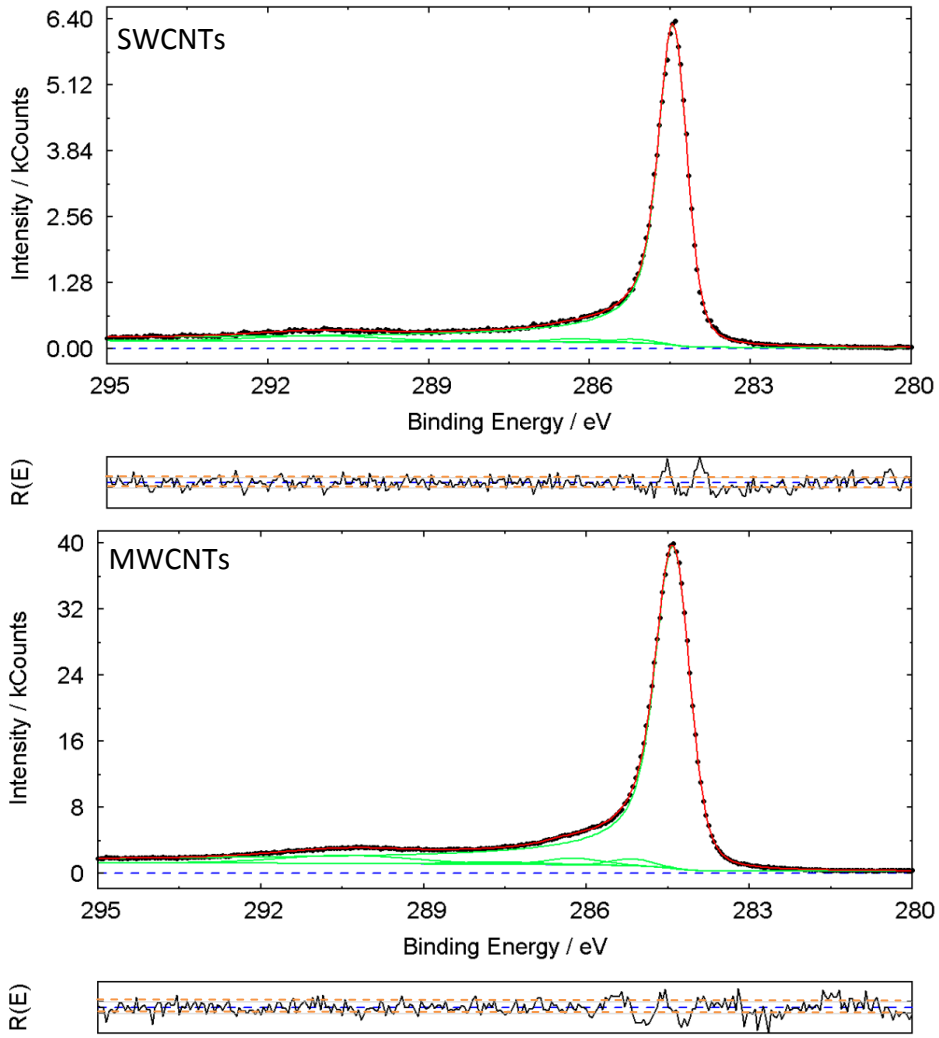

Figure 4.12

Fits to C1s spectra from the SWCNT sample (top panel) and the MWCNT sample (bottom panel). The red line is the fit, whilst the data is represented by the black dots. The components used during the fit are shown in green and the residuals are shown below each fit (the orange dashed line in the residuals represent ± 1 standard deviation).

Figure 4.12 displays examples of fits to the C1s peaks of the SWCNT sample (top panel) and the MWCNT sample (bottom panel) treating the background using the approach of Shirley [52]. A summary of the fit components is given in Table 4.5. Also given in Table 4.5 is the ratio of sp^3/sp^2 hybridised carbon which, like the D/G ratio in Raman spectroscopy, may be used to give a measure of how well graphitised the sample is (an ideal graphite sample would have a zero sp^3/sp^2 value). It is evident that from the sp^3/sp^2 value the tMWCNT sample contains the highest surface defect density. This conclusion is consistent with the D-band intensity found by Raman spectroscopy and the interpretation of the SEM and HRTEM images, discussed above. However, such analysis of the MWCNTs suggests that this sample contains a relatively low surface defect density. This does not support the

conclusions drawn from SEM, HRTEM and Raman spectroscopy. An explanation for this discrepancy may come in the form of the HRTEM image seen in Figure 4.7(d). In this sample it is seen that some of the MWCNTs are composed of chevron-like layers which, although poor from the point of view of CNT wall continuity, may nonetheless be well graphitised. Such a chevron-arrangement of the MWCNT walls leads to a presence of wall edges in these samples. Such features can be compared to those of graphene or nanoribbons, which have shown an enhanced *D*-band contribution in Raman spectroscopy [53-55]. Another source of the discrepancy between XPS and Raman spectroscopy may arise from the possibility that, unlike AES and XPS, Raman spectroscopy is unlikely to be significantly affected by the sp^3 hybridised character that is present in CNTs with high levels of curvature. Hence, Raman spectroscopy is sensitive to a different aspect of structural quality than the sp^3/sp^2 value of XPS, and the two techniques should be seen as complementary.

From the discussions above, it is clear that Raman spectroscopy provides a quick, easy and fairly reliable way of determining the structural quality of any given CNT sample, without any in depth data analysis. However, Raman spectroscopy is unable to verify the presence of any chemical contamination and, without HRTEM, is unable to verify the origin of the defect-related D-band (e.g., whether it is arises from wall discontinuity or defects within continuous walls). XPS measurements are more involved than those of Raman spectroscopy since they require measurements to be taken under UHV conditions and detailed analysis of the resulting spectra. However, XPS gives an incredibly powerful quantitative measure of the presence of surface contamination and level of graphitisation, which, once again, may only be fully understood if used in combination with HRTEM. Using HRTEM alone for analysis of CNT samples provides good qualitative measure of the structural nature of the samples but is unable to give information regarding the chemical nature of that sample.

In summary: in order to fully characterise the physical structure of the whole of a CNT sample, the chemical composition of its constituents, the structural quality of the CNT walls and the type of bonding within this walls, one must apply three techniques, for example: HRTEM, XPS and Raman spectroscopy.

Sample	Fitted Peaks				
	Position (eV)	Relative Intensity (At.%)	Origin	Gaussian Broadening (eV)	sp^3/sp^2 value (±0.001)
SWCNT	284.4 ± 0.1	90.4	sp^2, C-C	0.59	0.016
	285.2 ± 0.2	1.5	sp^3, C-C		
	286.3 ± 0.1	1.9	C-O		
	287.6± 0.2	1.0	C=O		
	290.4± 0.2	5.3	$\pi \rightarrow \pi^*$		
DWCNT	284.5 ± 0.1	92.4	sp^2, C-C	0.50	0.011
	285.3 ± 0.2	1.0	sp^3, C-C		
	286.4 ± 0.1	1.0	C-O		
	287.7± 0.2	0.5	C=O		
	290.9± 0.2	5.1	$\pi \rightarrow \pi^*$		
tMWCNT	284.4 ± 0.1	89.2	sp^2, C-C	0.50	0.026
	285.2 ± 0.2	2.3	sp^3, C-C		
	286.3 ± 0.1	2.0	C-O		
	287.8± 0.2	1.7	C=O		
	290.7± 0.2	4.9	$\pi \rightarrow \pi^*$		
MWCNT	284.4 ± 0.1	92.9	sp^2, C-C	0.49	0.011
	285.2 ± 0.2	1.0	sp^3, C-C		
	286.2 ± 0.1	1.2	C-O		
	287.8± 0.2	0.8	C=O		
	291.0± 0.2	4.2	$\pi \rightarrow \pi^*$		

Table 4.5

Summaries of the peaks fitted to the XPS C1s peak and the origins of the peaks. An example of the fits to the SWCNT and MWCNT sample is shown Figure 4.12.

4.4 Summary and Conclusions

In this chapter, four commercially sourced CNT samples with different characteristics (such as diameter distribution and number of walls) have been examined using a range of analytical techniques. Many of these techniques are applied in the literature in a 'stand-alone' fashion to evaluate nanotube samples but have never been compared through measurements on identical samples. From our results we are able to compare and contrast the information content of each analytical approach and have a complete characterisation of the materials which will be used for the work reported in Chapters 5 and 6 of this thesis.

The techniques employed in this chapter have been tested in their ability to characterise CNT samples. When considering the level of contamination within a CNT sample, it is clear that, in this respect, HRTEM provides invaluable information. We suggest that the chemical nature of all CNT samples may be found through application of XPS. AES and EDX may also be used, however discrepancies between the information provided by these techniques arises due to the sample volumes analysed in each case. When measuring the relative structural quality of the different CNT samples we find that some techniques provide a greater distinction between samples than others. This is due to the nature of the information provided by each of the techniques (e.g. sp^3 hybridisation of small diameter CNTs may influence AES and UPS data, whilst the number of walls, tube diameter and level of bundling affects EELS data). It is found that conclusions drawn from SEM and HRTEM measurements are generally supported by AES and UPS, though the information from these techniques is qualitative. Both Raman spectroscopy and XPS provide a good measure of slightly different aspects of CNT quality; whilst Raman spectroscopy provides qualitative information regarding the structural nature of the samples, XPS provides quantitative information regarding the nature of the carbon–carbon bonding within that sample. However, without direct observations of the structural nature of the CNT walls via HRTEM, the interpretation of data from both Raman spectroscopy and XPS may be flawed.

From our analysis it is clear that the SWCNT and DWCNT sample are highly bundled, even after purification. This is in contrast to the tMWCNT and MWCNT samples, which are well dispersed (especially the latter). We find that all samples contain traces of contamination from the production and purification processes used: For the SWCNT and

DWCNT samples, traces of iron catalyst particles are found along with chlorine residuals from the acid etching process; for the tMWCNT and MWCNT samples, iron and nickel catalyst particles are found respectively, along with chlorine. Additionally evidence is found for particles of the zeolite support used in the synthesis of these samples. All samples are found to contain traces of oxygen species, ranging from 2 at% to 5 at.%. Of all the samples, the DWCNT sample is found to be the most chemically pure, and the tMWCNT sample, the least. We find the SWCNT and DWCNT samples to be more pristine in terms of the continuity of the nanotube walls and the carbon-carbon bonding within these walls. The tMWCNT sample is found to be of poor structural quality, with both the continuity of the walls and the carbon-carbon bonding within these walls indicating a large number of defects. Through Raman spectroscopy it is found that the nanotube walls within the MWCNT sample are of poor quality; this is verified through HRTEM which shows that the walls of some of the nanotubes in this sample take on a chevron-like arrangement. Despite this, XPS measurements show that carbon-carbon bonding within these samples is highly graphitised.

As we have seen in this chapter, the use of a single analytical technique in the characterisation of SWCNT samples may yield misleading results if the nature of the information provided by that technique is not fully understood. Without doing so it is possible that similarities or differences between studies within the literature may be misinterpreted, especially since nearly all of these studies base conclusions on incompletely characterised materials. In order to overcome this issue it is vitally important that multiple techniques are used in the characterisation of CNT materials in order to gain a complete understanding of the nature of the sample being studied. Without addressing this problem, comparisons made between studies in the literature will always hold a level of uncertainty. From our observations we suggest that that HRTEM, XPS and Raman spectroscopy should be the minimum requirements for a complete characterisation of a CNT sample. These techniques provide information on the structure of the CNT walls, the bonding within those walls, the diameter distribution of the sample and the structure, chemical nature and level of contamination within these samples and whether is it directly bonded to the CNTs.

4.5 References

1. Lu, X., et al., *Synthesis of high quality single-walled carbon nanotubes at large scale by electric arc using metal compounds.* Carbon, 2005. **43**(9): p. 2020-2022.
2. Dresselhaus, M.S., G. Dresselhaus, and P. Avouris, *Carbon nanotubes : synthesis, structure, properties, and applications*. Topics in Applied Physics ; v. 80. 2001, Berlin: Springer. xv, 447 p.
3. Nikolaev, P., et al., *Gas-phase catalytic growth of single-walled carbon nanotubes from carbon monoxide.* Chemical Physics Letters, 1999. **313**(1-2): p. 91-97.
4. Park, T.J., et al., *Purification strategies and purity visualization techniques for single-walled carbon nanotubes.* Journal of Materials Chemistry, 2006. **16**(2): p. 141-154.
5. Chen, X.H., et al., *Non-destructive purification of multi-walled carbon nanotubes produced by catalyzed CVD.* Materials Letters, 2002. **57**(3): p. 734-738.
6. Chattopadhyay, D., I. Galeska, and F. Papadimitrakopoulos, *Complete elimination of metal catalysts from single wall carbon nanotubes.* Carbon, 2002. **40**(7): p. 985-988.
7. Kim, Y. and D.E. Luzzi, *Purification of pulsed laser synthesized single wall carbon nanotubes by magnetic filtration.* Journal of Physical Chemistry B, 2005. **109**(35): p. 16636-16643.
8. Grobert, N., *Carbon nanotubes - becoming clean.* Materials Today, 2007. **10**(1-2): p. 28-35.
9. Grobert, N., *Nanotubes - grow or go?* Materials Today, 2006. **9**(10): p. 64-64.
10. Collins, P.G., et al., *Nanotube nanodevice.* Science, 1997. **278**(5335): p. 100-103.
11. Tans, S.J., A.R.M. Verschueren, and C. Dekker, *Room-temperature transistor based on a single carbon nanotube.* Nature, 1998. **393**(6680): p. 49-52.
12. Rueckes, T., et al., *Carbon nanotube-based nonvolatile random access memory for molecular computing.* Science, 2000. **289**(5476): p. 94-97.
13. Liu, X.L., et al., *Carbon nanotube field-effect inverters.* Applied Physics Letters, 2001. **79**(20): p. 3329-3331.
14. Zhu, H.W., et al., *Direct synthesis of long single-walled carbon nanotube strands.* Science, 2002. **296**(5569): p. 884-886.
15. Thess, A., et al., *Crystalline ropes of metallic carbon nanotubes.* Science, 1996. **273**(5274): p. 483-487.
16. Ci, L.J., et al., *Double wall carbon nanotubes promoted by sulfur in a floating iron catalyst CVD system.* Chemical Physics Letters, 2002. **359**(1-2): p. 63-67.
17. Zhu, C.Y., Z.L. Xie, and K.M. Guo, *Formation of close-packed multi-wall carbon nanotube bundles.* Diamond and Related Materials, 2004. **13**(1): p. 180-183.
18. Mukhopadhyay, K., et al., *Bulk production of quasi-aligned carbon nanotube bundles by the catalytic chemical vapour deposition (CCVD) method.* Chemical Physics Letters, 1999. **303**(1-2): p. 117-124.
19. Dresselhaus, M.S., et al., *Raman spectroscopy of carbon nanotubes.* Physics Reports-Review Section of Physics Letters, 2005. **409**(2): p. 47-99.
20. Rao, A.M., et al., *Effect of van der Waals interactions on the Raman modes in single walled carbon nanotubes.* Physical Review Letters, 2001. **86**(17): p. 3895-3898.
21. Milnera, M., et al., *Periodic resonance excitation and intertube interaction from quasicontinuous distributed helicities in single-wall carbon nanotubes.* Physical Review Letters, 2000. **84**(6): p. 1324-1327.
22. Kim, U.J., et al., *Raman and IR spectroscopy of chemically processed single-walled carbon nanotubes.* Journal of the American Chemical Society, 2005. **127**(44): p. 15437-15445.
23. Venkateswaran, U.D., et al., *Probing the single-wall carbon nanotube bundle: Raman scattering under high pressure.* Physical Review B, 1999. **59**(16): p. 10928-10934.
24. Goldoni, A., et al., *Spectroscopic characterization of contaminants and interaction with gases in single-walled carbon nanotubes.* Carbon, 2004. **42**(10): p. 2099-2112.
25. Delhaes, P., et al., *A comparison between Raman spectroscopy and surface characterizations of*

multiwall carbon nanotubes. Carbon, 2006. **44**(14): p. 3005-3013.
26. Pichler, T., et al., *Potassium intercalated bundles of single-wall carbon nanotubes: electronic structure and optical properties.* Solid State Communications, 1999. **109**(11): p. 721-726.
27. Rauf, H., et al., *Detailed analysis of the Raman response of n-doped double-wall carbon nanotubes.* Physical Review B, 2006. **74**(23): p. 10.
28. Lemos, V., et al. *Li-inserted carbon nanotube Raman scattering.* Microelectronics Journal, 2005. **36**(11): p. 1020-1022
29. Brzhezinskaya, M.M., E.M. Baitinger, and V.V. Shnitov, *pi-plasmons in ion-irradiated multiwall carbon nanotubes.* Physica B-Condensed Matter, 2004. **348**(1-4): p. 95-100.
30. Lascovich, J.C., R. Giorgi, and S. Scaglione, *Evaluation of the Sp2/Sp3 Ratio in Amorphous-Carbon Structure by XPS and XAES.* Applied Surface Science, 1991. **47**(1): p. 17-21.
31. Mizokawa, Y., et al., *Comparison of the CKLL1st-Derivative Auger-Spectra from XPS and AES Using Diamond, Graphite, SiC and Diamond-Like-Carbon Films.* Surface Science, 1987. **182**(3): p. 431-438.
32. Estrade-Szwarckopf, H., *XPS photoemission in carbonaceous materials: A "defect" peak beside the graphitic asymmetric peak.* Carbon, 2004. **42**(8-9): p. 1713-1721.
33. Diaz, J., et al., *Separation of the sp(3) and sp(2) components in the C1s photoemission spectra of amorphous carbon films.* Physical Review B, 1996. **54**(11): p. 8064-8069.
34. Galuska, A.A., H.H. Madden, and R.E. Allred, *Electron-Spectroscopy of Graphite, Graphite Oxide and Amorphous-Carbon.* Applied Surface Science, 1988. **32**(3): p. 253-272.
35. Monthioux, M., et al., *Sensitivity of single-wall carbon nanotubes to chemical processing: an electron microscopy investigation.* Carbon, 2001. **39**(8): p. 1251-1272.
36. Buongiorno, N.M., *Mechanical properties, defects and electronic behaviour of carbon nanotubes.* Carbon, 2000. **38**: p. 1703-1711.
37. Iijima, S., et al., *Structural flexibility of carbon nanotubes.* Journal of Chemical Physics, 1996. **104**(5): p. 2089-2092.
38. Yoon, S.H., et al., *A conceptual model for the structure of catalytically grown carbon nano-fibers.* Carbon, 2005. **43**(9): p. 1828-1838.
39. Ajayan, P.M., S. Iijima, and T. Ichihashi, *Electron-Energy-Loss Spectroscopy of Carbon Nanometer-Size Tubes.* Physical Review B, 1993. **47**(11): p. 6859-6862.
40. Reed, B.W. and M. Sarikaya, *Electronic properties of carbon nanotubes by transmission electron energy-loss spectroscopy.* Physical Review B, 2001. **64**(19): p. art. no.-195404.
41. Lin, M.F. and D.S. Chuu, *pi plasmons in carbon nanotube bundles.* Physical Review B, 1998. **57**(16): p. 10183-10187.
42. Kramberger, C., et al., *Linear plasmon dispersion in single-wall carbon nanotubes and the collective excitation spectrum of graphene.* Physical Review Letters, 2008. **100**(19): p. 4.
43. Lingam, K., et al., *Effect of bundling on the [pi] plasmon energy in sub-nanometer single wall carbon nanotubes.* Carbon., 2011. **49**(12): p. 3803-3807.
44. Bianconi, A., S.B.M. Hagstrom, and R.Z. Bachrach, *Photoemission Studies of Graphite High-Energy Conduction-Band and Valence-Band States Using Soft-X-Ray Synchrotron Radiation Excitation.* Physical Review B, 1977. **16**(12): p. 5543-5548.
45. Chakraborty, A.K., et al., *A photoelectron spectroscopy study of ion-irradiation induced defects in single-wall carbon nanotubes.* Carbon, 2007. **45**(14): p. 2744-2750.
46. Dillon, A.C., et al., *Systematic inclusion of defects in pure carbon single-wall nanotubes and their effect on the Raman D-band.* Chemical Physics Letters, 2005. **401**(4-6): p. 522-528.
47. Jorio, A., et al., *Characterizing carbon nanotube samples with resonance Raman scattering.* New Journal of Physics, 2003. **5**: p. 17.
48. Benoit, J.M., et al., *Low-frequency Raman studies of multiwalled carbon nanotubes: Experiments and theory.* Physical Review B, 2002. **66**(7): p. 4.

49. Thomsen, C., et al., *Raman spectroscopy on single- and multi-walled nanotubes under high pressure.* Applied Physics a-Materials Science & Processing, 1999. **69**(3): p. 309-312.
50. Itkis, M.E., et al., *Comparison of analytical techniques for purity evaluation of single-walled carbon nanotubes.* Journal of the American Chemical Society, 2005. **127**(10): p. 3439-3448.
51. Doniach, S. and M. Sunjic, *Many-Electron Singularity in X-Ray Photoemission and X-Ray Line Spectra from Metals.* Journal of Physics Part C Solid State Physics, 1970. **3**(2): p. 285.
52. Shirley, D.A., *High-Resolution X-Ray Photoemission Spectrum of the Valence Bands of Gold.* Physical Review B, 1972. **5**(12): p. 4709.
53. Casiraghi, C., et al., *Raman Spectroscopy of Graphene Edges.* Nano Letters, 2009. **9**(4): p. 1433-1441.
54. Gupta, A.K., et al., *Probing Graphene Edges via Raman Scattering.* ACS Nano, 2009. **3**(1): p. 45-52.
55. Ryu, S., et al., *Raman Spectroscopy of Lithographically Patterned Graphene Nanoribbons.* ACS Nano. **5**(5): p. 4123-4130.

5. Reactivity of Ion-Irradiated SWCNTs to Ambient Atmosphere

In this chapter, x-ray photoemission spectroscopy is used to study the effect of deliberately introduced defects on the structural and electronic properties of SWCNTs and their reactivity to the ambient environment. In particular, the variation of oxygen content of samples exposed to ambient atmosphere as a function of defect density is investigated.

5.1 Introduction

The interaction of gases with CNTs has attracted both theoretical [1-11] and experimental [12-15] interest, with motivations for such study ranging from improving CNT growth processes [16] and manipulating CNT properties [6, 12, 17-20], to gas separation [1, 2], transportation and storage [3, 4, 21, 22]. The latter of these is of particular interest when considering CNTs for fuel cell technologies [23]. In particular, the reactivity of SWCNTs to oxygen from the ambient has attracted attention [2, 5-8, 12, 14, 20, 24-27]. This is for several reasons: (1) it is through oxidation that almost all CNT samples are purified [28]; (2) oxygen containing functional groups may be used to provide routes to more complex chemical modification, so providing a more usable material [15]; (3) it has been shown that oxygen functionalisation can be used to selectively and continuously tune the electronic properties of SWCNTs [12] and enhance their field emission current [29]; (4) consideration of the environmental stability of CNTs is vital when bearing in mind all potential applications.

Despite the many potential applications utilising the reactivity of CNTs to ambient gases, it is only recently that the influence of defects on gas adsorption has been considered explicitly [4, 9-11, 16, 30]. Such work has highlighted that defects play a significant role [9, 11], and may themselves be healed through the process of adsorption of ambient gasses, such as O_2, and desorption of carbon containing species, such as CO and CO_2 [16]. Indeed, in the work by Collins *et al.*, it was suggested that the increased reactivity of defects to ambient oxygen may provide a means by which the defect density of a sample can be ascertained [12].

When referring to CNTs, the term 'defect' may cover a wide range of deviations from the pristine nanotube structure described in Chapter 1. It may refer to changes that are topological in nature (the inclusion of non-hexagonal rings within the CNT lattice), arising from bond rotation (the so-called 'Stone-Wales' defect [31]) or it may refer to the inclusion of single or multiple vacancies within the CNT lattice [32]. The presence of each of these defects has been verified experimentally by Hashimoto *et al.* [33] as they tend to manifest themselves as an alteration in the CNT profile through variations of the tubule diameter along the length of the CNT [34]. As noted in Chapter 4, observation of this variation via scanning electron microscopy may be used to infer the topological defect density of a CNT sample. The term 'defect' may also refer to rehybridisation of carbon atoms from sp^2 to sp^3

hybridisation. This may occur due to the presence of carbon adatoms, adsorbates [21] or interstitials between nanotubes within a bundle [35] or between walls in a DWCNT or MWCNT [36].

At times the distinctions between these types of defect may become unclear and overlap. For example, the creation of a vacancy in a CNT wall may result in the ejected carbon atom becoming an adatom or interstitial which, in turn, may introduce some sp^3 character into the nanotube [37]. It is therefore difficult to categorically separate the effects each particular type of defect has on the physical properties of a CNT, though it is almost universally agreed that the defects can provide a means by which the properties of a CNT can be tailored for specific applications [4, 12, 17, 18, 26, 30, 38, 39].

Defects may be created during synthesis, purification or analysis of CNT materials. They may also be introduced 'artificially' through mechanical stress [40] or irradiation [25, 37, 41, 42]. The latter of these, specifically ion irradiation, offers great promise as a means by which defects can be selectively added to a CNT structure [43], potentially tailoring their properties in a controlled manner [44, 45]. For this reason, ion irradiation of CNTs has attracted wide ranging theoretical [4, 32, 35-37, 40, 41, 45-48] and experimental [18, 21, 25, 39, 45, 48-50] interest, and forms the focus of the work presented in this chapter.

When an ion is incident on a CNT, the resultant defect and subsequent behaviour of that defect is dependent on the incident ion species, ion energy, ambient temperature and the type of nanotube material being irradiated (i.e., the CNT curvature, diameter and number of walls) [32, 36, 44]. For ions such as argon, the ion energy threshold for defect creation in CNTs has been found to be ~50eV [41]. For ion energies below this threshold, there is preferential adsorption of the ion species on the surface of the CNT [48], whilst for ion energies above this threshold (in the range 50 eV to 3 keV), single vacancies, vacancy clusters and related defects [36, 41, 51] are the most prolific. At high ion energies, large clusters of atoms may be removed from the CNT walls, so creating large holes [37] or nanopores [10]. Break up and amorphisation of SWCNT samples is found at ion doses of ~$2x10^{15}$ ions/cm^2 for both 0.5 keV and 3 keV ions in theory [37] and experiment [50] and is associated with the sputtering of carbon atoms, which may remain as interstitials or adatoms on remaining CNT material.

In SWCNTs, vacancy defects are expected to be stable at room temperature, with immediate reconstruction of the lattice to reduce the number of dangling bonds (DBs) [25, 26, 30, 32, 46, 47]. Curvature effects in SWCNTs do not allow formation of vacancy clusters with six or more missing atoms, leading to either the splitting of such vacancies into smaller vacancy clusters [32] or a long range reconstruction of the CNT, resulting in a local reduction in the tubule diameter [42]. The large diameter CNTs and those with two or more walls are expected to be able to sustain larger vacancy clusters due to reduced curvature and monovacancy mobility [42]. These differences are discussed in detail in Chapter 6 in which the reactivity of irradiated DWCNTs and MWCNTs towards oxygen from the ambient is investigated.

Although there have been a significant number of investigations into the creation, behaviour and healing of vacancy defects, few have been systematic investigations and limited work has been performed on the reactivity of defective nanotubes to ambient oxygen [12, 14]. In this chapter the evolution of the structural, chemical and electronic properties of argon irradiated SWCNTs as a function of ion dose is examined using x-ray photoemission spectroscopy (XPS). In particular, the oxygen content of samples exposed to ambient atmosphere is ascertained and the nature of that oxygen is investigated (if and how it is bonded to the carbon nanotubes). This work precedes that presented in Chapter 6 in which the behaviour of argon irradiated CNTs with more than one wall is studied.

5.2 Experimental

Commercially sourced HiPCO SWCNT samples (described in Table 3.1) were purified using the method outlined in Section 3.1.1 and the resultant suspension of SWCNTs in IPA was deposited drop-by-drop onto a clean tantalum foil. The solvent was allowed to evaporate before further drops of the suspension were added. This process was repeated until an optically thick SWCNT film was created. Films created in this manner are robust and thus able to withstand transportation throughout the vacuum system of the x-ray photoelectron spectrometer and the *in-situ* cleaning processes used.

The measurements presented in this chapter were performed using the Scienta ESCA300 spectrometer at the National Centre for Electron Spectroscopy and Surface Analysis (NCESS), Daresbury, U.K. A monochromated Al *K*α source (1486.6 eV) was used to acquire the spectra, which were obtained at 0^{o} emission angle with the system operating at a total instrumental resolution of 0.45 eV (determined from the broadening of the Fermi edge of a silver reference sample) and a pressure of $5x10^{-10}$ mbar. The SWCNT films were cleaned by annealing to 700^{o}C for at least 3 hours under UHV. Further details of both the experimental system and the sample preparation methods are provided in Section 3.2.1 of Chapter 3.

Samples were irradiated using a defocused beam of 1.5 keV Ar ions or 0.5 keV O_2 ions in normal incidence geometry, so ensuring uniform irradiation of the sample. During irradiation, pressure in the sample preparation chamber (see Figure 3.1) increased to around $5x10^{-7}$ mbar. The irradiation dose of each sample was calculated by measuring the sample current, *I*, every 10 s using a pico-Ammeter. The total dose, *D*, delivered to the sample, in micro-Coulombs, is calculated by:

$$D(\mu C) = I_t(\mu A).t(s) = \sum_t 10I_t$$

Equation 5.1

The measured currents ranged from 0.5 μA up to around 15 μA, with a maximum calculated uncertainty in the dose of $\pm$ 20 μC due to fluctuations in the measured sample current over the duration of any given 10s interval. As a result of this uncertainty, it is therefore prudent to note that the term 'dose' throughout this chapter is synonymous with

'nominal dose', i.e. the dose that is assumed to be delivered to the sample, and these two terms will be used interchangeably throughout this chapter. Additional points to note are that there is some uncertainty over the footprint of the beam over the sample and sample holder (which, due to practical limitations also contributed to the measured current) and that no correction is made for secondary electron emission. Hence, we express our doses simply in terms of μC rather than as a fluence (dose per unit area). However, we estimate (from visual inspection) that the footprint of the ion beam is close to 1 cm^2 and thus our values for dose may be compared, to order of magnitude at least, to fluencies reported elsewhere.

It should be made clear that each measurement at a particular dose is made on a clean sample (i.e., the dosing is not cumulative) and so each measurement presented is independent of every other measurement. For each stated nominal dose, measurements (i.e., survey spectrum and detailed C1*s* and O1*s* spectra) were taken:

- after annealing, prior to irradiation (Ar-irradiated samples);
- immediately after irradiation (Ar and O irradiated samples);
- after exposure to atmosphere for 70 minutes (Ar-irradiated samples).

Through these measurements, we can therefore ascertain the effect of irradiation and of subsequent exposure to ambient atmosphere.

In order to gain further insight into the effects of irradiation on SWCNTs and how they subsequently react with ambient oxygen, both the C1*s* and O1*s* spectra were fitted in line with approaches used in the literature [52-54], using a Shirley background [55]. The C1*s* spectra were fit with five components (listed in Table 5.1) which, throughout this chapter, will be referred to as C1 to C5 on going from low binding energy to high binding energy. The main component, C1, (due to sp^2 hybridised, graphitic, carbon) was fit with a Doniach-Šunjic (DS)–type lineshape [56], a shape which is commonly used for the fitting of photoemission lineshapes in metallic systems. The asymmetry of the DS component is determined by the asymmetry parameter, α, which is dependent on the electronic density of states of the system in question. When fitting the C1*s* spectra for the irradiated SWCNT samples, the asymmetry parameter was fixed at a value found from fitting the spectra of clean CNT samples. In the case of this SWCNT sample α is found to be 0.12 ± 0.01 and is comparable to values of α found in previous studies using similar energy resolution [21]. The full width at half maximum (FWHM) of this component was allowed to vary without

bound in order to account for the dissimilar local environments of sp^2 bound carbon created during irradiation.

C1*s* components C2 through to C5 were fitted with Lorentzian functions, convolved with a Gaussian representing broadening due to both instrumental resolution and the effects of irradiation (as was the component C1). Whilst the widths of C2, associated with sp^3 hybridised carbon, and C5, the π-plasmon, were allowed to vary without bound, it was found that the width of C2 remained around ~0.9 eV, consistent with previous observations of hydrogenated SWCNTs [21]. The FWHM of C3 and C4, the spectral contributions due to oxygen bound to carbon, were limited to 1.2 eV and 2.0 eV respectively [57], since the electrons involved in these bonds are expected to be highly localised. An example of a fit using this fitting method is given in Figure 5.2 for a SWCNT sample irradiated with a nominal dose of 685 μC 1.5 keV Ar ions and exposed to air for 70 minutes..

O1*s* spectra were fit with three components, referred to throughout this chapter as O1, O2 and O3 on going from low binding energy to high binding energy. These components are associated with contributions due to carbonyl (C=O), ether/epoxy (C-O) (shown in Figure 5.3) [58] and physisorbed water respectively [59]. At this point it is worth noting that contributions to O2 and O3 may occur due to the presence of hydroxyl groups (C-OH). Such groups may be may be formed through the dissociation of adsorbed water: It has been seen that, whilst the majority of water molecules adsorb onto carbon nanotubes without dissociation, cleaving of an O-H bond may occur at the site of dangling bonds and topological defects [60]. Also worthy of note is that spectral features due to physisorbed molecular oxygen on graphite occur at binding energies above 537.5 eV [61] and therefore do not contribute to the O1s spectra presented in this chapter.

Components O1, O2, and O3, were fit by Lorentzian functions once more broadened by convolution with a Gaussian function representing instrumental resolution and the presence of disorder. The binding energies of these peaks were limited to ranges found for the associated species in the literature [58, 59]. The subsequent average binding energies of O1, O2 and O3 are given in Table 5.2. The widths of the components were found to be ~2.1 eV, ~0.9 eV and ~1.5 eV respectively which was maintained for all fits, so that comparability between data was reliable. An example of a fit to an O1*s* spectrum is shown

in Figure 5.3 and demonstrates the change in the intensities of O1, O2 and O3 features on going from clean SWCNTs, to SWCNTs irradiated with 685 μC 1.5keV Ar^+ ions, to the irradiated SWCNT samples exposed to air for 70 minutes.

Component	Binding Energy (eV)	Origin	Width (eV)
C1	284.4 ± 0.1	sp^2 hybridised carbon	various
C2	285.3 ± 0.1	sp^3 hybridised carbon	0.90± 0.05
C3	286.2 ± 0.1	C-O-C, C-O-H	1.20± 0.05
C4	287.6 ± 0.1	C=O	2.00± 0.05
C5	various	π plasmon	various

Table 5.1

Summary of the components, their binding energies and origins, fitted to the C1s spectra presented in this chapter, an example of which is given in Figure 5.1.

Component	Binding Energy (eV)		Origin
	Ar Irradiated + Air	O Irradiated	
O1	531.2 ± 0.3	531.7± 0.3	Carbonyl, C=O
O2	533.1 ± 0.2	533.2± 0.1	Epoxy/Ether, C-O
O3	535.9 ± 0.4	535.5± 0.3	Water, H_2O

Table 5.2

A summary of the components, their binding energies and origins, fitted to the O1s spectra. An example fit is given in Figure 5.3.

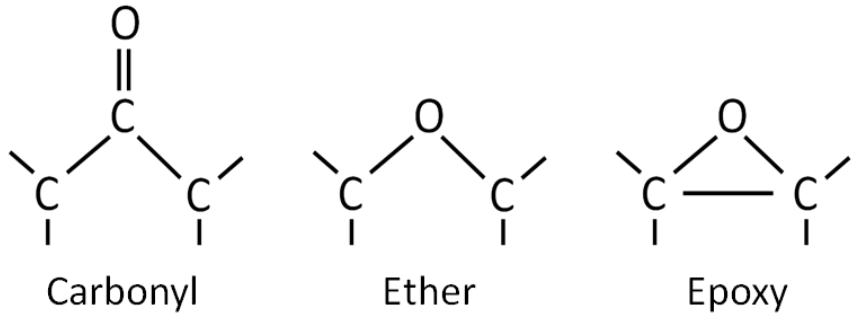

Figure 5.1

Schematic of the carbon-oxygen bonding in carbonyl, ether and epoxy groups.

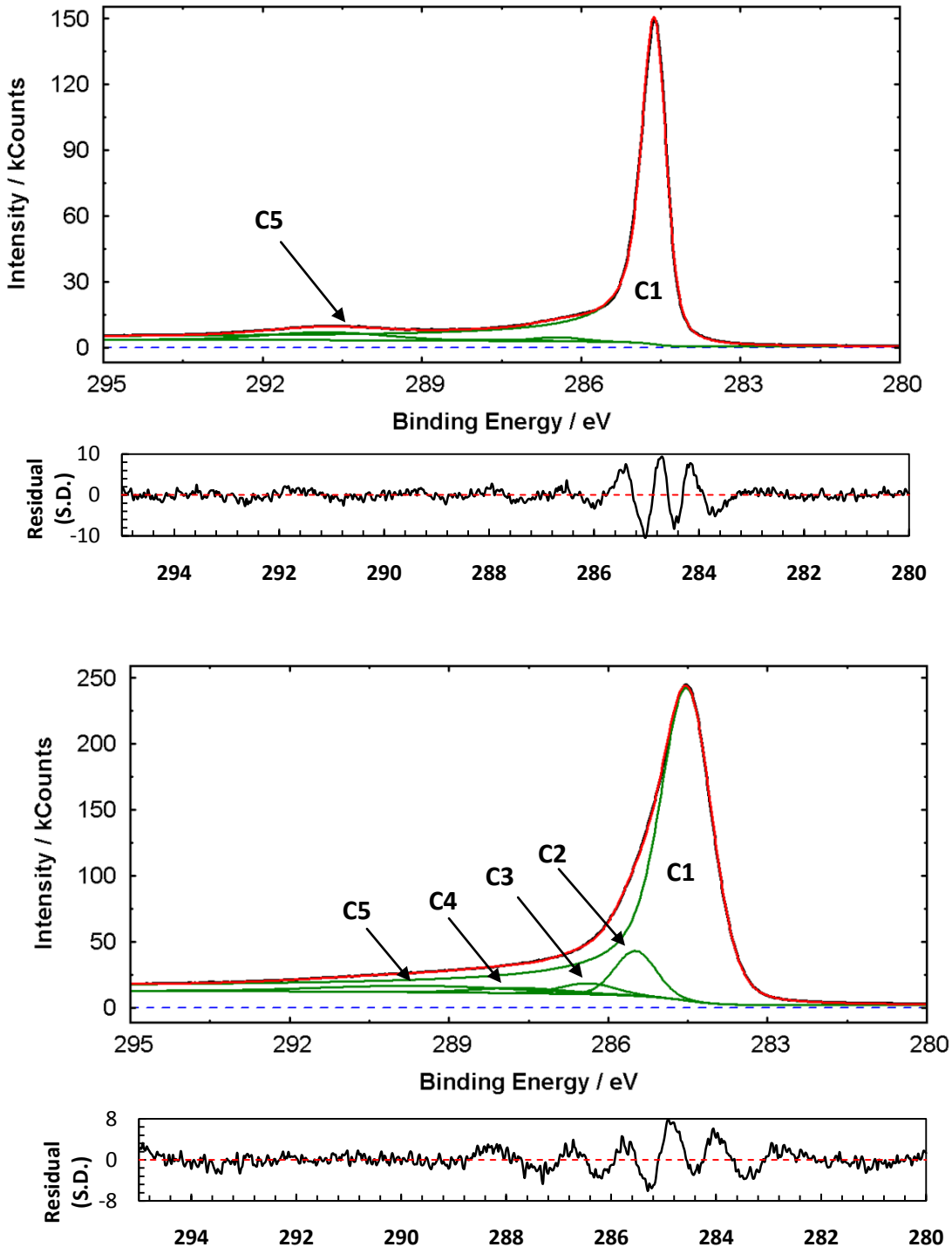

Figure 5.2

Top panel: An example of a fit the C1s spectrum of an annealed SWCNT sample.
Bottom panel: Fit to the C1s spectrum for SWCNTs irradiated with 685μC 1.5 keV Ar^+ ions. The binding energies and the origins of the components are given in Table 5.1. The residual of the fit is given below each spectrum and provides an impression of the suitability of the overall fit.

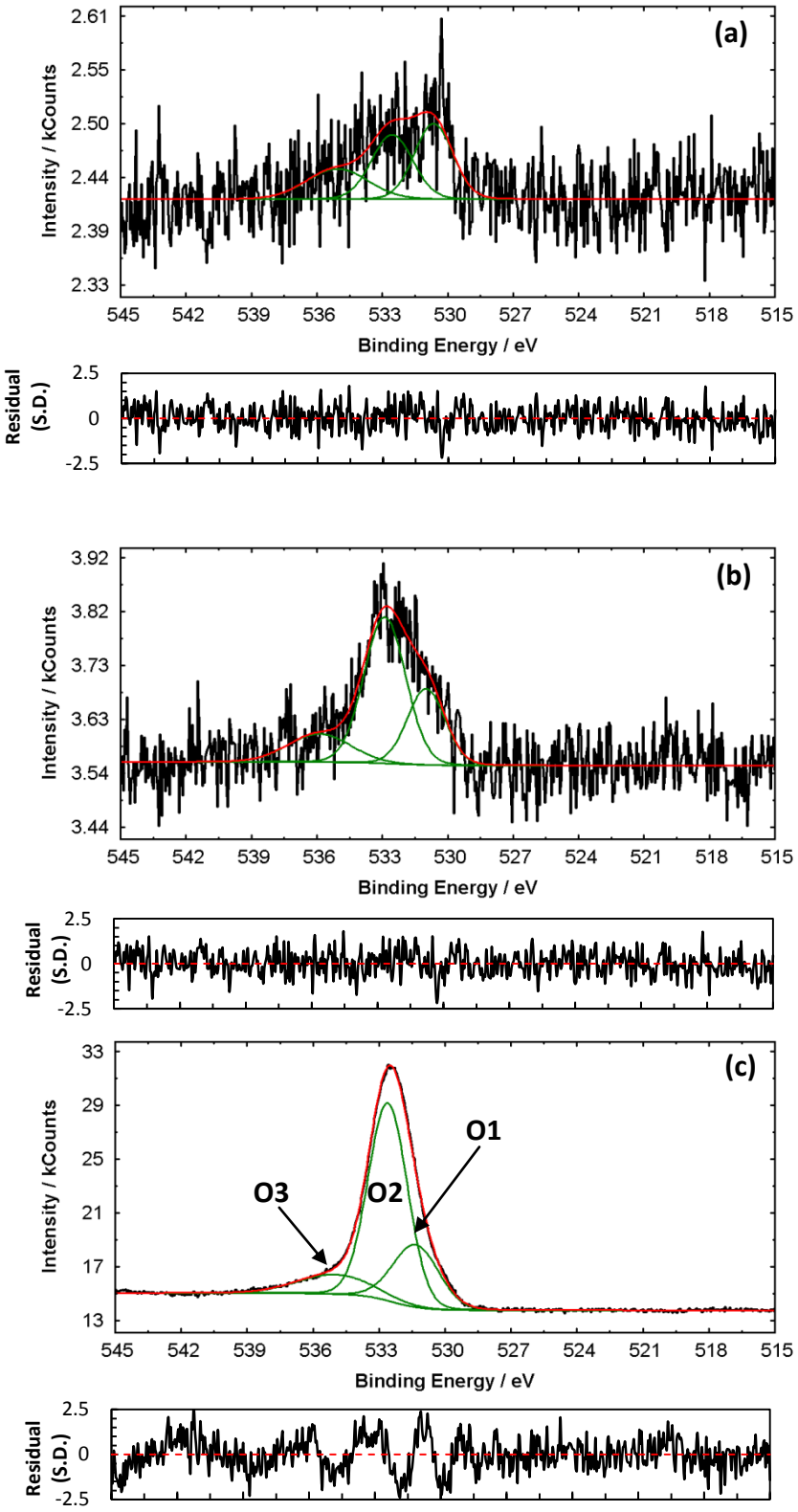

Figure 5.3

Example of O1s fits and residuals for a SWCNT (a) annealed, (b) irradiated with 377 μC 1.5 keV Ar ions and (c) after air exposure. The parameters of the three components and their origin are listed in Table 5.2

5.3 Results and Discussion

5.3.1 Ion Irradiation Effects in SWCNTs

Monte-Carlo simulations based on the binary collision approximation using the TRIM 2008 package [62], assuming a CNT density of 1.34 g.cm^{-3}, show that the 1.5 keV Ar^+ ions used in this experiment have a range of up to 10 nm within the sample, whilst the 0.5 keV O_2^+ ions [63, 64] have a range of around 7 nm. The calculations find that vacancies are produced throughout the ion ranges (by either direct impact or knock-on effects), with an average of 15-20 vacancies (~60 coordination defects [36, 37]) being created for every 1.5 keV Ar^+ ion and 4 vacancies (~16 coordination defects [37]) for every 0.5 keV O_2^+ ions (estimated from the damage created by two 0.25 keV O ions). However such values should be seen as an order of magnitude estimate, since TRIM considers samples to be amorphous.

Molecular dynamics (MD) simulations by Salonen *et al.* [65], aimed at addressing this issue, included the high level of anisotropy that it characteristic of SWCNTs. From that work it is possible to estimate that the number of co-ordination defects generated per 1.5 keV Ar^+ ion is in excess of 100 (extrapolating the linear ion energy- coordination defect relationship given in [65]). Moreover, Salonen *et al.* found that the ion-induced damage is concentrated at the intertube boundaries, not at the maximum calculated by TRIM (i.e. in Ref. 61 the damage within the sample shows peaks at distances periodic in the CNT diameter). However, this MD simulation only considered nanotube bundles in which the nanotubes are aligned perpendicular to the incoming ion beam and so, in reality, we expect that the periodicity will be smoothed out due to the varying nanotube orientation within our thin film samples.

The same work [65] also found that the maximum depth of the ions is overestimated by TRIM since it does not account for the bundled nature of SWCNTs, which allows for efficient dissipation of the energy of the incoming ion. Comparing the maximum depths calculated by TRIM and their MD simulations, Salonen *et al.* [65] found that where TRIM found a maximum ion depth of 8 nm for 0.5 keV Ar^+ ions, the MD simulations found a penetration depth of 5 nm (two nanotube diameters). Using this result, we can therefore assume that the penetration depth of the 0.5 keV O_2^+ ions is of the order of 5 nm, whilst for the 1.5 keV Ar^+ ions a depth of ~6.5 nm can be viewed as a sound estimate.

The results presented in Chapter 4 show that the SWCNT sample has a high carbon content (>95%) with trace amounts of contamination in the form of iron catalyst particles and chlorine from the purification process (see Chapter 3, Section 3.1.1). Our analysis also found that this particular batch of SWCNTs has a narrow diameter distribution, with an average SWCNT diameter of ~1.2 nm, and that the CNTs are packed into large ropes of diameter varying from ~10 nm up to ~200 nm. Using this information, we can deduce that the damage to the SWCNTs is as a result of the incident ion passing through the nanotubes and coming to rest within the ropes.

The information obtained using photoemission is dependent on the electron inelastic mean free path (IMFP) and the information depth (defined as three times the IMFP) of the C1*s* and O1*s* photoelectrons. For Al K_α excitation the C1*s* photoelectrons have an IMFP of 3.1 nm, whilst that for O1*s* photoelectrons is 2.6 nm, giving information depths (the depth from which 95% of the detected photoelectrons originate) of 9.3 nm and 7.8 nm respectively. This indicates that the spectra presented in this chapter are dominated by SWCNTs that have been damaged by the incoming ions. Figure 5.4 displays C1*s* spectra for clean SWCNTs (labelled 0 μC) and for SWCNTs irradiated with an increasing dose of 1.5 keV Ar^+ ions. It is clear that with increased irradiation dose and air exposure that the FWHM of the C1*s* line increases and the π-plasmon (the feature located at a binding energy of ~291 eV in the '0 μC' spectrum) broadens and shifts to lower binding energy. The C1*s* core line broadens for three reasons: first, there is an increased number of dissimilar carbon-carbon bonding environments due to the increasing defect density which produce contributions to the line with binding energies that differ very slightly from the main C1*s* (graphitic) peak of the pristine material [54]; second, there is an increase in intensity at ~285 eV due to the increased presence of sp^3 hybridised (defective) carbon [53]; third, there is an increase in intensity of the carbon-oxygen components situated at binding energies between ~286 eV and ~288 eV [54, 57]. The broadening and red-shifting of the π-plasmon can be primarily thought of as indicative of the ion-induced destruction of the delocalised π-bonding network in the SWCNTs [49, 66]. These observations are not atypical. Indeed, this behaviour holds true not only for the work presented here but also for SWCNTs irradiated with 3 keV Ar^+ ions [50], MWCNTs irradiated with 1 keV Ar^+ ions [49, 50] and graphite irradiated with argon, hydrogen and deuterium ions [57, 66, 67].

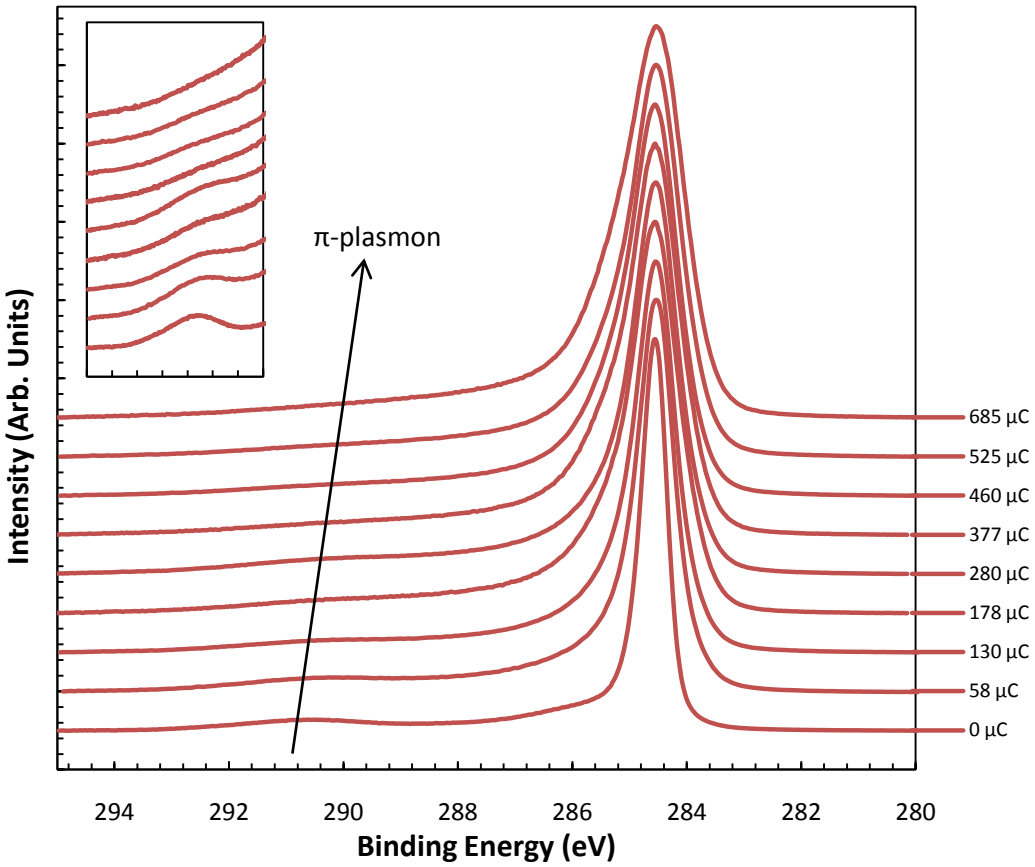

Figure 5.4

Evolution of the SWCNT C1s line with increased irradiation dose. The spectra have been normalised and the main peak shifted to a binding energy 284.4 eV for clarity (B.E. shifts are shown in Figure 5.5). Detail of the change to the π-plasmon is shown in the inset.

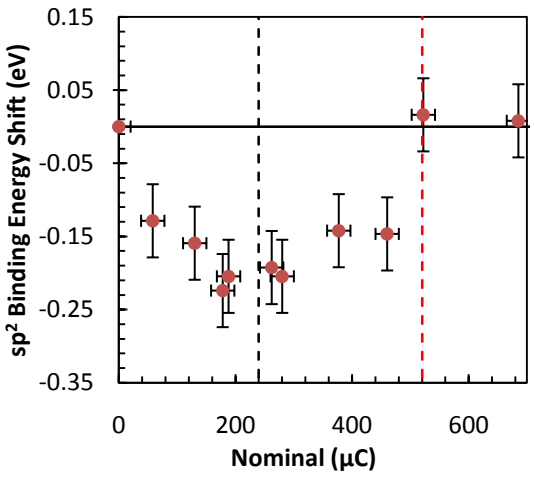

Figure 5.5

The binding energy shift of the main C1s component, C1, as a function of dose. The shifts are obtained by comparing the binding energy of the irradiated sample to the clean sample prior to irradiation. The black line represents the zero of the y-axis, whilst the black and red dashed vertical lines represent, respectively, the doses at which the maximum negative binding energy shift occurs, and the point at which this shift returns to zero.

Since components C2-C5 have binding energies fixed relative to C1, this shift also represents the shift of these components.

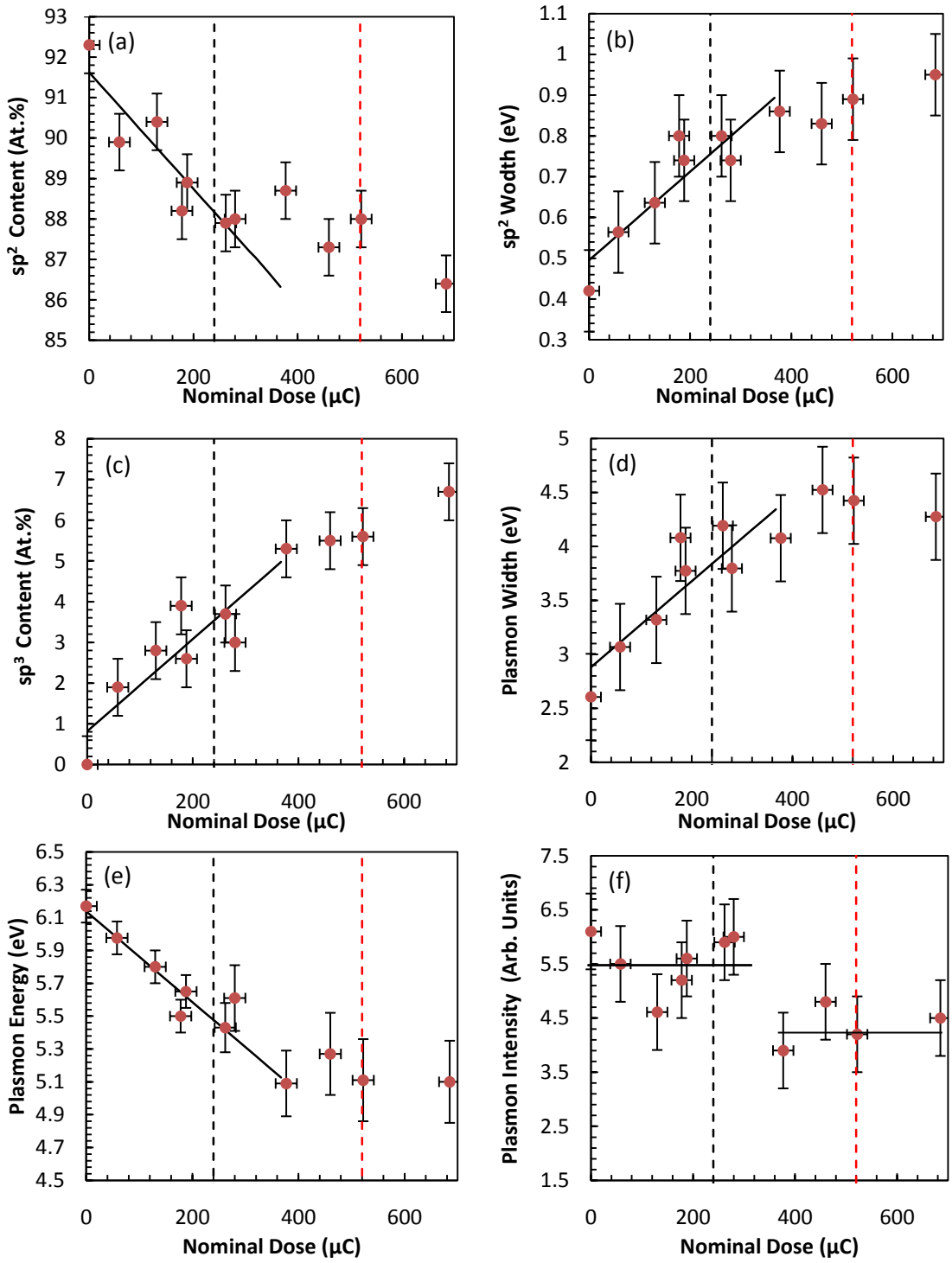

Figure 5.6

The influence of Ar irradiation on the C1s line of SWCNT samples: (a) the intensity of the sp^2 component, C1; (b) the width of C1; (c) the intensity of the sp^3 component, C2; (d) the width of the π-plasmon, C5; (e) the energy of C5; (f) the intensity of C5. The black and red dashed vertical lines indicate respective points at which there is a maximum shift in the binding energy and where this shift returns to zero. The solid black lines show linear fits of the data up to doses of ~380 µC (a dose which lays roughly half way between the limits set by the black and red dashed vertical lines).

Through decomposition of the C1*s* envelope, it is possible to track specific changes in the contributions to the lineshape. As suggested by the general observations above, the sp^2 component, C1, decreases in intensity and broadens (Figure 5.6 (a) and (b) respectively), whilst shifting to lower binding energy for ion doses below ~240 μC (Figure 5.5). For doses above this, the binding energy shift reverses direction until, at a dose of ~520 μC it returns to that of the pristine sample. Since the binding energies of components C2-C5 are measured relative to C1, this shift is also representative of the general movement of these components and thus, a close to rigid shift C1*s* spectrum as a whole. Similar shifts in C1*s* binding energy have been observed for Ar^+ irradiated C_{60} films [68] and SWCNTs [50] and are typical of hole doping in graphitic materials [69, 70], in this case due to the presence of defects. The reversal of this shift above doses of ~220 μC implies that the description of the SWCNT sample as a hole-doped graphitic system becomes increasingly invalid above this threshold due to the number of defects within the SWCNT lattice, i.e. there is destruction of the SWCNTs. The dose at which this occurs is in agreement with other experimental work [50] (in which 3 keV Ar^+ irradiated SWCNTs begin to break up at ~210 μC/cm^2), but is lower than values suggested by MD simulations [35] (in which 0.5 keV Ar^+ irradiated SWCNTs begin to break up at and ~320 μC/cm^2). The return of the C1*s* binding energy to that of the pristine material for doses of ~520 μC suggests that by this point there is complete amorphisation of the upper 6.5 nm of the sample, i.e. between ~240 μC and ~520 μC the best description of the sample shifts from 'SWCNT-like' to 'amorphous-carbon-like'. This behaviour under ion irradiation is of importance when considering the interpretation of the other data presented in this chapter.

As the above changes to the C1 component are occurring, there is a concurrent increase in the contribution from the sp^3 component, C2 (Figure 5.6(c)). There is a monotonic increase in the proportion of sp^3 hybridised carbon with irradiation dose, with the rate of increase slowing slightly at the point at which the maximum binding energy shift occurs (shown by way of the black dashed vertical line, which we term the 'amorphisation threshold'). We suggest that an initial linear increase in sp^3 content occurs under ion irradiation: below the onset of amorphisation defects are created sufficiently far apart to be treated as independent and existing within an intact nanotube structure. Once amorphisation begins the influence of existing defects (and hence structural degradation) upon further damage processes will change and substantially slow the increase in sp^3 content. Indeed, for ion doses of around 400 μC and above the sp^3 content is constant to within error. A similar

discontinuity occurs in the intensity and the FWHM of the sp^2 component, C1 (figure 5.6(a) and (b)) once more indicating that the rate of change in local carbon-carbon bonding decreases significantly for ion doses above ~240 μC. The origins of C2 may lie in either the presence of carbon interstitials created during irradiation [37] or chemisorbed species [21]. Here, the former is more likely in our data since irradiation and subsequent analysis are performed *in situ* under UHV conditions.

The behaviour of the π-plasmon peak, C5, as a function of irradiation dose is displayed in Figure 5.6(d)–(f). The plasmon width (Figure 5.6(d)) increases linearly with dose until the amorphisation threshold, beyond which point a plateau is reached. Likewise, the plasmon energy decreases linearly with dose, reaching a plateau between the points of maximum negative binding energy shift and the return of this shift to zero. Similar behaviour of the plasmon loss has previously been observed for defective graphitic systems [53, 66] and irradiated MWCNTs [49]. In these studies, the decrease in π-plasmon energy is attributed to a reduced overlap in the π-bonding network through increased interplanar spacing brought about by ion irradiation [49, 66], whilst broadening is attributed to the reduced plasmon lifetime due to increased defect-related scattering in the disrupted π-bonding network [49, 53]. The reduced overlap of the π-bonding network is clearly not a satisfactory explanation for the shift in π-plasmon energy as the same shift in observed here for SWCNTs. In the study by Brzhezinskaya [49] the relationship between the π-plasmon energy, and irradiation dose, ϕ, was approximated as:

$$E_{\pi}(\phi) = Ae^{-\kappa\phi}$$

Equation 5.2

where A is a constant and $\kappa \approx 0.074$ cm^2/μC for 1 keV Ar^+ irradiated MWCNTs. Here, we treat the π-electrons in the SWCNTs as a free electron gas (bearing in mind that this is a significant simplification and ignores interband transitions etc.), and directly link the π-plasmon energy to the π-electron density of the sample:

$$E_{\pi} = \hbar\omega_{\pi} = \hbar\sqrt{\frac{ne^2}{m_e^*\epsilon_o}}$$

Equation 5.3

where n is the electron density, e is the electronic charge, m_e^* is the effective electronic mass (taken to be $0.1 m_e$ [71]) and ϵ_o is the permittivity of free space. From Equation 5.4 it is clear that the relationship between the plasmon energy and the electron density is of the form:

$$E_\pi^2 = \mathbb{C}n$$

where

$$\mathbb{C} = \frac{\hbar^2 e^2}{m_e^* \epsilon_o}$$

Equation 5.4

At zero incident dose let the π-electron density, n, of the sample be n_o. If the number of π-electrons removed from the 'free electron gas' by irradiation is directly proportional to the number of ions incident on the sample then $n = n_o - k\phi$ where ϕ is the dose delivered to the sample and k is a constant. Thus:

$$E_\pi^2 = \mathbb{C}(n_o - k\phi)$$

Equation 5.5

From Equation 5.5 it is clear that a plot of $E_\pi^2/\mathbb{C}$ against ϕ should follow a linear relationship with intercept n_o and gradient k. The result of such an analysis is presented in Figure 5.7, which displays both a linear fit to the data (solid black line) and a fit using the approach of Brzhezinskaya *et. al* [49] (dashed black line). The 'Brzhezinskaya fit' considers all data points and is achieved using k=0.0009 cm^2/μC and A = 7.09x10^{27} eV in Equation 5.2. The linear fit considers all data points up to the point of complete amorphisation of the sample (indicated by the red vertical dashed line in Figure 5.7). From this analysis it is found that n_o = 2.74×10^{27} m^{-3} = 2.74×10^{21} cm^{-3} which is in line with the calculations of Mintmire *et al.* [72] who consider a bundle of 1 nm diameter SWCNTs. Furthermore, the gradient of the linear fit estimates that each Ar^+ ion removes ~0.17 π-electrons from the SWCNT system, which is much smaller than the number of co-ordination defects expected from the work of Salonen *et al.* [65]. This suggests that there is extensive healing of the π-bonding network during relaxation.

Reduced χ^2 values for both the linear fit and the 'Brzhezinskaya fit' are 0.98 and 1.00 respectively, indicating that both models provide good fits to experimental data. However since the model of Brzhezinskaya *et. al* [49] is derived on an empirical basis, rather than a

physical basis (which is the case of the linear relationship), it would be suggested that the latter model is more appropriate.

The π-plasmon intensity (Figure 5.6 (f)) shows a discontinuous drop between the amorphisation threshold and the point at which we believe amorphisation is complete. This is unlike the behaviour previously observed in irradiated MWCNTs or graphite [49, 53, 66], described above and is unlike the results obtained for similar studies on DWCNT and MWCNT samples discussed in Chapter 6. This discontinuity, in addition to the observations discussed above, provides strong evidence for a change in the physical structure of the sample between the onset of amorphisation and the completion of amorphisation (indeed, as will be seen later in this chapter, these changes can be linked with the oxygen content measurements of the samples). Moreover, the discontinuous nature of the behaviour of the π-plasmon, may suggest that the change between phases is rather abrupt.

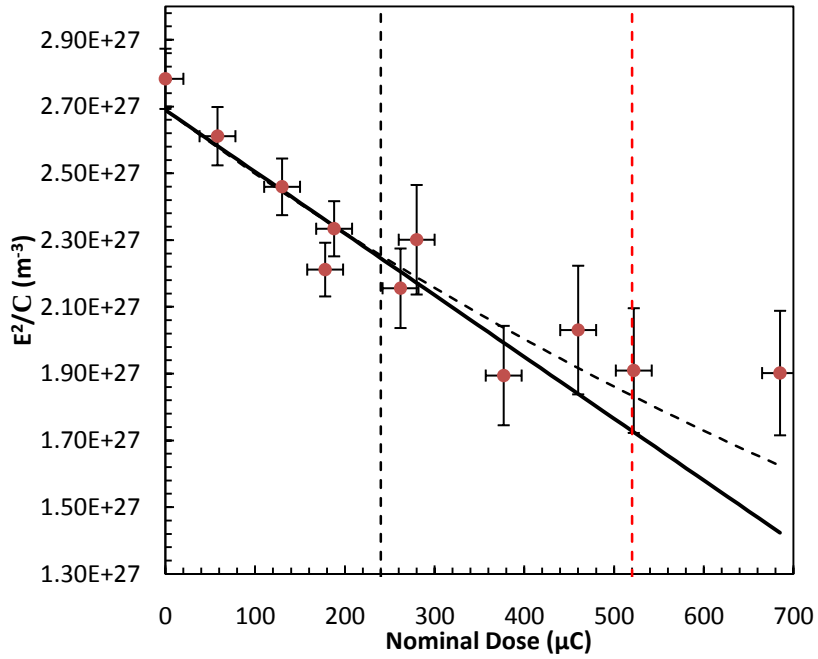

Figure 5.7

The linear relationship of π-plasmon energy, $E_\pi^2/\mathbb{C}$ with irradiation dose The black and red dashed vertical lines indicate the respective points at which there is a maximum shift in the binding energy and where this shift returns to zero. The solid black line is a linear line of best fit up to the point of compete amorphisation (the red dashed line). The dashed black line is a line of best fit created using the approach of Brzhezinskaya [49] (Equation 5.2). In this case k=0.0009 $cm^2/\mu C$ and $A = 7.09 \times 10^{27}$. The reduced χ^2 values for each of these fits are 0.98 and 1.00 respectively.

The oxygen content of the sample, represented by components C3 and C4 in the fit to the C1*s* line, show a very small increase upon irradiation. This is likely due to the interaction of the irradiated SWCNTs with oxygen-containing residual gases. For irradiated SWCNTs exposed to air, these components exhibit a more observable change (discussed in the following section).

5.3.2 Oxygen Uptake in Irradiated SWCNTs

Figure 5.8 displays the effect of exposing a clean annealed and non-irradiated (0 μC) SWCNT sample to air for 70 minutes. To the eye there are no discernable differences between the C1*s* spectra of the clean SWCNT sample held under vacuum (blue curve), and the same sample after exposure to atmosphere (red curve). The difference between the two spectra is in the form of a very small increase in the C1*s* width and in the intensity along the high binding energy side of the main C1*s* line. Apart from carbon, the only other element visible in survey spectra (not shown) taken after air exposure is oxygen. It is therefore likely that this small spectral contribution is due to a small amount of chemisorbed oxygen, perhaps on the site of naturally occurring defects that are present even after annealing. Examination of the O1*s* spectrum (inset to Figure 5.8) verifies that there is indeed a small increase (~0.75 at.%) in the oxygen content of the sample upon exposure to air for 70 minutes (red line), due to small amount of chemisorbed species (the contribution due to water groups is minimal).

In contrast to the behaviour of the pristine annealed samples, there are clearly observable differences between the C1*s* lineshape of irradiated SWCNTs before and after air exposure (Figure 5.9). Upon exposing irradiated SWCNTs to air there is a clear increase in intensity between binding energies of 286 eV and 289 eV. This region corresponds to oxygen species bound to carbon (see Table 5.1). Indeed, when fitting the C1*s* data from air-exposed irradiated SWCNTs it is found that whilst there is a noticeable increase in the intensity of the oxygen containing components C3 and C4, there are no changes to the π-plasmon and sp^3 fit parameters from those shown in Table 5.1.

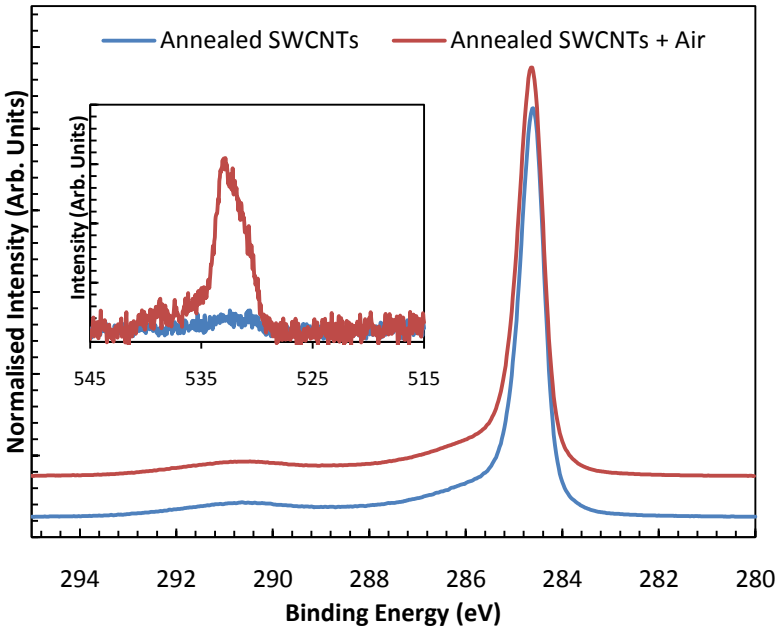

Figure 5.8

Comparison of the C1s lineshapes for a clean SWCNT sample before (blue curve) and after air exposure (red curve). The lineshape of the air exposed has been displaced upward for clarity.
The inset shows the O1s spectra for a clean sample before (blue curve) and after (red curve) it was exposed to air. There is a clear uptake of oxygen containing species.

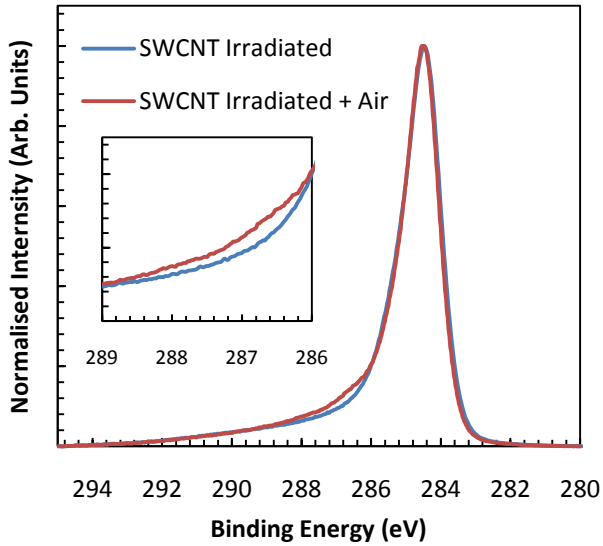

Figure 5.9

Comparison of the C1s lineshape for irradiated SWCNTs held under vacuum (blue curve) and for the same sample after air exposure (red curve). It is clear that there is an increase in intensity between ~286 eV – 289 eV (shown in the inset).

Figure 5.10 displays how the total oxygen content varies with dose for 1.5 keV Ar^+ irradiated SWCNTs exposed to air. It is clear that there is minimal (and constant) oxygen uptake for irradiated SWCNTs held under vacuum (blue circles), with the oxygen possibly arising from residual gas in the UHV chamber or impurities in the Ar used to supply the ion gun. For air-exposed irradiated SWCNTs (red circles) there is a linear increase in the

total oxygen content with irradiation dose, this uptake reaching a plateau at ~7 at.% at a dose of ~300 μC (just after the onset of sample amorphisation). This level of adsorbate uptake is in line with the CH_4 storage capacity (~9 at.%) of chemically etched and mechanically sheared MWCNTs [22] and the H_2 storage capacity (~11 at.%) of SWCNTs bombarded with atomic hydrogen [21]. In each of these cases the enhanced uptake in adsorbed species may be attributed to the creation of defects within the CNT lattice. Similarly, the observed enhanced oxygen uptake of the Ar^+ irradiated SWCNTs observed here can also be attributed to an increased defect density in these CNTs. It is also clear that this enhancement occurs in such a way that the level of oxygen uptake is proportional to the irradiation dose, up to the onset of sample amorphisation.

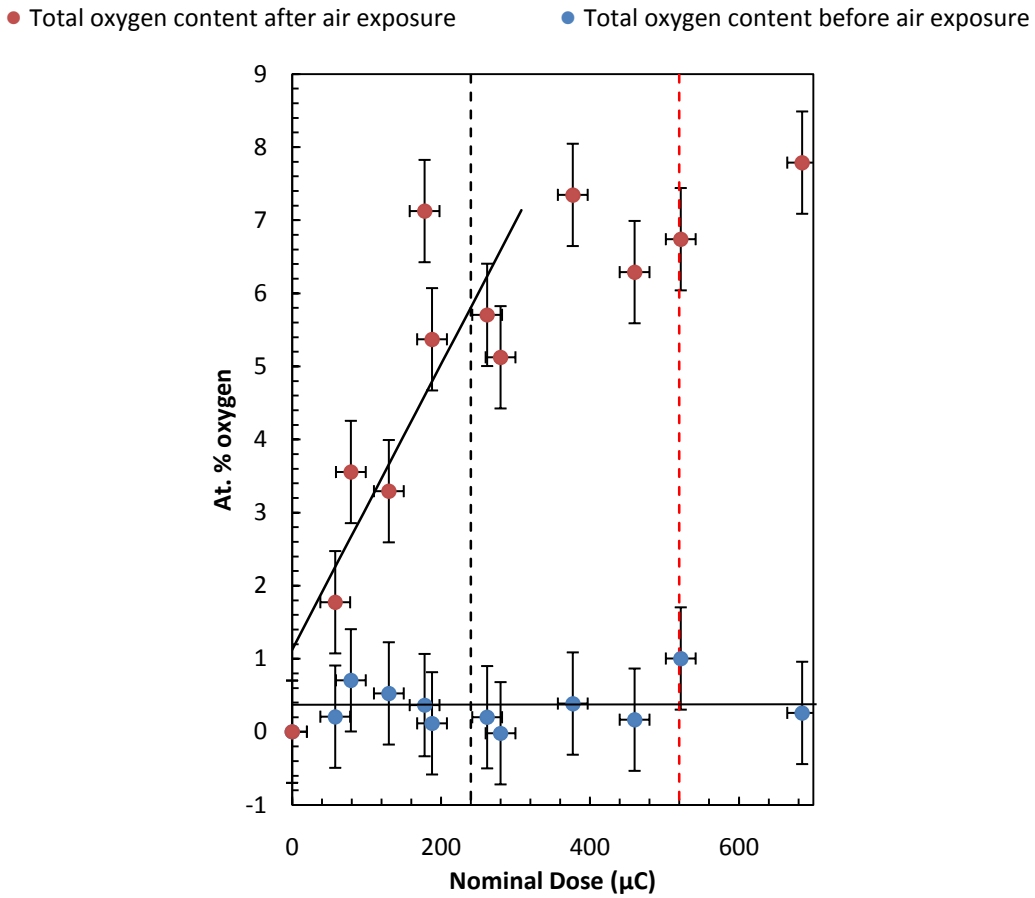

Figure 5.10

Total oxygen content for 1.5 keV Ar^+ irradiated SWCNTs as a function of dose before (blue circles) and after (red circles) air exposure. As in Figure 5.5, the black and red dashed vertical lines represent the thresholds for the start and completion of amorphisation respectively. The black solid lines are included to guide the eye.

Figure 5.11 displays the contributions to the O1*s* peak due to C-O bonds, C=O bonds and water after Ar^+ irradiation and air exposure. It is apparent that there is a linear increase in the C-O content (red data points) with irradiation up to the amorphisation threshold, at which point it saturates ~4.5 at.%. The C=O content (solid green circles) behaves in a similar fashion, although the initial increase is not as sharp and the plateau occurs at a concentration ~1.5 at.% (i.e., at the point of amorphisation there is three times as much C-O on the surface of the SWCNTs than C=O). The O1*s* contribution ascribed to water is shown as the blue circles in Figure 5.11. From these data it appears that there is also a very small linear increase in the water content of the sample, although this increase is only slightly larger than the experimental error.

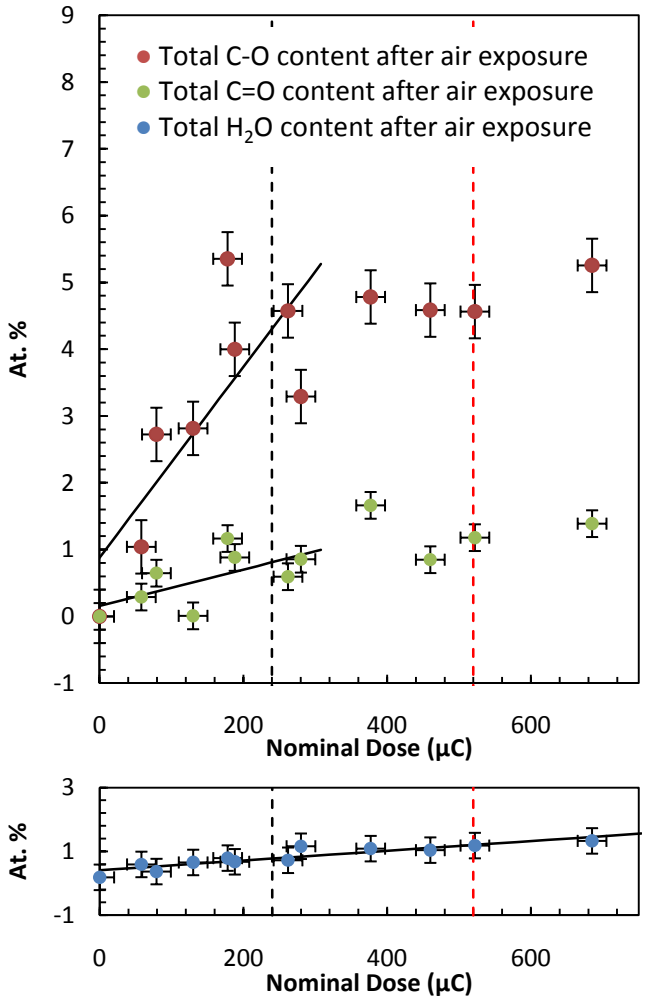

Figure 5.11

Oxygen content for 1.5 keV Ar^+ irradiated SWCNTs exposed to air as a function of dose. C-O content (red circles), C=O content (green circles) and spectral contribution due to hydroxyl containing species (blue circles), primarily assigned to water. The black and red vertical lines represent the onset and completion of amorphisation respectively. The solid black lines are present to guide the eye.

In order to put these results in context, we now compare the data from air exposed Ar^+ irradiated nanotubes to that for SWCNTs irradiated with oxygen ions. Figure 5.12 displays the spectral changes of both the C1*s* and O1*s* lineshapes upon O_2^+ ion irradiation. As is clear, upon irradiation the C1*s* lineshape shifts to higher binding energy by 0.2 eV, comparable to the shift seen for Ar^+ irradiated SWCNTs. It is also clear that there is significant broadening of the C1*s* lineshape along the high binding energy side of the main C1*s* peak. As with the Ar^+ irradiated SWCNTs, this change can be attributed to sp^3 hybridised carbon and oxygen containing species bound to carbon (see Table 5.1).

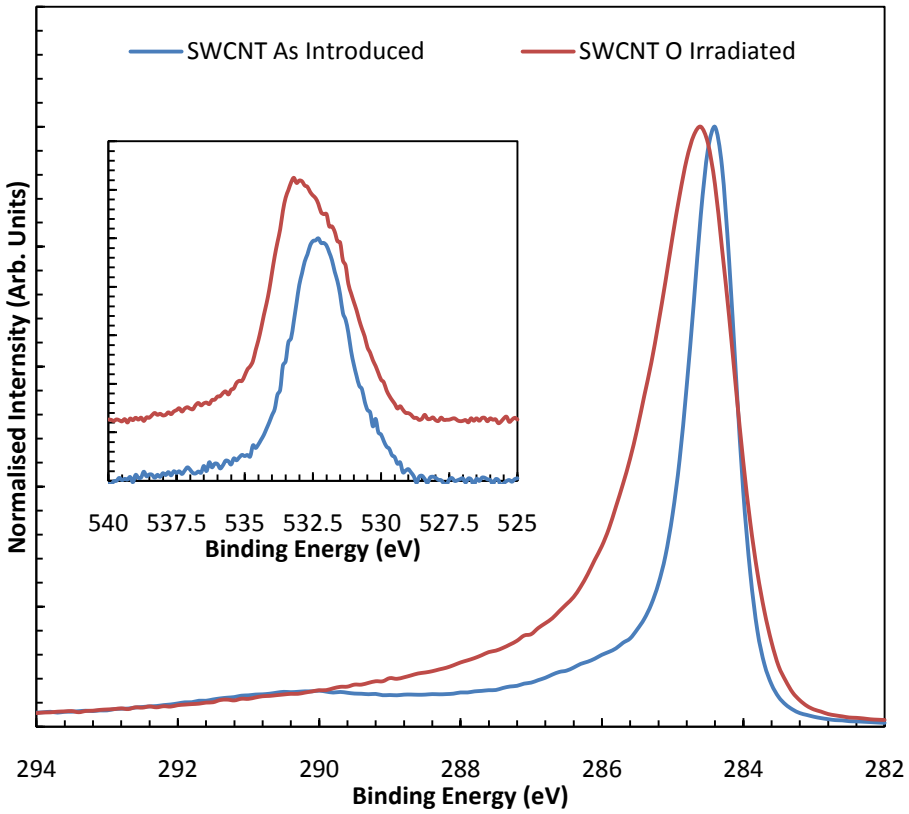

Figure 5.12

Comparison of the intensity normalised C1s lineshapes for an 'as introduced' SWCNT sample (blue curve) and after 18 μC O_2^+ ion irradiation (red curve).
The inset shows the intensity normalised O1s spectra for an 'as introduced' sample before (blue curve) and after (red curve) O_2^+ ion irradiation. The O1s lineshape of the O_2^+ irradiated SWCNTs (red curve) has been displaced upward for clarity

The inset of Figure 5.12 displays the changes that occur to the O1*s* lineshape upon O_2^+ ion irradiation. There are observable differences between the two lineshapes: the as-introduced SWCNT sample exhibits a symmetric O1*s* lineshape, whilst the oxygen irradiated SWCNT sample shows a clear asymmetry towards higher binding energy. Though the doses are

lower than those used in the Ar^+ irradiated samples, the O_2^+ irradiation-induced changes are much more dramatic, indicating that they arise from the interaction of the SWCNT with the oxygen rich atmosphere. In line with this, Figure 5.13 shows that the total oxygen content of O_2^+ irradiated SWCNTs quickly saturates at ~ 9 at.% after a dose of ~20 μC.

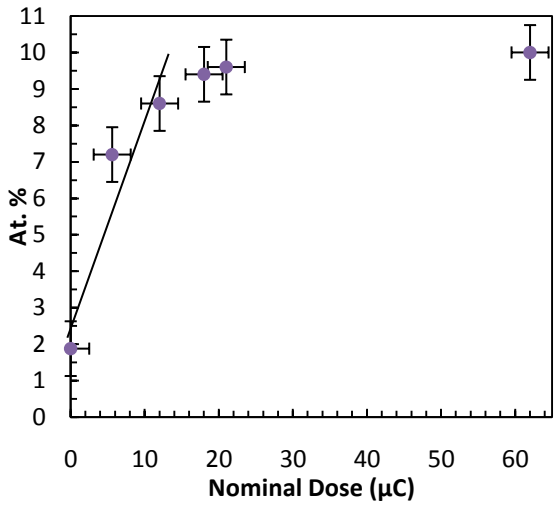

Figure 5.13

The total oxygen content (purple circles) of SWCNTs irradiated with 0.5 keV O_2^+ ions. The black line is to guide the eye.

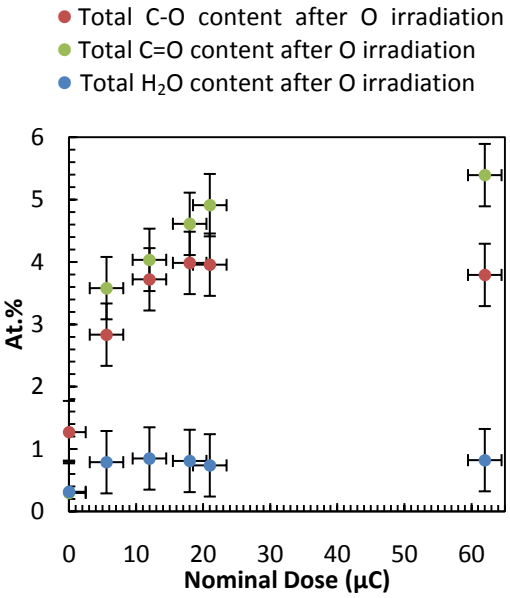

Figure 5.14

Relative intensity due to hydroxyl containing species (blue circles), oxygen singly bonded to carbon (red circles) and doubly bonded to carbon (green circles) for 0.5 keV O_2^+ irradiated SWCNTs extracted from the O1s fits.

Once again, analysis of the O1s peaks allows the contributions due to C-O bonds, C=O bonds and hydroxyl groups, including water, to be ascertained. Typical O1s fits are shown in Figure 5.15: Figure 5.15(a) shows the O1s fit for an 'as introduced' SWCNT sample, whilst Figure 5.15(b) and Figure 5.15(c) show O1s fits for SWCNT samples irradiated with 18 μC and 62 μC O_2^+ ions respectively. Figure 5.14 displays the results of such a fitting procedure. From these fits it is clear that unlike the 'low-dose' Ar^+ irradiated SWCNTs (in which C-O and C=O are present in a ratio 3:1), C-O and C=O are present in roughly equal

amounts for doses up to ~20 μC. After this the C-O and C=O content of the sample appears to saturate at ~4.5 at.%. Throughout O_2^+ ion dosing the spectral contribution due to hydroxyl groups remains the same to within experimental error at ~1 at.%.

From the data presented above there are clearly significant differences in relative amounts of C-O and C=O present on the surface of the CNT sample after O_2^+ ion irradiation and Ar^+ irradiation and air exposure. In the following section these differences will be discussed in terms of defects present in the SWCNT lattice.

5.3.3 The Role of Defects in Oxygen Uptake

As discussed in the introduction to this chapter the defects introduced into the SWCNT lattice by ion irradiation include monovacancies, vacancy clusters and carbon interstitials. A summary of the simplest reconstructed defects is given in Figure 5.16 and include, from left to right: the Stone-Wales defect (a C-C bond rotation), a carbon interstitial (formed by the removal of a carbon atom from within the graphene lattice and subsequent deposition on the outside of the tube); a single vacancy, which relaxes to a pentagonal ring defect and one dangling bond (referred to as 5-1DB defect); vacancy clusters which contain pentagonal defects and DBs (in Figure 5.16, the lowest-energy configurations [32] of reconstructed vacancy clusters are shown). The oxygen uptake of oxygen and argon irradiated SWCNTs will be considered in terms of these defects.

Ion-induced defects are created on the picosecond timescale and, in the absence of ambient gases, will reconstruct with little or no energy barrier and minimise the number of dangling bonds (DBs) present [42, 73]. The remaining dangling bonds are considered stable at room temperature [46, 54] and have been observed on graphite [74] and in MWCNTs [75]. For temperatures above ~200°C, monovacancies in SWCNTs are mobile and may migrate and coalesce to form divacancies which are immobile up to temperatures of ~1000°C [46]. At room temperature, the migrations barriers of both single vacancies and divacancies (>1 eV) means that these defects are essentially immobile.

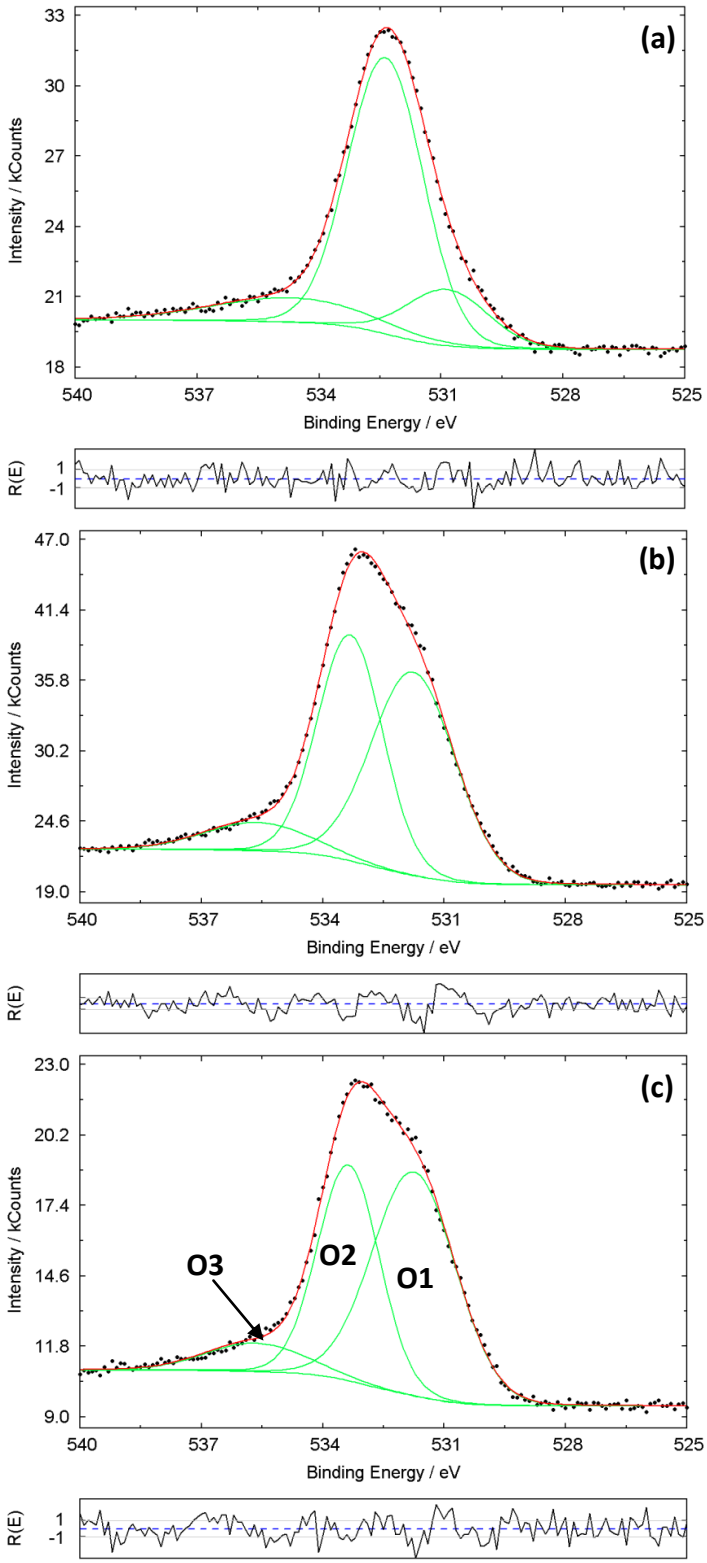

Figure 5.15

Examples of O1s fits and residuals for a SWCNT sample (a) as introduced, (b) irradiated with 18 μC 0.5 keV O_2^+ ions and (c) irradiated with 62 μC 0.5 keV O_2^+ ions. The parameters of the three components and their origin are listed in Table 5.2

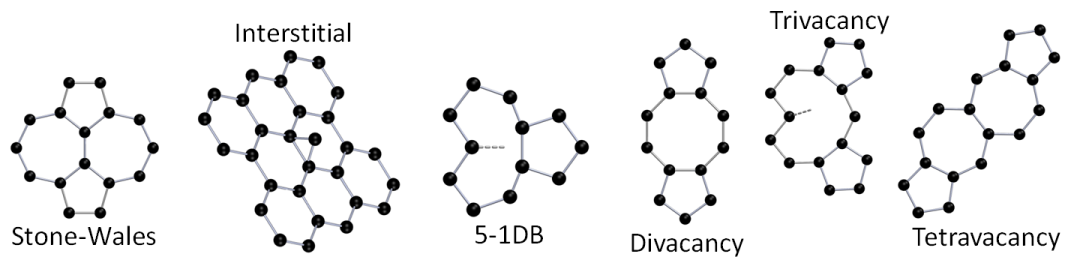

Figure 5.16

Adapted from [9, 11, 32, 54]: The types of stable defect in irradiated CNTs. The monovacancy (labelled 5-1DB) and tri vacancies have dangling bonds associated with them, the other types of defect do not.

Healing of defects in a graphene lattice may occur through the recombination of carbon interstitials with a vacancy. Such carbon adatoms on a graphene surface have been found to have a migration barrier of ~0.4eV and are expected to be mobile at room temperature [76]. Indeed HRTEM studies of point defects of graphene have shown evidence for such processes, with healing of vacancy defects occurring on timescales of ~4 s [77]. In SWCNTs, carbon interstitials may exist both on the inner and outer surface of the nanotube wall. On the inner wall, the negative curvature yields low migration barriers of 0.1 eV to 0.4 eV [78] (i.e., a mobility comparable to interstitials on graphene). On the outer wall, the higher curvature of the surface raises the migration barrier to between 0.5 eV and 1 eV [76]. Both of these migration barriers are dependent on nanotube curvature (diameter) and chirality. It is therefore expected that vacancy-adatom recombination processes are limited at room temperature and that some defects created under ion irradiation are stable on long timescales (a value of ~ 10 hours has been suggested [79]).

When irradiating nanotubes with oxygen the defects are created in an environment where the primary contribution to the residual gas atmosphere is oxygen. Moreover, oxygen ions come to rest local to the points at which defects are created. As a result, it is likely that any dangling bonds are rapidly saturated by oxygen (which dissociates in the presence of dangling bonds [80]), before they can reconstruct. A schematic of the creation of a monovacancy and saturation of dangling bonds with oxygen is shown in Figure 5.17, resulting in the formation of one carbonyl (C=O) and one ether (C-O) group. In graphene, the carbonyl group protrudes out of the plane by 32.11° to the normal and the ether group lies within the plane [54]. Figure 5.18 displays a schematic of the creation of a divacancy by O_2^+ ions and the immediate saturation of dangling bonds in an oxygen-rich atmosphere.

The result is the formation of two ether groups [54]. From these scenarios one can infer the spectral signature of a monovacancy, a divacancy and a (monovacancy + divacancy), created in an oxygen rich environment: For an oxygen-saturated monovacancy it would be expected that there are equal quantities of C-O and C=O in the O1*s* spectra; For an oxygen saturated divacancy, there would only be the C-O peak present in the O1*s* spectra; For an equal number of monovacancies and divacancies, both C-O and C=O peaks will be present with an intensity ratio of 3:1. Hence, based on the data from O_2^+ irradiated SWCNTs (equal quantities of C-O and C=O), we can speculate that the damage incurred by the SWCNTs in this case is predominantly in the form of monovacancies.

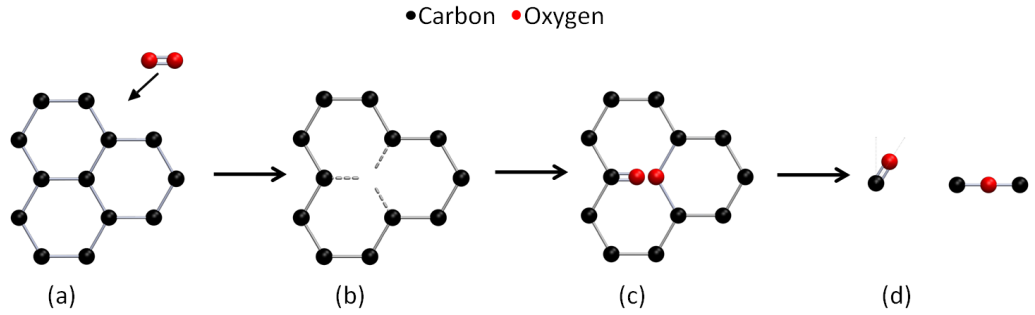

Figure 5.17

Adapted from Barinov et al. [54]: A schematic showing (a) irradiation of graphene by O_2^+ ions resulting in (b) the production of a monovacancy with (c) dangling bonds saturated by ambient oxygen. (d) The result is the formation of one carbonyl group (C=O) and one ether group (C-O).

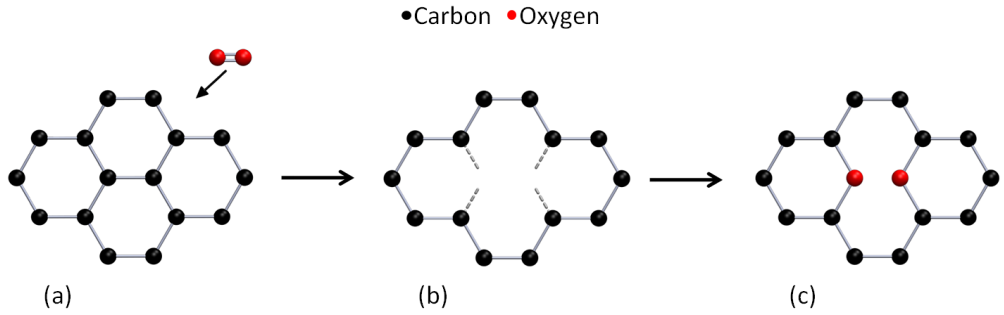

Figure 5.18

Adapted from Barinov et al. [54]: A schematic showing (a) irradiation of graphene by O_2^+ ions resulting in (b) the production of a divacancy with dangling bonds that are (c) saturated to form two ether groups (C-O).

As discussed above, in the absence of ambient gases ion-induced defects are expected to reconstruct and reduce the number of dangling bonds through the formation of pentagonal rings. For example, a monovacancy will reconstruct to form a single pentagonal ring, and a

9-membered ring containing one dangling bond. This is referred to as a 5-1DB defect. Furthermore, on the timescales of these experiments (~ 1 hour between irradiation and air exposure), it is expected that there will be some migration and recombination of carbon interstitials with vacancy defects, so healing the nanotube structure. Consequently, the C-O and C=O proportions observed in Ar^+ irradiated SWCNTs (and the differences to those observed in O_2^+ irradiated SWCNTs), occur due to the interaction of ambient oxygen with *relaxed* defect structures, which will now be considered.

Interaction of molecular oxygen with the 5-1DB defect is shown in Figure 5.17. In the presence of the dangling bond, the molecular oxygen dissociates [80] and forms a carbonyl group. Since there are no further dangling bonds to saturate, the remaining oxygen atom forms a surface epoxy group above a carbon bridge. It has been shown that the formation of epoxy in this way is the predominant bonding mechanism of atomic oxygen on graphite [54] and is energetically favourably in SWCNTs [7]. If one again considers the spectral signature of a relaxed, air exposed, monovacancy, it is clear that the O1*s* spectra will contain equal contributions due to C-O and C=O. Similarly, any defect containing an odd number of missing carbon atoms will have the same signature, since such defects also relax to form structures containing one dangling bond [32]. Thus, if this were the only mechanism by which chemisorbed oxygen species were formed in Ar^+-irradiated SWCNTs, one would expect the O1*s* contributions to be the same as those observed for the O_2^+ irradiated SWCNTs: equal contributions from C-O and C=O. As we have seen, from Figure 5.11, this is clearly not the case; for Ar^+ irradiated SWCNTs exposed to air, C-O and C=O are present in a ratio of 3:1.

Divacancies may be formed directly or via the coalescence of migrating monovacancies at elevated temperatures [46]. Figure 5.20 displays the direct formation and relaxation of a divacancy. As is apparent, for a reconstructed divacancy there are no dangling bonds, this is true for the lowest energy reconstructions of vacancy clusters containing an even number of missing atoms [32].

Calculations regarding the interaction of oxygen and other small molecules at the site of defects similar to the divacancy shown in Figure 5.20 have been carried out [9, 11, 16, 20, 27, 81] and yield varied results. As shown in Figure 5.20, a reconstructed divacancy contains no dangling bonds. However, such structures do contain highly strained bonds

(circled in blue in Figure 5.20) which may provide a potential site for chemisorption of oxygen. Figure 5.21 depicts a possible route for the formation of two epoxy groups by the interaction of molecular oxygen with the strained carbon-carbon bonds in a reconstructed divacancy. Such a process would explain the experimentally observed preference for the formation of C-O over C=O in Ar^+ irradiated SWCNTs. Though calculations have suggested that chemisorption does not occur at such a site, they have shown that there is an increase in the strength of the carbon-oxygen bond [20, 81]. Furthermore, interactions of oxygen in the excited (singlet) state with *pristine* SWCNTs have suggested that the dissociation of molecular oxygen and the formation of two epoxy groups is a viable process, with an energy barrier of 0.61 eV [24]. The authors of this work suggest it is possible that, 'small diameter nanotubes may be degraded by such a process after exposure to air and sunlight, in a similar way to the degradation of natural rubber and synthetic plastics' [24]. It is therefore possible that an already compromised SWCNT structure (i.e., one with an increased curvature/strain in the CNT lattice due to the inclusion of ion-induced defects) enables the chemisorption of molecular oxygen at the site of reconstructed defects. Such a process would also explain the occurrence of the small uptake in chemisorbed oxygen for SWCNTs annealed, under vacuum, to 700°C for 3 hours (Figure 5.8): such samples are unlikely to contain dangling bonds due to either the recombination of vacancies and interstitials, or the coalescence of monovacancies to form divacancies. The only remaining sites for chemisorption would be the strained bonds of reconstructed defects.

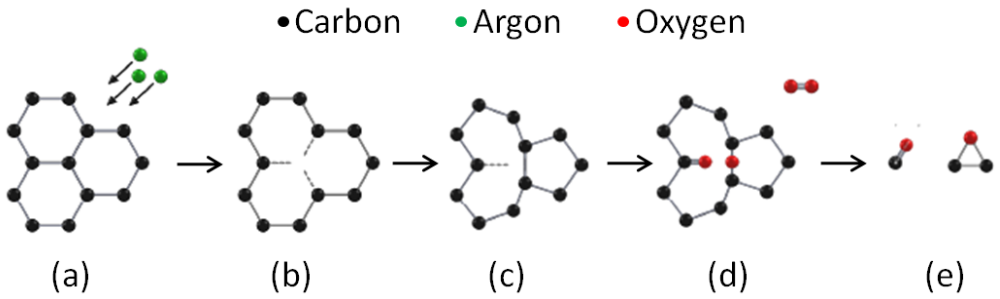

Figure 5.19

Schematic showing (a) the irradiation of a SWCNT wall by Ar^+ ions resulting in (b) the production of a monovacancy with three dangling bonds. (c) Saturation of two of the dangling bonds through the formation of a pentagon, forming the 5-1DB defect. (d) Exposure to molecular oxygen results in oxygen dissociation and (e) the formation of one carbonyl group (C=O) and one epoxy group (C-O).

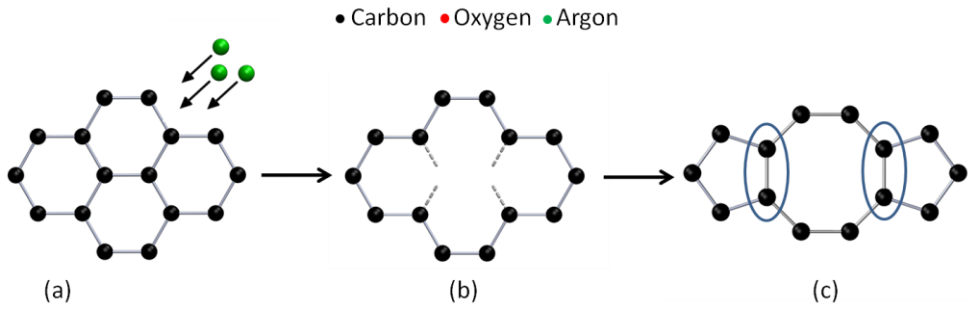

Figure 5.20

Schematic showing the irradiation of graphene by Ar ions, producing a divacancy that relaxes to form a 5-8-5 defect containing no dangling bonds.

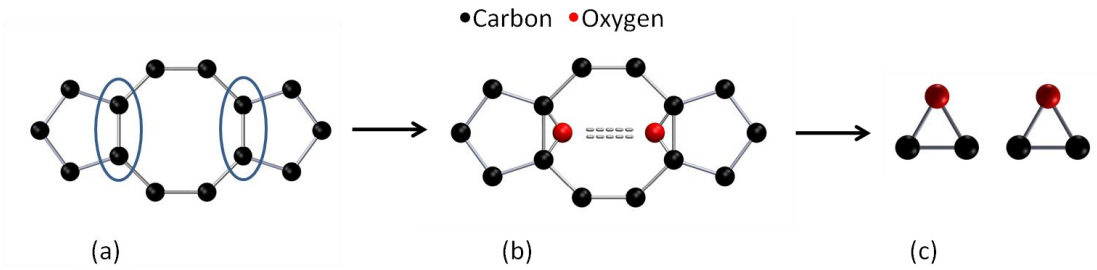

Figure 5.21

Schematic showing the interaction of a relaxed divacancy with ambient molecular oxygen.

5.4 Summary and Conclusions

Using x-ray photoemission spectroscopy, the effect of the deliberate introduction of defects in SWCNTs through both Ar^+ and O_2^+ ion irradiation has been studied, with a particular focus on how the oxygen content of these samples varies as a function of dose.

Through fitting the C1*s* peak we have identified evidence for nanotube break up under Ar^+ irradiation. We have also, using the free electron gas model, shown that the π-plasmon energy exhibits an E^2 relationship with irradiation dose Using this model we have estimated that the removal of π-electrons from the π-bonding network is ~0.17 electrons per ion. Such behaviour of the π-plasmon energy may provide a means by which the defect density of a sample can be ascertained.

We have observed prominent differences in the surface composition of 0.5 keV O_2^+ irradiated SWCNTs and 1.5 keV Ar^+ SWCNTs; namely a 1:1 ratio of C-O to C=O for O_2^+ irradiated SWCNTs and a 3:1 ratio of C-O to C=O for Ar^+ SWCNTs. Whilst the former has been attributed to the immediate saturation of dangling bonds with oxygen, the latter has been attributed to the interaction of *relaxed* defects with molecular oxygen. Furthermore, whilst the surface composition of O_2^+ irradiated SWCNTs is established after small doses (~20μC) and reaches a saturation of ~9 at.% oxygen, the surface composition of Ar^+ irradiated SWCNTs is dependent on the total dose delivered to the sample, up to the point of SWCNT break up and amorphisation. After this point the surface composition saturates at ~7 at.% oxygen.

We have therefore shown that the type of incident ion and irradiation dose delivered to the sample can be used to selectively control the level and nature of the surface composition of oxygen functionalised SWCNTs. This ability to *tune* the surface composition of SWCNTs in a relatively easy manner has exciting implications when considering CNTs for device applications.

5.5 References

1. Foroutan, M. and A.T. Nasrabadi, *Adsorption and separation of binary mixtures of noble gases on single-walled carbon nanotube bundles.* Physica E-Low-Dimensional Systems & Nanostructures. **43**(4): p. 851-856.
2. Lee, J. and N.R. Aluru, *Separation of gases from gas-water mixtures using carbon nanotubes.* Applied Physics Letters. **96**(13): p. 3.
3. Mantzalis, D., N. Asproulis, and D. Drikakis, *Filtering carbon dioxide through carbon nanotubes.* Chemical Physics Letters. **506**(1-3): p. 81-85.
4. Lu, A.J. and B.C. Pan, *Interaction of hydrogen with vacancies in a (12,0) carbon nanotube.* Physical Review B, 2005. **71**(16): p. 165416.
5. Ricca, A. and J.A. Drocco, *Interaction of O_2 with a (9,0) carbon nanotube.* Chemical Physics Letters, 2002. **362**(3-4): p. 217-223.
6. Jhi, S.-H., S.G. Louie, and M.L. Cohen, *Electronic properties of oxidized carbon nanotubes.* Physical Review Letters, 2000. **85**(8): p. 1710.
7. Dag, S., et al., *Oxygenation of carbon nanotubes: Atomic structure, energetics, and electronic structure.* Physical Review B, 2003. **67**(16): p. 10.
8. Zhu, X.Y., et al., *Adsorption and desorption of an O_2 molecule on carbon nanotubes.* Physical Review Letters, 2000. **85**(13): p. 2757-2760.
9. Andzelm, J., N. Govind, and A. Maiti, *Nanotube-based gas sensors - Role of structural defects.* Chemical Physics Letters, 2006. **421**(1-3): p. 58-62.
10. Orellana, W., *Reaction and incorporation of H_2 molecules inside single-wall carbon nanotubes through multivacancy defects.* Physical Review B, 2009. **80**(7): p. 075421.
11. Valentini, L., et al., *Role of defects on the gas sensing properties of carbon nanotubes thin films: experiment and theory.* Chemical Physics Letters, 2004. **387**(4-6): p. 356-361.
12. Collins, P.G., et al., *Extreme oxygen sensitivity of electronic properties of narbon Nanotubes.* 2000. p. 1801-1804.
13. Goldoni, A., et al., *Spectroscopic characterization of contaminants and interaction with gases in single-walled carbon nanotubes.* Carbon, 2004. **42**(10): p. 2099-2112.
14. Bermudez, V.M. and L.M. Ericson, *Infrared spectroscopic study of O_2 interaction with carbon nanotubes.* Langmuir, 2006. **22**(5): p. 2258-2263.
15. Lee, S.Y. and S.J. Park, *Effect of chemical treatments on hydrogen storage behaviors of multi-walled carbon nanotubes.* Materials Chemistry and Physics. **124**(2-3): p. 1011-1014.
16. Tsetseris, L. and S.T. Pantelides, *Adsorbate-induced defect formation and annihilation on graphene and single-walled carbon nanotubes.* Journal of Physical Chemistry B, 2009. **113**(4): p. 941-944.
17. Chandra, N. and S. Namilae, *Tensile and compressive behavior of carbon nanotubes: Effect of functionalization and topological defects.* Mechanics of Advanced Materials and Structures, 2006. **13**(2): p. 115-127.
18. Park, J.W., et al., *Effects of artificial defects on the electrical transport of single-walled carbon nanotubes.* Applied Physics Letters, 2002. **80**(1): p. 133-135.
19. Salehi-Khojin, A., K.Y. Lin, and R.I. Masel, *The role of defects on the performance of nanotube chemiresistors*, in *2010 Ieee Sensors*, Ieee: New York. p. 2620-2622.
20. Grujicic, M., G. Cao, and R. Singh, *The effect of topological defects and oxygen adsorption on the electronic transport properties of single-walled carbon-nanotubes.* Applied Surface Science, 2003. **211**(1-4): p. 166-183.
21. Nikitin, A., et al., *Hydrogenation of single-walled carbon nanotubes.* Physical Review Letters, 2005. **95**(22): p. 225507.
22. Yulong, W., et al., *Methane storage in multi-walled carbon nanotubes at the quantity of 80 g.* Materials Research Bulletin, 2008. **43**(6): p. 1431-1439.
23. Cheng, H.M., Q.H. Yang, and C. Liu, *Hydrogen storage in carbon nanotubes.* Carbon,

2001. **39**(10): p. 1447-1454.
24. Chan, S.-P., et al., *Oxidation of carbon nanotubes by singlet O_2.* Physical Review Letters, 2003. **90**(8): p. 086403.
25. Yang, D.Q., J.F. Rochette, and E. Sacher, *Controlled chemical functionalization of multiwalled carbon nanotubes by kiloelectronvolt argon ion treatment and air exposure.* Langmuir, 2005. **21**(18): p. 8539-8545.
26. Wang, C., et al., *Effects of vacancy-carboxyl pair functionalization on electronic properties of carbon nanotubes.* Applied Physics Letters, 2006. **89**(17): p. 173130-173130-3.
27. Giannozzi, P., R. Car, and G. Scoles, *Oxygen adsorption on graphite and nanotubes.* Journal of Chemical Physics, 2003. **118**(3): p. 1003-1006.
28. Ebbesen, T.W., et al., *Purification of nanotubes.* Nature, 1994. **367**(6463): p. 519-519.
29. Dean, K.A. and B.R. Chalamala, *Current saturation mechanisms in carbon nanotube field emitters.* Applied Physics Letters, 2000. **76**(3): p. 375-377.
30. Park, Y., G. Kim, and Y.H. Lee, *Adsorption and dissociation of hydrogen molecules on a Pt atom on defective carbon nanotubes.* Applied Physics Letters, 2008. **92**(8): p. 083108-083108-3.
31. Stone, A.J. and D.J. Wales, *Theoretical studies of icosahedral C_{60} and some related species.* Chemical Physics Letters, 1986. **128**(5-6): p. 501-503.
32. Kotakoski, J., A.V. Krasheninnikov, and K. Nordlund, *Energetics, structure, and long-range interaction of vacancy-type defects in carbon nanotubes: Atomistic simulations.* Physical Review B, 2006. **74**(24): p. 5.
33. Hashimoto, A., et al., *Direct evidence for atomic defects in graphene layers.* Nature, 2004. **430**(7002): p. 870-873.
34. Buongiorno, N.M., *Mechanical properties, defects and electronic behaviour of carbon nanotubes.* Carbon, 2000. **38**: p. 9.
35. Krasheninnikov, A.V., et al., *Ion-irradiation-induced welding of carbon nanotubes.* Physical Review B, 2002. **66**(24): p. 245403.
36. Pomoell, J.A.V., et al., *Ion ranges and irradiation-induced defects in multiwalled carbon nanotubes.* Journal of Applied Physics, 2004. **96**(5): p. 2864-2871.
37. Krasheninnikov, A.V. and K. Nordlund. *Irradiation effects in carbon nanotubes*. in *Symposium on Ion Beams for Nanoscale Surface Modifications held as the European-Materials-Research-Society*. 2003. Strasbourg, FRANCE: Elsevier Science Bv.
38. Barinov, A., *Defect-controlled transport properties of metallic atoms along carbon nanotube surfaces.* Physical Review Letters, 2007. **99**(4): p. 046803.
39. Fedoseeva, Y.V., et al., *High reactivity of carbon nanotubes and fluorinated carbon nanotubes irradiated by Ar^+ ions.* physica status solidi (b). **247**(11-12): p. 2691-2694.
40. Shibutani, Y. and S. Ogata, *Mechanical integrity of carbon nanotubes for bending and torsion.* Modelling and Simulation in Materials Science and Engineering, 2004. **12**(4): p. 599-610.
41. Krasheninnikov, A.V., et al., *Formation of ion-irradiation-induced atomic-scale defects on walls of carbon nanotubes.* Physical Review B, 2001. **63**(24).
42. Rodriguez-Manzo, J.A. and F. Banhart, *Creation of individual vacancies in carbon nanotubes by using an electron beam of 1Å diameter.* Nano Letters, 2009. **9**(6): p. 2285-2289.
43. Krasheninnikov, A.V. and F. Banhart, *Engineering of nanostructured carbon materials with electron or ion beams.* Nat Mater, 2007. **6**(10): p. 723-733.
44. Krasheninnikov, A.V. and K. Nordlund, *Ion and electron irradiation-induced effects in nanostructured materials.* Journal of Applied Physics, 2010. **107**(7): p. 071301-70.
45. Tolvanen, A., et al., *Modifying the electronic structure of semiconducting single-walled carbon nanotubes by Ar^+ ion irradiation.* Physical Review B, 2009. **79**(12): p. 13.
46. Krasheninnikov, A.V., et al., *Bending the rules: Contrasting vacancy energetics and migration*

in graphite and carbon nanotubes. Chemical Physics Letters, 2006. **418**(1-3): p. 132-136.
47. Krasheninnikov, A.V., K. Nordlund, and J. Keinonen, *Production of defects in supported carbon nanotubes under ion irradiation.* Physical Review B, 2002. **65**(16): p. 8.
48. Ni, B., et al., *A combined computational and experimental study of ion-beam modification of carbon nanotube bundles.* The Journal of Physical Chemistry B, 2001. **105**(51): p. 12719-12725.
49. Brzhezinskaya, M.M., E.M. Baitinger, and V.V. Shnitov, *π-plasmons in ion-irradiated multiwall carbon nanotubes.* Physica B-Condensed Matter, 2004. **348**(1-4): p. 95-100.
50. Chakraborty, A.K., et al., *A photoelectron spectroscopy study of ion-irradiation induced defects in single-wall carbon nanotubes.* Carbon, 2007. **45**(14): p. 2744-2750.
51. Banhart, F., *Irradiation effects in carbon nanostructures.* Reports on Progress in Physics, 1999. **62**(8): p. 1181-1221.
52. Estrade-Szwarckopf, H., *XPS photoemission in carbonaceous materials: A "defect" peak beside the graphitic asymmetric peak.* Carbon, 2004. **42**(8-9): p. 1713-1721.
53. Diaz, J., et al., *Separation of the sp^3 and sp^2 components in the C1s photoemission spectra of amorphous carbon films.* Physical Review B, 1996. **54**(11): p. 8064-8069.
54. Barinov, A., et al., *Initial stages of oxidation on graphitic surfaces: Photoemission study and density functional theory calculations.* The Journal of Physical Chemistry C, 2009. **113**(21): p. 9009-9013.
55. Shirley, D.A., *High-resolution x-ray photoemission spectrum of the valence bands of gold.* Physical Review B, 1972. **5**(12): p. 4709.
56. Doniach, S. and M. Sunjic, *Many-electron singularity in x-ray photoemission and x-ray line spectra from metals.* Journal of Physics Part C Solid State Physics, 1970. **3**(2): p. 285-&.
57. Giorgio, S., M. Luca, and A. Mariano, *The C1s core line in irradiated graphite*. 2007, AIP. p. 043504.
58. Gardner, S.D., et al., *Surface characterization of carbon fibers using angle-resolved XPS and ISS*. Carbon, 1995. **33**(5): p. 587-595.
59. Leftheriotis, G., et al., *Structural and electrochemical properties of opaque sol-gel deposited WO_3 layers.* Applied Surface Science, 2003. **218**(1-4): p. 276-281.
60. Ellison, M.D., et al., *Interaction of water with single-walled carbon nanotubes: Reaction and adsorption.* Journal of Physical Chemistry B, 2005. **109**(21): p. 10640-10646.
61. Nilsson, A., et al., *Orientation-dependent final-state effects in photoelectron spectra of physisorbed molecules.* Physical Review Letters, 1992. **68**(7): p. 982.
62. J. F. Ziegler, M.D.Z., J.P. Biersack *SRIM (PC version only).* (c)2007
63. Rapp, D. and Englande.P, *Total Cross Sections for Ionization and Attachment in Gases by Electron Impact .I. Positive Ionization.* Journal of Chemical Physics, 1965. **43**(5): p. 1464-&.
64. Vanzyl, B. and T.M. Stephen, *Dissociative Ionization of H-2, N2, and O2 by Electron-Impact.* Physical Review A, 1994. **50**(4): p. 3164-3173.
65. Salonen, E., A.V. Krasheninnikov, and K. Nordlund, *Ion-irradiation-induced defects in bundles of carbon nanotubes.* Nuclear Instruments and Methods in Physics Research Section B: Beam Interactions with Materials and Atoms, 2002. **193**(1-4): p. 603-608.
66. Portail, M., et al., *Study by HREELS of elementary reactions on graphite surface induced by Ar^+ and H^+ ion bombardment.* Surface Science, 2000. **454-456**: p. 384-389.
67. Klages, K.U., et al., *Deuterium bombardment of carbon and carbon layers on titanium.* Journal of Nuclear Materials, 2003. **313-316**: p. 56-61.
68. Zhu, Y., et al., *The interaction of C_{60} fullerene and carbon nanotube with Ar ion beam.* Applied Surface Science, 1999. **137**(1-4): p. 83-90.
69. Song, H.-F., J.-L. Zhu, and J.-J. Xiong, *Symmetry effect on the conductance of two-defect carbon nanotubes.* Physical Review B, 2002. **65**(8): p. 085408.
70. Larciprete, R., et al., *The electronic properties of carbon nanotubes studied by high resolution*

photoemission spectroscopy. Applied Surface Science, 2005. **248**(1-4): p. 8-13.
71. Marulanda, J.M. and A. Srivastava, *Carrier density and effective mass calculations in carbon nanotubes*. physica status solidi (b), 2008. **245**(11): p. 2558-2562.
72. Mintmire, J.W., B.I. Dunlap, and C.T. White, *Are fullerene tubules metallic?* Physical Review Letters, 1992. **68**(5): p. 631.
73. Lu, A.J. and B.C. Pan, *Nature of single vacancy in achiral carbon nanotubes*. Physical Review Letters, 2004. **92**(10): p. 105504.
74. Paredes, J.I., et al., *Atomic vacancy engineering of graphitic surfaces: Controlling the generation and harnessing the migration of the single vacancy*. Journal of Physical Chemistry C, 2009. **113**(23): p. 10249-10255.
75. Osváth, Z., et al., *STM imaging of carbon nanotube point defects*. physica status solidi (a), 2007. **204**(6): p. 1825-1829.
76. Krasheninnikov, A.V., et al., *Adsorption and migration of carbon adatoms on carbon nanotubes: Density-functional ab initio and tight-binding studies*. Physical Review B, 2004. **69**(7): p. 073402.
77. Meyer, J.C., et al., *Direct imaging of lattice atoms and topological defects in graphene membranes*. Nano Letters, 2008. **8**(11): p. 3582-3586.
78. Banhart, F., J.X. Li, and A.V. Krasheninnikov, *Carbon nanotubes under electron irradiation: Stability of the tubes and their action as pipes for atom transport*. Physical Review B, 2005. **71**(24): p. 4.
79. Krasheninnikov, A.V. and K. Nordlund, *Stability of irradiation-induced point defects on walls of carbon nanotubes*. Journal of Vacuum Science & Technology B, 2002. **20**(2): p. 728-733.
80. Lee, S.M., et al., *Defect-induced oxidation of graphite*. Physical Review Letters, 1999. **82**(1): p. 217.
81. Grujicic, M., et al., *UV-light enhanced oxidation of carbon nanotubes*. Applied Surface Science, 2003. **214**(1-4): p. 289-303.

6. Irradiation-Induced Effects in DWCNTs & MWCNTs

In this chapter, x-ray photoemission spectroscopy is used to study the effect of ion-irradiation induced defects on the reactivity of DWCNTs and MWCNTs, in particular to ambient atmosphere. The presence of two or more walls leads to significant changes in oxygen uptake in comparison with the results for SWCNTs presented in Chapter 5 and the origin of these differences is discussed.

6.1 Introduction

The types of defect created within double-walled carbon nanotubes (DWCNTs) and multiple-walled carbon nanotubes (MWCNTs) are expected to primarily consist of monovacancies and vacancy clusters, as observed for irradiated SWCNTs (discussed in Chapter 5). However, the relaxation process of vacancy defects is expected to differ, since such processes depend on CNT curvature, diameter and number of walls [1-3]. Hence the subsequent structure of these samples and their reactivity to ambient oxygen may be expected to be different for the different CNT species.

At room temperature vacancy defects in SWCNTs have been found to reconstruct to reduce the number of dangling bonds [1, 2] and vacancy clusters containing more than 6 missing atoms in armchair SWCNTs with Hamada indices (10, 10) and (5,5), will either split to form smaller vacancy clusters or lead to the degradation of nanotube structure [2]. Whilst it is suggested that they are more stable against reconstruction, dangling bonds within DWCNTs and MWCNTs may be saturated through the formation of inter-wall covalent bonds or carbon interstitial bridges [3]. However, it has been shown that it is possible to remove large clusters of atoms from a single shell in a MWCNT and that such vacancy clusters are stable at room temperature, becoming mobile at elevated temperatures [4]. Monovacancies in SWCNTs are expected to be highly mobile at temperatures above ~200°C [1]. In contrast, the smaller curvature of DWCNTs and MWCNTs is expected to lead to a reduced mobility [1] of monovacancies and suggests that single vacancies, complete with associated dangling bonds, are stable at room temperature [5]. Such defects are akin to those observed in graphene [6].

One might therefore expect that DWCNTs and MWCNTs, would have an enhanced reactivity towards ambient atmosphere and that physisorbed oxygen molecules will dissociatively chemisorb with little or no energy barrier at the strained and dangling bond sites [7] – indeed, previous studies have suggested this is the case [8, 9]. It is, however, also expected that the healing of vacancy defects through carbon interstitial-vacancy recombination is more prevalent in larger diameter CNTs. This is due to the inherent dependence of the carbon-interstitial migration barrier on CNT curvature: For SWCNTs it is expected that the high migration barrier experienced by carbon interstitials at room temperature limits the interstitial-vacancy recombination process [10]. For larger diameter

CNTs, it is expected that carbon interstitials experience a migration barrier is close to that observed on graphene (~0.4eV) [10], and so interstitial-vacancy recombination is more likely at room temperature.

Understanding differences between SWCNTs, DWCNTs and MWCNTs is of significance when concerning potential applications. In the present study we consider Ar^+ ion irradiation induced defects in DWCNTs and MWCNTs and how such defects alter the reactivity of the nanotube to ambient atmosphere. This work extends that presented in Chapter 5 and provides more detailed understanding of how vacancies and vacancy clusters behave in the different CNT species. It is shown that CNTs with more than one wall exhibit a smaller oxygen uptake when compared with SWCNTs for a given ion irradiation dose, suggesting that dangling bond saturation and defect healing, through interstitial-vacancy recombination, is more effective in the presence of multiple walls.

6.2 Experimental

The experimental apparatus is the same as that outlined in Chapter 5. The difference is that in this chapter, the samples studied include DWCNTs, *thin* MWCNTs (referred to as tMWCNTs) and *thick* MWCNT samples. The nature of these commercially sourced samples is described in detail in Chapter 4. The key attributes of each sample are as follows:

- **DWCNTs** have a highly bundled structure, much like the SWCNT samples. There is very little contamination present and that which exists is in the form of iron catalyst particles, chlorine and a few MWCNTs. From Raman spectroscopy the average diameter of the DWCNT inner wall is found to be 1.2±0.1 nm, whilst the outer wall has an average diameter of 1.6±0.2 nm.
- **tMWCNTs** consist mainly of individual CNTs, with diameters ranging from ~7 nm to ~30 nm (average diameter~15 nm). Contamination is present in the form of nickel catalyst particles, chlorine and trace amounts of other elements indicating the presence of residual material from the support used in synthesis (see Table 4.1, Chapter 4).
- **MWCNT** samples consist of isolated CNTs with diameters ranging from ~25 nm to ~90 nm (with an average of ~45 nm). Contamination is minimal, with some carbon encapsulated nickel nanoparticles being identified.

The series of experiments and the manner in which data are analysed is as reported in Chapter 5. XPS spectra were fit with 5 components for the C1*s* peak (see Table 6.1 and Figure 6.1), and 3 components in the case of the O1*s* peak (see Table 6.2 and Figure 6.2). The specific approach used in fitting spectra has been discussed in detail in Chapter 5.

For clarity the data from each of the samples have been colour-coded in this chapter: data from SWCNT samples is displayed in red (as in Chapter 5), that from DWCNTs in green; the data obtained from tMWCNTs in yellow, and MWCNT samples in blue.

Component	Binding Energy (eV)	Origin	Width (eV)
C1	284.4 ± 0.1	sp^2 hybridised carbon	various
C2	285.3 ± 0.1	sp^3 hybridised carbon	0.90± 0.05
C3	286.2 ± 0.1	C-O-C, C-O-H	1.20± 0.05
C4	287.6 ± 0.1	C=O	2.00± 0.05
C5	various	π-plasmon	various

Table 6.1

Summary of fit components for C1s spectra of irradiated CNTs. An example of a typical fit is given in Figure 6.1.

Component	Binding Energy (eV)				Origin
	SWCNTs	DWCNTs	tMWCNTs	MWCNTs	
O1	531.1 ± 0.2	531.1 ± 0.2	531.3 ± 0.2	531.1 ± 0.1	Carbonyl, C=O
O2	532.7 ± 0.2	532.8 ± 0.1	532.8 ± 0.1	532.7 ± 0.1	Epoxy/Ether, C-O
O3	535.5 ± 0.4	535.6 ± 0.1	535.5 ± 0.2	535.3 ± 0.2	Water, H_2O

Table 6.2

A summary of the fit components used to model O1s spectra of the CNT species. An example of a typical O1s fit is given in Figure 6.2.

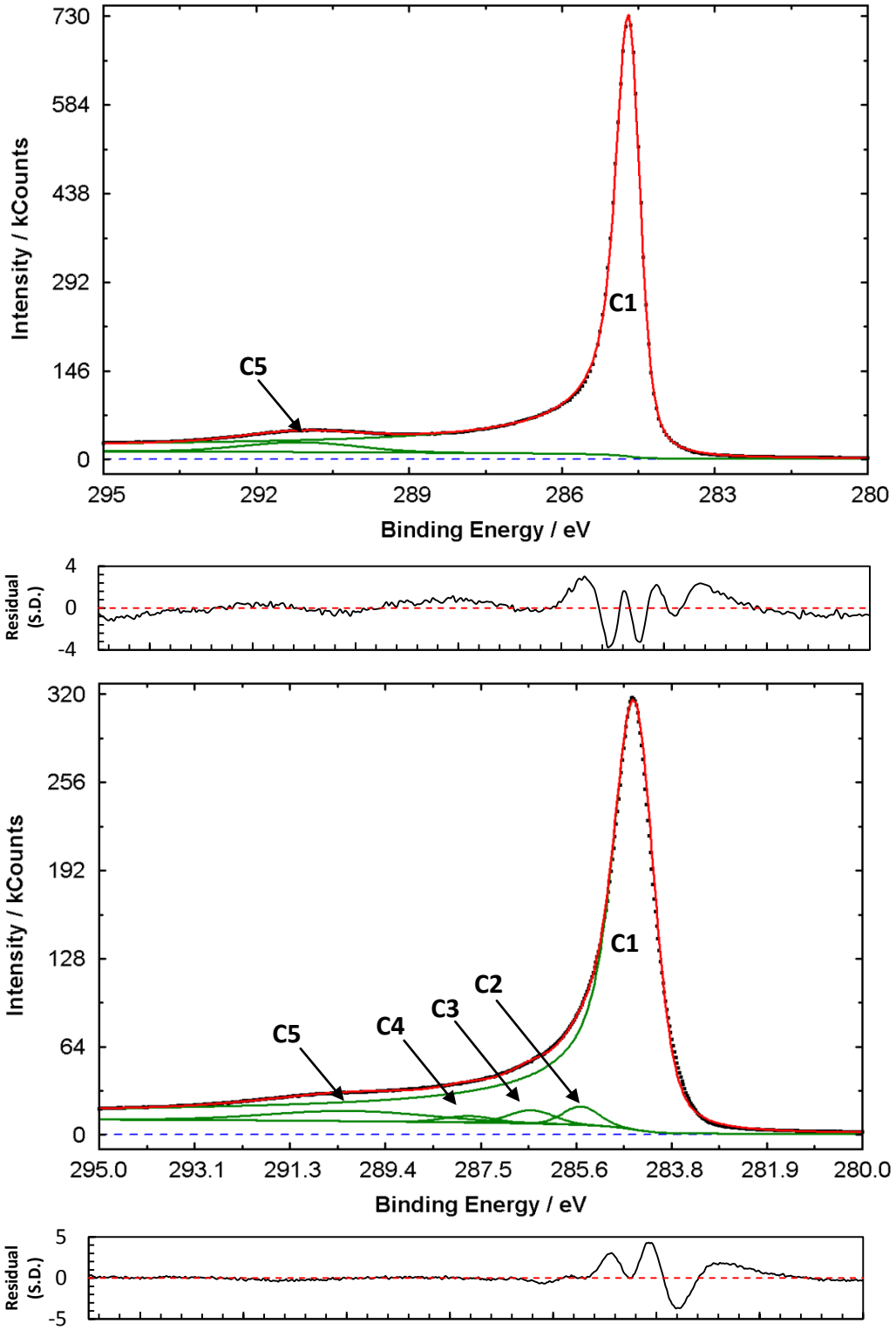

Figure 6.1

Fits to C1s spectra from (top panel) an annealed DWCNT sample and (bottom panel) a DWCNT sample irradiated with 1.5 keV Ar^+ ions to a dose of 683 μC and exposed to air. The origin of each of the components is given in Table 6.1, whilst the fit residuals are given below each spectrum.

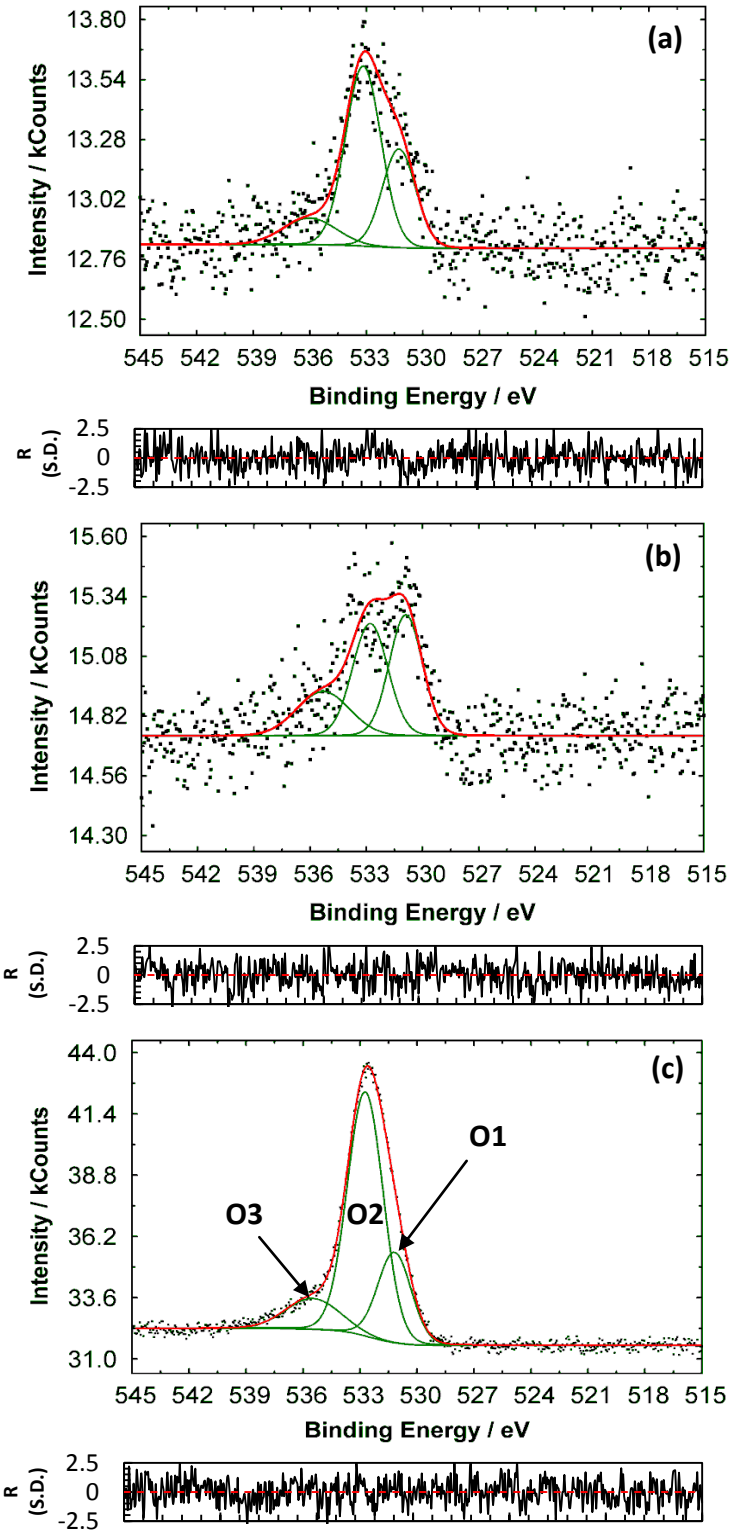

Figure 6.2

Typical O1s spectra, fits and residuals for (a) annealed and (b) irradiated MWCNTs. (c) is measured after exposing the irradiated MWCNTs to air. The key parameters of the three fit components and their origin are listed in Table 6.2.

6.3 Results and Discussion

6.3.1 Ion-Irradiation effects in DWCNTs, tMWCNTs and MWCNTs

As discussed in Chapter 5, the range of 1.5 keV Ar^+ ions in SWCNT bundles is expected to be ~6.5 nm [11], slightly less than that obtained from TRIM calculations (~10 nm). This is due to the bundled nature of the SWCNTs, which efficiently dissipates the energy of the incoming ion. In contrast, MD simulations by Pomoell *et al.* [3] show that the ranges of Ar^+ ions incident on MWCNTs along the normal to the tube axis are in good agreement with those obtained by TRIM (~10 nm), despite the anisotropic nature of the sample. The same work also revealed that as the angle of ion impact decreases (in particular, for angles below 50°), TRIM becomes increasingly inaccurate since it fails to take into account channelling in the inner space of the CNT – a process by which the ion can travel hundreds of nanometres with very little energy lost. Despite this, the penetration depths of the 1.5 keV Ar^+ ions used in this work are expected to be such that the photoemission spectra obtained are dominated by nanotubes that have been damaged by the passage of an incident ion.

Though the defects created in SWCNTs and CNTs with more than one wall are qualitatively the same (i.e., they consist of monovacancies, vacancy clusters and interstitials [12]), such defects are present in varying levels, and subsequent relaxation may include unique structures, such as inter-tube or inter-wall linkages. SWCNTs and DWCNTs are highly bundled, which allows for efficient dissipation of the energy of an incident ion. It is also expected that ion-induced damage is concentrated at the inter-tube boundaries [11] up to depths of ~6.5 nm, though this effect will be smoothed out due to the different orientations of the CNTs within the sample. It is clear that the damage to the SWCNTs and DWCNTs is due to the passage of the ion *through* the whole nanotube, with the ion coming to rest somewhere within the bundle. It is expected that such ion-sample interactions generate ~15-20 vacancies per incident ion at the incident energy (1.5 keV) used in this study [3, 12].

In tMWCNT and MWCNT films the nanotubes are not closely packed together, hence an incident ion interacts with what can be regarded as an isolated CNT. The thickness of the MWCNTs also ensures interaction with a single tube since the range of the ion is not sufficient to traverse the thickness. As a result, the damage to the sample is due to the

passage of an ion that comes to rest either between walls or within the inner channel. Since DWCNTs, tMWCNTs and MWCNTs consist of concentric walls, deformation is more difficult and the walls of these structures have an enhanced stiffness over those of SWCNTs. This means that the threshold for the creation of a vacancy is higher, and that the overall structure is expected to be more robust against the passage of an incident ion. Consequently, whereas amorphisation of SWCNTs is expected to occur at ~$1.3x10^{15}$ ions/cm^2 (~210μC.cm^{-2}) for 3 keV Ar^+ ions [9], amorphisation of MWCNTs is expected to occur at ~$4x10^{16}$ ions/cm^2 (~6400 μC.cm^{-2}) [12] for the same beam energy. Since the doses used in this investigation are far below this value, the amorphisation of the (t)MWCNT samples is not expected.

Once the threshold for vacancy creation is exceeded in DWCNTs and (t)MWCNTs the higher density of these samples means that the damage caused by the ion is greater than that caused in SWCNTs due to a higher probability of interaction of the sample with both primary ions and secondary ions created by vacancy formation. Consequently, where a single 1.5 keV Ar^+ ion is expected to produce around 15 coordination defects (number of carbon atoms with number of carbon-carbon bonds ≠3) in an isolated SWCNT, the same ion is expected to generate around 30 coordination defects in DWCNTs and around 45 coordination defects in CNTs with three walls [3].

Figure 6.3 displays the changes to the C1*s* line of DWCNT (green) and MWCNT (blue) samples with increasing ion dose (spectra from tMWCNT samples are not shown since they are qualitatively the same as those from both the DWCNT and MWCNT samples). As observed for SWCNT samples (discussed in Chapter 5), the C1*s* lineshape of the DWCNT and MWCNT samples exhibit an increased FWHM with increased irradiation dose. There is a concurrent broadening of the π plasmon loss which also shifts to lower binding energy. As discussed previously, the reasons for this broadening include the creation of disorder within the sample [13], an increased concentration of sp^3-hybridised carbon [14], and disruption of the π bonding network [15, 16].

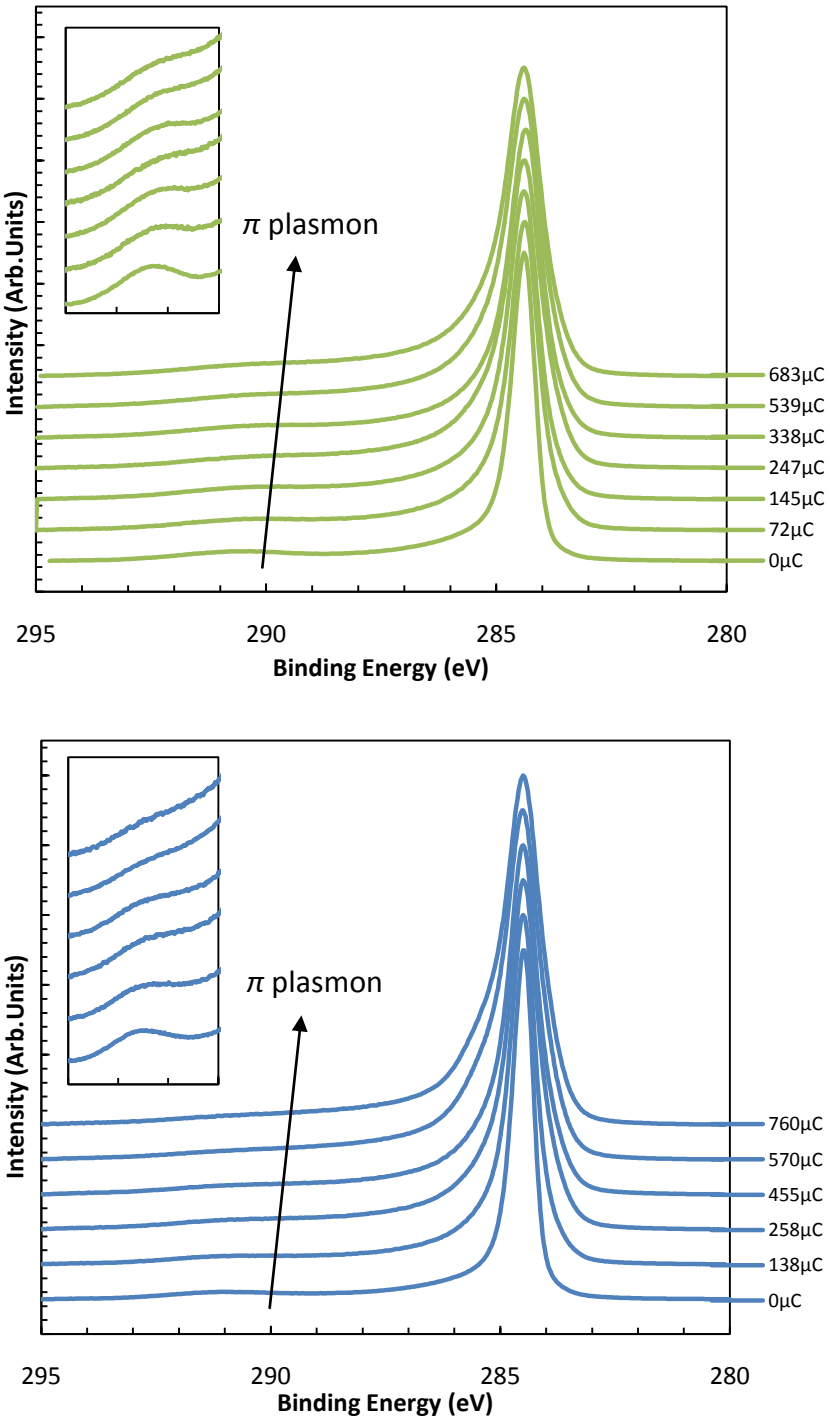

Figure 6.3

Changes to the C1s line of DWCNT (green spectra) and MWCNT (blue spectra) samples as a function of ion dose. The spectra have been normalised and shifted to the binding energy of the clean sample in each case. The detail of the π-plasmon for each spectrum is shown in the inset of each graph. The binding energy shifts for each of the sample are shown in Figure 6.4.

Decomposition of the C1*s* spectra allows changes in the lineshape to be associated with specific changes in the CNT structure. Fitting reveals that the main C1*s* component, C1,

broadens and reduces in intensity, in a similar manner to that observed for the SWCNT samples discussed in Chapter 5. In Chapter 5, we also saw that the main component of the C1*s* line of the SWCNT sample shifted to lower binding energy for doses below ~240 μC. Above this value the direction of binding energy shift reversed, becoming zero at a dose of ~520 μC. The initial change in C1*s* binding energy was attributed to the introduction of ion-induced acceptor-like states within the sample [17, 18]. The maximum negative shift occurred just before the onset of nanotube amorphisation and then returned to the original binding energy as the upper layer of the sample became completely amorphous. From this behaviour, we can predict the binding energy shifts of the C1*s* line from DWCNT and (t)MWCNT samples: We would expect that for samples with more than one wall, the return to the binding energy of the 'pristine' material will occur at higher doses (if at all) since the spread of damage over multiple walls and their relative rigidity mitigates against amorphisation.

Figure 6.4 displays the C1*s* binding energy shifts for DWCNTs, tMWCNTs and MWCNTs irradiated with 1.5 keV Ar^+ ions. It is clear that a similar behaviour exhibited by all samples, but detailed observation reveals the behaviour predicted above. It is clear that all samples exhibit an initial decrease in C1*s* binding energy with irradiation dose which is maximal at a dose of ~200 μC. However, the magnitudes of this maximum binding energy shift vary: for SWCNTs it is ~0.2 eV; for DWCNTs, ~0.15 eV, and for tMWCNTs and MWCNTs, ~0.1 eV. It is also notable that where the binding energy shift of the SWCNT sample returns to zero (~520 μC), the DWCNT, tMWCNT and MWCNT samples do not exhibit such behaviour, and show a saturation in binding energy shift. These observations can be explained relatively straightforwardly: the amorphisation threshold for nanotubes with multiple walls is expected, as described above, to be higher than that for SWCNTs. Hence it is likely that we have not reached this regime in the dose range considered in this study (the work of Zhu *et al* [17], in which MWCNT amorphisation was observed, employed substantially higher ion doses). The saturation of C1*s* binding energy shift in DWCNTs and (t)MWCNTs and the smaller value of maximum binding energy shift in comparison with SWCNTs is also easy to rationalise: nanotubes with more than one wall will have a higher DOS close to the Fermi level (E_F) – although it is still very small compared with typical metals – and a more rapid rise in DOS moving away from E_F than is found in SWCNTs. In consequence, a given level of doping (number of defects) will lead to a smaller shift in E_F in DWCNTs/(t)MWCNTs than SWCNTs giving rise to a smaller resultant shift in C1*s*

binding energy. The rapid increase in DOS in moving away from E_F in DWCNTs/(t)MWCNTs, rather like that observed in graphite [19], will result in a rapid decrease of the shift of E_F with increased doping and the apparent saturation observed. Indeed the maximum value of C1*s* shift is largest for SWCNTs, followed by DWCNTs then the MWCNT samples, as would be expected from a consideration of the DOS at E_F introduced by interlayer interaction. A similar effect is seen in *n*-doping of SWCNTs and MWCNTs by potassium doping [20] in which saturation of the doping induced C1*s* shift occurs at larger values in the SWCNTs than MWCNT samples.

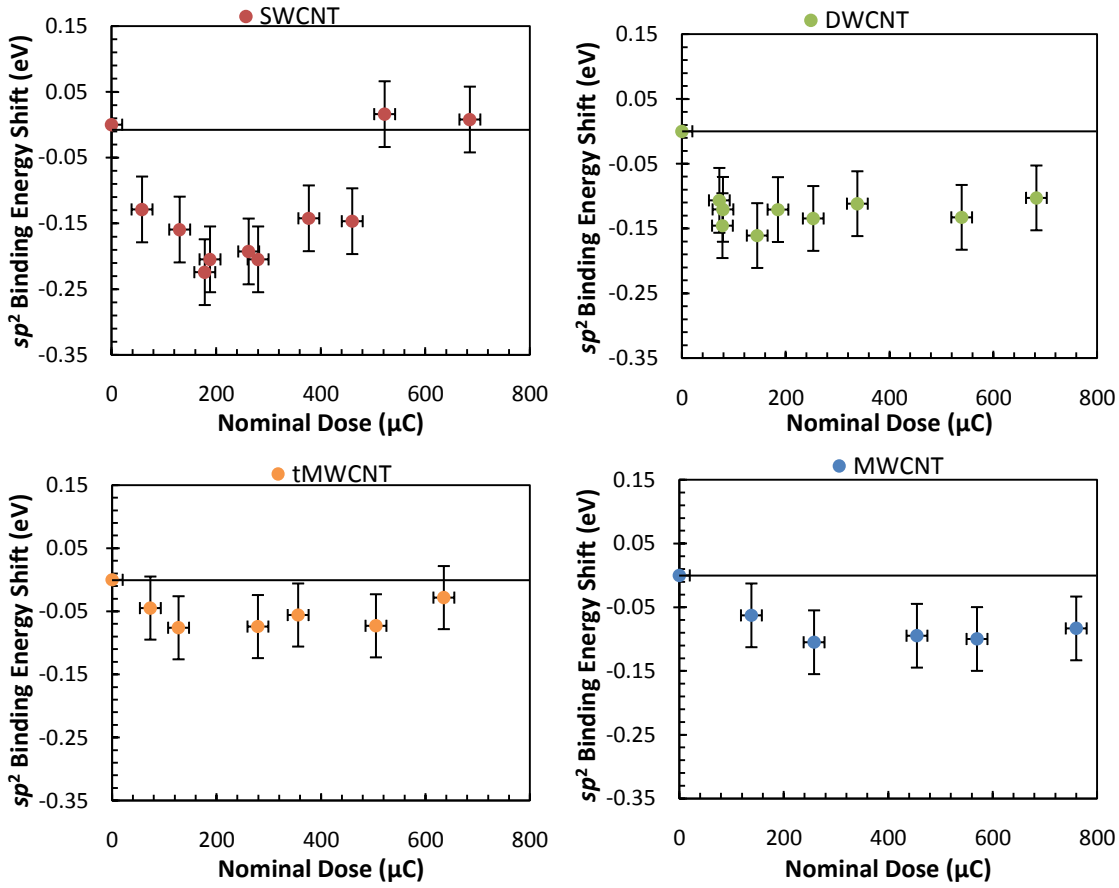

Figure 6.4

Binding energy shifts of the main C1s component, C1, as a function of ion dose. The shifts are obtained by comparing the binding energy of the irradiated sample to that of the clean sample prior to irradiation. The black lines represent zero change in binding energy, the SWCNT data is reproduced from Chapter 5.

Figure 6.3 displays the evolution of the concentration of sp^3 bound carbon with irradiation dose, and shows an increase in intensity with dose for all samples. The sp^3 bound carbon arises from the presence of carbon interstitials [12], chemisorbed species [21] and/or the formation of inter-wall links in CNTs with more than one wall [3]. These C1*s* spectra were

obtained under UHV conditions and hence the contribution from chemisorbed species is expected to be minimal and the sp^3 component is dominated by the presence of carbon interstitials and inter-wall links. In Chapter 5, we saw that the concentration of sp^3 hybridised carbon in SWCNTs initially increased linearly with irradiation, from 0 at.% to ~5.5 at.%, slowing slightly after a dose of ~320 μC. This behaviour is consistent with increased damage in the SWCNTs with increasing ion dose. Above a dose of ~320 μC the slow of the rate of increase in the concentration sp^3-bound carbon was attributed (Chapter 5, Section 5.3.1) to the onset of amorphisation. For reference, this data is reproduced in Figure 6.5 (red circles).

For DWCNTs, tMWCNTs and MWCNTs a similar increase in sp^3 content with dose is also observed, again consistent with increasing damage. The behaviour of the DWCNTs (green circles in Figure 6.5), however, shows that the sp^3 content of these samples for a given ion dose is much lower than that for the SWCNTs, with the sp^3 content increasing from 0 at.% to ~2.5 at.%, suggesting that the DWCNTs are more stable against ion irradiation. However, in contrast to this, analysis of the π plasmon position (see below) suggests that the number of π electrons 'removed' per ion in the DWCNTs is greater than in the SWCNTs, so suggesting a higher level of damage to the π bonding network. This will be discussed in further detail below.

The sp^3 content of the tMWCNT and MWCNT samples is also displayed in Figure 6.5, shown as the yellow and blue circles respectively. It is clear that the increase in sp^3 content for these samples can be reasonably described as linear with dose; there is no tail-off at higher doses. Although amorphisation of the (t)MWCNTs is not expected, the measured increase in the concentration of sp^3 bound carbon (from 0 at.% to ~5.5 at.%.) is similar to that observed for the SWCNTs. As noted previously, the number of defects caused per ion is expected to increase with the number of walls due to a higher probability of damage originating from subsequent knock-on impacts [3]. It would therefore be expected that the (t)MWCNT samples would exhibit a higher sp^3 content (associated with ion-induced coordination defects) than the SWCNT sample. A further enhancement of this difference should also arise due to the different ion ranges in the two types of sample: SWCNTs (and DWCNTs) are highly bundled into ropes and, consequently, the ion ranges in these materials are reduced due to effective dissipation of the energy of the incoming ion. The fact that similar sp^3 concentrations are observed implies that there is extensive healing of

coordination defects in CNTs with more than one wall. This is also reflected in the oxygen uptake of ion irradiated DWCNTs/(t)MWCNTs, discussed below. In the DWCNT sample, both the reduction in ion range due to bundling and the addition of an extra wall results in a measured sp^3 content that is lower than both the SWCNT and (t)MWCNT samples.

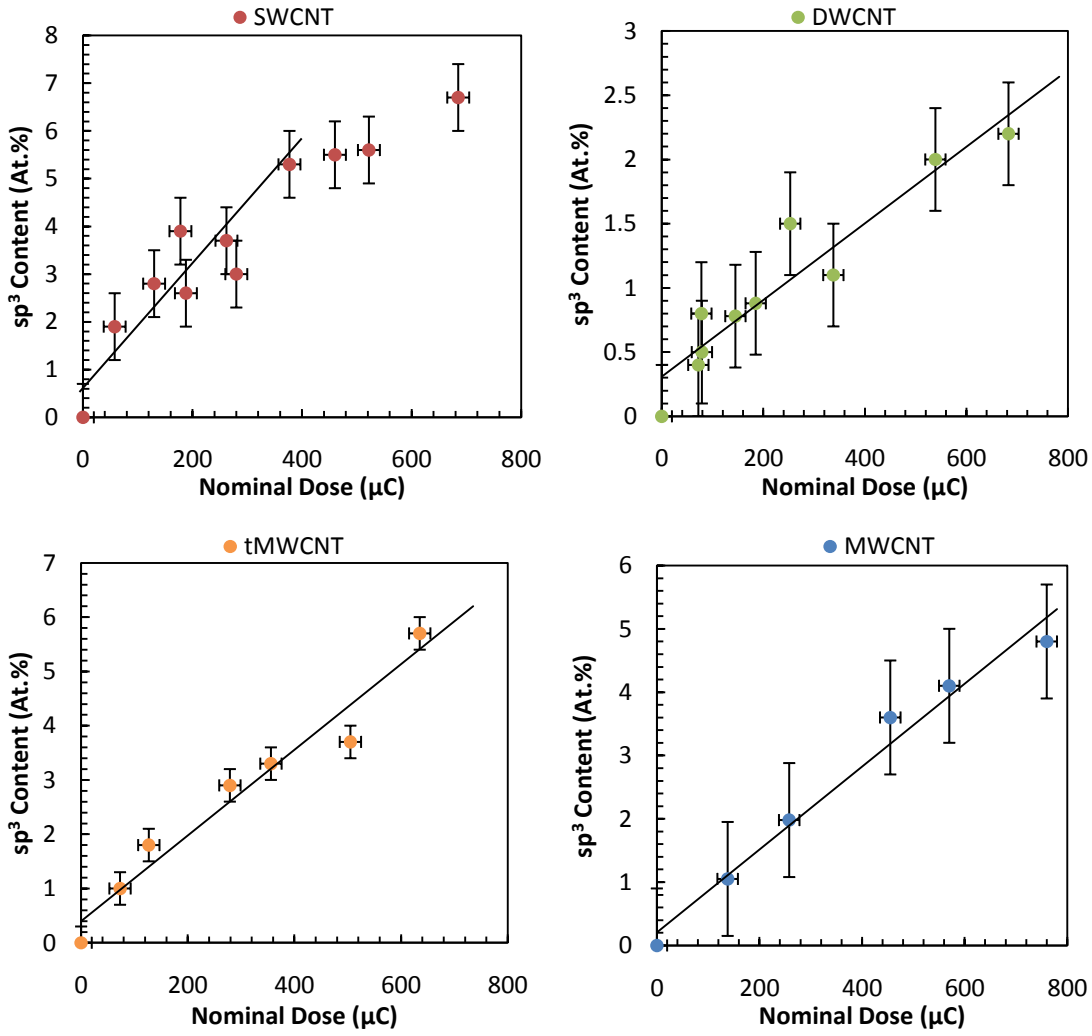

Figure 6.5

The intensity of the sp^3 component to the C1s line, C2, as a function of dose for SWCNTs (red), DWCNTs (green) and tMWCNTs (yellow) and MWCNTs (blue).

The π plasmon loss in C1*s* spectra from the DWCNT and (t)MWCNT samples broadens with increasing irradiation dose in the same manner as that of the SWCNTs and is attributed to reduced lifetime due to the increase in defect density [14, 15]. In addition to the broadening of the π plasmon, a discontinuous drop in the intensity of this feature was observed in irradiated SWCNTs at a dose of ~320 µC and associated with the onset of amorphisation. Figure 6.6 displays the π plasmon intensity for DWCNT (green), tMWCNT (yellow) and MWCNT (blue) samples as a function of dose and reproduces the SWCNT

data from Chapter 5 (shown in red). It is clear there is no discontinuity in the π plasmon intensity for samples with more than one wall, supporting the argument that the structural integrity of these samples is less affected by ion irradiation that that of the SWCNTs.

Contrary to our results, an EELS study performed by Brzhezinskaya *et al.* [15] shows an observable decrease in plasmon intensity (though this parameter is not investigated in [15]) in Ar^+ irradiated MWCNTs with irradiation dose. The doses used by Brzhezinskaya *et al.* [15] and in the work presented in this chapter are similar. Likewise, the diameter of the MWCNTs in [15] are comparable to those of the tMWCNT sample studied here. The main differences between the two studies are the ion energies (2.5 keV [15] compared to 1.5 keV here) and the diameter of the incident ion beam (1 mm [15] compared to ~1 cm). Consequently, it would be expected that the number of defects per ion in the work reported in [15] will be higher than that here. However this does not fully explain the discrepancy between the two studies.

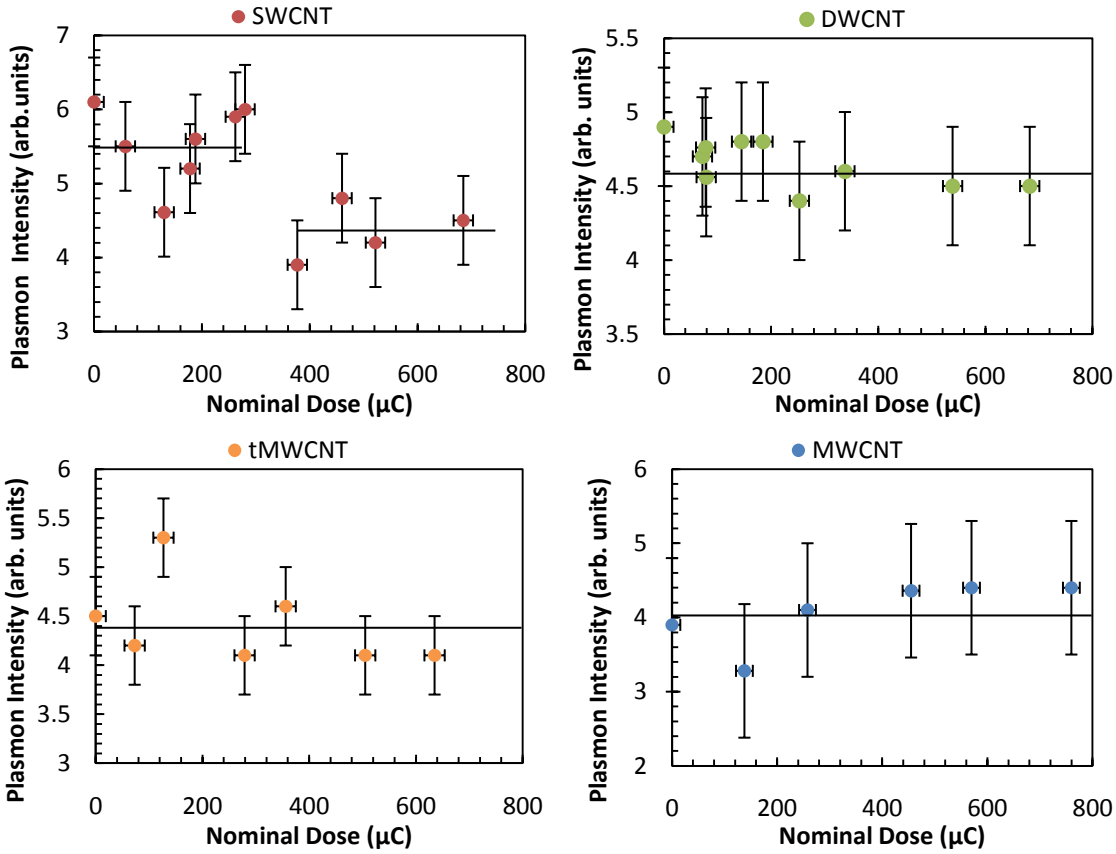

Figure 6.6

The behaviour of the π-plasmon intensity with irradiation dose. The SWCNT data (shown in red) is reproduced from Chapter 5 for comparison, in addition to the corresponding data for the DWCNT (green), tMWCNT (yellow) and MWCNT (blue) samples.

In Chapter 5 we attempted to quantify the ion induced damage in SWCNTs through the π plasmon before the onset of amorphisation by considering the π electrons as behaving as a free-electron gas and using the classical Drude expression for plasmon energy:

$$E_{\pi} = \hbar\omega_{\pi} = \hbar\sqrt{\frac{ne^2}{m_e^*\epsilon_o}}$$

Equation 6.1

That is, the π plasmon energy is linked directly to the π electron density of the CNTs. Analysis of the DWCNT and (t)MWCNT data by this approach is shown in Figure 6.7, in the form of a plot of $E_{\pi}^2/\mathbb{C}$ against ϕ ($\mathbb{C} = \hbar^2e^2/m_e^*\epsilon_o = 7.31\text{x}10^{25}$ J.m^3 and ϕ is the nominal ion dose incident upon the sample). The vertical intercept provides the π-electron density of the pristine samples and is it clear that for an increasing number of walls, the π-electron density increases (see Table 6.3). This behaviour can be attributed to a decrease in wall curvature with increasing wall number/diameter which reduces curvature-induced rehybridisation. Linear fits are made to all data (including the SWCNT data presented in Chapter 5) for doses up to ~350 μC, i.e. over a range of dose for which it can be safely assumed that all samples remain intact (see discussion of C1s position above) and allow an estimation of the number of π electrons lost from the system per ion. These results are summarised in Table 6.3 and clearly show that the number of π electrons lost per ion from CNTs with more than one wall is greater than that lost from the SWCNTs. This is not inconsistent with the observed sp^3 content in each of these samples (Figure 6.5) since defect healing processes at room temperature may not lead to a complete recovery of π conjugation in the nanotube (e.g. due to topological defects etc.). However, this suggested higher level of π bonding damage does not necessarily translate into a higher reactivity to ambient atmospheric oxygen, as we shall see later in this chapter. This suggests that there is a difference between the number of reactive defect sites and those that give rise to a decrease in π conjugation.

CNT Species	SWCNT	DWCNT	tMWCNT	MWCNT
π plasmon Energy (eV)	6.19 ± 0.03	6.40 ± 0.05	6.50 ± 0.08	6.63 ± 0.02
π electron density (cm^{-3})	2.74x10^{21}	2.99x10^{21}	3.09x10^{21}	3.21x10^{21}
π electron removal (ion^{-1})	0.17±0.05	0.29±0.04	0.38±0.09	0.24±0.05

Table 6.3

The π-plasmon energies for each of the different CNT species. The increase in plasmon energy with number of walls can be linked to the electron density of the CNT sample through Equation 6.1.

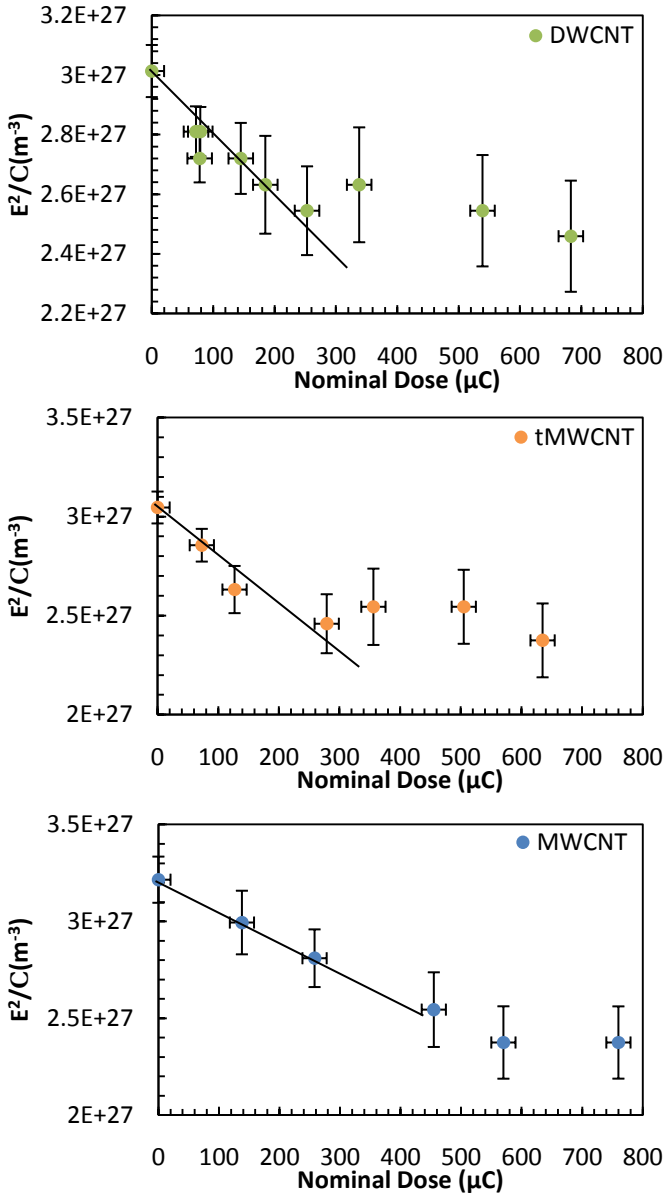

Figure 6.7

The linear relationship between, E_π^2 and irradiation dose for DWCNTs (green), tMWCNTs (yellow) and MWCNTs (blue). The black lines indicate the lies of best fit to data corresponding to doses below 400 μC

6.3.2 Oxygen Uptake in Ar^+ Irradiated DWCNTs, tMWCNTs and MWCNTs

Figure 6.8 displays the effect of exposing a clean (0 μC) DWCNT sample (light blue spectrum) to atmosphere for 70 minutes (purple spectrum). As in the SWCNT case, it is clear that there is no observable change in the C1*s* spectrum upon air exposure, whilst there is a small observed increase in O1*s* intensity (shown in the inset of Figure 6.8), indicative of an uptake of oxygen containing species upon air exposure (however, this increase is not as

pronounced as that observed for SWCNTs). The same result is also found for tMWCNT and MWCNT samples, data for which are not shown here for sake of brevity. In the SWCNT case, the uptake in such oxygen species was attributed to a small amount of chemisorbed species at the site of defects still present after annealing.

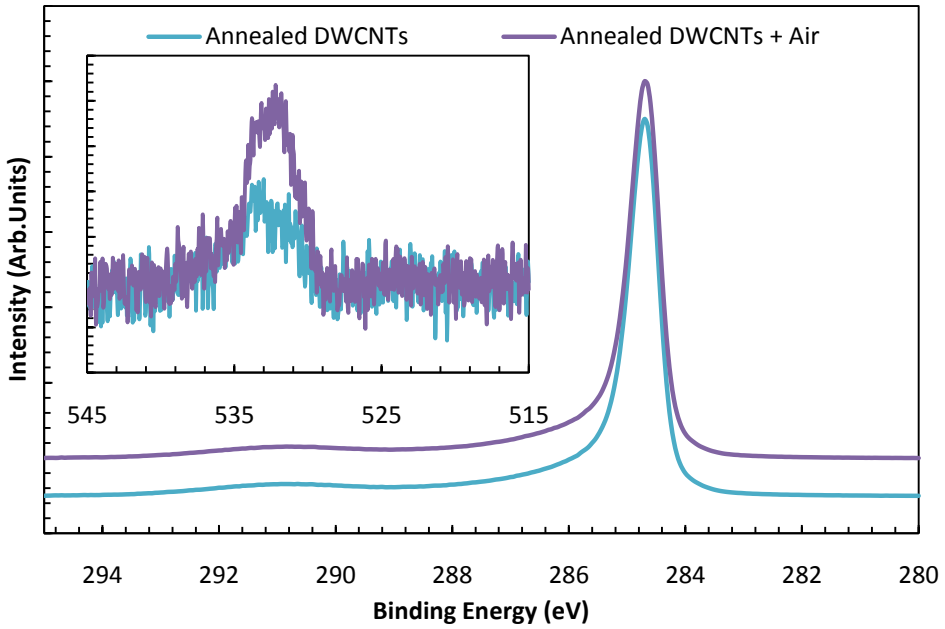

Figure 6.8

C1s lineshape for a clean DWCNT sample (light blue curve) and the same sample exposed to air (purple curve). The spectrum for the air exposed sample has been displaced vertically for comparison.
The inset shows the associated change in the O1s spectra for a clean sample (light blue curve) and the same sample exposed to air (purple curve).

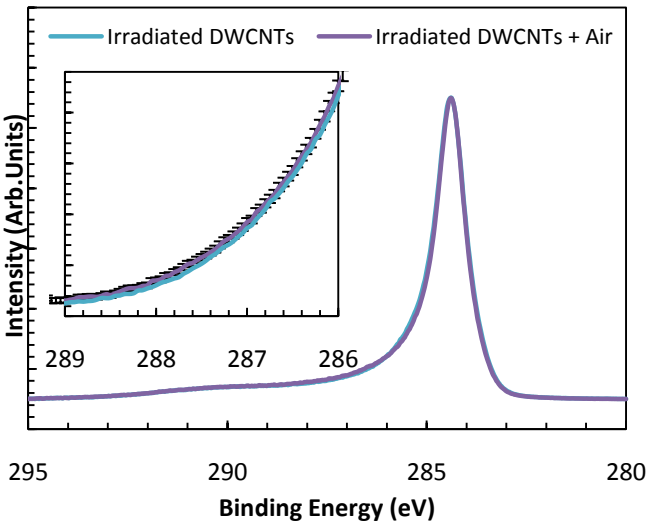

Figure 6.9

C1s line from irradiated DWCNTs held under vacuum (light blue curve) and for the same sample after air exposure (purple curve). There is a small increase in the intensity between 286 eV and 289 eV (shown in the inset), but this is within the limit of Poissonian noise.

Figure 6.9 displays the result of exposing an irradiated DWCNT sample (light blue curve) to air for 70 minutes (purple curve) on the C1*s* line. There is an enhanced intensity in the binding energy region between 286 eV and 289 eV (the binding energy region dominated by oxidised carbon, see Table 6.2), the same as seen with the SWCNT samples. However, the enhancement in intensity in this region is not as pronounced as that found for the SWCNT samples (Chapter 5, Section 5.3.2) and, indeed, is within experimental error. The same result is observed for the tMWCNT and MWCNT samples which are, again, not shown for sake of brevity. The difference in the concentration of chemisorbed oxygen containing species between the SWCNTs and CNTs with more than one wall is more clearly observed in Figure 6.10, and is discussed below.

Figure 6.10 displays how the total oxygen content of each of the samples varies with ion dose and air exposure. It is clear from Figure 6.10 that, whilst there is minimal uptake of oxygen for irradiated samples held under vacuum (bottom panel), there is an increase in the total oxygen content of all CNT samples with increasing irradiation dose (top panel). The behaviour of the SWCNTs was discussed in Chapter 5 (the data is reproduced in Figure 6.10 for reference). In particular, it was noted that the total oxygen content of the sample increased linearly with dose up to ~ 200 μC, after which point a plateau was reached at ~7 at.%. This behaviour was attributed ion-induced defects in the samples that enhance oxygen uptake until the onset of amorphisation. For the DWCNT and (t)MWCNT samples, there is a linear increase in the total oxygen content with irradiation dose and no obvious plateau is present. This is consistent with the previous arguments regarding the smaller dose required for the onset of amorphisation in SWCNTs. Differences between the SWCNT and the DWCNT and (t)MWCNT samples also arises in the content of these samples: In general, the SWCNT samples contain approximately twice as much oxygen as the DWCNT and (t)MWCNT samples for a given irradiation dose.

Figure 6.11 displays the C-O, C=O (top panels) and water (bottom panel) contributions to the O1*s* peak of the DWCNT and (t)MWCNT samples after Ar^+ irradiation. Unlike the C-O content of the SWCNT sample which reaches a plateau at ~4.5 at.% at the onset of amorphisation, the C-O content of the DWCNT and (t)MWCNT samples increases linearly with dose without reaching a plateau. Throughout the doses investigated here, the C-O content of the DWCNT and (t)MWCNT samples is consistently less than that of the SWCNT samples. In Chapter 5, the C=O content of the SWCNT samples was found to

show a small linear increase and plateau at ~1.5 at.% at the onset of amorphisation. From Figure 6.11 it is clear that there is a similar increase in the C-O content of the DWCNT and (t)MWCNT samples with irradiation dose though, once again, the amount of C=O present on the surface of these samples is, in general, less than that observed for SWCNTs. Like the observations made for the SWCNT samples in Chapter 5, the contributions to the O1*s* peak due to water exhibits a slight increase with irradiation dose, though this increase is within the experimental error.

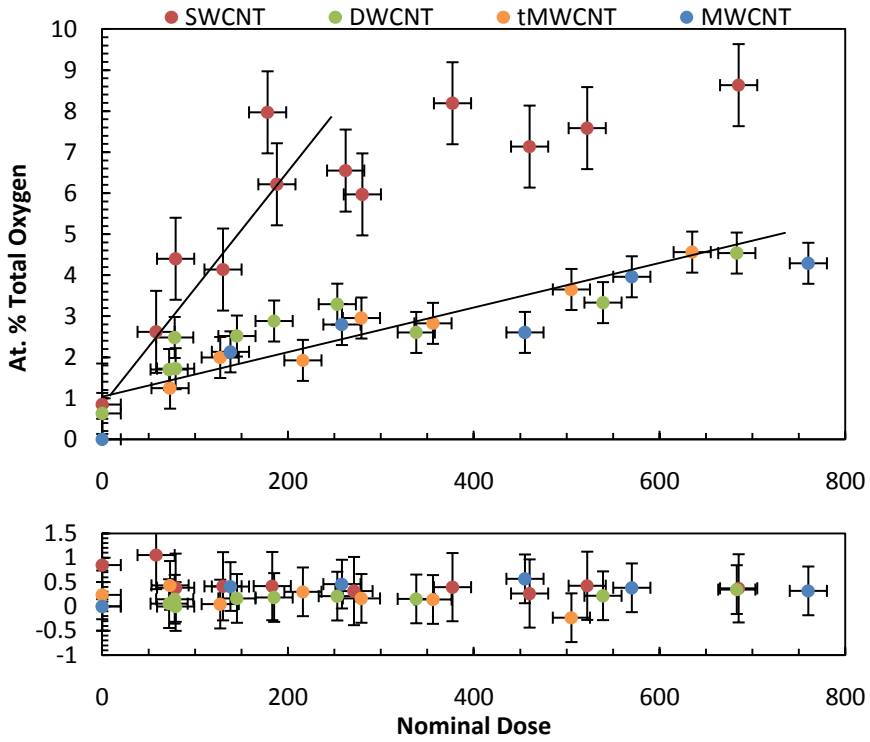

Figure 6.10

The top panel displays total oxygen content (extracted from the O1s peak) for air-exposed 1.5 keV Ar ion irradiated SWCNTs (red), DWCNTs (green), tMWCNTs (yellow) and MWCNTs (blue) as a function of dose, whilst the bottom panel displays the total oxygen content of the irradiated samples held under vacuum. From this data it is clear that SWCNTs exhibit an enhanced uptake of oxygen over the other samples, which behave similarly.

In Chapter 5, the observation was made that for air exposed Ar^+ irradiated SWCNTs, the O1*s* contributions due to C-O and C=O were present in the ratio 3:1. For DWCNT and (t)MWCNT samples, here we see that this ratio may still hold. However, due to the small quantities of C=O measured and the errors associated with them, it is not possible to give a firm conclusion. However, what is clear from these results is that CNTs with more than one wall behave very similarly upon Ar^+ irradiation and subsequent air exposure in terms of

level of oxygen uptake and the nature of the chemisorbed oxygen species. Furthermore, we note that the behaviour of CNTs with more than one wall is similar to that of the SWCNTs observed in Chapter 5, with main differences arising in the level of total oxygen uptake and the fact that CNTs with even just one more wall are more robust against ion irradiation.

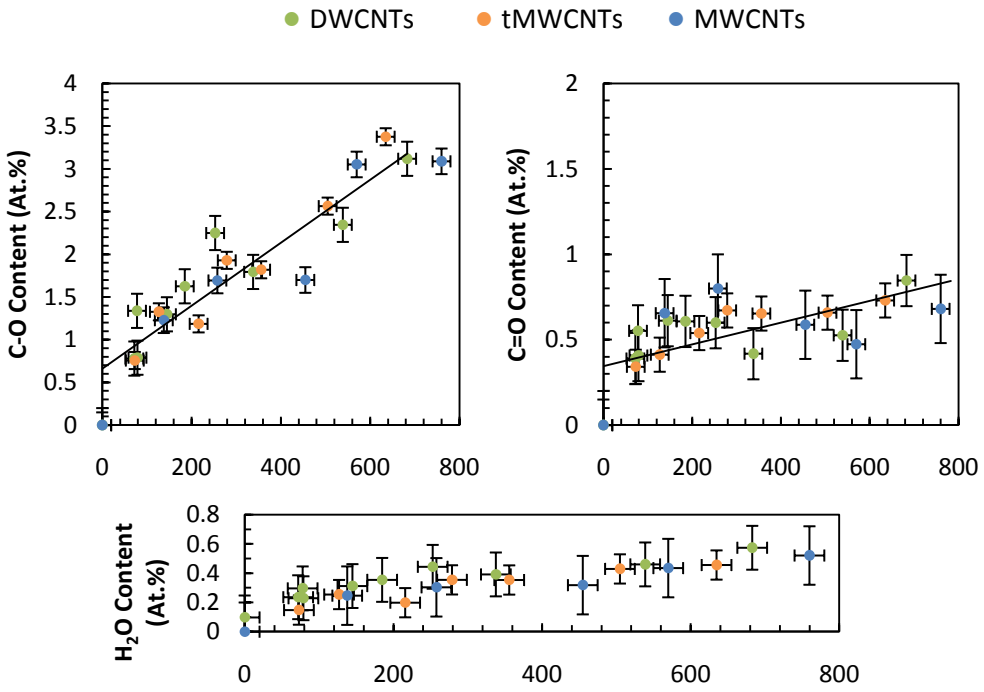

Figure 6.11

Top panels: The chemical state of oxygen in air-exposed irradiated CNTs determined from fitting the O1s core line. The black lines are a guide to the eye. The bottom panel represents the contribution due to water.

6.3.3 The Role of Defects in Oxygen Uptake

As discussed previously, the types of defects generated within ion-irradiated CNTs with more than one wall are expected include monovacancies, vacancy clusters, carbon interstitials and inter-wall linkages. In SWCNTs these defects reconstruct in order to reduce the number of dangling bonds present, whilst in CNTs with more than one wall, defects containing dangling bonds are expected to be more stable and consequently reconstruction is inhibited. From this, one might therefore expect that DWCNTs and (t)MWCNTs, with their ability to support structures containing dangling bonds and a larger number of defects produced per incident ion, would display a larger oxygen uptake upon

air exposure. However, the data presented in this chapter clearly show that the content of chemisorbed oxygen is, in fact, larger for SWCNTs.

From the analysis of the π plasmon of each of the CNT species, it is found that the number of π electrons lost (i.e., the amount of damage done to the π bonding network) per incident ion increases with the number of walls, as expected [3]. However, it was seen that this increased damage to the π bonding network does not directly translate to an increased level of sp^3 hybridised carbon within the samples, nor does it imply that the reactivity of these CNT species to ambient atmospheric oxygen will be enhanced. There are three potential explanations for this behaviour: (1) defects formed during irradiation are able to heal themselves on the timescales of this experiment (approximately 60 minutes between Ar^+ ion irradiation and air exposure), possibly through either inter-wall links or the recombination of carbon interstitials with vacancies. Such healing of defects would therefore reduce the number of 'active' sites for the chemisorption of ambient oxygen. Furthermore, the healing of defects through vacancy/interstitial recombination would lead to the observed suppression of the sp^3 hybridised carbon content; (2) in the presence of more than one wall, inter-wall interactions such as the formation of inter-wall links and the trapping of interstitials between walls could also reduce the number of available bonding sites for the chemisorption of oxygen; (3) in SWCNTs all atoms are at the surface of the material whilst even in a DWCNT the inner wall is no longer at the surface and can be shielded from oxygen adsorption when damaged by the outer. Protection of inner walls in this way is a rather interesting prospect as one could use irradiation induced defects to controllably alter the properties of the inner walls of a multi-wall nanotube without the concern that they may not be stable under exposure to the environment.

The photoemission signature of the different types of defects in SWCNTs was discussed in Chapter 5 and it was shown that the enhancement of C-O over C=O content in Ar^+ irradiated CNT material exposed to air is indicative of the interaction of oxygen containing species with reconstructed defects. From the data presented in this chapter, it is clear that the same process is taking place in the DWCNTs and (t)MWCNTs and with SWCNTs thus implying that curvature effects [1] do not dominate the relaxation processes and that reconstruction of defects can occur in samples with more than one wall, although the mechanisms may not be the same.

6.1 Summary and Conclusions

X-ray photoelectron spectroscopy has been used to investigate Ar^+ irradiation induced defects in DWCNTs, tMWCNTs and MWCNTs. The influence of defects on the doping induced binding energy shifts in the C1*s* line has been studied and it has been shown that an increased number of walls (and hence DOS close to E_F) decreases the impact of doping on Fermi level position. Whilst clear signatures of amorphisation could be observed in SWCNTs at the doses employed in this thesis (Chapter 5), no such behaviour was observed in nanotubes with more than one wall, which can be attributed to higher damage thresholds, increased rigidity of the nanotube walls and enhanced opportunities for defect 'healing' through inter-wall links and by trapping interstitials between walls (which can, for example, aid vacancy – interstitial recombination). Hence, the presence of even a second wall can substantially enhance the resistance of carbon nanotubes to radiation-induced damage.

Through fitting of O1*s* photoemission line it has been found that in chemisorption of oxygen is significantly smaller in DWCNTs and (t)MWCNTs for a given ion dose. This behaviour is in contradiction to some theoretical studies [5] which indicate that DWCNTs and (t)MWCNTs, with their ability to support structures containing dangling bonds, should be more reactive to molecular oxygen. We suggest that extra routes for defect reconstruction, healing and/or the protection of inner walls by outer walls can explain the smaller oxygen uptake and suggests that defect-induced chemisorption primarily occurs at the outermost nanotube wall.

6.2 References

1. Krasheninnikov, A.V., et al., *Bending the rules: Contrasting vacancy energetics and migration in graphite and carbon nanotubes.* Chemical Physics Letters, 2006. **418**(1-3): p. 132-136.
2. Kotakoski, J., A.V. Krasheninnikov, and K. Nordlund, *Energetics, structure, and long-range interaction of vacancy-type defects in carbon nanotubes: Atomistic simulations.* Physical Review B, 2006. **74**(24): p. 5.
3. Pomoell, J.A.V., et al., *Ion ranges and irradiation-induced defects in multiwalled carbon nanotubes.* Journal of Applied Physics, 2004. **96**(5): p. 2864-2871.
4. Huang, J.Y., F. Ding, and B.I. Yakobson, *Vacancy-hole and vacancy-tube migration in multiwall carbon nanotubes.* Physical Review B, 2008. **78**(15): p. 5.
5. Rodriguez-Manzo, J.A. and F. Banhart, *Creation of individual vacancies in carbon nanotubes by using an electron beam of 1Å diameter.* Nano Letters, 2009. **9**(6): p. 2285-2289.
6. Hashimoto, A., et al., *Direct evidence for atomic defects in graphene layers.* Nature, 2004. **430**(7002): p. 870-873.
7. Zhu, X.Y., et al., *Adsorption and desorption of an O_2 molecule on carbon nanotubes.* Physical Review Letters, 2000. **85**(13): p. 2757-2760.
8. Yang, D.Q., J.F. Rochette, and E. Sacher, *Controlled chemical functionalization of multiwalled carbon nanotubes by kiloelectronvolt argon ion treatment and air exposure.* Langmuir, 2005. **21**(18): p. 8539-8545.
9. Chakraborty, A.K., et al., *A photoelectron spectroscopy study of ion-irradiation induced defects in single-wall carbon nanotubes.* Carbon, 2007. **45**(14): p. 2744-2750.
10. Krasheninnikov, A.V., et al., *Adsorption and migration of carbon adatoms on carbon nanotubes: Density-functional ab initio and tight-binding studies.* Physical Review B, 2004. **69**(7): p. 073402.
11. Salonen, E., A.V. Krasheninnikov, and K. Nordlund, *Ion-irradiation-induced defects in bundles of carbon nanotubes.* Nuclear Instruments and Methods in Physics Research Section B: Beam Interactions with Materials and Atoms, 2002. **193**(1-4): p. 603-608.
12. Krasheninnikov, A.V. and K. Nordlund. *Irradiation effects in carbon nanotubes*. in *Symposium on Ion Beams for Nanoscale Surface Modifications held as the European-Materials-Research-Society*. 2003. Strasbourg, FRANCE: Elsevier Science Bv.
13. Barinov, A., et al., *Initial stages of oxidation on graphitic surfaces: Photoemission study and density functional theory calculations.* The Journal of Physical Chemistry C, 2009. **113**(21): p. 9009-9013.
14. Diaz, J., et al., *Separation of the sp^3 and sp^2 components in the C1s photoemission spectra of amorphous carbon films.* Physical Review B, 1996. **54**(11): p. 8064-8069.
15. Brzhezinskaya, M.M., E.M. Baitinger, and V.V. Shnitov, *π-plasmons in ion-irradiated multiwall carbon nanotubes.* Physica B-Condensed Matter, 2004. **348**(1-4): p. 95-100.
16. Portail, M., et al., *Study by HREELS of elementary reactions on graphite surface induced by Ar^+ and H^+ ion bombardment.* Surface Science, 2000. **454-456**: p. 384-389.
17. Zhu, Y., et al., *The interaction of C_{60} fullerene and carbon nanotube with Ar ion beam.* Applied Surface Science, 1999. **137**(1-4): p. 83-90.
18. Song, H.-F., J.-L. Zhu, and J.-J. Xiong, *Symmetry effect on the conductance of two-defect carbon nanotubes.* Physical Review B, 2002. **65**(8): p. 085408.
19. Zunger, A., *Self-Consistent LCAO Calculation of Electronic Properties of Graphite .1. Regular Graphite Lattice.* Physical Review B, 1978. **17**(2): p. 626-641.
20. Hunt, M.R.C. 2011.
21. Nikitin, A., et al., *Hydrogenation of single-walled carbon nanotubes.* Physical Review Letters, 2005. **95**(22): p. 225507.

7. Adsorption of C_{60} on HOPG(0001) & Ni(110)

In this chapter, STM, UPS, XPS and LEED are used in conjunction with computer simulation and modelling to investigate the growth mechanisms of C_{60} films on HOPG(0001) and Ni(110).

7.1 Introduction

The structural, chemical and electrical properties of fullerenes [1] have led to these molecules being regarded as promising candidates for nanoscale technologies [2-4], many of which [5-7] require a detailed understanding of their interaction with surfaces and the growth of ultra-thin films. Of particular interest is the growth of ultra-thin films of C_{60} on solid surfaces, in which substrate-adsorbate bonding (and thus the physical properties of the overlayer) is strongly dependent on the substrate [8-18].

On surfaces such as graphite, the bonding between the adsorbed C_{60} and the substrate is through weak van der Waals forces. This leaves the C_{60} highly mobile on the surface at room temperature [19] and growth of overlayers occurs in the form of a close-packed film [9, 20], with the intermolecular bond being close to that found in bulk C_{60} (1.004 nm). Scanned probe microscopy studies of the initial growth of C_{60} films on graphite at room temperature have indicated both bilayer growth [19] in agreement with theory [20], and monolayer growth [9, 21]. The growth of subsequent layers has also shown a variety of morphologies from dendritic [9] to close packed, highly facetted islands [9, 11]. It has been suggested [9] that these differences can be explained by the high sensitivity of the growth mode to sample cleanliness.

On surfaces such as Al [14], the bonding between C_{60} and the substrate is enhanced compared to that on graphite and films take on one of three overlayer phases depending on the substrate temperature. Even stronger substrate-adsorbate bonding is found for C_{60} on surfaces such as Si [11, 22], Pt [15, 23, 24], Ag [13] Au[13, 16, 25], Mo [18] and Cu [26, 27], with the bonding taking on a predominantly covalent [11, 14, 18, 22] or an ionic [13, 16, 26, 27] character. Such strong adsorbate interaction gives rise to the formation of a number of different overlayer structures, some of which involve a reconstruction of the surface of the substrate [22, 25, 26, 28, 29]. The growth of C_{60} thin films on Ni(110) is a strong-bonding system which has attracted significant interest [13, 15, 17, 23, 26]. Such studies have given insight into the interaction between the adsorbate and the substrate, with early studies suggesting a charge transfer of 2 ± 1 electrons from the substrate to each molecule [13]. More recent work on this system [17, 23, 26] indicates that a simple charge transfer mechanism is unable to fully describe the substrate-adsorbate interaction and that there is a significant covalent component in which hybridisation of the substrate and overlayer states

plays an important rôle. The resultant strong adsorbate-substrate interaction is expected to fix the orientation (and therefore coordination) of the C_{60} molecules [13].

Ordered monolayers (ML) of C_{60} on Ni(110) can be formed through evaporation onto substrates held at > 350°C [15], or by annealing a film previously deposited at room temperature (RT). The resulting layers may adopt one of several structures depending on the coverage and the substrate temperature used during deposition or post-deposition annealing. For a substrate temperature of ~350°C-390°C monolayers may adopt one of several structures: Initial growth of a (5x3) phase up to a coverage of ~ 0.8 *physical* monolayers (area coverage of the surface by C_{60} molecules) [13, 23, 26], the formation of a partly commensurate quasi-hexagonal (QH1) phase [13, 15, 26] for coverages above this and, for higher substrate temperatures (~390°C-450°C), a QH2 phase which comprises of domains rotated by 30° to one another [13]. C_{60} monolayers deposited on Ni(110) substrates held below ~350°C are disordered.

In this chapter, particular interest is paid to growth of C_{60} on HOPG and Ni(110) under UHV conditions at both room temperature and elevated temperatures. Analysis is carried out using a combination of STM, LEED, UPS, XPS and computer modelling.

7.2 Experimental

7.2.1 C_{60} on HOPG (0001)

The experiments on the C_{60}-HOPG(0001) system were performed using the Omicron UHV-SPM at Durham University described in Chapter 3, Section 3.2.2. A highly oriented pyrolytic graphite (HOPG) surface of (0001) orientation was prepared by the methods outlined in Chapter 3, Section 3.1.2 and C_{60} films were produced through the sublimation of C_{60} powder from a tantalum cell. Coverages were determined from the analysis of large area images. STM tips were mechanically cut from Pt-Ir wire and used in constant current mode. Such tips were found to have effective tip radii of ~2 nm and were able to resolve atomic scale features on graphite (see Figure 7.1). Unless otherwise stated the images were acquired at room temperature.

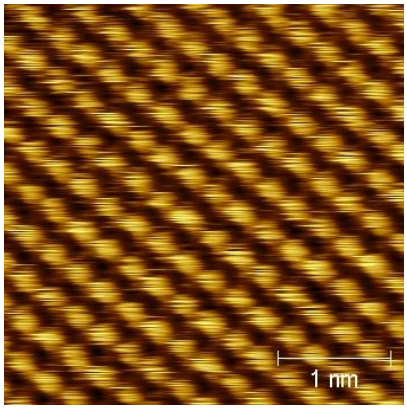

Figure 7.1

Atomic resolution STM image of the clean HOPG(0001) substrate used in this study.

The computer modelling reported in this work used a seed-induced, Monte-Carlo simulation. The adsorbate particles are located on a planar lattice with periodic boundary conditions and follow a random walk in any of 6 directions (oriented at 30°, representing high symmetry directions on the surface) within the lattice. The motion of the adsorbates is modelled by an Arrhenius-type probability which depends on the activation energy needed to transfer a molecule from one location to another, E_a, the temperature of the system, T, and the change in the coordination of the molecule, Δ, (which ensures that it is more favourable to increase the number of nearest neighbours than decrease them):

$$P_{move} = exp\left(\frac{E_a \Delta}{k_B T}\right) = exp\left(\frac{C}{T}\right)$$

Equation 7.1

After testing a range of system sizes and finding that the number of free particles is independent of array size (to within error), it was decided that all simulations would be carried out on arrays of 800 x 800 elements using 5000 particles as a best compromise between required computational time and effects due to particle saturation. Periodic boundary conditions were applied to avoid edge effects and a reduction in the total number of particles through diffusion out of the system: a particle moving out of one side of the simulation cell instantly moves back through the opposite side of the cell with the same position and trajectory.

Island growth is found to centre on a central fixed defect which is placed on the lattice at the start of the simulation. Once part of an island, a molecule may undergo temperature dependent diffusion within, to and from the island. A copy of the simulation program is given in Appendix A, whilst example data are shown in Figure 7.2.

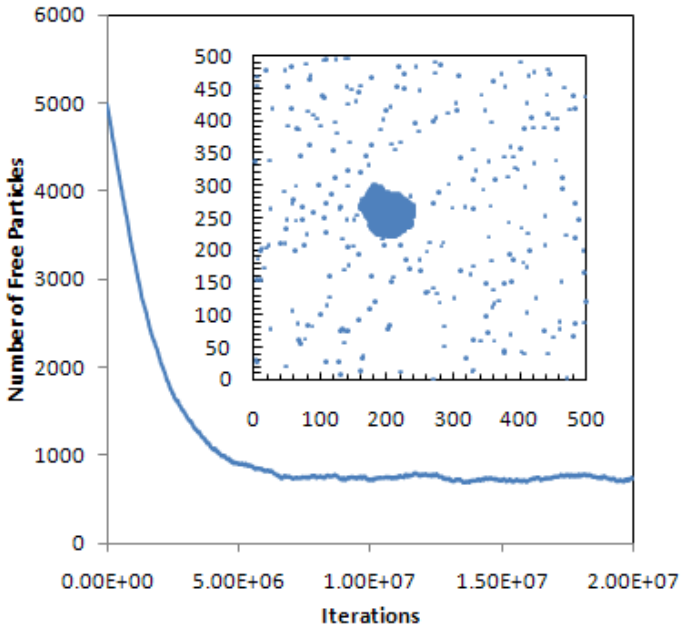

Figure 7.2

Typical data obtained from a computational simulation of C_{60} adsorption on graphite. The main graph shows the number of free particles, i.e. those within the C_{60} gas, and clearly shows that a steady state is reached after ~$7x10^6$ iterations. The inset shows the resultant island and 'sea' of C_{60} molecules in a 500 x 500 array. C/T = 0.825, where C is as defined in Equation 7.1.

7.2.2 C_{60} on Ni(110)

LEED, XPS and UPS measurements were carried out on the surface analysis system at the University of Liverpool. This system is described in detail in Chapter 3, Section 3.2.3. The Ni(110) surface was cleaned using the approach out lined in Chapter 3, Section 3.1.2. As in the case of C_{60} on HOPG(0001), the films in this instance were grown through sublimation of C_{60} powder from a tantalum cell. The C_{60} coverage was calibrated by comparing the C1*s*:Ni2*p* ratio for a given film to that associated with a saturated physical monolayer produced by annealing a thick film [13], until no further changes could be detected.

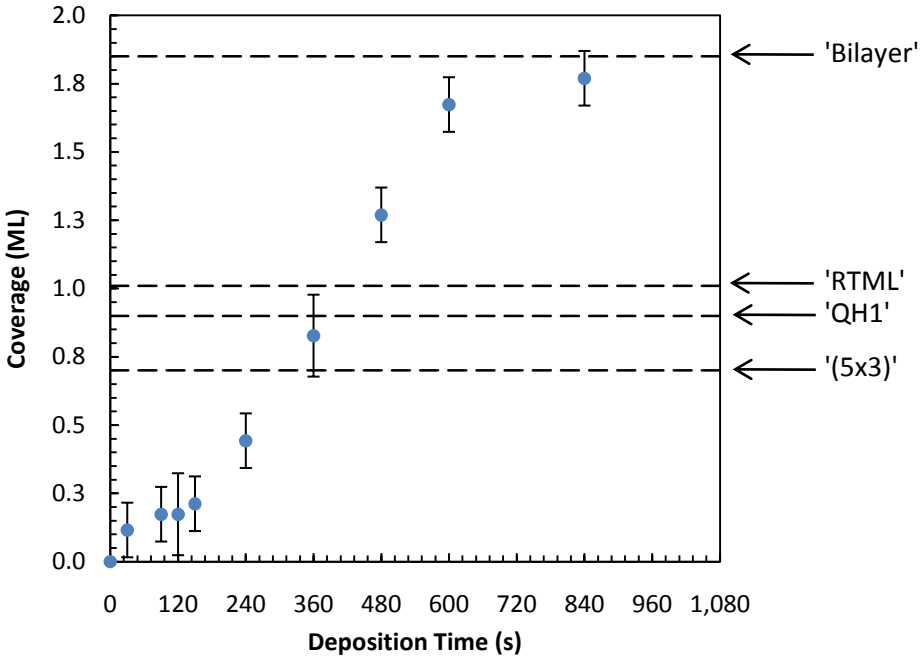

Figure 7.3

Calibration curve for the Ni(110) coverage from XPS measurement of the C1s to Ni2p ratio. The C1s:Ni2p intensity ratio was then converted to monolayer (ML) through measurement of the C1s and Ni2p XPS peaks for a saturated monolayer. On the right are listed the terms used to describe each coverage studied here and their approximate placement on the calibration curve.

7.3 Results and Discussion

7.3.1 C_{60} on HOPG(0001)

Figure 7.4 displays the result of deposition of C_{60} onto an HOPG(0001) substrate held at room temperature. In contrast to the growth seen on the Ni(110) surface (discussed later), weak van der Waals interaction between substrate and overlayer allows the formation of hexagonally close-packed (hcp), faceted, islands with a measured height of 0.8 ± 0.1 nm (Figure 7.4(a)). Such islands are not commensurate with the graphite lattice and the arrangement of the 1st layer molecules is determined by step edges on the substrate, from which the islands nucleate and grow [30]. It is clear that second layer growth begins before completion of the first. Likewise, the growth of the third layer begins before the completion of second layer, and the fourth layer before the completion of the third layer and so on. From this one may infer that molecules deposited on 1st (and higher) layer(s) are unable, at room temperature, to overcome the Ehrlich-Schwoebel barrier [31] and move to the layer below.

The structures formed by second layer molecules are striking –growth occurs through the formation of three-armed 'Y'- shaped structures (Y-structures) with the 'arms' spaced at 120º intervals, the orientation of which reflects the symmetry of the underlying hcp layer. This appears to be the normal growth mode unless there is grain boundary/defect in the underlying lattice that causes rotation ≠ 60° (Figure 7.5). All higher layers also follow the same growth mode with the formation of Y-structures, implying that the interaction of molecules with those in the first layer is the same as with subsequent layers.

Symmetry-breaking structures, like the Y-structures seen here, are commonly observed in homoepitaxial metal growth at low temperatures (~135 K) [32, 33] and arise due to anisotropic corner diffusion from what are termed 'A-sites' and 'B-Sites' (see Figure 7.6); B-sites are energetically more stable than A-sites and therefore diffusion of peripheral molecules along a B-edge occurs at a slower rate than diffusion along an A-edge. Furthermore, diffusion around a corner from a B-edge to an A-edge has an energy barrier (for example, ~0.15 eV for Ag atoms on Ag(111)) [33]. The result of these two factors is a diffusion anisotropy of peripheral molecules of the island. For metals this anisotropy is only significant at low temperatures and, as the system is brought to 'high' (room)

temperature, the growth mode changes to the formation of close-packed islands and the symmetry of the underlying lattice is replicated. Here it is apparent that anisotropic corner diffusion is present for second and higher layers in *room temperature* growth of C_{60} on C_{60}; a system that is a much more weakly interacting than the metallic systems discussed in the previous paragraph. An investigation into such anisotropic corner diffusion of the C_{60}-HOPG system has previously been performed using STM and MD simulation [34] and found that the same A-edge/B-edge diffusion anisotropy is present.

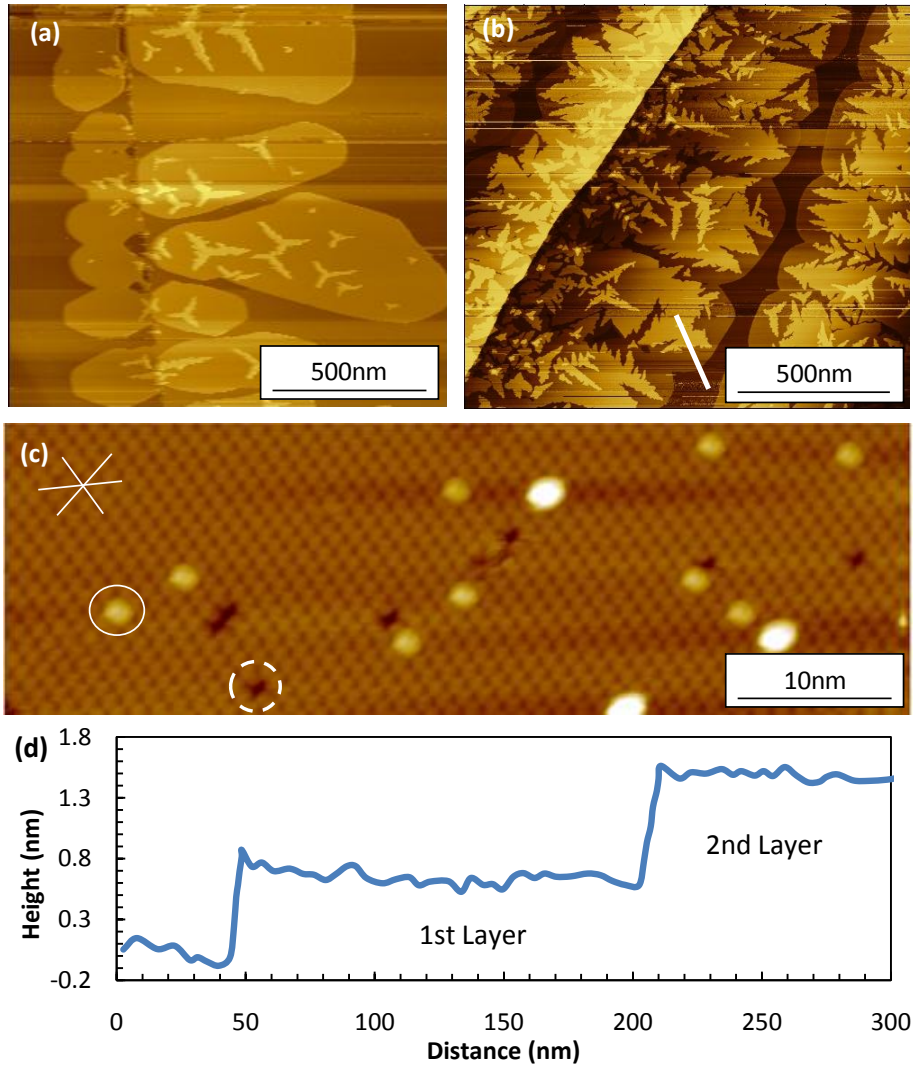

Figure 7.4

Large area STM image of the growth of C_{60} islands formed on HOPG at coverages of ~0.6 ML (a) and ~1.3ML (b). The first layer islands are clearly faceted and nucleate from the graphite steps. Second and higher layer growth follows and initial formation of Y-structures (a), which 'fill in' the layers shown in (b). (c) Molecular resolution image of a monolayer with the symmetry directions highlighted. Also observed are point defects within the close packed lattice (dashed circle) and initial second layer growth (solid circle). From the line profile shown in (d) it is clear that each observed layer is a single molecule thick.

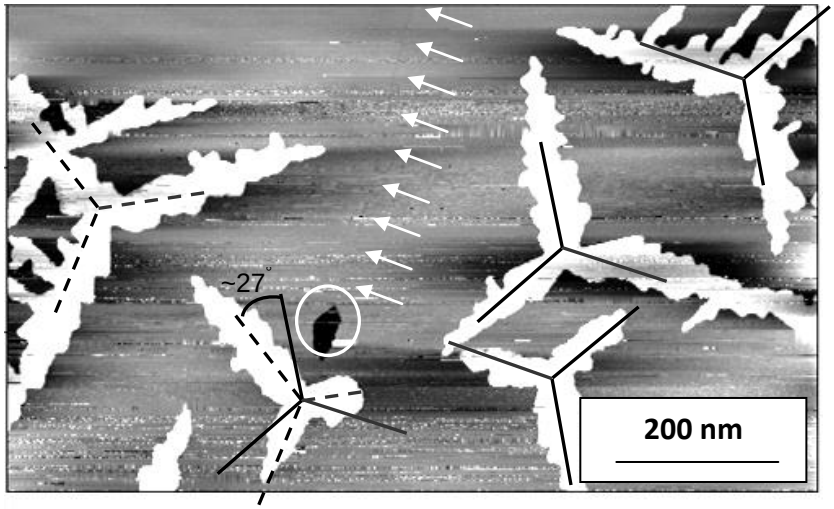

Figure 7.5

Grain boundary (shown by the white arrows) in the first layer leading to the rotation of dendrites and failure to close the first layer (circled).

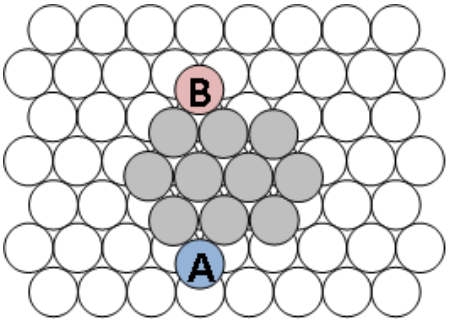

Figure 7.6

Adapted from [33]: The A-sites (along an A-edge) and B-sites (along a B-edge) on the periphery of a 2nd layer island on 1st layer hcp growth. A B-site is energetically more stable than an A-site and therefore diffusion of peripheral molecules along a B-edge occurs at a slower rate than diffusion along an A-edge. Furthermore, diffusion around a corner from a B-edge to an A-edge has an energy barrier. The overall result is a diffusion anisotropy of peripheral molecules of the island.

When imaging, the presence of 'streaks' within an STM image of the C_{60}-HOPG system is normally attributed to the presence of highly mobile C_{60} molecules which have been moved by the STM tip [34, 35]. From the STM work presented here it is clear that the tip-sample interaction is weak enough to avoid this scenario, streaks are not observed for C_{60} growth on the first (or higher) layers, nor at the edges of close packed islands on the HOPG surface. In contrast to this, the HOPG surface itself appears to be littered with free molecules (confirmed by examination of the line profiles presented in Figure 7.7(a)), the number density of which does not decrease with time, or vary with tunnelling conditions (i.e., the tip sample interaction), as shown in Figure 7.7(b). Since the number density of such molecules does not decrease with time this implies that the 1st layer molecules on the HOPG exist in a steady-state equilibrium with 2D solid C_{60} islands surrounded by a 2D C_{60} vapour, and molecules are continually condensing from the vapour state into the solid state

and subliming from the solid state into the vapour state. Figure 7.7(d) displays an STM image of the same sample with the substrate temperature increased by ~30 K. It is clear that even such a relatively small increase in temperature results in a substantial increase in the number of vapour phase molecules.

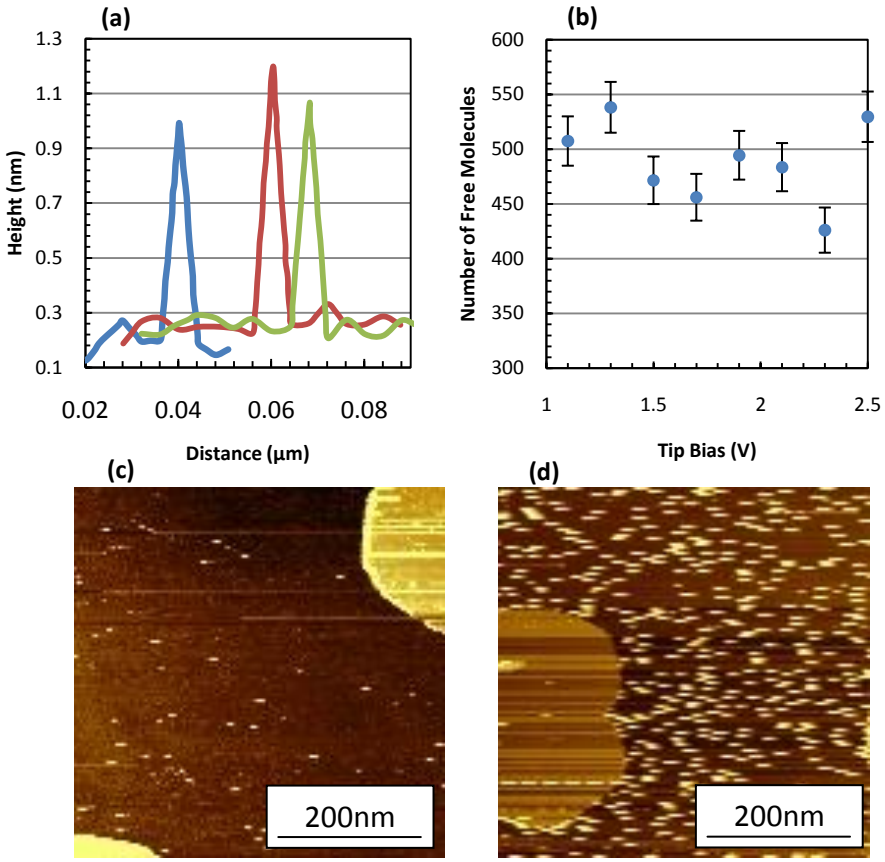

Figure 7.7

The 'C_{60} sea'; free moving vapour phase molecules between islands which appear as 1 nm spikes. The left image shows the 'sea' at ~300 K, whilst the right image shows the result of increasing the substrate temperature to ~330 K. It is clear that there is an increase in the number of vapour phase molecules.

If the 1st layer molecules are indeed behaving as a 2D solid/vapour system, one can make simple predictions regarding their behaviour as a function of temperature: at higher temperatures one would expect that more molecules would exist in the vapour phase, whilst at lower temperatures more molecules would exist in the solid phase. More detailed predictions can be made through derivation of the *coexistence curve* (which represents the discontinuous phase transition between two phases of matter) by way of the Clausius-Clapeyron equation:

$$\frac{dP}{dT} = \frac{\mathcal{L}}{T\Delta A}$$

where

$$\Delta A = A_v - A_s$$

Equation 7.2

In this instance, the change in the pressure, P, of the system with respect to temperature, T, can be described by the temperature of the system, the latent heat (the energy needed to transfer 1 kg of material from one phase to another), $\mathcal{L}$, and the change in area (since this is a 2D system), ΔA, occupied by the molecules. ΔA can therefore be described in terms of the area occupied by the vapour, A_v, and the area occupied by the solid, A_s.
If $A_v \gg A_s$ (which is usually the case), then:

$$\frac{dP}{dT} = \frac{\mathcal{L}}{TA_v}$$

Equation 7.3

If we assume that the free C_{60} molecules in the vapour phase behave as a two dimensional ideal gas (a reasonable assumption given the small intermolecular interaction), then:

$$PA_v = RT$$

Equation 7.4

where *R* is the ideal gas constant. Thus:

$$\frac{dP}{dT} = \frac{\mathcal{L}P}{RT^2}$$

Equation 7.5

Separation of variables and integration leads to:

$$\ln(P) = -\frac{\mathcal{L}}{RT} + \alpha$$

Equation 7.6

where α is a constant of integration. However, from kinetic theory, the pressure of an ideal gas may be related to the number of molecules, n, that constitute that gas, the area of that gas and the temperature of the gas:

$$P = \frac{nk_BT}{A_v}$$

Equation 7.7

Since, in this case, the area which the gas can occupy can be considered constant (i.e., that of the sample), and assuming that the solid islands occupy a negligible fraction of this area, Equation 7.7 becomes:

$$P = \beta nT$$

Equation 7.8

where $\beta = k_B/A_v =$ 1.38 x 10^{-11} $J.K^{-1}.m^{-2}$ if n is counted over 1 μm^2 Substitution of Equation 7.8 into Equation 7.6 yields a coexistence curve of the form:

$$\ln(n) = \alpha - \ln(\beta) - \frac{\gamma}{T} - \ln(T)$$

Equation 7.9

where γ is a constant (equal to $\mathcal{L}/R$). The functional form of Equation 7.9 is given in Figure 7.8 for α, β and γ specified in the caption.

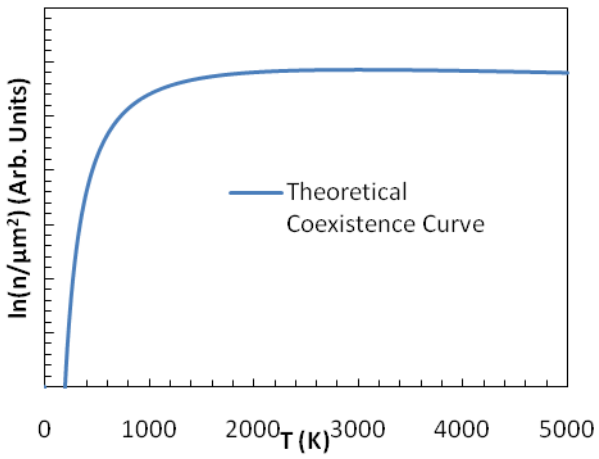

Figure 7.8

The functional form of the coexistence curve given in Equation 7.9 for:
$\alpha = 4.3$,
$\beta = 1.38 \times 10^{-11}$
and
$\gamma = 3000$.

Figure 7.10 displays the results from STM measurements (red circles) of the number of vapour phase molecules as a function of temperature plotted along with data from the lattice gas simulation (green circles) and the theoretically derived coexistence curve. Values used in fitting the coexistence curve and simulation data to the experimental results are specified in Table 7.1.

It is clear that the experimental data are in good agreement with both the theoretical and simulated curves, demonstrating that 1st layer molecules on HOPG are in a steady state equilibrium in which the vapour phase molecules exhibit (to within error) ideal-gas behaviour. Furthermore, the agreement with the simulated data shows that a simple Arrhenius-type behaviour for the movement of the 1st layer molecules (dependent on temperature, activation energy and number of nearest neighbours) is sufficient to describe this system. It is therefore possible to extract a value for the energy needed to sublime a molecule from the solid to the vapour state. From the coexistence curve, a value of ~0.19 eV per molecule is obtained, whilst a value of ~0.28 eV is obtained from computer simulation. These values are in good agreement with the C_{60}-C_{60} interaction energy calculated by Girifalco (0.28 eV) [36] and are comparable to the activation barrier for diffusion of a molecule away from a 2nd layer island (0.21 to 0.43 eV) calculated by Liu *et al.* [34].

At low temperatures, the computer simulation predicts that almost all particles are present within an island; either the one formed around the original centrally located defect, or one that has formed independently due to the inability of molecules to reduce their coordination (Figure 7.9). The simulation also shows that it takes longer for the stable state to be reached and that the resultant island morphology is no longer compact. These observations are expected for particles with a reduced mobility due to the lack of energy available in the system. The coexistence curve predicts that this will happen at temperatures of just below 200 K (equivalent to a thermal energy of ~0.02 eV), since at this temperature $\ln(n/\mu m^2) = 0$, that is., $n/\mu m^2 = 1$ (i.e., the number of molecules in the vapour phase effectively becomes zero, and all are present in the solid phase).

Theoretical fit	α	$\beta(=k_B/A_v)$	$\gamma\ (=\mathcal{L}/R)$	E(eV)
	4.3	1.38×10^{-11}	3000	~0.19
Simulation	C			
	320			~0.28

Table 7.1

Summary of the values extracted from the theoretical and simulation data. For definitions of a, β, γ and C, see Equation 7.9 (and associated text) and Equation 7.1 respectively.

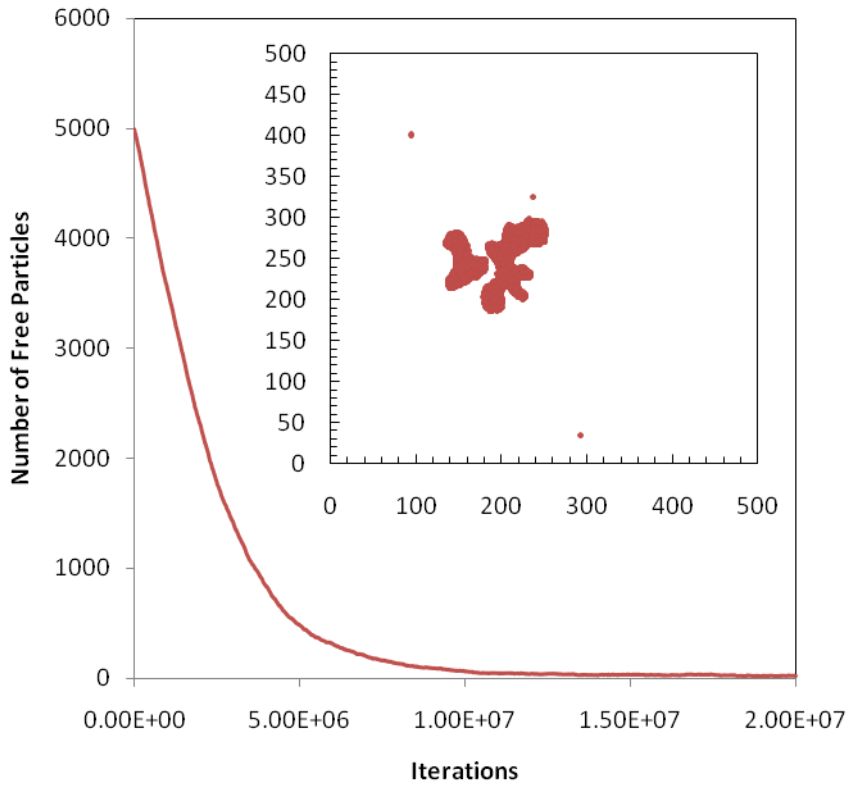

Figure 7.9

Low temperature data (C/T=1.25) obtained from the computational simulation of C_{60} adsorption on graphite. The main graph shows the number of free particles, i.e. those within the C_{60} vapour, and clearly shows that a steady state is reached after ~1×10^6 iterations, with very few particles exist within the vapour phase. The inset shows the final positions of the particles in a 500 × 500 array.

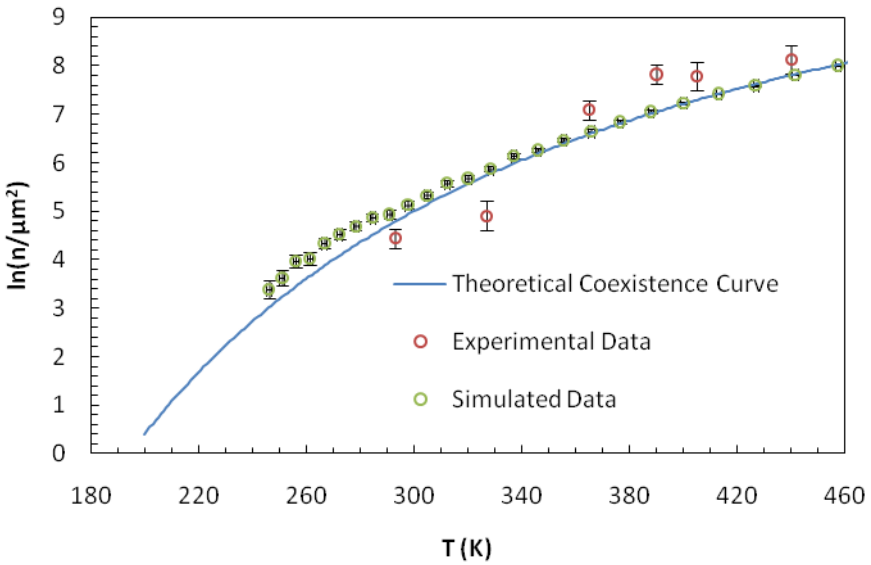

Figure 7.10

Coexistence curve for an ideal 2D gas (blue curve, reproduced from Figure 7.8) and the simulation data (green circles) fitted to experimental data (red circles). It is clear that the variation of the coexistence curve and simulation data with temperature agrees well with experiment.

7.3.2 C_{60} on Ni(110)

Figure 7.11 displays the result of room temperature growth of a monolayer (1.00 ± 0.09 ML) of C_{60} on Ni(110). It can be seen that such layers exhibit only local ordering in either hexagonally close packed or square geometries (see inset of Figure 7.11) and, consequently the first layer is not completely close-packed. Second layer molecules are seen as bright areas in Figure 7.11 and have a measured height of ~1 nm, comparable to the diameter of the C_{60} molecule. This interlayer height difference is comparable to that observed for C_{60} on HOPG (discussed below) and so one may infer that for the C_{60}-Ni(110) system there is little interaction between the first layer and second layer molecules, consistent with previous EELS observations [37]. In contrast to this, first layer molecules have a measured height of ~0.4 nm indicating that, even at room temperature, these molecules have a different local density of states under the tunnelling conditions employed and are likely to be chemisorbed on the Ni(110) surface. Furthermore, some first layer molecules appear to exhibit local height variations, with clusters of some molecules appearing as ~0.3 nm depressions (indicated by the dashed circle in Figure 7.11), and randomly distributed molecules appearing as ~0.2 nm protrusions (indicated by solid circle in Figure 7.11). This height difference can arise from one or both of two sources: (1) a reconstruction of the nickel surface under the C_{60} molecules (for example, like that suggested by Weckesser *et al.* [29] for C_{60} on Pd(110)) which is kinetically limited and thus incomplete at room temperature; (2) differences in bonding of the C_{60} to the nickel surface. As discussed in Chapter 2, an STM image is a mixture of both topographical information and the LDOS of both the tip and sample and consequently, variations in height may be linked with differences in the adsorbate-substrate interaction (for example, like that suggested for C_{60} on Au(111) at room temperature [38] where variations in the measured height of the adsorbed molecules occurred with changing tunnelling bias, indicating an electronic component to the observed image). Since imaging as a function of bias was not examined in this study, a definitive comment cannot be made on the origin of this height difference. However, when compared to the interlayer spacing of Ni(110) (~0.13 nm [39]), it is unlikely that a local reconstruction of the nickel surface is taking place and that it might be a variation in the C_{60} Ni(110) bond that is being observed.

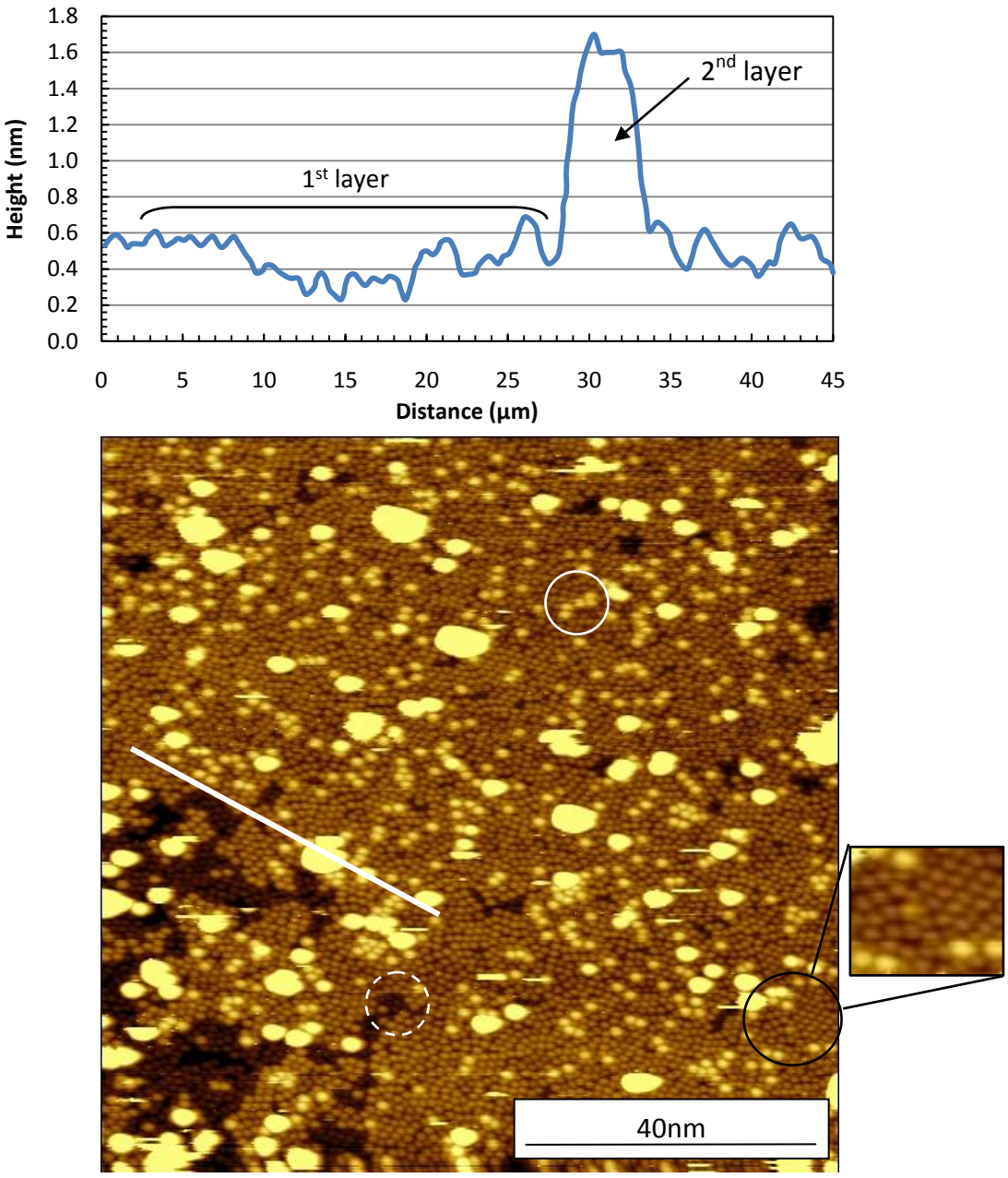

Figure 7.11

Room temperature growth of C_{60} on Ni (110) with a coverage of 1.00 ± 0.09 ML. It is clear that the layer is disordered. The first layer has varying height (seen as the darker patches) whilst the second layer also does not form any ordered structure.

As discussed in the introduction to this chapter, ordered overlayers of C_{60} on Ni(110) can be formed through evaporation of C_{60} onto a Ni substrate held at > 350°C [15], or by annealing a film deposited at room temperature (RT). The resulting overlayers may adopt one of several structures depending on the substrate temperature used and the coverage. Figure 7.12 shows an example of these differences: Figure 7.12(a) displays the result of growing a monolayer at a nominal temperature of 380°C with a coverage of ~1 ML, Figure

7.12(b) displays a lower coverage, ~0.3 ML (obtained from the C1*s* to Ni2*p* ratio), produced at the same temperature. There are significantly different structures in these layers: the layer shown in Figure 7.12(b) shows the formation of islands which appear to be elongated in the [1$\bar{1}$0] direction, whilst that in Figure 7.12(b) shows an overlayer with structures running in the [001] direction.

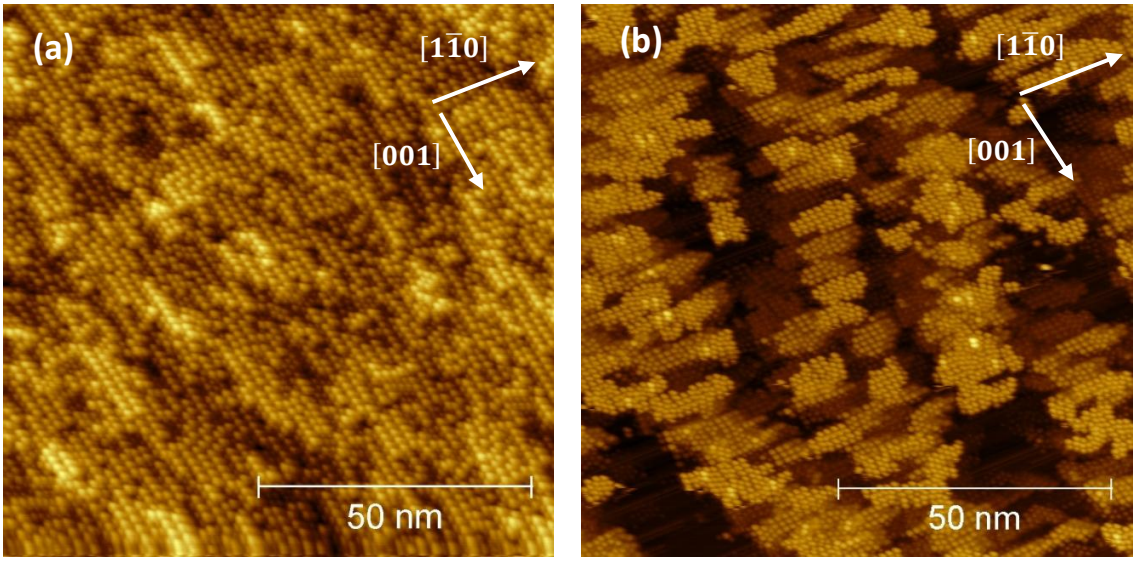

Figure 7.12

Examples of two different structures of C_{60} on Ni(110) on which the crystallographic directions of the Ni(110) substrate are indicated.(a) shows the monolayer produced when depositing C_{60} onto a Ni(110) substrate held at 380°C. The coverage of this overlayer is ~1 ML. (b) shows lower coverage (~0.3ML) deposited at the same temperature. The orientation of sample is the same in each case.

Figure 7.13(a) and Figure 7.14(a) display STM images and LEED patterns (in which the colours have been inverted for clarity) obtained from the clean Ni(110) surface, with the [1$\bar{1}$0] direction indicated. This orientation of the Ni(110) substrate is maintained for all STM and LEED data presented here. The STM was calibrated laterally against the interatomic spacing of the clean Ni(110) surface [40].

Figure 7.13(b) and Figure 7.14(b) display STM and LEED data from the partly commensurate QH1 phase obtained after deposition of C_{60} onto a substrate held at 420°C, resulting in coverage of 0.92 ± 0.08 ML. STM measurements of this phase (Figure 7.12(a)) show almost complete coverage of the Ni surface, in which the general structure of the monolayer is found to consist of corrugations perpendicular to [1$\bar{1}$0] which range in amplitude from 0.15 nm to 0.20 nm. In a previous study [26], similar structures were observed for the QH1 phase and were attributed to a reconstruction of the Ni(110)

substrate involving the addition or removal of [001] rows. However, Murray *et al.* [30] did not investigate the (5x3) structure, which can be produced directly [13, 23, 26] or by annealing the QH1 phase.

Figure 7.13(c) and Figure 7.14(c) display STM and LEED data from the (5x3) phase, which was produced by annealing the QH1 phase at 400°C for 5 minutes. Both show that the structure of the layer has changed from hexagonal to rectangular. STM images show (Figure 7.12(b)) the (5x3) phase to be well ordered and exist as two-dimensional islands on the Ni surface. For the image shown in Figure 7.13(c) the coverage of the Ni surface is reduced by 0.21 ML to 0.72 ± 0.06 ML and implies that some loss of molecules from the surface occurs. The measured coverages are consistent with those previously reported [15].

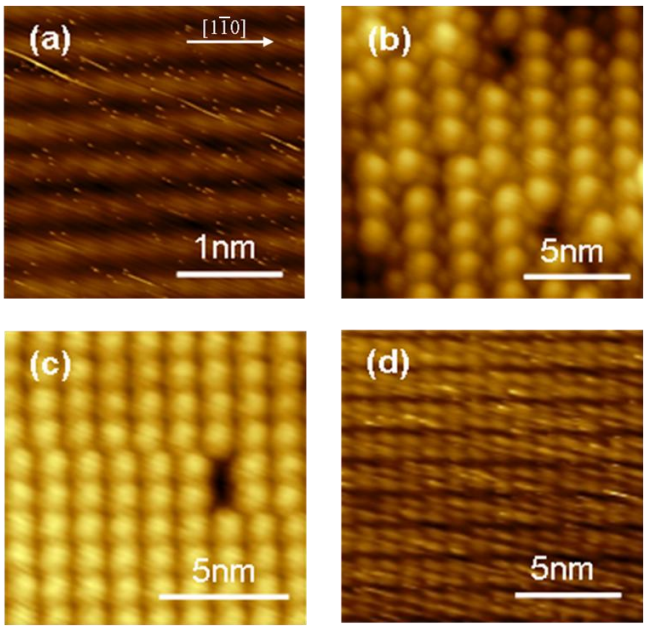

Figure 7.13

STM images of the C_{60}/Ni(110) system: (a) displays the clean Ni(110) surface; (b) the QH1 phase; (c) the (5x3) phase created by annealing the QH1 phase and (d) the (4x5) carbide phase produced by further annealing the (5x3) phase. Corresponding LEED images are shown in Figure 7.14.

Figure 7.13(d) and Figure 7.14(d) display STM and LEED data taken after annealing the (5x3) phase at a temperature of 500°C for 2 minutes. The LEED pattern displays a (4x5) carbide pattern as observed by Cepek *et al.* [15] rather than the graphitic rings observed by Saltas *et al.*[17]. This is supported by STM which clearly displays the (4x5) carbide structure [41]. The carbide layer is created through catalytic decomposition of the fullerene molecules and desorption/dissolution of molecular and atomic carbon [15, 26]. Further

annealing of the carbide phase results in the observation of a clean Ni(110) LEED.

By assuming that the surface periodicity exhibited in the LEED patterns of the QH1 and (5x3) phases reflect simple overlayer structures (an assumption supported by STM imaging), the molecular separation in the two phases can be determined using the LEED pattern of the bare Ni(110) surface for calibration. For the QH1 phase, the intermolecular spacing along the $[1\bar{1}0]$ and [001] are found to be 1.05±0.05 nm and 1.73±0.05 nm respectively. The (5x3) phase displays an intermolecular separation of 1.05±0.05 nm along $[1\bar{1}0]$ and 1.24±0.05 nm along [001]. These measurements are in agreement with the intermolecular distances obtained using STM (summarised in Table 7.2) within experimental uncertainty and are consistent with those found in the literature [13, 26]. Thus both the (5x3) and QH1 phases have an expanded nearest neighbour distance compared with that found in bulk C_{60} (1.004 nm). This is a growth mode that is not observed for C_{60} on noble metal surfaces [37] and indicates that the C_{60}-Ni(110) bond is significantly stronger than the (predominantly van der Waals) adsorbate-adsorbate interaction.

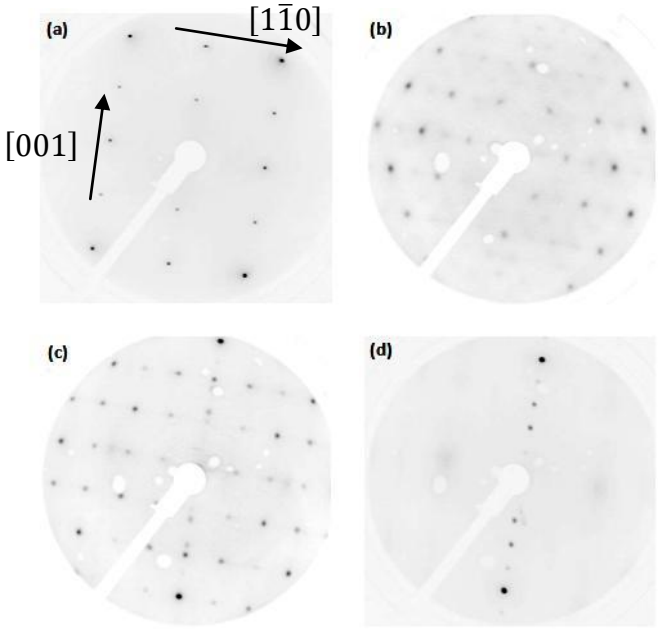

Figure 7.14

LEED pattern of (a) the clean Ni(110) surface, obtained with an incident beam energy of 164 eV. The respective LEED patterns (b) to (d) display the as-grown QH1 phase, the (5x3) phase produced by annealing the QH1 phase and the result of further annealing at ~500°C for 2 minutes. (b), (c) and (d) are obtained with incident beam energy of 31 eV. Corresponding STM images are shown in Figure 7.13.

Figure 7.15 displays the intensity normalised valence band spectra for the phases shown in Figure 7.13 and Figure 7.14, along with that for a fullerene bilayer, a monolayer deposited at room temperature and the clean Ni(110) surface. The most apparent difference between the valence band spectra of Figure 7.15 is the increase in relative intensity and definition of the peaks associated with the highest occupied molecular orbital (HOMO), the next highest occupied molecular state (HOMO-1), and deeper lying ($\pi+\sigma$)-like MOs [42] (labelled A to D in Figure 7.15) on progressing from the (5x3) phase to the QH1 phase, RTML and, finally, the bilayer.

Phase	LEED Spacing (nm)		STM Spacing (nm)		(nx3) Model Spacing (nm)	
	$[1\bar{1}0]$	[001]	$[1\bar{1}0]$	[001]	$[1\bar{1}0]$	[001]
Ni(110)	0.25	0.35	0.29±0.02	0.41±0.01	0.25	0.35
QH1	1.73±0.05	1.05±0.05	1.70±0.06	1.05±0.03	1.73	1.05
(5x3)	1.24±0.05	1.05±0.05	1.13±0.05	1.04±0.04	1.24	1.05
Murray QH1	-	-	1.58[26]	1.05[26]	1.50	1.05
Murray (5x3)	-	-	-	-	1.24	1.05

Table 7.2

Ni(110) and C_{60} intermolecular spacings in the $[1\bar{1}0]$ *and* [001] *directions.*
This table shows the C_{60} intermolecular spacings for the QH1 and (5x3) phases from LEED measurements, STM measurements and the (nx3) substrate reconstruction model. As is clear both the LEED and STM intermolecular separations are in agreement with those used in the (nx3) substrate reconstruction model. Also included are intermolecular separations along the high symmetry directions derived from the QH1 structure suggested by Murray et al. [26] and a similar 'Murray-Type' reconstruction for the (5x3) phase.

In the RTML phase all features in the valence band spectrum show a consistent shift to lower binding energy when compared with the spectrum from the bilayer. The HOMO and HOMO-1 states broaden and become asymmetric, with the asymmetry of the former extending significantly to lower binding energy. The relatively strong perturbation of the valence band features suggests that the substrate-adsorbate bond in the disordered room temperature deposited layer is relatively strong and that there is hybridisation of the fullerene and Ni states. Hence, the C_{60} is immobile and the overlayer is disordered.

The valence band of the QH1 phase shows a strong broadening of all features. In

particular the HOMO-1, and the HOMO display a clear shoulder to lower binding energy. Splitting of the HOMO state has previously been observed in C_{60} adsorption on Al [14], and is particularly pronounced on the Al(110) surface [44], where it has been attributed to symmetry reduction upon the formation of a substrate-adsorbate bond. For this latter case it was argued that, upon adsorption, the resulting states become non-degenerate due to differences in final state screening arising from different degrees of overlap with the substrate, and the formation of a covalent bond between surface and molecule. It was also suggested that the molecular orbitals are not significantly perturbed from their free molecular state. A similar splitting is, however, not obvious in C_{60} adsorption on either Pt(111) [23] or Mo(110) [45] whilst symmetry considerations [44] would certainly suggest an effect in the latter. Whether the shoulder for the C_{60}/Ni(110) phase arises from the mechanism suggested by Scheissling *et al.* [44], or by the formation of bonding/anti-bonding orbitals by hybridisation with the substrate, the degree of broadening of both HOMO and HOMO-1 derived states is large in comparison with that typically observed for fullerenes on metal surfaces classified as displaying weak or intermediate strength bonding. Such broadening therefore indicates the formation of a strong, predominantly covalent bond between substrate-adsorbate in the QH1 phase. In both the RTML and QH1 phases the coverage is similar (1.01±0.09 ML and 0.92±0.08 ML) and STM shows that there is no second layer growth in either phase. Hence, the changes which are observed upon annealing must reflect a change in substrate-adsorbate bonding for which an activation barrier exists. The differences between bonding evidenced in the RTML phase and the QH1 phase are similar to those observed when annealing a C_{60} monolayer on Mo(110) [45]. Further broadening and asymmetry of the HOMO is observed in the valence band of the (5x3) phase, in addition to the significant reduction in the definition of the HOMO-1 feature which suggests that the substrate-adsorbate bond is enhanced in this phase in comparison to the QH1 phase. An explanation for these changes is that pronounced reconstruction of the Ni(110) surface is required in order to bring about the phase changes from RTML to QH1 to (5x3), hence the presence of an activation barrier.

The effects of adsorption are also evident through the change in the energy separation of the HOMO and HOMO-1 features (Δ_{AB}) and the deeper-lying ($\pi+\sigma$)-like MOs (Δ_{BC}) (marked with * in Table 7.3). From these values it is becomes apparent that the π-like MOs (HOMO and HOMO-1) are significantly modified by the interaction between the C_{60} and the Ni(110) surface – an effect which is seen in the C_{60}/Au(110) system [46], where

significant shifts of all valence band features are observed and are attributed to strong hybridisation between substrate and π-like MOs.

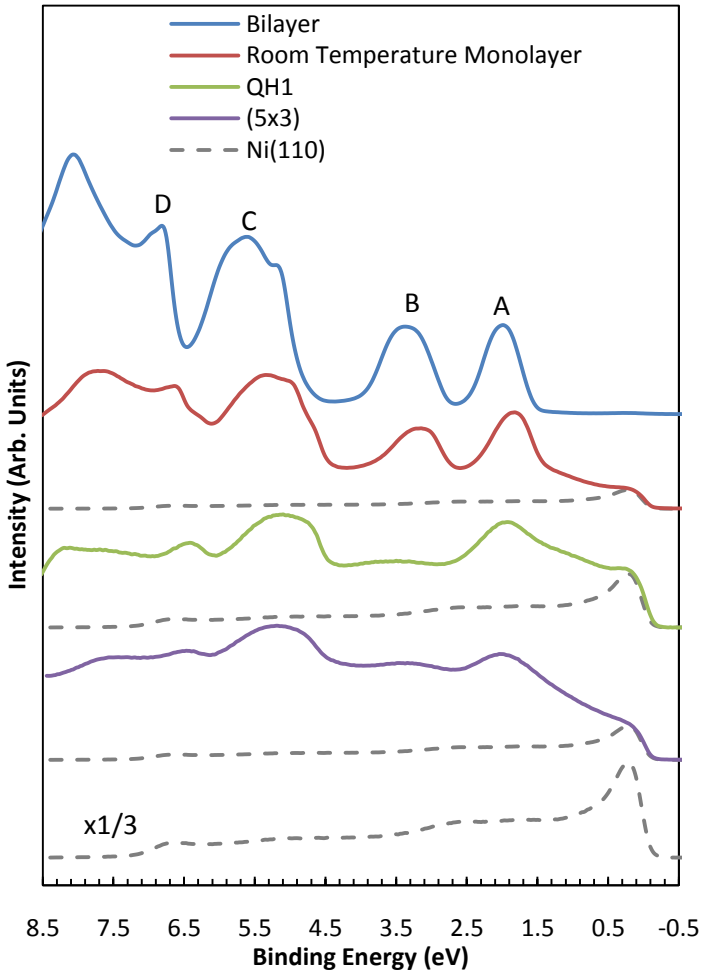

Figure 7.15

Valence band spectra (hν = 21.21 eV) from the bilayer, RTML, QH1 and (5x3) phases. From bottom to top: clean Ni(110), (5x3) C_{60} phase (coverage (0.72 ± 0.06) ML), QH1 phase (coverage (0.92 ± 0.08) ML), RTML (coverage (1.01 ± 0.09) ML) and a bilayer (coverage (1.85 ± 0.18) ML). Dotted lines in spectra from the C_{60} monolayers correspond to that from clean Ni(110) with appropriate scaling.

X-ray photoemission spectra demonstrate that the differences observed between the RTML, QH1 and (5x3) valence band spectra are mirrored in the lineshape and binding energy of the C1*s* line (Table 7.3). A shift of binding energy of the monolayer and sub-monolayer (namely the RTML, QH1 and (5x3) phase) C1*s* peaks to lower binding energy occurs from that of the bilayer by 0.25±0.04 eV. This shift is if the order of that reported previously for the C_{60}/Ni(110) system [23]. The binding energy shift is accompanied by an increase in the full-width half maximum of the C1*s* component for the monolayer and sub-

monolayer phases from that of the bilayer and is primarily due to an asymmetry to higher binding energy (Table 7.3).

VB Peak Separation (eV)	Multilayer	RTML	QH1	(5x3)
Δ_{AB}	1.36 ± 0.01	1.33 ± 0.03	1.60 ± 0.04*	1.30 ± 0.05
Δ_{BC}	1.81 ± 0.01	1.83 ± 0.05	1.34 ± 0.08*	1.6 ± 0.1*
Δ_{CD}	1.63 ± 0.01	1.59 ± 0.05	1.55 ± 0.08	1.6 ± 0.1
C1s Position (eV)	284.35 ± 0.02	284.06 ± 0.03	284.08± 0.04	284.01±0.06
C1s FWHM	0.71 ± 0.01	0.92 ± 0.02	0.92 ± 0.01	0.95±0.05

Table 7.3

Binding energies, peak separation and full-width at half maximum (FWHM) derived from valence band and core level photoemission spectra. See text for details.

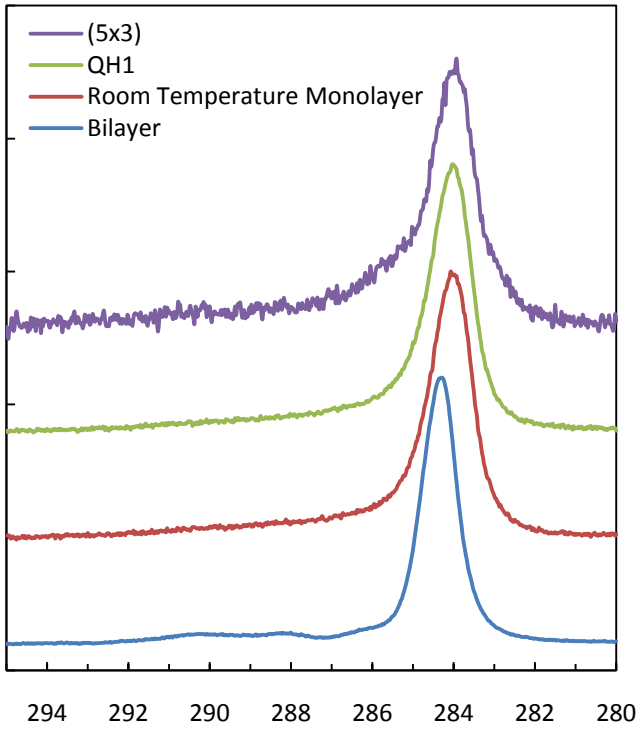

Figure 7.16

C1s spectra from bilayer, RTML, QH1 and (5x3) phases. (hν=1486.6 eV). There is an apparent shift to lower binding energy on going from the bilayer to the (5x3) phase. This is coupled with and increased FWHM and lineshape asymmetry towards higher binding energy.

The broadening, change in position and the introduction of asymmetry into the C1*s*

lineshape can again be attributed to changes in the bonding and hybridisation between the molecular and substrate orbitals [15, 16, 23]. However, the symmetry of C_{60} is reduced both by adsorption onto a surface and due to the production of a core hole [47] during the photoemission process. The resultant reduction in symmetry can be manifested as an asymmetric broadening of spectral features [48]. Therefore it is difficult to separate contributions to the FWHM from increased interaction of the molecule with the substrate and symmetry reduction upon adsorption.

From the spectroscopic data discussed above, it is clear that the molecules in QH1 and (5x3) are more strongly bound to the surface when compared with those of the RTML and that the thermal energy used to produce these phases could lead to a reconstruction of the surface and/or reorientation of the molecules. Such a phenomenon is not uncommon, with C_{60} – induced reconstructions of metallic surfaces being suggested for, for example on Au [49], Cu [27], Pd [29, 50] and Ni [26].

For the QH1 phase, a reconstruction/roughening of the surface has been considered by Murray *et al.* [26] (a 'Murray-type' reconstruction is shown in Figure 7.17). The reconstruction suggested in Ref, 30 involved the addition or removal of [001] rows, forming (100) microfacets. This reconstruction fails to satisfy the intermolecular separation we find experimentally (Table 7.2). Furthermore, if a Murray-type reconstruction is considered for the (5x3) phase (Figure 7.17), we find that significant mass transport involving both Ni atoms and C_{60} molecules is required in the transition from the QH1 phase to the (5x3) phase – a scenario which is unlikely since this transition occurs at modest temperature.

For fcc transition metals, missing $[1\bar{1}0]$ type reconstructions are common and may be induced by the presence of adsorbates (for example Ni, Cu and Ag) or may occur spontaneously (for metals such as Au and Pt) [51, 52]. For Ni(110), where the clean surface exhibits and unreconstructed (1x1) geometry, higher order missing row reconstructions may be induced by the presence of a variety of adsorbates [53-55]. Here we consider a reconstruction of the Ni(110) surface where every third $[1\bar{1}0]$ row is missing (an (*n*x3) type reconstruction such as that observed when nitrogen is adsorbed on Ni(110) [53]). This model is supported by the STM image in Figure 7.18(a), in which a (5x3) overlayer (produced by annealing the QH1 phase to ~500°C for 2 minutes) is shown. In this image,

clear dark stripes (Figure 7.18(b)) can be observed emanating from the edges of (5x3) islands. These dark stripes have a measured depth of 0.13±0.05 nm – consistent with the interlayer spacing of Ni(110) [39] – and are 0.8±0.1 nm apart, consistent with 3 spacings in the [001] direction. In Figure 7.18(c) raised lines lines can also be observed. These rows are 0.13±0.06 nm in height which is consistent with identification as added rows which have been created from Ni atoms removed elsewhere during reconstruction of the surface. Comparison of the above (5x3) film (created by annealing the QH1 phase) to a directly deposited (5x3) film (Figure 7.12(b)) shows that, whilst both missing and added Ni rows are seen for the former, only added Ni rows are seen for the latter (Figure 7.19). Again, this suggests that the missing row reconstruction of the Ni(110) surface is brought about by the adsorption of C_{60}, and that it is only through removal of C_{60} molecules (through annealing) that these missing rows are exposed.

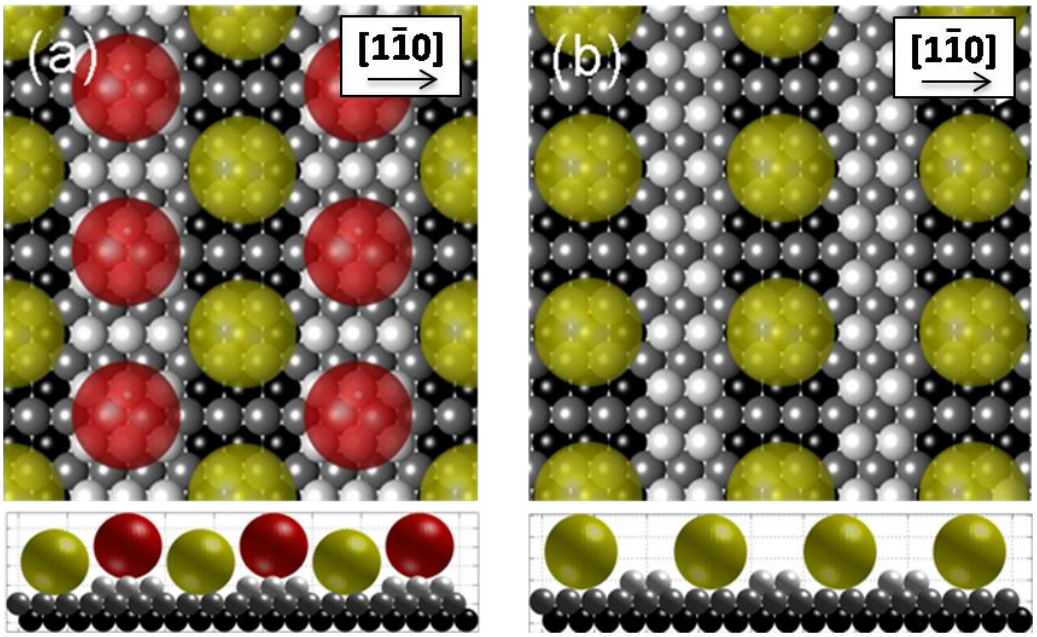

Figure 7.17

Schematic diagram of Murray-type reconstructions for (a) the QH1 phase and (b) (5x3) phase.

By considering (*n*x3) type reconstructions it is found that the C_{60} intramolecular distances in the (5x3) phase can easily be reproduced (Figure 7.20(a)). Moreover, through expansion of the (5x3) phase, the QH1 C_{60} intermolecular spacing can be reproduced by placing C_{60} molecules on top of the double row of Ni atoms (Figure 7.20(b)). Such an arrangement leads to two distinct types of adsorption sites for the C_{60} molecules. The first of these is the '(5x3)' type molecules which lie in the troughs on the surface created by the missing row. Given the coordination of these molecules (>6), they are expected to be strongly bound to

the surface. However, given sufficient energy they may migrate in the [1$\bar{1}$0] direction along a trough - possibly through the 'rolling' mechanism described by Weckesser *et al.* [50]. The second type of molecule is the 'QH1' molecule – these molecules adsorb on top of the remaining double row of Ni atoms and have a reduced coordination compared with that of the '(5x3)' type molecules. It is therefore expected that these molecules may be more weakly bound to the surface and is most likely the origin of the differences observed in the valence band spectra between the (5x3) and QH1 phases, in which the former shows evidence for a stronger substrate-adsorbate bond. The bonding differences between the two adsorption sites suggests that, through heating, one may preferentially remove the 'QH1' type molecules, leading to the formation of the (5x3) phase. By considering such a reconstruction of the Ni(110) surface, the molecules at (5x3) sites sit lower on the surface, within the [1$\bar{1}$0] troughs. From the scaled schematic shown in Figure 7.20(b), the corrugation amplitude formed in the process is ~0.14 nm, a value which is consistent with both our STM measurements and those of Murray *et al.* [26].

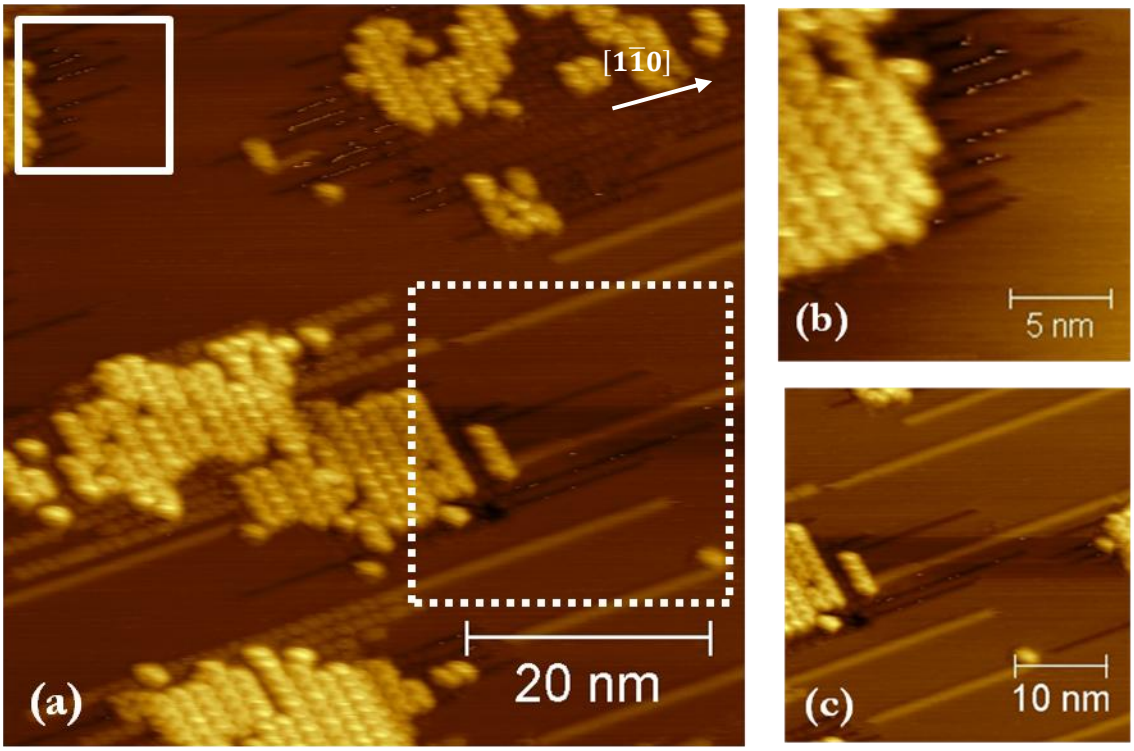

Figure 7.18

(a) 0.25 ML C_{60} on Ni(110), produced by annealing a QH1 phase to ~500°C for 2 minutes. (b) an expanded image of the region indicated by the solid square in (a) and shows the presence of missing Ni [1$\bar{1}$0] *rows emanating from the end of the (5x3) island. (c) shows a zoomed region indicated by the dashed square in (a) in which added Ni* [1$\bar{1}$0] *rows can be seen.*

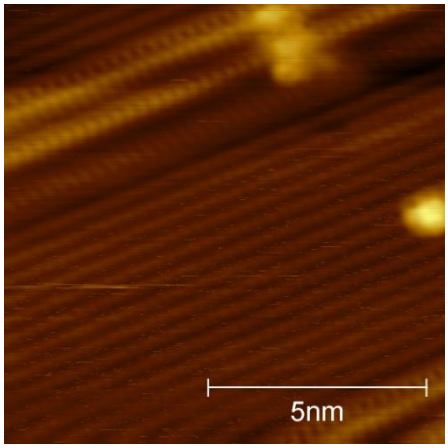

Figure 7.19

The Ni surface as seen between (5x3) islands (see Figure 7.12(b)). The [1$\bar{1}$0] *rows of the Ni substrate are clearly seen, along with 1st and 2nd layer Ni* [1$\bar{1}$0] *rows.*

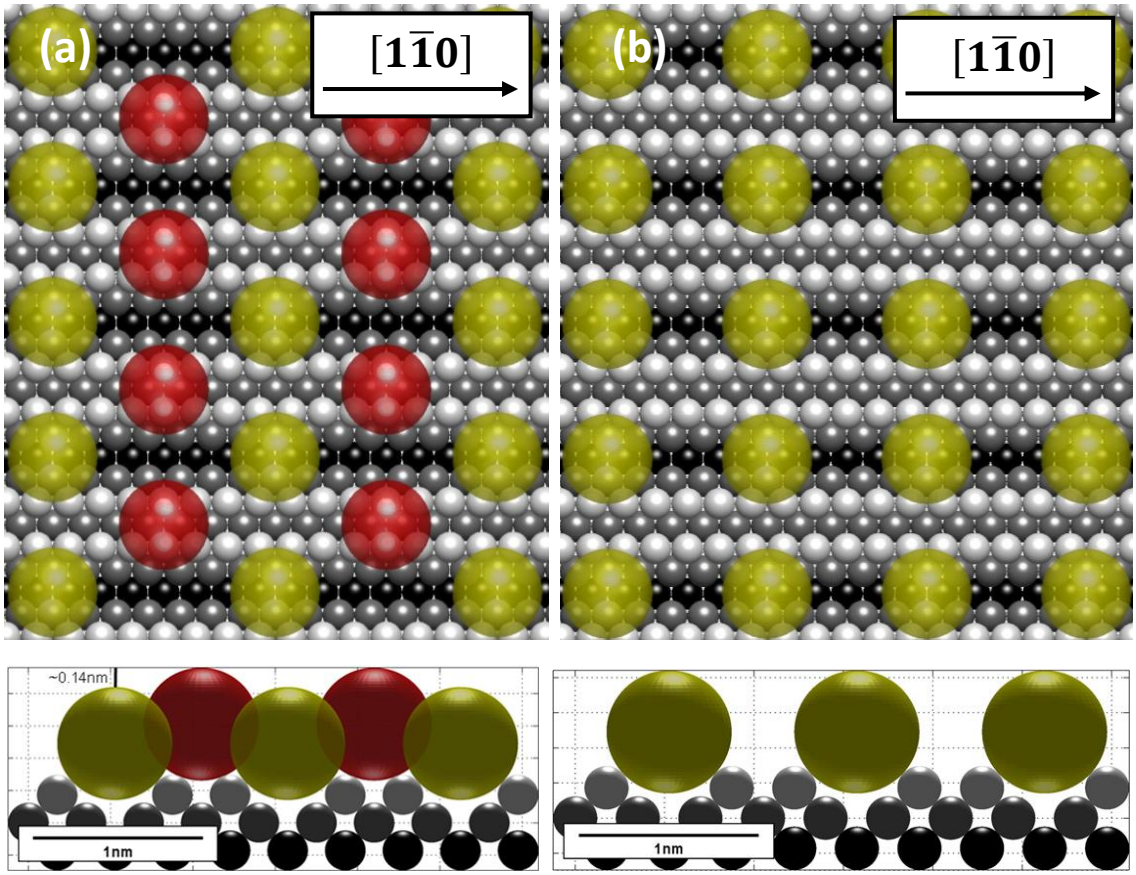

Figure 7.20

Schematic diagrams of the (5x3) and QH1 phases: (a) QH1 phase on a reconstructed surface in which every [1$\bar{1}$0] *row is removed: '(5x3)' type molecules sit in the* [1$\bar{1}$0] *troughs and 'QH1' type molecules sit on the two remaining* [1$\bar{1}$0] *rows. The height difference between '(5x3)' and 'QH1' type molecules is ~0.14 nm. (b) After removing the 'QH1' type molecules (shown in red) through heating, the '(5x3)' type molecules (shown in gold) are able to freely migrate in the* [1$\bar{1}$0] *direction and so form the (5x3) phase shown in (b).*

7.4 Summary and Conclusions

STM has been used to image C_{60} overlayers on HOPG(0001) and Ni(110) at both room and higher temperature. For C_{60} on HOPG it is seen that first layer growth follows a hcp configuration and that all subsequent layers follow a dendritic 'Y' structure formation on initial growth before the completion of the previous layers. This growth mode is due to anisotropic corner diffusion. The behaviour of a 2D C_{60} submonolayer vapour/solid phase on HOPG has been studied using STM. Using first principles, it has been found that the behaviour of this vapour can be described both as an ideal gas and through simple simulations. Using these approaches, it is estimated that the energy needed to transfer a C_{60} molecule from the solid phase to the vapour phase is ~0.19 eV and ~0.28 eV respectively for the two approaches. These values are in good agreement with the C_{60}-C_{60} interaction energy found in the literature.

For C_{60} on Ni(110), room temperature growth comprises a disordered overlayer with only local ordering. Apparent height measurements of the first layer suggest that the C_{60} overlayer is chemisorbed at room temperature. Measurements at elevated temperatures have been complemented by LEED and PES. Paying particular attention to the (5x3) and QH1 phases, it is found that the Ni(110) reconstruction previously suggested by Murray *et al.* [26] is incorrect. Instead a (*n*x3) type reconstruction is proposed in which every third $[1\bar{1}0]$ row is removed. In this model two types of adsorption site exist for the fullerene molecules: '(5x3)' sites in which molecules sit in the troughs formed by the loss of a $[1\bar{1}0]$ row and 'QH1' sites where molecules sit above pairs of $[1\bar{1}0]$ rows. These differences are reflected in valence-band photoemission spectra which show clear differences between the two phases and with a disordered monolayer deposited at room temperature. These changes are related to differences in bonding and co-ordination associated with the differing adsorption sites.

7.5 References

1. Dresselhaus, M.S., G. Dresselhaus, and P.C. Eklund, *Science of fullerenes and carbon nanotubes*. 1996, San Diego: Academic Press. xviii, 965p.
2. Wang, J.B., et al., *Self-Assembly Made Durable: Water-Repellent Materials Formed by Cross-Linking Fullerene Derivatives*. Angewandte Chemie-International Edition, 2009. **48**(12): p. 2166-2170.
3. Bakry, R., et al., *Medicinal applications of fullerenes*. International Journal of Nanomedicine, 2007. **2**(4): p. 639-649.
4. Brabec, C.J., N.S. Sariciftci, and J.C. Hummelen, *Plastic solar cells*. Advanced Functional Materials, 2001. **11**(1): p. 15-26.
5. Al-Mohamad, A. and A.W. Allaf, *Fullerene-60 thin films for electronic applications*. Synthetic Metals, 1999. **104**(1): p. 39-44.
6. Kanbara, T., et al., *N-channel field effect transistors with fullerene thin films and their application to a logic gate circuit*. Chemical Physics Letters, 2003. **379**(3-4): p. 223-229.
7. Robinson, A.P.G., et al., *A Fullerene derivative as an electron beam resist for nanolithography*. Applied Physics Letters, 1998. **72**(11): p. 1302-1304.
8. Hunt, M.R.C. and R.E. Palmer, *The structural and vibrational properties of C_{60} adsorbed on the graphite(0001) surface*. Surface Review and Letters, 1996. **3**(1): p. 937-942.
9. Liu, H. and P. Reinke, *C_{60} thin film growth on graphite: Coexistence of spherical and fractal-dendritic islands*. Journal of Chemical Physics, 2006. **124**(16): p. 5.
10. Chao, Y., et al., *Photoemission study of chemisorption of C_{60} on InP(100)*. Physical Review B, 2001. **64**(23): p. 6.
11. Chen, D. and D. Sarid, *Growth of C_{60} Films on Silicon Surfaces*. Surface Science, 1994. **318**(1-2): p. 74-82.
12. Schmidt, J., et al., *Film growth and surface reactions of C_{60} on Si(100)H(2x1)*. Physical Review B, 1997. **56**(15): p. 9918-9924.
13. Hunt, M.R.C., et al., *Charge-Transfer and Structure in C_{60} Adsorption on Metal-Surfaces*. Physical Review B, 1995. **51**(15): p. 10039-10047.
14. Maxwell, A.J., et al., *Electronic and geometric structure of C_{60} on Al(111) and Al(110)*. Physical Review B, 1998. **57**(12): p. 7312-7326.
15. Cepek, C., A. Goldoni, and S. Modesti, *Chemisorption and fragmentation of C_{60} on Pt(111) and Ni(110)*. Physical Review B, 1996. **53**(11): p. 7466-7472.
16. Maxwell, A.J., et al., *Photoemission, Autoionization, and X-Ray-Absorption Spectroscopy of Ultrathin-Film C60 on Au(110)*. Physical Review B, 1994. **49**(15): p. 10717-10725.
17. Saltas, V. and C.A. Papageorgopoulos, *Adsorption and decomposition of C_{60} on Ni(110) surfaces*. Surface Science, 2001. **488**(1-2): p. 23-31.
18. Hunt, M.R.C., et al., *Temperature-dependent chemisorption of C_{60} on Mo(110): precursors to cage destruction*. Surface Science, 2000. **454-456**: p. 267-272.
19. Kenny, D.J. and R.E. Palmer, *Nucleation and growth of C_{60} thin films on graphite*. Surface Science, 2000. **447**(1-3): p. 126-132.
20. Rey, C., et al., *Clusters and layers of C_{60} molecules supported on a graphite substrate*. Physical Review B, 1997. **55**(11): p. 7190-7197.
21. Luo, M.F., Z.Y. Li, and W. Allison. *Initial stages of C_{60} thin film growth on graphite*. Chinese Physical Letters, 1997. **21**(12): p. 2493-2495
22. Stimpel, T., et al. *STM studies of C_{60} on a Si(111): B surface phase*. in *Spring Meeting of the European-Materials-Research-Society*. 2001. Strasbourg, France: Elsevier Science Sa.
23. Pedio, M., et al., *C_{60}/metal surfaces: adsorption and decomposition*. Surface Science, 1999. **437**(1-2): p. 249-260.
24. Liu, C.D., et al., *Molecular orientations and interfacial structure of C_{60} on Pt(111)*. Journal of Chemical Physics. **134**(4): p. 6.
25. Zhang, X., et al., *The C_{60}/Au(1 1 1) interface at room temperature: A scanning tunnelling*

microscopy study. Surface Science, 2008. **602**(4): p. 885-892.
26. Murray, P.W., et al., *Growth of C_{60} on Cu(110) and Ni(110) surfaces: C_{60}-induced interfacial roughening*. Physical Review B, 1997. **55**(15): p. 9360-9363.
27. Abel, M., et al., *Scanning tunneling microscopy and x-ray photoelectron diffraction investigation of C_{60} films on Cu(100)*. Physical Review B, 2003. **67**(24): p. 245407.
28. Gimzewski, J.K., et al., *Observation of a New Au(111) Reconstruction at the Interface of an Adsorbed C_{60} Overlayer*. Chemical Physics Letters, 1993. **213**(3-4): p. 401-406.
29. Weckesser, J., et al., *Binding and ordering of C_{60} on Pd(110): Investigations at the local and mesoscopic scale*. Journal of Chemical Physics, 2001. **115**(19): p. 9001-9009.
30. Shin, H., et al., *Floating two-dimensional solid monolayer of C_{60} on graphite*. Physical Review B. **82**(23): p. 11.
31. Schwoebel, R.L., *Step Motion on Crystal Surfaces. II*. Journal of Applied Physics, 1969. **40**(2): p. 614-618.
32. Brune, H., et al., *Anisotropic corner diffusion as origin for dendritic growth on hexagonal substrates*. Surface Science, 1996. **349**(1): p. L115-L122.
33. Cox, E., et al., *Temperature dependence of island growth shapes during submonolayer deposition of Ag on Ag (111)*. Physical Review B, 2005. **71**(11): p. 115414.
34. Liu, H., et al., *Fractal Structures in Fullerene Layers: Simulation of the Growth Process*. The Journal of Physical Chemistry C, 2008. **112**(12): p. 4687-4695.
35. Tsai, J.T.H., et al., *Electric conduction improvement of well-structured multi-walled carbon nanotubes*, in *Tencon 2010: 2010 Ieee Region 10 Conference*, T. Okado, K. Araki, and H. Nishino, Editors, Ieee: New York. p. 963-965.
36. Girifalco, L.A., *Molecular-Properties of C_{60} in the Gas and Solid-Phases*. Journal of Physical Chemistry, 1992. **96**(2): p. 858-861.
37. Hunt, M.R.C., P. Rudolf, and S. Modesti, *Localization of substrate-induced modification in the electronic structure of C_{60} at fullerene-metal interfaces*. Physical Review B, 1997. **55**(12): p. 7882-7888.
38. Gardner, S.D., et al., *Surface characterization of carbon fibers using angle-resolved XPS and ISS*. Carbon, 1995. **33**(5): p. 587-595.
39. Vanderveen, J.F., et al., *Effect of Oxygen Coverage on Surface Relaxation of Ni(110) Measured by Medium Energy Ion Scattering*. Surface Science, 1979. **79**(1): p. 212-218.
40. Owen, E.A. and et al., *An X-ray investigation of pure iron-nickel alloys. Part 4: the variation of lattice-parameter with composition*. 1937. p. 315.
41. Klink, C., et al., *Carbidic carbon on Ni(110): An STM study*. Surface Science, 1996. **360**(1-3): p. 171-179.
42. Benning, P.J., et al., *Electronic States of Solid C_{60} - Symmetries and Photoionization Cross-Sections*. Physical Review B, 1991. **44**(4): p. 1962-1965.
43. Tzeng, C.T., et al., *Photoemission, near-edge x-ray-absorption spectroscopy, and low-energy electron-diffraction study of C_{60} on Au(111) surfaces*. Physical Review B, 2000. **61**(3): p. 2263-2272.
44. Schiessling, J., et al., *Origin of molecular orbital splitting of C_{60} on Al(110)*. Journal of Physics-Condensed Matter, 2004. **16**(36): p. L407-L414.
45. Hunt, M.R.C., et al. *Temperature-dependent chemisorption of C_{60} on Mo(110): precursors to cage destruction*. Surface Science, 2000. **454**(1): p. 267-727
46. Maxwell, A.J., et al., *C 1s ionisation potential and energy referencing for solid C_{60} films on metal surfaces*. Chemical Physics Letters, 1996. **260**(1-2): p. 71-77.
47. Wastberg, B., et al., *Is X-Ray-Absorption Spectroscopy of C_{60} - the Effects of Screening and Core-Hole Relaxation*. Physical Review B, 1994. **50**(17): p. 13031-13034.
48. Rudolf, P., M.S. Golden, and P.A. Bruhwiler, *Studies of fullerenes by the excitation, emission, and scattering of electrons*. Journal of Electron Spectroscopy and Related Phenomena, 1999. **100**: p. 409-433.

49. Gardener, J.A., G.A.D. Briggs, and M.R. Castell, *Scanning tunneling microscopy studies of C60 monolayers on Au(111).* Physical Review B, 2009. **80**(23): p. 235434.
50. Weckesser, J., J.V. Barth, and K. Kern, *Mobility and bonding transition of C_{60} on Pd(110).* Physical Review B, 2001. **64**(16): 161403.
51. Chen, S.P. and A.F. Voter, *Reconstruction of the (310), (210) and (110) Surfaces in FCC Metals.* Surface Science, 1991. **244**(1-2): p. L107-L112.
52. Zhang, J.-M., H.-Y. Li, and K.-W. Xu, *Reconstructed (1 1 0) surfaces of FCC transition metals.* Journal of Physics and Chemistry of Solids, 2006. **67**(8): p. 1623-1628.
53. Voetz, M., et al., *Nitrogen Induced Ni(110)-(2x3) Reconstruction - A Structure Determination with Ion-Scattering Spectroscopy and Scanning Tunnelling Microscopy.* Surface Science, 1993. **292**(3): p. 211-222.
54. Foss, M., et al., *X-Ray Diffraction Investigation of the Sulfur Induces 4x1 Reconstruction of Ni(110).* Surface Science, 1993. **296**(3): p. 283-290.
55. Ruan, L., et al., *A Scanning-Tunnelling Microscopy Investigation of the Ni(110)-P(4x1)s Phase.* Surface Science, 1993. **296**(3): p. 275-282.

8. Summary, Conclusions & Further Work

In this chapter a *summary of the thesis will be given and set in context. Potential avenues for further investigation will also be discussed.*

8.1 Summary

In the introduction to this thesis, the incredible physical properties of carbon nanotubes and their potential applications were discussed. This discussion also introduced the idea that, in order for such applications to be fully realised, the nature of the CNT material being used needs to be completely understood. Chapter 4 set out to address this issue in part by taking four commercially available CNT materials and characterising them using a number of techniques - techniques that are often applied in the literature for 'stand alone' CNT characterisation. From this investigation it was found there are indeed a number of issues with the interpretation of data from some techniques due to the nature of the information provided. Consequently, when applying a single technique to different CNT materials, one may find a reduced distinction/ lack of comparability between CNT species. It was also shown that, certainly, characterisation of CNT materials should not be carried out using a single technique. More positively, it was found that the current (and most widely used) techniques for CNT characterisation, namely HRTEM and Raman spectroscopy, are fairly reliable at characterising CNT materials. However, it was highlighted that the information provided by these techniques is incomplete; they are not able to chemically characterise the samples, nor can they provide nature on the carbon-carbon bonding within the CNTs. Thus it was suggested that, with the addition of XPS, Raman spectroscopy and HRTEM are able to characterise a material fully. A benchmark of CNT 'quality' might therefore include information on of the nature of the walls in a CNT sample and the carbon-carbon bonding within those walls. It might also include the level, structure and chemical nature of any contamination present within the sample.

In the introduction to this thesis it was also noted that the number of defects within a CNT lattice will play a significant role in defining CNT 'quality', since the presence of such defects strongly influence the physical and chemical properties of these materials. Using the information gleaned in Chapter 4, Chapters 5 and 6 set out to understand how ion-induced defects affect the behave in different CNT species. Whilst clear signatures of amorphisation could be observed in SWCNTs, for the same doses no such behaviour was observed in nanotubes with more than one wall. This was attributed to higher damage thresholds, increased rigidity of the nanotube walls and enhanced opportunities for defect 'healing' through inter-wall links and vacancy – interstitial recombination. Hence, the presence of even a second wall can substantially enhance the resistance of carbon nanotubes to radiation-induced damage.

In Chapters 5 and 6 it was also seen that, upon the inclusion of ion-irradiated defects, there is an increase in the reactivity to ambient oxygen of all CNT species (i.e., the number of defects within a CNT lattice directly influences the environmental stability/chemical reactivity of these samples). Furthermore it was shown that the level of chemisorbed oxygen can be controlled through the total dose delivered to the sample. When comparing between the different CNT species, it was also shown that the level of chemisorbed oxygen is higher in SWCNTs than in CNTs with more than one wall and this was attributed to the enhanced healing effects in CNTs with more than one wall. For all CNT species it was shown that the type of oxygen uptake in Ar^+ irradiated air exposed CNTs consists of C-O and C=O present in a ratio of 3:1. This indicates that the interaction between the irradiated tubes and ambient oxygen is the same for all CNT species, suggesting that defect-induced chemisorption primarily occurs at the outermost nanotube wall. In Chapter 5 it was shown that, in SWCNTs, this ratio can be changed to 1:1 if oxidation occurs through O_2^+ ion irradiation. Since the electrical properties are strongly influenced by chemisorbed oxygen species, being able to change this is a controlled manner is a highly exciting prospect.

The interaction of fullerenes with surfaces, in particular C_{60}, is of great interest when considering the potential applications. In the current climate, the application of C_{60} films in solar cell technologies is of particular interest. To enable such applications to reach their maximum potential, fully understanding the interactions occurring at the interfaces in these materials, and the perturbations these interactions induce, is critical. In Chapter 7, the interaction of C_{60} with two different surfaces was considered; one in which the interaction between substrate and adsorbate is weak (graphite) and one in which this interaction is strong (nickel). Despite the weakly interacting nature of the C_{60}/graphite system, novel behaviour is clearly observed: first, the spontaneous symmetry breaking of second and higher layers to form dendritic Y-structures; second, the existence of the first layer molecules in a two-dimensional solid/vapour phase, the vapour phase shown to exhibit ideal gas behaviour. The existence and the behaviour of such two dimensional phases is extremely important in a world where technology is ever shrinking. It is known that C_{60} induces reconstructions of many surfaces and, once again it is important to understand the nature of such reconstructions from both a fundamental and technological viewpoint. In the C_{60}/Ni(110) system the previously suggested nickel reconstruction for a QH1 overlayer was shown to be incorrect.

8.2 Further Work

8.2.1 Carbon Nanotubes

Progression of the work on carbon nanotubes might include extending the work carried out in Chapter 5 and 6 using the additional techniques suggested in Chapter 4 (i.e., Raman spectroscopy and HRTEM). Such work would not be a trivial undertaking, but would serve two main purposes: first, to make inroads into really understanding how defects can be identified, characterised, and quantified by XPS, Raman spectroscopy and HRTEM; second, the identification of the number and type of defects introduced into the different CNT species under ion irradiation.

Further investigation of the effect of ion-irradiation-induced defects on reactivity to other ambient species should be undertaken. For example, it would be interesting to note if there are any changes to the O1*s* lineshape of O_2^+ irradiated SWCNTs exposed to air. This would give information on whether all oxygen-terminated dangling bonds are stable under air exposure and whether the relative amounts of surface C-O and C=O species are permanently fixed. In this respect O_2^+ ion irradiation of DWCNTs and (t)MWCNTs should be investigated. Similarly, Ar^+ ion irradiation in an ambient environment in which the main constituent is oxygen would confirm directly that the observed differences in O1*s* seen in this thesis are due to the relaxation of ion-induced defects before exposure to oxygen. Investigation into the influence of the length of 'relaxation time' (time between irradiation and air exposure) on the ratio of C-O to C=O might also yield interesting results. The following route of investigation is also apparent: comparison of SWCNTs irradiated by low energy, low dose ions of the species to be added to the lattice (e.g., N_2^+, H_2^+, CH_4^+ etc) and exposure of Ar^+ ion irradiated CNTs to ambient environments in which the main constituent is chosen to be that species (e.g., N_2, H_2, CH_4 etc.).

Investigation into the evolution of the π plasmon in the different irradiated CNT species should be pursued. To determine, in particular, whether the free-electron-type model applied in this thesis is suitable. It would be suggested that, in this instance, EELS is used rather than XPS since this would make measurements more accurate.

8.2.2 C_{60}

A natural progression of the work on the C_{60}/HOPG(0001) system includes monitoring the behaviour of the ideal gas behaviour of the free molecules at low temperatures. In the study presented in this thesis, the high temperature limit of this work was reached without compromising the measurements through double counting of molecules and desorption of molecules from the graphite surface. Another interesting avenue of investigation might include looking at the first layer growth of higher fullerenes on the graphite in order to establish whether such systems exhibit a mixed two-dimensional solid/vapour phase. Given the computer simulation used to model the C_{60} gas was simplistic, a clear route for the progression of this work would be the improvement of this simulation, through, for, example, the inclusion of a diffusion barrier or a more realistic energy-dependence of the diffusion probability once a molecule exists within an island. Furthermore, the theoretical coexistence curve derived in this work could be modified to include the van der Waals interactions that are expected to be present between C_{60} molecules. Such an inclusion may account for the deviation between simulation and theory seen at low temperatures.

In terms of the work on the C_{60}/Ni(110) system, the suggested reconstruction could be confirmed through the use of x-ray diffraction or I(V)-LEED measurements. Indeed the latter measurements have been carried out for both the (5x3) and QH1 phases of C_{60} on Ni(110). However, since this analysis of such data is computationally expensive, it has not yet been completed. The reconstruction of the Ni(110) surface presented in Chapter 7, unlike previous models, takes into account both the (5x3) and QH1 models. However, due to time constraints, the work in Chapter 7 did not take into account the experimentally observed QH2 phase. Investigation of such a phase using STM, LEED, UPS and I(V) LEED, and how it fits in with the observed Ni(110) reconstruction for the (5x3) and QH1 phases, would therefore be an extremely interesting and informative route to pursue. Further confirmation of the Ni(110) reconstruction presented in Chapter 7 could be carried out in the form of a check of the reversible nature of the QH1 to (5x3) phase change. Such an experiment would require fine control of the substrate temperature so that the formation of carbide is avoided.

Appendix A: C_{60} Vapour Simulation

```
////////////////////////////////////////////////////////////
/// Motion of C60 on surface: v0.9.1 Last updated 05/02/08 ///
////////////////////////////////////////////////////////////

#include <cstdlib>
#include <iostream>
#include <cmath>
#include <fstream>
#include <iomanip>
#include <dislin.h>//plotting package
#include <windows.h>
#include <gsl/gsl_multimin.h>

using std::cout;
using std::endl;
using std::ios;
using std::setw;
using std::setiosflags;
using std::setprecision;
using std::ifstream;
using std::ofstream;

//GLOBAL CONSTANTS AND VARIABLES:

int lattice[800][800]; //Sample lattice
int particles[500000][4]; //Particle Directions (cols 0&1) and positions (cols 2&3)
int particles_total=13000; //Number of particles-> total particles +7 seeds

double G = 0.475; // the ratio of E/kT
double probability[13];//
double pmax = exp(6.0*G);//maximum probability used for normalising p

int fixed_particles=1; //number of fixed particles (start with seeds & corners)
int c;//variable used to only write particle if stuck particle moves
int added_particles = 1; //particles added every iteration
int j=0;// no particles in c60 gas

//FUNCTION PROTOTYPES:
void WriteOutputFixed(void);
void WriteOutputAll(void);
void InitialDistribution(void);
void MakeDefect(void);
void TestForFix(int particle_number);
void MoveParticle(int particle_number);
void Rebirth(int particle_number);
void ChangeDirection (int particle_number);
void Diffusion (int particle_number);
void TestIfFree (int particle_number);
void Probability (void);
void PlotOutput (void);
void Writexy (void);
void CountFixed(int particle_number);
void AddParticles(void);
void WriteFree(void);

/////////////////
//MAIN PROGRAM://
/////////////////

int main()
{
	//srand((unsigned)time(0)); // Seed the random function so output not
repeatable

	int particle=0;
	int iteration=0;
	int a=0;//variable used to reduce number of output images
	MakeDefect();
```

```
	InitialDistribution();
	Probability();

	for(particle=0;particle<particles_total;particle++){
		TestForFix(particle);
	}

	for(iteration=0;iteration<20000000;iteration++)
	{

		for(particle=0;particle<particles_total;particle++)
		{
			MoveParticle(particle);
			TestForFix(particle);
			Diffusion(particle);
			CountFixed(particle);
		}

		a=a+1;
		if (a==2000)//only create image file every a iterations
		{
			cout<<"Iteration: "<< iteration<<"\r";
		//AddParticles();
		WriteOutputFixed();
		//PlotOutput();
		WriteOutputAll();

		j = particles_total-fixed_particles;

		ofstream WriteFile( "Free.txt", ios::app );

		WriteFile << setw(15) << iteration
			  << setw(15) << j
			  << endl ;

		a=0;
		}

		fixed_particles=1;

	}
	WriteOutputAll();
	WriteOutputFixed();

	system("PAUSE");
	return EXIT_SUCCESS;
}

//////////////////////
//FUNCTION DEFINITIONS:
//////////////////////

void MakeDefect(void){
// create defects
//lattice[200][100]=-1;
//lattice[100][100]=-1;
//lattice[300][200]=-1;
lattice[400][400]=-1;
//lattice[100][200]=-1;
//lattice[300][300]=-1;
//lattice[200][300]=-1;
}

void InitialDistribution(void){

	int a,x,y,z;

	for (a=0;a<particles_total;a++)
	{

		x=1+rand()%798;
		y=1+rand()%798;
```

```
                z=rand()%6;

                while(lattice[x][y]!=0)// check to see if lattice site is occupied
                {
                        x=1+rand()%798;// if occupied give a new x,y and random
                direction
                        y=1+rand()%798;
                        z=rand()%6;
                }

                lattice[x][y]=a;
                particles[a][2]=x;
                particles[a][3]=y;

                switch(z){

                        case 0:
                                particles[a][0]=1;
                                particles[a][1]=0;
                                break;

                        case 1:
                                particles[a][0]=1;
                                particles[a][1]=1;
                                break;

                        case 2:
                                particles[a][0]=0;
                                particles[a][1]=1;
                                break;

                        case 3:
                                particles[a][0]=-1;
                                particles[a][1]=0;
                                break;

                        case 4:
                                particles[a][0]=-1;
                                particles[a][1]=-1;
                                break;

                        case 5:
                                particles[a][0]=0;
                                particles[a][1]=-1;
                                break;
                        }
        }
}

void ChangeDirection (int particle)//function to designate each particle a random
dire
{
        int z;
        z=rand()%6;


        switch(z){

                case 0:
                        particles[particle][0]=1;
                        particles[particle][1]=0;
                        break;

                case 1:
                        particles[particle][0]=1;
                        particles[particle][1]=1;
                        break;

                case 2:
                        particles[particle][0]=0;
                        particles[particle][1]=1;
                        break;
```

```
                case 3:
                        particles[particle][0]=-1;
                        particles[particle][1]=0;
                        break;

                case 4:
                        particles[particle][0]=-1;
                        particles[particle][1]=-1;
                        break;

                case 5:
                        particles[particle][0]=0;
                        particles[particle][1]=-1;
                        break;
                }
                // cout<< "CD" << endl;
}

void TestForFix (int particle){

        int x, newx;
        int y, newy;
        int c=0;

        x=particles[particle][2];
        y=particles[particle][3];

        if (x<799 && y<799 && x>0 && y>0)//to avoid confusion with particles
crossing bound
        {
        if (   lattice[x+1][y] == -1 // check whether nearest neighbours are stuck
            || lattice[x][y+1] == -1
            || lattice[x-1][y] == -1
            || lattice[x][y-1] == -1
            || lattice[x+1][y+1] == -1
            || lattice[x-1][y-1] == -1 )
            {
                lattice[x][y]=-1;// particle sticks if any of nearest neighbours is
        stuck
                particles[particle][0]=0; // reset direction to zero
                particles[particle][1]=0;

                if (c==0)
                {c=c+1;}
                }
}
}

void MoveParticle(int particle){

        int x;
        int y;
        int newx;
        int newy;
        double p,r;


        x=particles[particle][2];
        y=particles[particle][3];

        newx = x + particles[particle][0];
        newy = y + particles[particle][1];

        if (newx>799)// boundary conditions applied
                { newx=0;}

        if (newy>799)
                {newy=0;}

        if (newx<0)
                {newx=799;}
```

```
        if (newy<0)
                {newy=799;}

        p= exp(-G);

        r = (float)rand()/RAND_MAX; // random number between 0 and 1
        //cout<<p<<endl;

                if (lattice [newx][newy]==0 && r<=p)//if new lattice position is
        empty
                {
                        particles[particle][2]=newx;//move particle
                        particles[particle][3]=newy;
                        lattice[x][y]=0;//set old position to zero
                        lattice[newx][newy]=particle;//set new lattice point as
                particle
                }
        ChangeDirection(particle);//change direction of particle for random hopping
}

void Rebirth(int particle){

        int x;
        int y;
        int z;

        x=1+rand()%798;
        y=1+rand()%798;
        z=rand()%6;

        while(lattice[x][y]!=0)
        {
                x=1+rand()%798;
                y=1+rand()%798;
                z=rand()%6;
        }

lattice[x][y]=particle;
particles[particle][2]=x;
particles[particle][3]=y;

        switch(z){

                case 0:
                        particles[particle][0]=1;
                        particles[particle][1]=0;
                        break;

                case 1:
                        particles[particle][0]=1;
                        particles[particle][1]=1;
                        break;

                case 2:
                        particles[particle][0]=0;
                        particles[particle][1]=1;
                        break;

                case 3:
                        particles[particle][0]=-1;
                        particles[particle][1]=0;
                        break;

                case 4:
                        particles[particle][0]=-1;
                        particles[particle][1]=-1;
                        break;

                case 5:
                        particles[particle][0]=0;
                        particles[particle][1]=-1;
```

```
                    break;
                }
}

void WriteOutputFixed(void)
{
ofstream WriteFile( "ParticlePositionsFixed.txt", ios::out );

int x=0;
int y=0;
int a=0;

for (a=0;a<particles_total;a++)
{

        x=particles[a][2];
        y=particles[a][3];

        if(lattice[x][y]==-1)
        {
                WriteFile << setw(15) << static_cast<double>(x)-(static_cast<double>
                          << setw(15) << y
                          << endl ;
        }
}
//seeds
x=200;
y=400;
WriteFile << setw(15) << x
          << setw(15) << y
          <<endl;
// x=0;
// y=200;
// WriteFile << setw(15) << x
// << setw(15) << y
// <<endl;
// x=50;
// y=100;
// WriteFile << setw(15) << x
// << setw(15) << y
// <<endl;
// x=50;
// y=300;
// WriteFile << setw(15) << x
// << setw(15) << y
// <<endl;
// x=150;
// y=300;
// WriteFile << setw(15) << x
// << setw(15) << y
// <<endl;
//
// x=200;
// y=200;
// WriteFile << setw(15) << x
// << setw(15) << y
// <<endl;
//
// x=150;
// y=100;
// WriteFile << setw(15) << x
// << setw(15) << y
// <<endl;
//corners
x=-50;
y=350;
WriteFile << setw(15) << x
<< setw(15) << y
<<endl;
x=-50;
y=50;
WriteFile << setw(15) << x
```

```
<< setw(15) << y
<<endl;
x=250;
y=50;
WriteFile << setw(15) << x
<< setw(15) << y
<<endl;
x=250;
y=350;
WriteFile << setw(15) << x
<< setw(15) << y
<<endl;
}

void WriteOutputAll(void)
{
ofstream WriteFile( "ParticlePositionsAll.txt", ios::out );

int x=0;
int y=0;
int a=0;

for (a=0;a<particles_total;a++)
{
       x=particles[a][2];
       y=particles[a][3];

       WriteFile << setw(15) << static_cast<double>(x)-(static_cast<double>(y)/2)
                 << setw(15) << y
                 << endl ;
       }
       x=200;
       y=400;
       WriteFile << setw(15) << x
                 << setw(15) << y
                 <<endl;
}

void Diffusion(int particle)

     { int x,y,z;
       int newx,newy;
       int a=0;
       int b=0;
       int delta;
       double r;// random number between 0 and 1
       double p;// probablility of moving

       x=particles[particle][2];
       y=particles[particle][3];

if(lattice[x][y]==-1)
{
// { //cout<< particle<< " :D" << endl;
               if (lattice[x+1][y] ==-1)//count current number of nearest neighbours
               {a=a+1;}
               if (lattice[x][y+1] ==-1)
               {a=a+1;}
               if (lattice[x-1][y] ==-1)
               {a=a+1;}
               if (lattice[x][y-1] ==-1)
               {a=a+1;}
               if (lattice[x+1][y+1] ==-1)
               {a=a+1;}
               if (lattice[x-1][y-1] ==-1)
               {a=a+1;}

               //cout <<"a : " << a << endl;

               z=rand()%6;//give particle a possible random direction

               switch(z){
```

```
                case 0:
                        particles[particle][0]=1;
                        particles[particle][1]=0;
                        break;

                case 1:
                        particles[particle][0]=1;
                        particles[particle][1]=1;
                        break;

                case 2:
                        particles[particle][0]=0;
                        particles[particle][1]=1;
                        break;

                case 3:
                        particles[particle][0]=-1;
                        particles[particle][1]=0;
                        break;

                case 4:
                        particles[particle][0]=-1;
                        particles[particle][1]=-1;
                        break;

                case 5:
                        particles[particle][0]=0;
                        particles[particle][1]=-1;
                        break;
                }

        newx = x + particles[particle][0];//calculate nex x and y
        newy = y + particles[particle][1];

        {if (lattice[newx+1][newy] ==-1)//count possible number of NN
        {b=b+1;}
        if (lattice[newx][newy+1] ==-1)
        {b=b+1;}
        if (lattice[newx-1][newy] ==-1)
        {b=b+1;}
        if (lattice[newx][newy-1] ==-1)
        {b=b+1;}
        if (lattice[newx+1][newy+1] ==-1)
        {b=b+1;}
        if (lattice[newx-1][newy-1] ==-1)
        {b=b+1;}

        //cout <<"b : " << b << endl;

        r = (float)rand()/RAND_MAX; // random number between 0 and 1

        delta = b-a;//difference in new- current NN

        p = probability[delta];

        if (lattice[newx][newy]==0)//if new possible lattice site is empty
                {
                if (r<=p)//conditions for particle to move
                {//cout<<"delta"<<delta<<endl;
                particles[particle][2]=newx;
                particles[particle][3]=newy;
                lattice[newx][newy]=-1;
                lattice[x][y]=0;
                x=newx;
                y=newy;

                if(c==0)
                {c=c+1;}
                }
        }
TestIfFree(particle);// if particle has no NN then it is a free particle
```

```
        particles[particle][0]=0;//reset direction of motion to zero
        particles[particle][1]=0;
}
        }
}

void TestIfFree (int particle){

int x;
int y;

x=particles[particle][2];
y=particles[particle][3];

               if (lattice[x+1][y] == 0 // check whether particle has become free
                && lattice[x][y+1] == 0
                && lattice[x-1][y] == 0
                && lattice[x][y-1] == 0
                && lattice[x+1][y+1] == 0
                && lattice[x-1][y-1] == 0 )
                {lattice[x][y]=particle;
                // cout<< "particle is free"<<endl;
               }
}

void Probability (void) {

        double p;
        int i;

        for (i=-6;i<=6;i++)
        {probability[i]= exp(G*(float)i)/pmax;
        }
}

void PlotOutput (void) {

        int particle;
        // float n[particles_total],m[particles_total];//plot all particles
        float n[fixed_particles],m[fixed_particles];//plot fixed particles

        ifstream fin("ParticlePositionsFixed.txt");//
        //ifstream fin("ParticlePositionsAll.txt");//

        //for(particle=0;particle<particles_total; particle++)
        //{fin >>n[particle]>>m[particle];
        //}

        for(particle=0;particle<fixed_particles; particle++)
        {fin >>n[particle]>>m[particle];
        }
        metafl("TIFF");
        disini();

        pagfll(255);//white background
        color("black");//black data symbols
        hsymbl(9);//symbol size
        marker(1);//symbol type
        ticpos("revers", "x");//set x ticks to inside
        ticpos("revers", "y");//set y ticks to inside
        name("x(nm)","x");//x axis label
        name("y(nm)","y");//y axis label

        qplsca(n,m,fixed_particles);//scatter plot
        //qplsca(n,m,particles_total);//scatter plot
        //disfin();
        }

void CountFixed (int particle){

int x,y;
```

```
        x=particles[particle][2];
        y=particles[particle][3];
        if (lattice[x][y] == -1) // if particle is stuck
                {
                fixed_particles=fixed_particles+1;//count number of fixed particles
                }
}

void AddParticles(void)// constant flux of particles.
{
int a,x,y,z;

for (a=0;a<added_particles;a++)
{
x=rand()%800;
y=rand()%800;
z=rand()%6;

while(lattice[x][y]!=0)// check to see if lattice site is occupied
{
        x=rand()%800;// if occupied give a new x,y and random direction
        y=rand()%800;
        z=rand()%6;
}

lattice[x][y]=a;
particles[a][2]=x;
particles[a][3]=y;

switch(z){

        case 0:
                particles[a][0]=1;
                particles[a][1]=0;
                break;

        case 1:
                particles[a][0]=1;
                particles[a][1]=1;
                break;

        case 2:
                particles[a][0]=0;
                particles[a][1]=1;
                break;

        case 3:
                particles[a][0]=-1;
                particles[a][1]=0;
                break;

        case 4:
                particles[a][0]=-1;
                particles[a][1]=-1;
                break;

        case 5:
                particles[a][0]=0;
                particles[a][1]=-1;
                break;
        }
}
        particles_total = particles_total + added_particles;
        //cout <<particles_total<<endl;
}

void WriteFree(void)
{

}
```